

"Far-red and near-infrared emitters for cell imaging"

Zur Erlangung des akademischen Grades eines

DOKTORS DER NATURWISSENSCHAFTEN

(Dr. rer. nat.)

von der KIT-Fakultät für Chemie und Biowissenschaften

des Karlsruher Instituts für Technologie (KIT)

genehmigte

DISSERTATION

von

M. Sc. Roberta Tabone

aus Licata

Dekan: Prof. Dr. Hans-Achim Wagenknecht

Referent: Dr. Claudia Bizzarri

Korreferent: Prof. Dr. Andreas Neil Unterreiner

Tag der mündlichen Prüfung: 18.07.2023

German Title of this Thesis:

**“Tiefrot- und Nahinfrarot-Emitter
für Zell-Imaging”**

*A mio nonno Carmelo,
la figura paterna che ha creduto
in me prima ancora che lo facessi io.*

“I am not afraid of storms, for I am learning how to sail my ship”.

Louisa May Alcott

Honesty Declaration

The present work was carried out at the Karlsruhe Institute of Technology, Faculty of Chemistry and Biosciences, Institute of Organic Chemistry in the period from January 15th, 2020, to June 12th, 2023, under supervision of Dr. Claudia Bizzarri, including a visit period at the, University of Edinburgh, EastChem School of Chemistry, in the period from May 1st, 2022, to August 1st, 2022, under the supervision of Prof. Dr. Jason Love.

The present work was supported in the scope of the project GRK 2039, Research Training Group, “Molecular Architectures for Fluorescent Imaging of Cells”.

Hereby I, *Roberta Tabone*, declare truthfully that I have prepared this thesis autonomously except for the help explicitly stated in the treatise itself; that I have exhaustively and accurately indicated all auxiliary means; and that I have marked all portions taken, verbatim or in altered form, from the work of others or my own publications. This thesis has not been submitted to any university before.

Die vorliegende Arbeit wurde im Zeitraum vom 15. Januar 2020 bis 12. Juni 2023 am Institut für Organische Chemie der Fakultät für Chemie und Biowissenschaften am Karlsruher Institut für Technologie (KIT) unter der Leitung von Dr. Claudia Bizzarri, und im Zuge eines Forschungsaufenthalts an der University of Edinburgh vom 1. Mai 2022 bis 1. August 2022 unter der Leitung von Prof. Dr. Jason Love, durchgeführt.

Diese Arbeit wurde im Rahmen des GRK 2039 Graduiertenkollegs „Molecular architecture for fluorescent cell imaging“ gefördert.

Hiermit versichere ich, die vorliegende Arbeit selbstständig verfasst und keine anderen als die angegebenen Quellen und Hilfsmittel verwendet sowie Zitate kenntlich gemacht zu haben.

Karlsruhe, June 12th, 2023, Roberta Tabone

Abstract

In recent decades, fluorescence has gained significant importance in biological sciences applications. In particular, the field of optical imaging has witnessed the development of far-red to near-infrared (NIR) dyes. By extending the emission wavelengths into the so-called *biological window*, these dyes have overcome limitations associated with background interferences, tissue absorption and autofluorescence, thus enabling deeper tissue penetration and improving sensitivity, reshaping the landscape of imaging and diagnostic. Nevertheless, the design of an ideal imaging probe which fulfills all the requirements, *i.e.*, fluorescence maxima ranging from 650 to 900 nm, large Stokes shifts, high fluorescence quantum yields in polar solvents accompanied by high stability and low toxicity, still represents a major challenge. Alongside the copious repertoire of organic NIR dyes, coordination metal complexes have gained increasing prominence, propelling the field forward. Despite their remarkable performances, several challenges persist.

Although dipyrrens have long been considered trivial compounds, in this work the synthetic approaches exploited to access far-red dipyrrens are highlighted, including the π -conjugation with aromatic groups *via* functionalization of the α positions of the core, the replacement of the *meso* carbon e.g., the formation of aza-dipyrrens, the benzannulation at the *a* bond of the skeleton by introducing fused structures and the formation of Schiff-base macrocycles. With the tailor-made design proposed in this thesis, several heteroleptic bis(dipyrrenato)Zn^{II} complexes with emissions up to 800 nm and enhanced quantum yields in polar solvents were obtained. These molecular architectures feature the advantage of working on two distinct chelating units, thereby enabling the modulation of the dye properties achieving enhanced stability, tunable photophysical properties and resistance to photobleaching, thus ensuring reliable imaging. The detailed investigations through confocal microscopy confirmed the versatility of these luminescent complexes, which are suitable for the use as probes for live- and fixed-cell imaging. Further, the peculiar design of these dyes ensures large *pseudo* Stokes shifts, an appealing property which improves the accuracy of fluorescence detection, corroborating their relevance in bioimaging applications.

Each section of this thesis presents the retrosynthetic strategy accompanied by a detailed explanation of the synthetic procedures and the conducted characterization performed.

Kurzzusammenfassung

In den letzten Jahrzehnten hat die Bedeutung von fluoreszenten Molekülen in biologischen Anwendungen deutlich zugenommen. Insbesondere in der optischen Bildgebung wurde die Entwicklung von Farbstoffen für den tiefroten bis nahinfraroten (NIR) Bereich vorangetrieben. Durch die Verschiebung der Emissionswellenlängen in das sogenannte „biologische Fenster“ (engl. *biological window*) können durch diese Farbstoffe Limitierungen wie Hintergrundinterferenz, Gewebeabsorption und Autofluoreszenz umgangen werden. Dies erzielt das Eindringen in tiefere Gewebeschichten und eine erhöhte Sensitivität. Dennoch stellt das Design von optimalen bildgebenden Farbstoffen weiterhin eine Herausforderung dar, da diese eine Zahl an Anforderungen erfüllen müssen: Eine Emission im Bereich von 650 bis 900 nm, einen großen Stokes-Shift, hohe Quantenausbeuten in polaren Lösungsmitteln in Kombination mit einer hohen Stabilität und niedrigen Toxizität. Neben der großen Bandbreite an organischen NIR-Farbstoffen, gewinnen Koordinationskomplexe an Popularität. Trotz ihrer bemerkenswerten Performanz bestehen weitere Herausforderungen.

Obwohl Dipyrrine lange Zeit als triviale Verbindungen abgetan wurden, wird in dieser Arbeit auf die synthetischen Herangehensweisen eingegangen, um Zugang zu tiefroten Dipyrrinen zu erhalten. Dazu werden im Folgenden Methoden zur Erweiterung des konjugierten π -Systems mit aromatischen Gruppen über die Funktionalisierung der α -Position der Gerüststruktur, der Austausch des meso-Kohlenstoffs zum Zugang zu aza-Dipyrrinen, der Benzannulierung an der α -Bindung der Gerüststruktur, durch die Einführung von fusionierten Strukturen, und die Bildung von Schiff-basen Makrozyklen beschrieben. Mit dem maßgeschneiderten Design, welches in dieser Arbeit vorgeschlagen wird, konnten eine Zahl an heteroleptischen bis(dipyrrinato)Zn^{II} Komplexen mit einer Emission von bis zu 800 nm und verbesserten Quantenausbeuten in polaren Lösungsmitteln erreicht werden. Diese molekularen Strukturen bieten den Vorteil des Arbeitens an zwei unabhängigen chelatisierenden Einheiten, wodurch die Modulierung der Farbstoffeigenschaften erleichtert wird. Daraus resultiert eine erhöhte Stabilität, einstellbare photophysikalische Eigenschaften und eine Resistenz gegenüber Photobleaching, wodurch verlässliche Bildgebung gewährleistet wird. Detaillierte Untersuchungen mit Hilfe von Konfokalmikroskopie zeigten die Vielseitigkeit dieser lumineszenten Komplexe, die sich als geeignete Sonden für die Bildgebung in lebenden und fixierten Zellen. Des Weiteren sorgt das einzigartige Design für einen großen pseudo-Stokes-Shift, eine erwünschte Eigenschaft, die zu einer Verbesserung der Präzision in der

Fluoreszenzdetektion führt, und damit deren Relevanz in biologischen Anwendungen unterstreicht.

In den Kapiteln dieser Arbeit werden die retrosynthetischen Strategien, die detaillierten Erklärungen der synthetischen Verfahren, sowie der durchgeführten Charakterisierungen beschrieben.

Table of Contents

Honesty Declaration.....	I
Abstract.....	III
Kurzzusammenfassung	V
1. Introduction	1
1.1 Phosphorescence and fluorescence	1
1.2 Fluorophores: definition and characteristics	4
1.2.1 Organic dyes	6
1.3 Bioimaging: past, present and future.....	8
1.3.1 Imaging techniques.....	9
1.3.2 Optical imaging: advantages of near infrared window.....	10
1.4 Near-infrared dyes for fluorescence imaging.....	12
1.5 Dipyrrins: overall backdrop	16
1.5.1 Structures and tautomers.....	17
1.5.2 Building blocks in nature.....	20
1.6 Dipyrrinato metal complexes: structures and geometries	22
1.6.1 N ₄ -and N ₆ - donor set-geometries.....	22
1.6.2 N ₂ O ₂ -type.....	23
1.7 Bis(dipyrrinato)Zn ^{II} complexes.....	25
1.7.1 How to tune the fluorescence	25
1.7.2 Applications.....	28
1.8 Boron-dipyrromethene complexes	34
1.9 Luminescent coordination compounds for cell imaging	36
1.9.1 Zinc complexes.....	37
2. Aim of the thesis	41
3. Main Part.....	43

3.1 <i>Meso</i> -substituted plain dipyrin ligands	43
3.1.1 Synthesis.....	45
3.1.2 Functionalization with alkyne groups.....	50
3.1.3 Synthesis of water-soluble derivatives	53
3.1.4 Photophysical properties.....	57
3.2 π -expanded dipyrin ligands.....	61
3.2.1 Knoevenagel condensation: general background	62
3.2.2 Synthesis.....	63
3.2.3 Photophysical properties.....	70
3.3 Homoleptic bis(dipyrinato)Zn ^{II} complexes.....	79
3.3.1 Synthesis.....	80
3.3.2 Photophysical properties.....	81
3.4 Heteroleptic bis(dipyrinato)Zn ^{II} complexes.....	87
3.4.1 Synthesis.....	88
3.4.2 Photophysical properties.....	89
3.4.3 Photophysical properties at 77 K.....	97
3.4.4 Transient absorption spectroscopy	100
3.5 π -extended bulky pyrroles.....	107
3.5.1 Synthesis.....	107
3.5.2 Complexation.....	108
3.5.3 Photophysical properties.....	112
3.5.4 Synthesis of 2-methyl-4-phenyl-1 <i>H</i> -pyrrole	113
3.6 Aza-dipyrinato ligands.....	117
3.6.1 Synthesis from α , β -unsaturated ketones	118
3.6.2 Synthesis from pyrrole building blocks.....	122
3.7 Benzo[<i>a</i>]- and [<i>b</i>]fused dipyrins: strategy	124
3.7.1 Benzo[<i>a</i>]fused systems with aryl groups in <i>meso</i> position.....	125

3.7.2 Benzo[<i>a</i>]fused systems with an imine in <i>meso</i> position.....	141
3.7.3 Benzo[<i>b</i>]fused systems with aryl groups in <i>meso</i> position.....	143
3.7.4 Benzo [<i>b</i>]fused system with aza group in <i>meso</i> position.....	144
3.8 Applications in bio-imaging.....	146
3.8.1 Cell viability tests	146
3.8.2 Photophysical insights	152
3.8.3 Confocal microscopy of the heteroleptic bis(dipyrrinato) Zn ^{II} complexes	159
3.8.4 Encapsulation in liposomes	172
3.9 Schiff-base dipyrin macrocycles.....	182
4. Subproject_3DNAActive.....	191
4.1 General background	191
4.2 Synthetic procedure.....	193
4.3 Post-functionalization.....	194
4.4 Further strategy	195
5. Conclusion	198
5.1 <i>Meso</i> -substituted plain dipyrins	198
5.2 π -expanded dipyrins.....	199
5.3 Homo-and heteroleptic bis(dipyrrinato)Zn ^{II} complexes	201
5.4 Expanded and azadipyrins	203
5.5 Benzofused systems	204
5.5 Macrocycles	205
6. Experimental Section.....	208
6.1 General Remarks	208
6.1.1 Materials and Methods	208
6.1.2 Solvents and chemicals.....	208
6.1.3 Reaction monitoring and product purification.....	208
6.1.4 Devices and analytical instruments	209

6.1.5	Cell tests.....	211
6.1.5.1	Cytotoxicity Assay	211
6.1.5.2	Confocal laser microscopy and co-staining experiments.....	211
6.1.5.3	Cross-linking fixative procedure and fixed-cell imaging.....	212
6.2	Synthetic procedures and analytical data	213
6.2.1	<i>Meso</i> -substituted dipyrins	213
6.2.2	π -expanded dipyrins	224
6.2.3	Homoleptic bis (dipyrinato)Zn ^{II} complexes.....	237
6.2.4	Heteroleptic bis (dipyrinato)Zn ^{II} complexes.....	243
6.2.5	π -extended systems	254
6.2.3	Benzofused systems	259
6.2.4	Schiff-base dipyrin macrocycles.....	263
6.2.5	Subproject.....	272
7.	List of abbreviations	273
8.	Bibliography	275
9.	Appendix.....	293
9.1	Curriculum Vitae.....	293
9.2	Publications and conference contributions.....	294
9.3	Acknowledgments.....	295

1. Introduction

Science has long been a pivotal presence in people's lives, driving significant advancements. Not unexpectedly, the discoveries made centuries ago have reflected their impact on modern society, continuing to shape and enhance the world.

Traditionally, there has been the widespread belief that the diverse scientific disciplines are entirely separate and different from one another. However, upon closer examination, it becomes clear that they are inextricably linked and interdependent, each contributing to the progress and enrichment of the others.

This is the fundamental underlying concept of the Research Training Group (RTG) 2039, the financial institution that has supported this research project. This interdisciplinary approach aims to develop fluorescent probes, that empower researchers to investigate biological questions using optical imaging techniques.

The basic principles governing the versatility of such probes will be explored, providing a detailed and accurate insights into the subject matter.

Within this context, chemistry assumes a key role as the core discipline from which it is possible to develop molecules suitable for this application.

1.1 Phosphorescence and fluorescence

Luminescence is a fascinating and essential phenomenon, having a wide range of applications, present in our modern daily lives.

The term *luminescence*, derived from the Latin word *lumen* (light), was first introduced by the physicist Eilhard Wiedemann in 1888, to indicate all light phenomena not caused solely by a rise in temperature, known as incandescence.^[1] Specifically, this process is nowadays defined as the spontaneous emission of radiation from an electronically or vibrationally excited species.^[2]

Devices can generate light by forming transient electronically excited states, which, partially or totally, deactivate *via* the emission of electromagnetic radiations in the different spectral regions forming the electromagnetic spectrum.

Depending on the excitation process, the luminescence can be differentiated into: *thermoluminescence*, that refers to the emission of light due to heating; *electroluminescence*,

which is caused by an electrical field; *piezo/triboluminescence*, taking place upon a mechanical action; *chemiluminescence* which is originated by a chemical reaction, and *photoluminescence*, caused by the absorption of light.^[3] Although many new luminescence types have been discovered and investigated, they all belong to the six categories mentioned above and proposed by Wiedemann.

Over the past two decades, there has been a significant rise in the interest surrounding photoluminescence due to the growing demand for sustainable and efficient solutions in analytical chemistry, lighting, displays, and clinical applications.

As previously anticipated, photoluminescence is the emission of light from direct photoexcitation of the emitting species, which can be distinguished into phosphorescence and fluorescence.^[2] The word *phosphorous* comes from the ancient Greek φώς (phos), meaning light, and the suffix φόρος (-phoros), meaning “to bear”. Thus, phosphorescence means “tending to bear light”. This term had been used since the Middle Ages to describe minerals that glowed in the dark after exposure to light.^[3,4]

Later on, in the mid-19th century, Sir Gabriel George Stokes introduced in his famous paper entitled “On the Refrangibility of Light” the term *fluorescence* to describe the ability of *fluorspar* (also named *fluorite*) to change colour from uncoloured to blue upon irradiation.^[5] Initially, the distinction between the two phenomena was based on the emission duration after the end of the excitation: in fluorescence the emission disappeared immediately, while in phosphorescence the emitted light persisted. The usual condition to observe phosphorescence is that the excited species pass through an intermediate state before the emission, as stated for the first time by Francis Perrin in 1929.^[6] More precisely, in the framework of molecular photochemistry, the spin multiplicity is retained in the case of fluorescence, whereas in phosphorescence a change typically from singlet to triplet is observed.

A helpful approach to understand the details of the excitation and the emission processes is to render it as a diagram, first conceived by Alexander Jablonski in the 1930s (**Figure 1**).^[7]

The absorption of light (photons) by a population of molecules induces the transition of electrons from the singlet ground electronic level S_0 to an excited state S_n ($n > 1$). At the excited state a molecule is unstable; therefore, from S_n it returns to the lowest vibronic energy level of the first excited state S_1 by dissipating a part of energy in the surrounding environment through *internal conversion* or vibronic relaxation pathways.

It should be noted that, because of the much more significant energy gap, the internal conversion from S_1 to S_0 is possible but less efficient than the conversion from S_2 to S_1 . The

excited molecule will reach the ground state S_0 following several competitive processes with different probabilities.^[8]

Fluorescence is the emission of photons accompanying the $S_1 \rightarrow S_0$ transition having a radiative rate constant k_r . Being an emission where the spin multiplicity of the molecule is preserved,^[9] it is permitted by the selection rules determining a process in the nanosecond timescale. Part of the absorbed energy is dissipated non-radiatively in the medium as heat, with a rate constant k_i .

Excited molecules can release some of their energy to the nearby molecules through an *energy transfer*, which occurs with a rate constant k_q in the case of *collisional quenching* or with a rate constant k_t in the case of *energy transfer at a distance*.

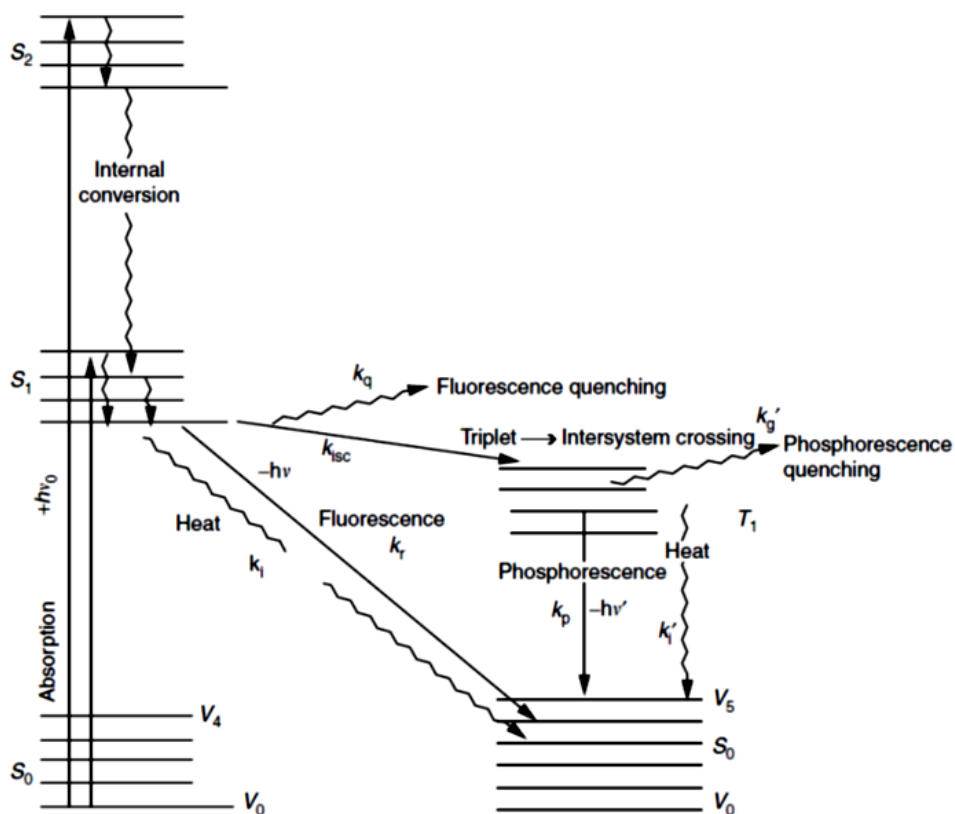


Figure 1: Exemplary Perrin-Jablonski diagram illustrating possible relaxation processes to the ground state S_0 for an excited photon. Thick lines represent electronic energy levels; thin lines are the associated vibrational levels. Straight arrows represent radiative processes, whereas wavy arrows stand for nonradiative ones.^[10]

In some cases, a transition can occur from S_1 to the excited triplet state T_1 located at lower energy, *via intersystem crossing*, with a rate constant k_{isc} . Similarly to what was observed for S_1 , the molecule can return to the ground state S_0 by *dissipation of non-radiative energy* with a

rate constant k'_i and/or by *energy transfer* to another molecule at a distance (rate constant k'_i) or by collision (rate constant k'_q). Otherwise, a photon is emitted from the triplet excited state, with a rate constant k_p , through *phosphorescence*. The process is a spin-forbidden transition since it involves states of different multiplicity; thus, it is usually slower (in the micro- and millisecond timescale) than fluorescence.

However, as predicted by Perrin, the distinction based only on the emission duration is not valid. It is well-established that there are long-lived fluorescence states whose decay times are comparable to those of short-lived phosphorescence (ca. 0.1-1 μ s).^[11]

In **Table 1**, are outlined the lifetime associated for each specific photophysical process.

Table 1: Time scale of each photophysical process occurring in the Perrin-Jablonski diagram in order of fastest to slowest.

Process	Time Scale (seconds)
Absorption (Excitation)	10^{-15}
Internal Conversion	$10^{-14} \sim 10^{-10}$
Vibrational Relaxation	$10^{-12} \sim 10^{-10}$
Fluorescence	$10^{-9} \sim 10^{-7}$
Intersystem Crossing	$10^{-10} \sim 10^{-8}$
Non-Radiative Relaxation / Quenching	$10^{-7} \sim 10^{-5}$
Phosphorescence	$10^{-3} \sim 10^2$
Non-Radiative Relaxation / Quenching	$10^{-3} \sim 10^2$

1.2 Fluorophores: definition and characteristics

In recent years, luminescent organic molecules have gained significant attention in materials science, biology, and optoelectronics.^[12] Their emissive properties arise from the presence of a chromophore, which is responsible of absorbing and subsequently emitting light of a different wavelength. A chromophore that emits a photon is called “fluorophore”, even if not all chromophores exhibit fluorescence.

The emission spectrum, which is independent of the excitation wavelength according to Kasha’s rule,^[9] is typically a “mirror image” of the absorption spectrum of the $S_0 \rightarrow S_1$ transition. This can be observed in **Figure 2**, where are reported the absorption and emission spectra of coumarin.^[13] The electronic excitation does not significantly alter the nuclear

geometry, thus the spacing of the vibrational energy levels of the excited states is identical to the ground state. According to Perrin-Jablonski diagram (**Figure 1**), fluorescence occurs at lower energies (longer wavelengths) than the first absorption band.

The gap between the maximum of the first absorption band and the maximum of fluorescence is called “Stokes shift,” since the phenomenon was first observed by Sir G.G. Stokes (**Figure 2**).^[5]

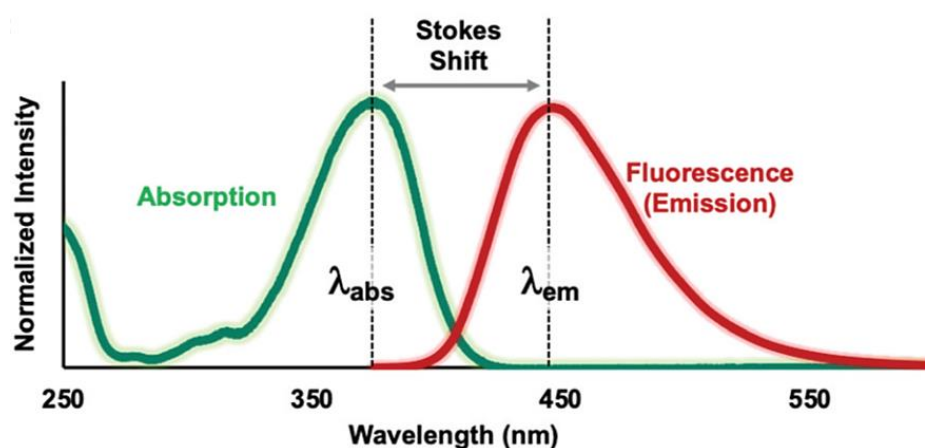


Figure 2: Absorption and fluorescence spectra of coumarin, with schematic view of the Stokes shift, absorption maximum (λ_{abs}) and emission maximum (λ_{em}). Reprinted with permission from RSC, J. Jun, D. M. Chenoweth, E. J. Petersson, *Org. Biomol. Chem.*, **2020**, 18, 5747.

The Stokes shift is calculated as the difference (in energy, wavenumber, or frequency units) between the maxima of absorption and emission spectra of the same electronic transitions. They are often reported in wavelength units, but this is incorrect because it depends on the absorption wavelength.^[11]

The severe crosstalk between the excitation and emission spectra generally results in poor signal-to-noise ratio and self-quenching on current microscope configurations.^[14] Much effort is devoted to enlarging the Stokes shift due to the growing demand for fluorescent dyes in super-resolution microscopy.^[15,16] Other alternatives to achieve fluorophores with significant and tuneable Stokes shift include solvent cage relaxation,^[17] twisted intramolecular charge transfer,^[18,19] and pseudo-Stokes shift through donor-acceptor energy transfer.^[19,20]

Photoluminescent lifetime and quantum yield are two additional essential parameters that define the emissive properties of a fluorophore.^[11] The former represents the time window of observation of the dynamic phenomena and can be calculated, for example, by measuring the

fluorescence intensity over time after the excitation with pulse irradiation sources (TCSPC, time-correlated single photon counting). Instead, the photoluminescent quantum yield (PLQY) measures the efficiency of the emissive process and it is the ratio between the number of photons emitted by the fluorophore and the number of photons absorbed.

1.2.1 Organic dyes

Organic emitters are nowadays pervasive in human existence (from TVs, smartphones, prototypical and commercial chemical sensors, to photovoltaic cells) because of their advantages, including easy tunability of optical and electrical properties by tailoring the molecular structure, flexibility, and relatively low cost.^[21]

Most organic molecules developed and studied usually emit light within the visible range, from violet to red. From a practical point of view, display technologies require the emission of light that the human eye can see and therefore photodetectors for recognizing visible light are usually elementary and relatively affordable.^[22] In the second place, detecting light in the near-infrared (NIR) range is usually more challenging, since the photodetectors usually require to be cooled to cryogenic temperatures to limit background noise.^[23]

Nonetheless, there is a growing emphasis on developing suitable materials for efficient near-infrared emission (700-1000 nm), to enable new classes of applications, spanning from through-space, short-range communications to biomedical sensors, night vision, and more generally, security applications.^[24]

In principle, the emission in the NIR is beneficial for the stability of the materials and, thus, for the durability of the devices. In fact, the energy involved in the generation and decay of the excited species is much smaller for NIR than for UV emission (~ 1.1 - 1.18 eV in the 700-1000 nm window *vs.* ≥ 3.1 eV for emission below 400 nm), thereby limiting the possible side reactions and increasing the expected stability of materials and devices.^[24]

The principal hurdle in organic materials suitable for NIR emission is their lower luminescent efficiency compared to visible emitters. This is generally due to a combination between a greater tendency to form detrimental cofacial J or H aggregates^[25] because of more extended planar π -conjugated systems, and the so-called “*energy gap law*”,^[26] that favours nonradiative decay paths. Although NIR-emitters are less common than NIR-absorbing organic materials, they started to become a quickly expanding and increasingly popular field of investigation.^[27]

For instance, using NIR-absorbing organic semiconductors can extend the absorption of the material even beyond 1000 nm, which can potentially double the current power conversion efficiency of organic solar cells,^[28] since nearly 50% of the solar energy is dissipated as NIR radiation. Additionally, nowadays there is an extensive utilization of NIR dyes in security authentication technologies exploiting biometrics, such as imaging of finger veins and iris recognition,^[29,30] communication networks,^[31] semiconductors^[32,33] and transistors.^[34]

The long history of dye chemistry has given rise to a diverse array of fluorophores, exhibiting absorption and emission wavelengths spanning from the UV to the NIR range. By employing different approaches, including structural modifications, such as introducing groups that can induce electronic effects, increasing the conjugation length, and manipulating the excited state, it is possible the fine-tuning of the photophysical properties of the molecules to suit specific applications or desired spectral ranges.^[35]

For example, the fluorescent scaffolds depicted in **Figure 3**, are commonly used core structures employed in contemporary biological research.^[36] Through derivatization, each backbone can be transformed into dyes with enhanced photophysical and chemical properties.

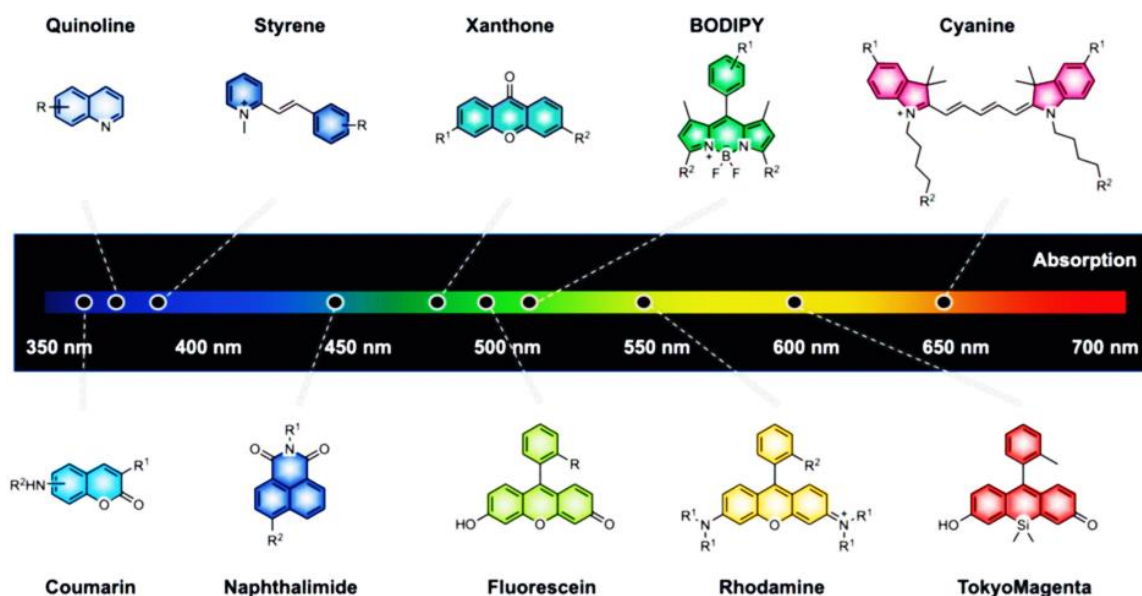


Figure 3: Chemical structures of the most common core fluorescent scaffolds listed in order of increasing absorption values. The R groups indicate potential sites for common functionalization. Reprinted with permission from RSC, J. Jun, D. M. Chenoweth, E. J. Petersson, *Org. Biomol. Chem.*, **2020**, 18, 5747.

With specific regard to this class of emitters, the semitransparency of biological tissue in the 700-1000 nm window^[37] makes this range particularly appealing for optical probes. Likewise, bioimaging may be considered the field of application that primarily entails using organic molecular probes active in the NIR region.

Considering the primary objective of this work, an in-depth analysis of the specific application of bioimaging will be conducted.

1.3 Bioimaging: past, present and future

The simplest definition of “imaging” refers to a visual representation obtained with a detector or electromagnetic beam.^[38] Limiting the technique to its purely clinical purpose, the concept of “medical imaging” was introduced by Wilhelm Röntgen in 1895 after he observed the first X-rays using his wife’s hand.^[39] His investigations on this topic earned him the first Nobel Prize in Physics in 1901.^[40]

From there, medical imaging has emerged as a highly effective methodology to acquire and process biomedical information, opening endless opportunities for diagnostic and therapeutic procedures.^[41]

The Molecular Imaging Center of Excellence (MICoE) members have formally defined molecular imaging as “the visualization, characterization, and measurement of biological processes at the molecular and cellular levels in humans and other living systems”.^[42]

From the definition itself, it is thus intuitive to see how it can be interpreted as a crossroads, with molecularly targeted imaging agents expected to broadly allow the visualization of *in vivo* biological processes, revolutionizing the way of studying the inner workings of the human body, diseases diagnostics, drug design, developments and assessment of therapy.^[43] Generally speaking, it involves specialized instruments, used alone or in combination with targeted imaging agents. The data generated can be used not only to identify regions of pathology but also to detect the expression and activity of specific molecules, and to provide insights regarding the mechanism of disease and nanoscale reactions, such as protein-protein interaction and enzymatic conversion.^[44]

The areas of research and medicine that involve molecular imaging are incredibly vast and varied. Therefore, an explosive implementation of medical multimodality imaging can be expected in the next future.^[45]

1.3.1 Imaging techniques

Recent advances in biomedical imaging have made a revolutionary impact on diagnostic radiology and health care. Molecular imaging has emerged as a cornerstone discipline to quantitatively map specific cells- and tissues-events within an organism.^[46]

The most used clinical imaging techniques for radiological applications include X-ray/computed tomography (X-ray/CT), magnetic resonance imaging (MRI) and its derivatives, such as single photon emission computed tomography (SPECT), positron emission tomography (PET) and ultrasound.

Depending on the underlying physical process, each medical imaging method uses a specific radiation.^[47] The relative frequencies of electromagnetic radiations are shown in **Figure 4**.

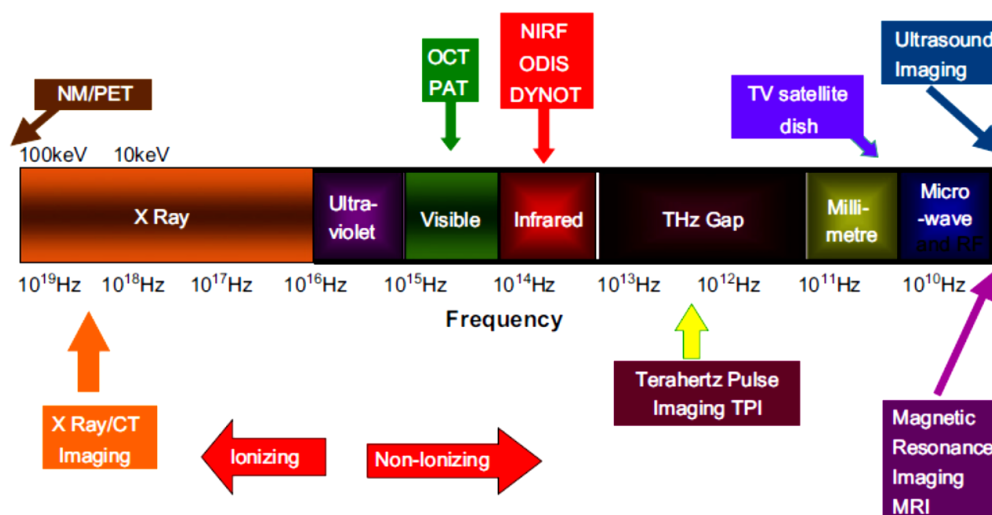


Figure 4: Frequency spectrum of electromagnetic radiation imaging technologies. Reprinted with permission from Wiley, from L.Fass, *Mol. Oncol.* **2008**, 2, 115-152.

These systems are based on the interaction of electromagnetic radiation with body tissues and fluids. High-frequency electromagnetic radiation using gamma rays, X-rays, or UV light is ionizing and can cause damage to the human body leading to cancer.

Therefore, dosage considerations are essential to apply these types of systems.

Non-ionizing electromagnetic radiation imaging methods, such as optical-based molecular imaging techniques, are thus preferable, as they restrict undesired effects during the translation from *in vitro* to *in vivo* application.^[37]

1.3.2 Optical imaging: advantages of near infrared window

Optical molecular imaging techniques have become essential to study small-animal models, substantially impacting basic and translational medical research.^[48] The advantages of this methodology are mainly related to its non-invasiveness, high spatial and temporal resolution, and sensitivity, in combination with detection limits in the picomolar range.

This technique allows to obtain detailed images of organs and tissues and smaller structures, including cells and molecules and even the visualization of protein dynamics. Since it does not involve the use of ionizing radiation, it can be performed in real-time, allowing researchers to monitor processes as they occur.^[49] A key challenge for optical imaging probes and instruments is to overcome attenuation and scattering of light by tissue and to optimize light penetration.

Considering body tissues as a bulk medium, when light propagates through its heterogeneous multilayers, it suffers from wavelength-dependent processes, that determine the loss of light intensity with the penetration depth.^[50] It is worth mentioning that the absorption of light occurs only if its frequency is resonant with the transition frequencies of the atoms in that medium, while unabsorbed light is transmitted.

On the other hand, scattering is the phenomenon in which the light changes direction and sometimes also its frequency after interacting with the medium. The total number of photons is unchanged, but the number of photons going in the forward direction decreases because the light is deviated in other directions.^[51]

For visible light, the absorption by molecules may reduce optical signals by approximately 10-fold per centimetre of tissue.

Using NIR instead of Vis or UV irradiation is critical to address the demand for deep-tissue imaging, in particular when the wavelengths fall in the so-called *biological windows*. Within this range, three distinctive wavelength regions have been identified: the first biological window covers the wavelength range from 700 to 950 nm (**NIR-I**), the second one includes the region from 1000 to 1350 nm (**NIR-II**), and the third one extends from 1550 to 1870 nm (**NIR-III**).^[52]

Each window provides increasing transparency toward biological matter. Anderson *et al.*^[53] presented a model for the optics of the human skin describing its wavelength-dependent transparency (**Figure 5**).

The pigment melatonin has been identified as the major skin-located radiation absorber in the region ranging from 350 to 1200 nm.

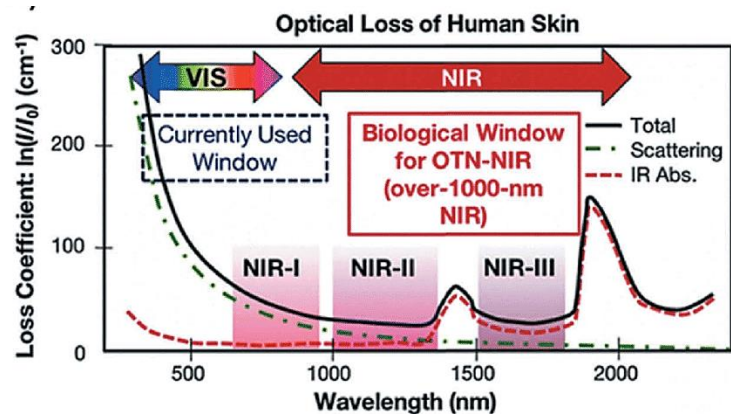


Figure 5: Absorption spectrum of human skin showing the first (NIR-I), second (NIR-II) and third (NIR-III) biological windows. Reprinted with permission from RSC, from F. Yang, Q. Zhang, S. Huang, D. Ma, *J. Mater. Chem. B.*, **2020**, 8, 7856.

Beyond skin, in human subcutaneous adipose tissue, a reduced scattering coefficient was observed increasing the wavelength in the spectral range from 400 to 1500 nm. **Figure 6** shows the attenuation coefficient of blood, skin and fatty tissues in of the first optical window.^[54]

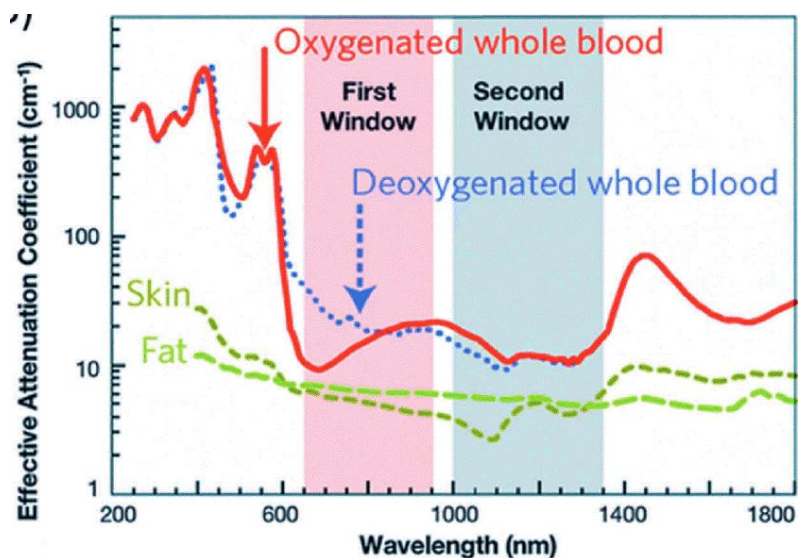


Figure 6: Plot of the effective attenuation coefficient (on a log scale) versus wavelength, showing the quantitative relevance of different body substances: oxygenated blood, deoxygenated blood, skin and fatty tissue. Reprinted with permission from RSC, from E. Hammer, A. Benayas, F. Legare, F. Vetrone, *Nanoscale Horizon.*, **2016**, 1, 168.

Specifically, under 800 nm excitation, the 1500-1700 nm region can afford nearly zero tissue autofluorescence, thus allowing to enhance the contrast from the exogenous bio-probes emitting fluorescent signals that match those specific ranges.^[55]

The improvement of fluorescence imaging requires the comprehensive knowledge of the optical properties of biological tissues to faithfully resolve structures with a high signal-to-noise ratio. To pursue this aim, two main approaches have been investigated: the development of new imaging instruments, such as confocal microscopy and two- and multi-photon microscopy, and the design of new imaging agents, such as fluorophores with superior spectral and biocompatibility properties.

The most extensively investigated window is NIR-I and it is also the one that is aimed to be covered in this work. The sensitivity for NIR fluorescence imaging in the region between 650 and 900 nm is greatly enhanced, potentially enabling to detect the tomographic optical imaging signals at depths of 7–14 cm.^[48]

1.4 Near-infrared dyes for fluorescence imaging

The ideal fluorophore for bioimaging should exhibit high quantum yield (Φ), with tuneability to any wavelength and negligible toxicity, demonstrate exceptional stability under all levels of illumination and function effectively in various biological systems.

While such dyes do not exist, researchers strive to accomplish enhanced molar absorption coefficient, quantum yield and achieve large Stokes shifts, since they can reduce self-quenching resulting from molecular self-absorption, thus matching with the practical requirements of imaging systems.

By modifying the chemical structures, through synthetic adjustments, it is also possible to confer cell permeability, fluorogenicity in the NIR windows, thus enabling deeper tissue penetration.^[56] Additionally, it can be impart rigidity to the fluorophore core, thereby achieving resistance to photochemical reactions that lead to its degradation, *e.g.* photobleaching.^[56] Although drawing a distinct border line is complex and somewhat arbitrary, fluorescent materials can be divided into different classes to generalize the common factors, properties, trends and drawbacks.

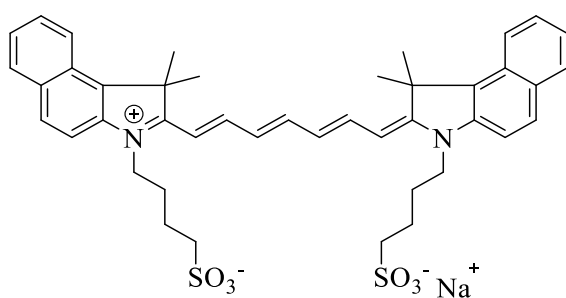
NIR fluorescent materials can be differentiated into inorganic and organic compounds.

Among the former, semiconductor nanoparticles, usually called “quantum dots” (QDs), have progressively assumed a pivotal position.^[57] They consist of combinations of elements from metalloids groups as well as phosphorus, sulphur, and selenium, and they are divided into: “core-type”, “core-shell”, “alloyed and doped”, and “silicon” quantum dots. Carbon nanomaterials such as nano-diamonds, carbon dots and graphene-related materials have been used for deep tissue imaging and numerous sensing applications,^[58,59] as well as rare-earth nanoparticles (NPs) and metal clusters.^[60]

However, in the last decade, the concept of inorganic-organic hybrid nanoparticles as a class of fluorescent nanoparticles, has gained increasing attention.^[61]

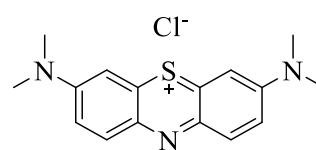
Compared to inorganic probes, organic NIR fluorescent dyes are suitable candidates for imaging because of their tuneable photophysical properties and feasible conjugation with different specific molecules, such as amino acids, proteins, nucleotides, DNA and antibodies.^[62]

The US Food and Drug Administration (FDA) approved the first NIR fluorophore, indocyanine green (ICG),^[63] for in-human clinical use as a fluorescent indicator in 1959, followed by methylene blue (MB) (both structures represented in **Figure 7**, feeding advances in biomedical fluorescence imaging in NIR-I window in the past decades.



ICG

$\lambda_{\text{ex}} = 775 \text{ nm}$, $\lambda_{\text{em}} = 831 \text{ nm}$
 Φ : 9.3% in serum



MB

$\lambda_{\text{ex}} = 665 \text{ nm}$, $\lambda_{\text{em}} = 686 \text{ nm}$
 Φ : 9.6% in serum

Figure 7: Chemical structure of indocyanine green (ICG) and methylene blue (MB).

ICG and MB have been used in NIR-fluorescence-based intraoperative imaging for structural visualization of anatomical features, including blood and lymphatic vessels, the gastrointestinal tract, bile duct and ureters, and intra-operative image-guided surgical removal of diseased tissues.^[64,65]

Besides the FDA-approved ICG and MB, the past years have witnessed the development of several functional NIR-I fluorophores for precise anatomic and molecular imaging.

Within the plethora of organic fluorophores, the ones mostly applied fall within the core-structures of cyanines, squaraines and BODIPYs.^[63]

Cyanines. The basic structural motif of classical cyanine dyes (**Figure 8**) is a polymethine chain bridging two aromatic nitrogen-containing heterocycles.^[66]

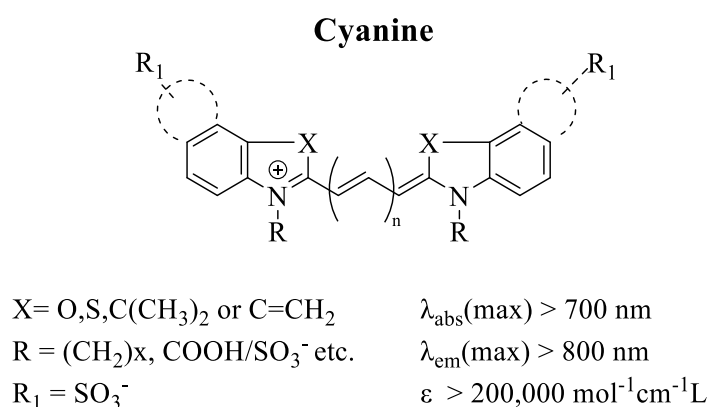


Figure 8: Core structure of cyanine dyes and related photophysical properties.

The length of the polymethine bridge is the key to tune the dye excitation/emission profile from the Vis to the NIR. For instance, each vinylene group in the bridging chain introduces nearly a 100 nm bathochromic shift.

Cyanines are characterized by narrow absorption bands and high molar extinction coefficients ($\epsilon > 10^5 \text{ M}^{-1} \text{ cm}^{-1}$), but they are weakly luminescent due to the flexibility of the polymethine bridge that undergoes isomerization at the excited state. However, the introduction of a R group in the polymethine chain has been found to stiffen the structure, thereby improving the quantum yield and the photostability.^[67]

Squaraines. Squaraines are a class of dyes (**Figure 9**) characterized by a donor-acceptor-donor type substitution pattern that consists of electron-rich aromatic or heterocyclic moieties on both sides of an electron-deficient oxocyclobutenolate core.^[64]

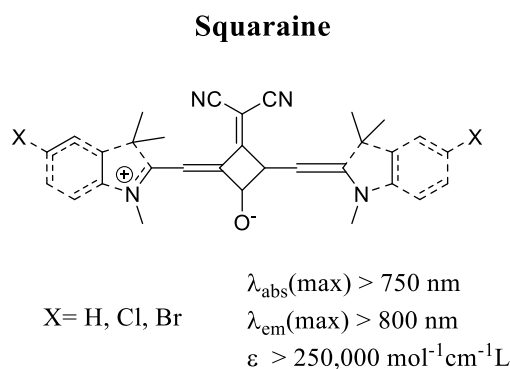


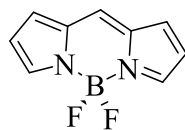
Figure 9: Core structure of squaraine dyes and related photophysical properties.

Squaraines dyes exhibit high molar extinction coefficients, quantum yields and photostability. However, their planar and highly conjugated structure determines poor solubility in water.^[68] A common strategy to prevent the aggregation of squaraines in aqueous solution and protect them from chemical attack is encapsulation.

BODIPY dyes. Organoboron compounds based on the 4,4-difluoro-4-borata-3a-azonia-4a-aza-*s*-indacene molecules (**Figure 10**), commonly designated as BODIPY, are one of the most versatile fluorophores that gained increasing popularity over the past two decades.^[69]

Their chemical robustness, high thermal resistance, low photodegradation, and mainly their unique photophysical features, which deeply depend on the molecular structure have led to the synthesis of a huge family of derivatives extensively used in bioimaging.^[70,71]

BODIPY



$$\lambda_{\text{abs}}(\text{max}) > 630 \text{ nm}$$

$$\lambda_{\text{em}}(\text{max}) > 700 \text{ nm}$$

$$\varepsilon > 250,000 \text{ mol}^{-1}\text{cm}^{-1}\text{L}$$

Figure 10: Core structure of BODIPY dyes and related photophysical properties.

The nomenclature itself suggests that these are *boron-dipyrromethenes* compounds; therefore, the class of dipyrromethenes will be extensively described.

1.5 Dipyrrens: overall backdrop

Dipyrrens constitute one of the most extensive and fascinating classes of organic chromophores with an open chain oligopyrrole structure.^[72]

The most well-known compounds derived from dipyrromethenes are the previously described BODIPYs, which have somewhat overshadowed the simple dipyrren core. Undoubtedly, the introduction of a boron atom leads to increase the rigidity of the molecule that results in an enhancement in the luminescence.

However, it should not be underestimated that the photophysical properties derive mainly from the dipyrrolic core and the selection of substituents in its various position.

The investigation on dipyrren chemistry has traditionally been oriented towards synthesizing porphyrins because of the historical application of dipyrrens as porphyrin's building blocks and the familiarity with pyrrole chemistry.^[73] It is not a coincidence that, even though the first dipyrren was isolated by Piloty *et al.* in 1914,^[74] the studies of these compounds started after the studies conducted lately by Fisher, who employed these molecules as a precursor to natural porphyrin.^[75]

Dipyrrens may be regarded as “half-porphyrins” due to their analogous electronic, geometrical, and structural parameters. They are, indeed, fully conjugated planar molecules containing 12- π -electrons. The unsubstituted dipyririn and the free-base porphyrin, which was denoted as the base structure containing two acidic protons attached to the four nitrogen atoms of the pyrrole rings, are shown in **Figure 11**.^[76]

The scheme for the nomenclature of the dipyririn skeleton shown in **Figure 11** is recommended by the International Union of Pure and Applied Chemistry (IUPAC).^[77]

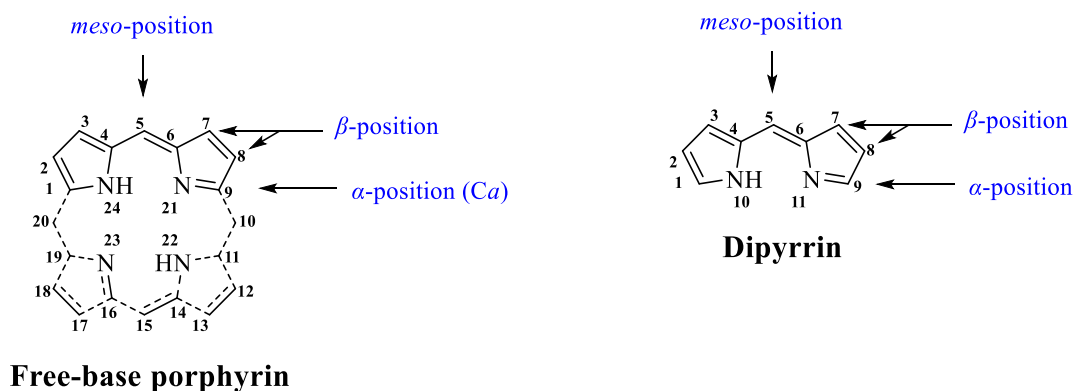


Figure 11: Structure of a free-base porphyrin and IUPAC numbering scheme for dipyririn unit.

The **1-** and **9-**positions are often referred as the α -positions, and the **2-**, **3-**, **7-** and **8-** positions as the β -positions, following the historical pyrrole nomenclature. The **5-**position is the *meso*-position, a term borrowed from the nomenclature of porphyrins. The terms α -, β - and *meso*-positions are not recommended by the IUPAC nomenclature but are commonly used to address the available positions.

1.5.1 Structures and tautomers

Dipyrrens are formerly composed by a pyrrole ring and an azafulvene attached through the 2-positions. More straightforwardly, it can be considered as a dipyrromethane with an extra degree of unsaturation, therefore a dipyrromethene (**Figure 12**).

This supplementary level of unsaturation affords the delocalization of the electron density across the dipyrrens, determining that the two pyrrolyl units are equivalent when they are identically substituted.

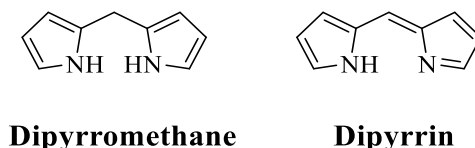


Figure 12: Structures of the dipyrromethane and dipyrin essential core.

The stability of dipyrrens is significantly influenced by the type and number of substituents. It has been reported that fully unsubstituted dipyrrens are unstable in solution, at temperatures above $-40\text{ }^{\circ}\text{C}$, due to the susceptibility of the unsubstituted ring positions to electrophilic and nucleophilic attacks.^[78]

Remarkably, the *meso* position holds particular significance in determining the ultimate stability of the compound. Alkyl and aryl substituents at the *meso* position allow the isolation of stable dipyrin, making them more suitable for opto-electrochemical applications.^[79]

Since the dipyrrens are prepared after the oxidation of dipyrromethane, the pyrrolyl group of dipyrrens can rotate around the central methane carbon, consequently producing different conformations.

Delving further into the intricacies of this context, in principle, the unsymmetrically substituted 2,2'-dipyrrens exhibit four degenerate tautomer pairs, which can be attributed to the extremely rapid exchange between the two tautomers with the hydrogen atom attached to the two electronegative nitrogen atoms.

Furthermore, a pair of diastereomers with *Z*- and *E*-configurations is possible owing to the exocyclic double bond. Moreover, the presence of the exocyclic single bond determines the formation of two conformers for each diastereomer assigned as *syn* and *anti*.

Using the algorithm developed by Dolhaine,^[80] it was possible to compute the number of substitutional isomers, considering the molecular symmetry for the interconversion of these eight species (**Figure 13**).

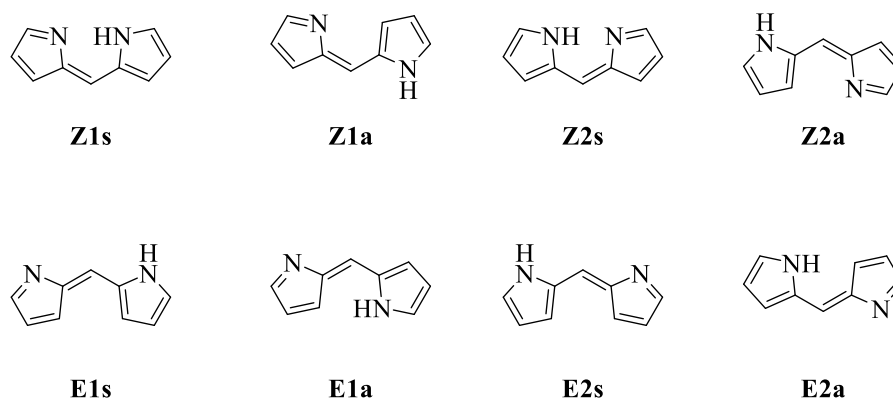


Figure 13: Interconversion of the unsymmetrically substituted dipyrrens. Z and E indicate the configurations of diastereomers; 1 and 2 refer to tautomers, and rotamer; s and a indicate *syn* and *anti*, respectively.

The differences in the energy barrier for the three types of interconversions, *i.e.*, tautomerization ($E_a = 5\text{-}110$ kJ/mol), diastereomerisation ($E_a = 100\text{-}320$ kJ/mol) and rotation ($E_a = 5\text{-}150$ kJ/mol) are moderate.

X-ray diffraction of the dipyririn free-bases displays a planar *syn-Z* conformation stabilized by intramolecular N-H \cdots N hydrogen bonding.^[81] The acidic proton is statistically disordered between the two N atoms, while the pyrrolic rings and the methine bridge in dipyrrens are coplanar and highly conjugated.

Thus, these systems can easily undergo tautomerization *via* proton transfer between the two nitrogen atoms, which are strongly dependent on the substituents on the pyrrolic ring (**Figure 14**).



Figure 14: Dipyrromethene valence tautomers.

In the presence of two non-equivalent N atoms, the tautomeric exchange would be too fast to be measured by NMR techniques even at low temperatures, and it may be observed only on the X-ray photoelectron spectroscopic time scale.^[82]

1.5.2 Building blocks in nature

The biological chemistry of oligopyrroles and their derivatives is massive due to their unique electronic and structural characteristics, which give them a wide range of applications.^[83]

Dipyrrens are present in biological systems as metabolites of porphyrins and as part of a group of oligopyrroles called “bile pigments”.^[84]

At first, these entities were regarded primarily as model compounds for the study of conformational preference and bonding characteristics for more significant compounds from a biochemical point of view.^[84] In **Figure 15** some of the dipyrrenoids derivatives that have received considerable attention within the scientific community are presented.^[85–88]

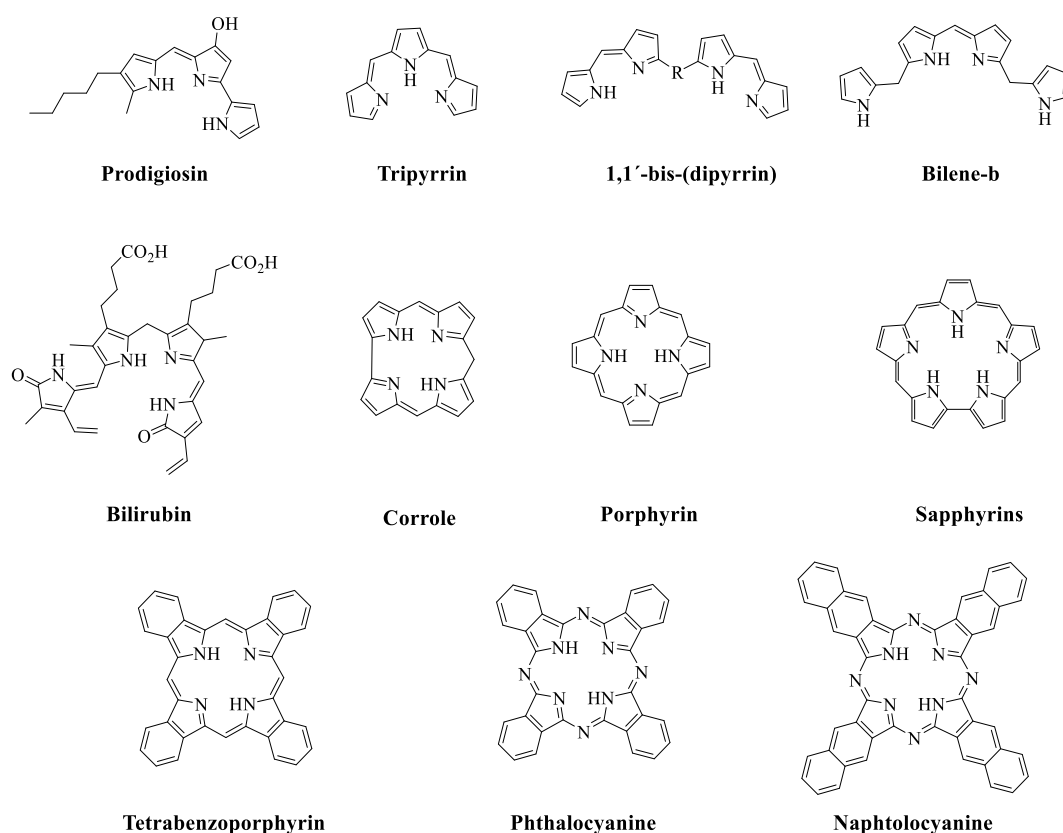


Figure 15: A selection of structures with a dipyrren core occurring in scaffold present in the body and the most common macrocycles.

Dipyrromethenes are frequently considered fundamental units for the construction of macrocycles,^[89] including corroles,^[85,87] sapphyrins^[90] and the previously mentioned porphyrins.^[86]

As previously stated, Piloty^[74] serendipitously isolated a dipyrin derivative as a by-product of the decomposition of bilirubin (**Figure 15**) which is a red-orange bile pigment,^[91] produced by heme catabolism.^[92] Bilirubin consists of an open-chain tetrapyrrole responsible of the yellow colour of healing bruises and the yellow discolouration in jaundice.

Prodigiosin is the red pigment produced by many strains of the bacterium *Serratia marcescens*, a widely distributed, non-pathogenic bacterium.^[93]

The red pigment, one of the alleged marvels of microbiology¹, was isolated, and its chemical structure was initially determined through absorption spectra.^[88] Nowadays, prodiginines are a family of natural, red-pigmented secondary metabolites produced by different bacteria and characterized by a standard pyrrolyl-pyrromethene skeleton, currently in the preclinical phase study for pancreatic cancer treatment.^[94]

Despite their initial limited investigation,^[95] tripyrin units have recently attracted attention for their exceptional coordinating ability^[96,97] and as a precursor for the synthesis of smaragdyrins, congener of expanded porphyrins family consisting of five heterocyclic rings.^[98]

¹ The discovery of prodigiosin is associated with an Eucharistic miracle that took place in Bolsena, Italy, in 1263. During the celebration, the priest Pietro da Praga observed that a consecrated host began to bleed onto a corporal. The presence of bleed was considered a miracle that affirmed the Catholic doctrine of transubstantiation, stating that the bread and wine become the Body and Blood of Christ during the consecration. The pontiff Pope Urban IV declared the supernatural event and to commemorate it, he extended to the entire Church the solemnity called *Corpus Domini*. The Catholic Church officially recognized the Eucharistic miracle, and the relics are preserved in the Orvieto Cathedral. However, similar miracles occurred in different Churches during the same period, which sparked curiosity within the scientific community. Johana Cullen, a researcher at Georgetown University in Washington, was able to reproduce the effects of the alleged miracle in the laboratory, suggesting the presence of a common bacterium, *Serratia marcescens*, which produces a vibrant red pigment, called *prodigiosin* on bread, in warm and humid conditions. The experiment conducted by Cullen was replicated by different researchers in various universities, providing the same explanation.

1.6 Dipyrinato metal complexes: structures and geometries

Dipyrins are fully conjugated bi-pyrrolic molecules with a strong tendency to chelate metals. They are essentially π -conjugated bidentate monoanionic ligands, which can accommodate several metals upon deprotonations.

The bulk of the known structural bis(dipyrinato) coordination complexes contain metals in oxidation state (II) chelated thus by an N_4 -donor set (**Figure 16**). Ter(dipyrinato) chelated complexes, N_6 -donor set, can be attainable by α -unsubstituted dipyrins because of steric reasons, bearing metals in oxidation state (III).

Dipyrinato metal complexes, in which the coordination number of the metal centre is higher than four, are either mixed ligand systems or the oxygen atoms of α -substituents in the core act as an additional donor from N_2O_2 -donor set (**Figure 16**).^[72]

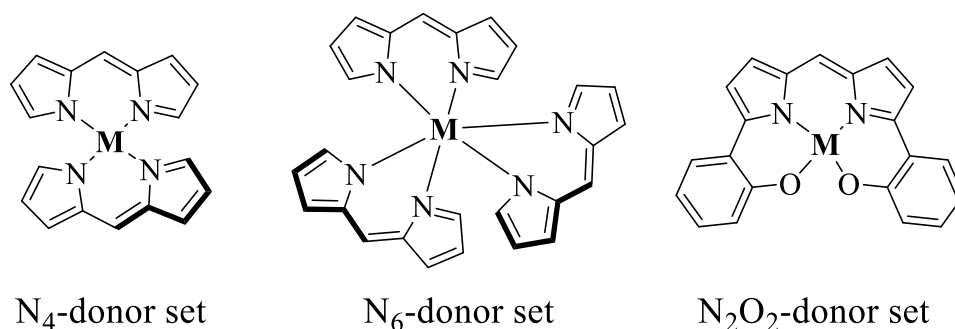


Figure 16: Basic structure of N_4 -, N_6 - and N_2O_2 -donor set.

1.6.1 N_4 - and N_6 - donor set geometries

The coordination geometry of dipyrinato metal complexes is influenced by the steric interaction between substituents at the 1,9-positions (α -positions) of multiple ligands brought into proximity by complex formation. These steric requirements force tetrahedral or octahedral coordination geometries in homoleptic complexes, bearing two or more identical ligands on the metal centre.^[72]

Even if the square-planar geometry is usually preferred especially for metal (II) ions, the steric hindrance between the α -substituents of dipyrrens determined the distortion of the coordination geometry to a pseudo-tetrahedral configuration. In addition, the *meso*-phenyl concomitant with π -substituents induces intraligand steric interactions that can lead to deviations and distortions from planarity.^[99]

The Zn(II) species represent the most widely investigated type of luminescent dipyrromethene metal complexes. However, due to the possibility of accepting a wide variety of metal ions, there are several dipyrromethene complexes chelating Mg(II), Ca(II), Mn(II)/(III), Fe(II)/(III), Co(II)/(III), Ni(II), Cu(II), Ga(III), In(III), Sn(II), Pt(II), Ir(III), Rh(III) and Re(I).^[72]

The stereochemistry of the ligands around the metal centre is strongly dependent on the metal considered. For example, the preference for Zn(II) and Ni(II) for tetrahedral coordination and, even more so, for Cu(II) for a square-planar coordination sphere is well documented.^[99] The Co(II) complex of 5-phenyl dipyrren was difficult to isolate, and the transformation to the octahedral tris(dipyrrenato)Co(III) complex was observed.^[100]

1.6.2 N₂O₂-donor set geometry

The N₂O₂-type dipyrrens (**Figure 17**) are particularly interesting as tetracoordinated ligands, since they increase the structural rigidity of the complexes, thus suppressing nonradiative decay pathways and therefore enhancing the quantum yield.

The incorporation of group 13 and 14 elements into the N₂O₂-type *meso* aryl-dipyrrens ligand affords stable complexes emitting in the deep red spectral region.^[101,102]

Aluminium and boron complexes of N₂O₂-type dipyrrens (**N₂O₂-Al** and **N₂O₂-B** in **Figure 17**) were the first reported,^[103] both a deep red emission with fluorescent quantum yield in chloroform up to 72%. The aluminium ion sits in the dipyrren N₂O₂ site and has an octahedral coordination geometry with the pyrrole and the phenol rings nearly coplanar to afford the planar N₂O₂ donor atoms in the equatorial plane and two water oxygen atoms in the axial position.

Studies on the delocalization of the π -electronic system of **N₂O₂-Pt** complexes showed a significantly downfield shifted, suggesting the involvement of the platinum atom in the radical spin density.^[104]

The complex exhibited a π -stacking array in the crystals with absorption and emission in the deep-far red. The effect of heavy atoms, such as Si, Ge and Sn, on the red-shift and the enhancement of N_2O_2 -type tetradentate dipyrin were investigated.

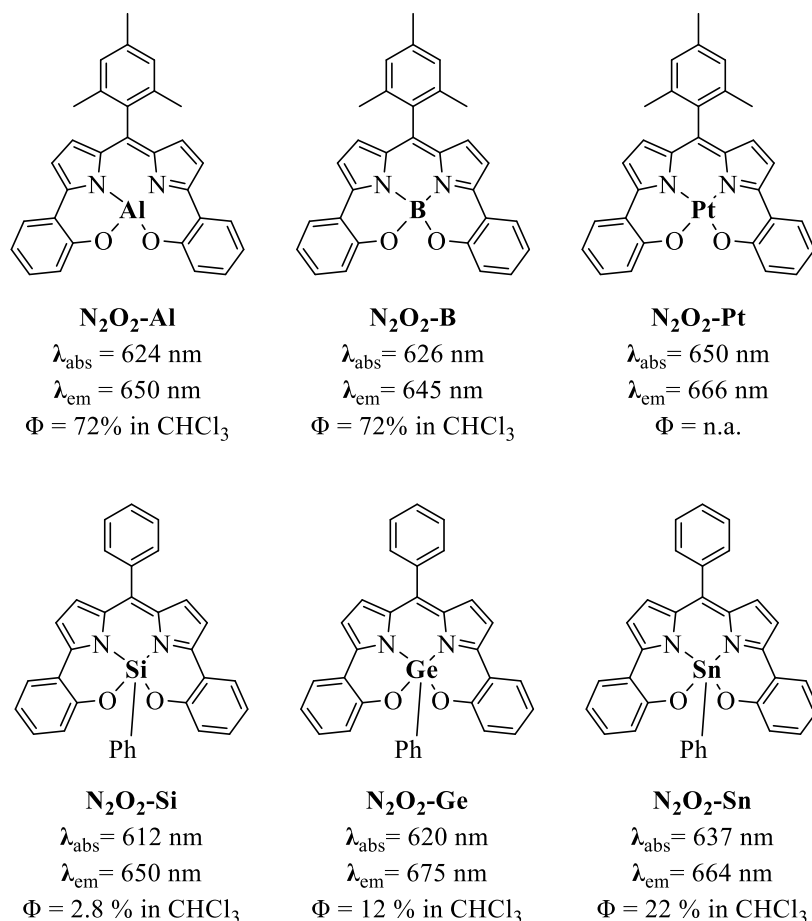


Figure 17: Structures of selected dipyrinato metal complexes with a N_2O_2 donor set.^[105,106]

The central group14 atoms of the complexes have geometries close to trigonal bipyramidal, in which the contribution of the square-pyramidal character becomes higher as the central atom is heavier.^[106] Furthermore, it was observed that the emission wavelengths are red-shifted for N_2O_2 -Ge and N_2O_2 -Sn compared to that of N_2O_2 -Si. The relative fluorescent quantum yields increase according to the order of the periodic table.^[107]

Recently, studies of the structure-property relationship for the rational design of Indium (III) N_2O_2 -type dipyrins complexes with targeting optical properties were reported.^[108] Nabeshima *et al.*^[109] reported a zwitterion of the N_2O_2 type dipyrin by formation of the phosphate ester, which works as a water-soluble fluorescence probe responsive to the environmental pH.

1.7 Bis(dipyrrinato)Zn^{II} complexes

Initially, akin to the dipyrin ligands, dipyrinato metal complexes were obtained as side-products during the synthesis of sterically crowded porphyrins.^[110] More specifically, it was observed that the steric hindrance provided by ortho-substituents of the aromatic aldehyde in *meso* position render the cyclization very difficult, thus yielding predominantly the dipyrinato complexes.^[111]

A few years later, in 1979, Falk *et al.*^[112] investigated the properties of bile pigments, including an examination of the luminescent properties of a bis(dipyrrinato)Zn^{II} complex. However, their luminescent properties were considered inadequate, and their potential was systematically marginalized in comparison to their boron counterparts.

For this reason, dipyrin complexes were initially employed as additional components to more sophisticated structures in light-harvesting arrays for supramolecular chemistry.^[113]

1.7.1 How to tune the fluorescence

Over the years, a deeper understanding has been directed toward the achievement of significant luminescence from bis(dipyrrinato)Zn^{II} complex. Hereafter are described the strategies employed in this regard.

Steric hindrance at the *meso* position

As described before, only a limited number of dipyrin-based compounds lack an aryl substituent at the *meso* position, primarily due to their inherent instability.

The aryl group substantially influences the excited state dynamics and the luminescence properties of BODIPY dyes. Specifically, a facile rotation of this moiety represents a non-radiative deactivation pathway from the S₁ excited state.^[114]

Lindsey and co-workers^[115] demonstrated the importance of the organic backbone rigidity by studying the effect of the steric hindrance at the peripheral aryl group.

The replacement of phenyl rings at the 5,5'-positions (in **a.1**, **Figure 18**) of an homoleptic bis(dipyrrinato)Zn^{II} complex with mesityl groups (in **a.2**, **Figure 18**) transforms the molecule from a very weak emitter that deactivates after photoexcitation ($\Phi = 0.6\%$; $\tau = 90$ ps) to a highly

fluorescent chromophore, with a long-lived singlet excited state ($\Phi = 36\%$; $\tau = 3\text{ns}$) in toluene.^[116]

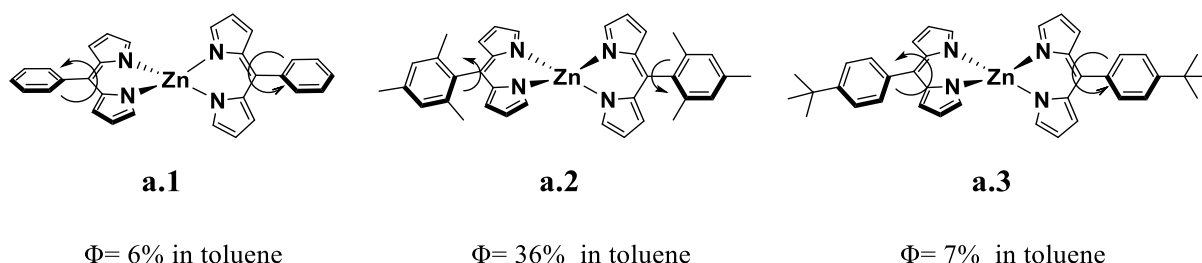


Figure 18: Luminescent $\text{Zn}(\text{dpm})_2$ -**a.1-3** complexes investigated by Lindsey *et al.*^[116]

The photophysical behaviour of complex **a.3** ($\Phi = 0.7\%$; $\tau = 90\text{ ps}$), which contains a 4-*tert*-butylphenyl group, resembles **a.1**, indicating that electronic effects are not the source of altered excited-state behaviour. The critical difference is that the 2,6-dimethyl groups on the aryl ring in **a.2** strongly hinder the internal rotation, thus, altering the excited state properties.

The modulation of the photophysical properties of bis(dipyrinato) Zn^{II} complexes was obtained employing structural modifications, thus rendering them appropriate for applications where high fluorescence is required.

Despite this, the quantum yields of homoleptic complexes are strongly dependent on solvent polarity. Several nonradiative deactivation pathways were suggested for the photoinduced excited state of homoleptic zinc dipyrins.

Shift from homoleptic to the heteroleptic complexes

Studies conducted by Nishihara *et al.*^[117] demonstrated that the transition from homoleptic to heteroleptic complexes results in a significant increase in fluorescence, even in a polar solvent such as dichloromethane.

To elucidate the increase and decrease of Φ , they evaluated the frontier molecular orbital of different homoleptic (**Figure 19**) and heteroleptic (**Figure 20**) complexes by means of DFT calculations.^[118] They presumed that the most significant issue in the low Φ of bis(dipyrinato) Zn^{II} complexes was related to the thermal transition/equilibrium from/between the emissive

lowest singlet excited state ${}^1\pi\text{-}\pi^*$ ($\mathbf{D}^*\text{-Zn-D}$ or $\mathbf{D-Zn-D}^*$) localized on each dipyrinato ligand, to/and a non-emissive charge separated (CS) state (*i.e.* $\mathbf{D}^+\text{-Zn-D}^-$ or $-\mathbf{D}^-\text{-Zn-D}^+$), where D denotes dipyrinato ligand, and Zn is the Zn^{2+} ion.

Considering the DFT calculations, they suggested a plausible explanation for the enhancement and the decrease of fluorescence in heteroleptic over homoleptic complexes in dichloromethane.

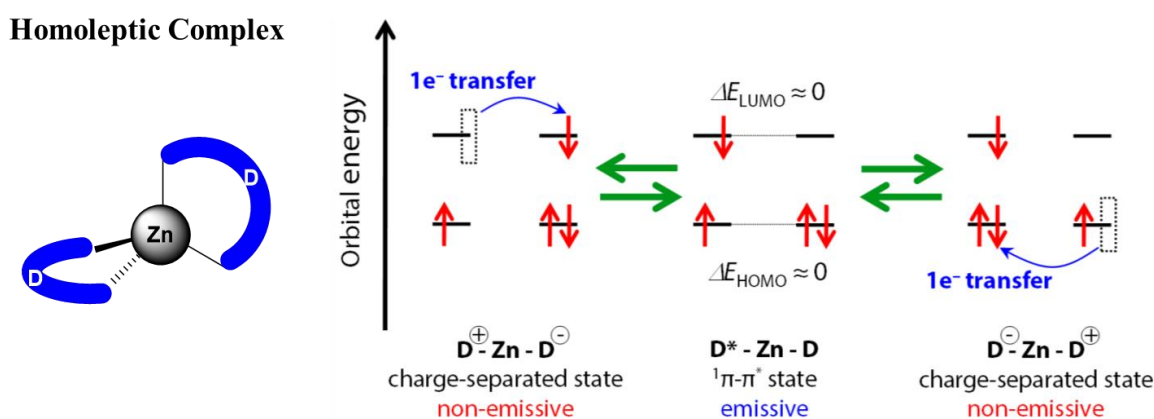


Figure 19: Schematic illustration of homoleptic Zn^{II} complex (right) and plausible thermal equilibrium between the two non-emissive charge-separated states $\mathbf{D}^+\text{-Zn-D}^-$ and $-\mathbf{D}^-\text{-Zn-D}^+$ and emissive ${}^1\pi\text{-}\pi^*$ excited state $\mathbf{D-Zn-D}^*$ localized on the dipyrinato ligand **D** in dichloromethane. Adopted from reference. ^[118]

Homoleptic complexes shows degenerate highest occupied and lowest occupied molecular orbitals (HOMOs and LUMOs) (**Figure 19**), reflecting the identical electronic structure of the two ligands (identified with D).

Photoexcitation of these systems results in the formation of a charge-separated state (CS)^[119] which is generated by one electron transfer, and it is known to be stabilized in polar solvent, thus causing the quenching of the fluorescence.

The degeneracy between HOMOs and LUMOs is cancelled in heteroleptic complexes (**Figure 20**) due to the two different types of dipyrinato ligand (D_1 and D_2) with drastic difference in their electronic structure because of an intrinsic dissimilarity lying in the frontier molecular orbitals.

Heteroleptic complexes have greater energy gap for ${}^1\pi\text{-}\pi^*$ state to transit to both charge separated states than the homoleptic complexes. Consequently, they possess higher quantum yields, especially in polar solvents.

Heteroleptic Complex

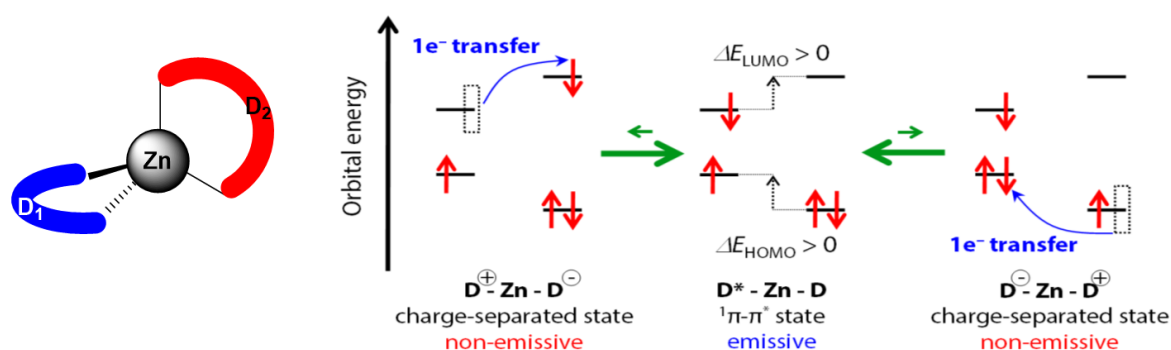


Figure 20: Schematic illustration of heteroleptic Zn^{II} complex (right) and plausible thermal equilibrium between the two non-emissive charge-separated states $\mathbf{D}_1^+ \text{-Zn-D}_2^-$ and $\text{-D}_1^- \text{-Zn-D}_2^+$ and emissive ${}^1\pi\text{-}\pi^*$ excited state $\mathbf{D}_1\text{-Zn-D}_2^*$ localized on the dipyrinato ligand D₁ and D₂ in dichloromethane. Adopted from reference.^[118]

Strong exciton coupling between non-orthogonal ligands was also suggested as another nonradiative deactivation pathway of zinc π -extended dipyrin complexes.^[120] Even so, exciton coupling^[121] between the nearly plain orthogonal ligands in homoleptic complexes is negligible, therefore it cannot be used to explain the decrease in luminescent efficiency compared to their heteroleptic counterparts.

Trinh *et al.*^[122] corroborated the above-mentioned findings, demonstrated that the symmetry breaking charge transfer (SBCT) in polar solvents drastically increase nonradiative decay pathways for the electronic excited states of homoleptic zinc dipyrins.

Specifically, SBCT occurs when an exciton formed initially on one molecule or ligand undergoes intramolecular charge transfer, leading to a state in which a hole and an electron are localized on different molecules or ligands, with very little coupling between the hole and electron. The SBCT sheds light on the origin of the low fluorescent quantum yields exhibited by homoleptic zinc complexes in polar solvents.

1.7.2 Applications

From the previous section it emerges how the attention was focused on BODIPY as luminescent materials in biosensors applications, whereas dipyrromethene metal complexes were more frequently employed in the field of materials. Even so, the latter has gained

prominence within the scientific community and have managed to gain a *momentum*, achieving significant success in various field.

Multichromophoric systems displaying SBCT properties play an important role in both organic electronics and photosynthetic light harvesting.^[123] These systems contain two or more virtually identical and symmetrical chromophores. Molecular materials which are capable of undergoing SBCT are required in organic photovoltaics, photonics and artificial photosynthesis.^[124] They also possess a strong absorption in the visible spectrum, making these compounds of great interest in solar light-harvesting systems.

In this context, in our working group, were developed bis(dipyrrinato)Zn^{II} complexes^[125] with symmetric and asymmetric dipyrrins (**Figure 21**).

All complexes absorb intensely in the region from 450 to 650 nm, showing high quantum yields in non-polar solvent (Φ up to 66 % in cyclohexane) and the expected luminescence quenching in polar solvent.

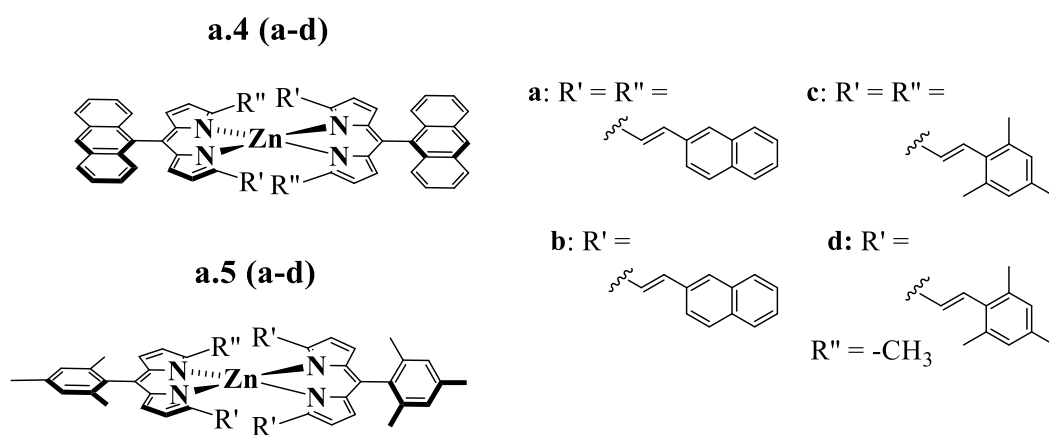


Figure 21: Structures of homoleptic bis(dipyrrinato)Zn^{II} complexes investigated as light-harvesting systems.^[125]

Multitopic dipyrrin derivatives have been studied as promising scaffolds for self-assemblies and, in combination with various spacer units, they are used to fabricate supramolecular structures and fine-tuned nanoscale morphologies by means of bridging metal cations.^[126]

The spontaneous coordination of bis and tris(dipyrrinato) ligands with many metal ions affords intriguing supramolecular structures.^[127,128] As a result of an appropriate design, dipyrrin metal complexes can construct self-assembled nano-architectures, such as supramolecular and coordination polymers that form one-dimensional nanowires, two-dimensional nanosheets and metal-organic frameworks (MOFs).^[129–133]

These complexes can self-assemble via hydrogen bonding, leading to extended architectures, or upon association of the metallatectons with a second metal centre, forming heterometallic architectures.^[134,135]

Dipyrrin derivatives, bearing additional coordinating groups at their periphery, have been used for the preparation of homo- and heterometallic architectures with Ag⁺ cations. These MOFs are constructed by coordination as well as Ag- π -interactions depending on the nature of the peripheral coordinating group and the coordination geometry of the metallatecton.^[136]

More in detail, homoleptic Zn(II) and Cu(II) complexes of dipyrrin type ligands (**a.6** and **a.7** in **Figure 22**), bearing mono- and dicyanophenyl groups, when combined with silver cations lead to the formation of Ag(I)-C=C double bond interactions in the crystalline phase, leading to 2D networks.^[137]

Heteroleptic Cu(II) and Co(III) complexes (**a.8-11** in **Figure 22**) using dipyrrins with pyridyl and cyanoacetylacetonate (acacCN) groups showed a similar behaviour. Upon assembly of the metallatectons with silver salts, through coordination of the peripheral pyridyl groups to the copper and the cobalt centre, one- and two-dimensional coordination polymers were obtained in crystalline forms.^[138]

Heteroleptic cyclometallated Pd(II) and Pt(II) complexes (**a.12** and **a.13** in **Figure 22**) bearing benzonitrile groups were investigated from a photophysical perspective, revealing intriguing properties.^[139] However, their behaviour in the construction of more sophisticated structures was not reported.

The introduction of additional pyridyl coordinating units at the periphery of Cd (II)-based dipyrrin complexes (**a.14** in **Figure 22**) enabled the formation of luminescent coordination polymers by self-assembly.^[140]

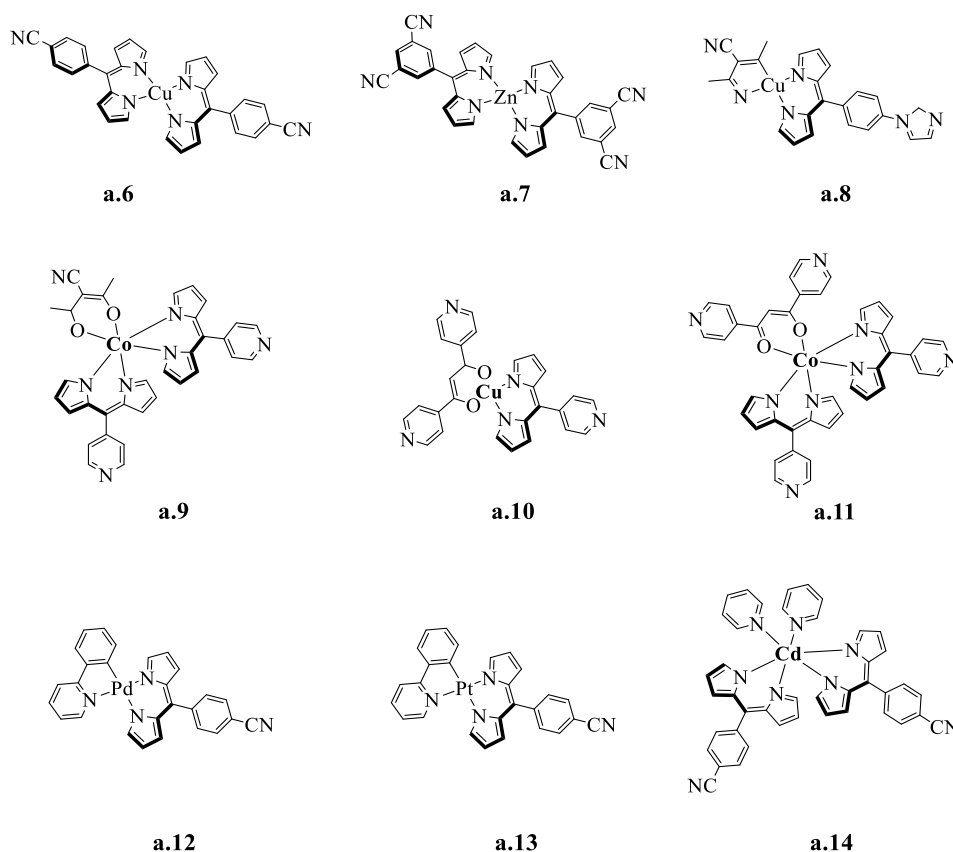


Figure 22: Selection of metallotecton motif based on dipyrinato metal complexes used for the construction of MOFs materials.

The formation of the robust Ag(I)-C=C interaction was exploited also in a tris(dipyrinato) Co^{III} complex (**a.15** in **Figure 23**), which was designed as synthon for the construction of MOFs.^[141]

The single-crystal X-ray structure of complex **a.15** displays a distorted octahedral coordination geometry and the three nitrile groups, positioned in a pseudo-3-fold symmetric motif around the Co(III) metal centre, are linked to the Ag(I) ion *via* their nitrogen atoms.

The resultant heterometallic MOF was homochiral, due to the handedness at the octahedral tris(chelate) metal centres. Moreover, the supramolecular structure obtained demonstrated the ability to absorb a variety of aromatic guest molecules, and the robustness to heat and solvent loss.^[141]

Additional metallo-ligand systems (**a.16-19** in **Figure 23**) were explored to determine how the central metal would affect the template process and hence the topology of the resultant MOFs.^[142] It was observed that the selection of the Ag(I) was crucial for the kinetics and the topological arrangement of the metal in the final structure.

Additionally, the extension of the framework by insertion of a rigid phenyl-quinoline spacer, revealed a distortion in the trigonal plane. However, the Ag(I)-C=C interactions did not change significantly.

Only a limited number of examples were found in literature. Several highly detailed reviews on dipyrin motif used in supramolecular structures are available.^[133,143–148]

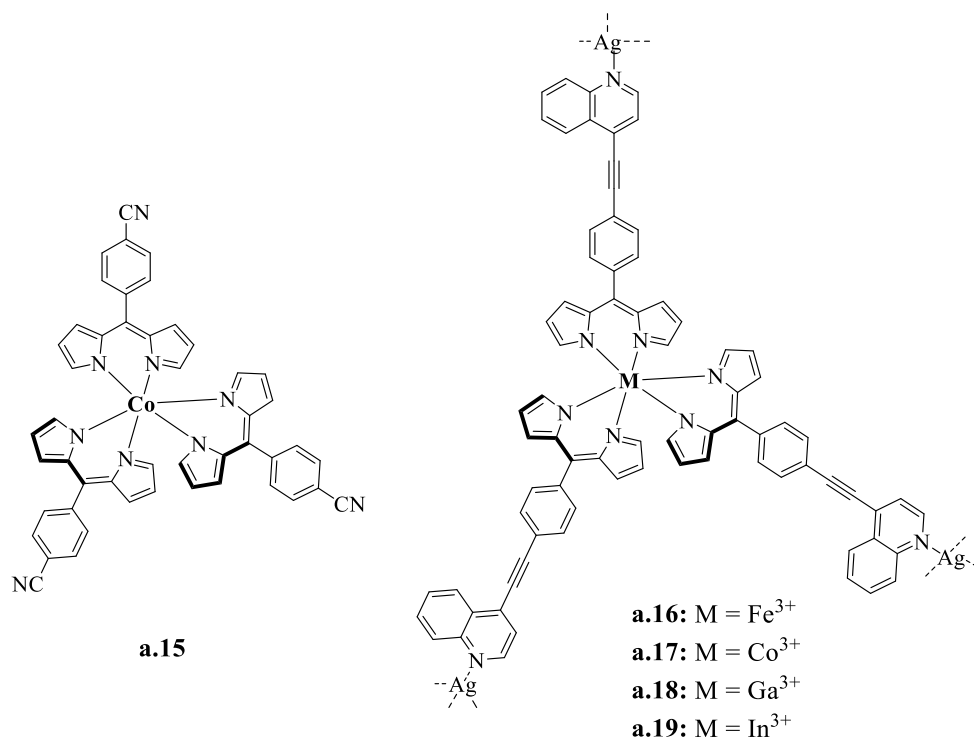


Figure 23: Selection of tris(dipyrinonato) metal(III) complexes used as synthon for the construction of heterometallic MOFs.

The predominance of the SBCT phenomenon in homoleptic dipyrinonato complexes is desirable for certain applications, but it restricts their implementation in biological purposes. One of the strategies employed was the encapsulation in structures of various nature.

The assembly approach employed by Sani *et al.*,^[149] specifically encapsulating two homoleptic bis(dipyrinonato)Zn^{II} complexes into a spatially constraining host structure, was highly satisfactory in terms of overall rigidity enhancement and overcoming fluorescence quenching in polar solvents. The obtained host-guest materials, where the role of the host is played by mesoporous silica of the COK-12 type, showed a significant increase of quantum yield in dichloromethane solutions, from $\Phi = 0.3\%$ and 0.5% to $\Phi = 3.5\%$ and 55% respectively.

Therefore, the absence of solvent stabilization and the rigid environment reduced the nonradiative deactivation pathways leading to the enhanced emission also in a polar solvent such as dichloromethane.

A comparable method was employed by Gasser's group, involving the encapsulation of literature known homoleptic bis(dipyrrinato)Zn^{II} complexes^[150] within a polymeric matrix with biotin end groups to form nanoparticles.

The resulting particles selectively accumulated in the lysosomes of transfected cancerous cells because of the presence of the biotin targeting moiety.^[151] Subsequently, they introduced iodine atoms at position 2 and 6 (**Figure 24**) of the same previously reported^[151] homoleptic bis(dipyrrinato)Zn^{II} complexes and evaluated their efficacy as photodynamic agents.^[152]

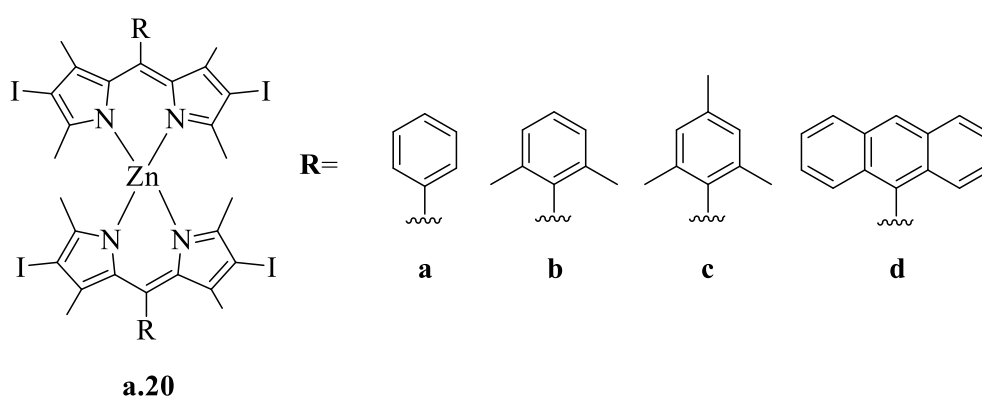


Figure 24: Homoleptic bis(dipyrrinato)Zn^{II} complexes investigated as potential photodynamic agents.

In this instance, the aforementioned complexes were encapsulated within a polymer matrix and, upon light irradiation, the obtained nanoparticles caused cell death at very low micromolar concentrations in monolayer cancer cells. The complexes encapsulated in the nanoparticles act as photosensitizers (PS) and, once they reach the excited triplet state ³PS, they can interact with molecular oxygen to generate singlet oxygen.

The effectiveness of these compounds was compared by varying metals, Ni (II) and Cu (II) complexes with the same structure were studied.^[153] Photophysical investigation demonstrated that they were poorly emissive and barely cytotoxic upon irradiation.

Interesting phototoxicity properties and strong antibacterial activity was obtained from fluorophenyl-substituted dipyrrinato-iridium complexes, underlining their potential use for medical applications.^[154]

In general, the complexes presented have inherent drawbacks.

Firstly, it is necessary to encapsulate them to circumvent the limitations dictated by their homoleptic nature and therefore their attitude to undergo fluorescence quenching in polar solvents.

Secondly, their emission range is limited to 600 nm, thus still far from the near-infrared window, which allows imaging with minimal autofluorescence from biological samples, reduced light scattering and tissue penetration. Finally, they exhibit a self-absorption effect attributed to the small Stokes shifts, that is unfavourable for *in vivo* application, demonstrating a low sensitivity of fluorescence microscopy.

Therefore, the development of dipyrinato-based metal complexes with long-wavelength emission and significant Stokes shift is in great demand to improve the probe's performance.

1.8 Boron-dipyrromethene complexes

As anticipated in §1.4, boron complexes, namely BODIPY, are the most well-known derivatives of dipyrromethene. The first report about BODIPYs dates back to 1968, when they were first discovered by Treibs and Kreuzer.^[155]

However, relatively little attention was given to the discovery until the end of the Nineties, when the potential use of BODIPY as a label compound was complemented by its known ability to function as a tuneable laser dye, because of their absorption and emission in the range of 350-600 nm, where pump lasers are available.^[156]

BODIPY is usually described as being boradiazaindacene by analogy with the all-carbon tricyclic ring, and the numbering of any substituents follows the rules for the carbon polycycle (**Figure 25**).

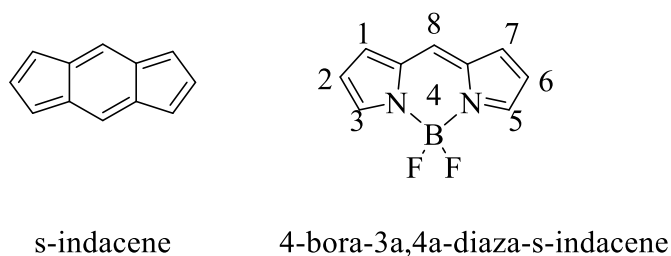


Figure 25: Core structure and numbering scheme for the BODIPY framework derived from s-indacene.

The greatly restricted flexibility leads to unusually high fluorescence yields from the BODIPY framework. Indeed, the main reason for the success and versatility of BODIPY relies on its chromophoric core, which is readily available to a wide assortment of organic synthetic routes, such as electrophilic and nucleophilic substitutions.

Thus, an extensive library of functional groups can be bonded to the indacene core with specific regioselectivity.^[157]

Owing to its adaptable photophysical properties and huge synthetic possibilities of derivatization, several BODIPYs are commercially available with specific substitution patterns to ameliorate their biocompatibility or enable their grafting to biomolecules, from lipids to nucleic acids.^[158–160]

As the demand for NIR dyes has escalated in past decades, the research on developing NIR-emitting BODIPYs has flourished.^[161,162] According to the literature,^[64] the two BODIPYs drawing in **Figure 26** are in the preclinical phase.

In **BPA-5**, the emission wavelength is red-shifted by introducing in 5-position the dimethylaminophenylfuranyl groups.

Selective binding of β -amyloid (A β) plaques, which formation is regarded as an initial event in the pathogenesis of Alzheimer's disease, was observed and it is currently under preclinical investigation.^[163]

While the previous molecule was a neutral compound, on the other hand **mPB (Figure 26)** is an amphiphilic molecule obtained through conjugation with polyethylene glycol (MPEG), which can self-assemble into polymeric nanoparticles, thus enabling the passive targeting in tumour sites.^[164]

Although they do not show specific tissue-targeting properties, these vesicles are in the preclinical phase for both therapeutic and diagnostic imaging scope.

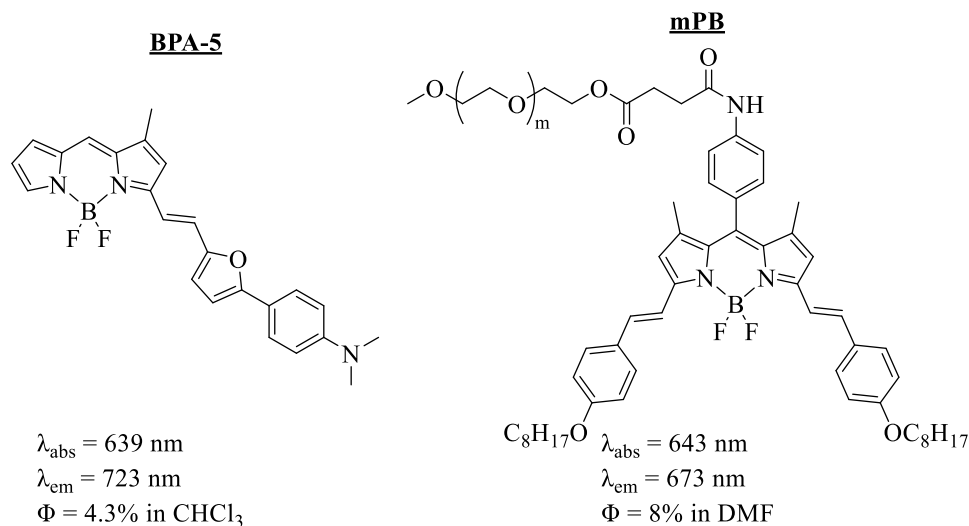


Figure 26: NIR-I BODIPY fluorophores in the preclinical phase for tumour imaging.

Chemical modifications of the BODIPY skeleton have been developed to render them efficient photosensitizers involving long-lived triplet-emitting states and enabling bimolecular sensitisation, e.g. singlet oxygen production for photodynamic therapy (PDT).^[165] Regardless of the large number of approaches, the most used strategy is the introduction of heavy atoms, in particular iodine and bromine, that can favour the intersystem crossing and thus the population of triplet excited states.

In this context, BODIPY probes are gaining increasing popularity as agents for PDT.^[166–168]

1.9 Luminescent coordination compounds for cell imaging

The integration of coordination chemistry into the realm of biology has attracted significant attention.^[169]

Natural occurring metal ions have been well recognized to impart utility to biology, thereby the introduction of synthetic metal complexes offers the potential to explore and manipulate biology by expanding the functional repertoire of inorganic elements beyond their natural availability.

Along with a rapid development of fluorescence microscopy, luminescent transition metal complexes are becoming an emerging class of fluorescent labels in molecular imaging, complementing the predominant use of organic fluorophores in commercial cellular labelling.^[169]

Compared to traditional organic fluorophores, metal complexes possess general chemical properties, such as including tuneable charge, versatile coordination spheres, high luminescence, high brightness, and large Stokes shift. In addition, the remarkable photostability exhibited by coordination compounds provides a solution to the problem of photobleaching, thus enabling prolonged imaging without the substantial degradation of the fluorescence signal.^[169]

Significant progress has been made over the past two decades in the design of luminescent metal complexes for labelling and sensing purposes. Particularly, second and third row transition metal complexes with d^6 , d^8 and d^{10} electronic configurations, such as Ir(III), Ru(III), Os(II), Re(I), Pt(II), Pd(II), Ag(I) as well as lanthanide-based complexes, have demonstrated their utility in various bioimaging applications, both *in vitro* and *in vivo*.^[170]

Although they display excellent performance, several challenges persist with regard to those metal complexes, such as (i) intrinsic cytotoxicity from heavy metals, (ii) emission wavelengths far from the “biological window” in the NIR region (iii) unclear relationship between structure and cellular compartmentalization due to variable coordination spheres exhibited from these metals and (iv) high cost.^[171]

To address these issues, the utilization of the first row-transition elements, that are biologically available, presents an opportunity to design luminescent probes with low cytotoxicity, even if some features, typically associated with second and third row transition metals, such as large Stokes shift, may be sacrificed.

Typically, Cu(II) and Zn(II) complexes have commonly been employed as promising candidates for cell imaging applications.^[172] The main focus will be on the latter.

1.9.1 Zinc complexes

Zinc is a group 12 metal with an electronic configuration of $[\text{Ar}]3d^{10}4s^2$. When the outer shell 4s electrons are lost, zinc forms a divalent cation Zn^{2+} with the electronic configuration of $[\text{Ar}]3d^{10}$.

This closed shell configuration endows the following characteristics: (1) absence of geometry-dependent ligand-field stabilization energy; (2) redox inertness with divalent zinc being the dominant oxidation state and (3) diamagnetism, with absence of d-d transition.^[173]

Zinc complexes commonly exhibit coordination geometries such as tetrahedral, trigonal bipyramidal, square pyramidal and octahedral (**Figure 27**). The coordination geometries are primarily determined by electrostatic and steric interactions with the ligands since ligand-field stabilization energy is absent.^[174]

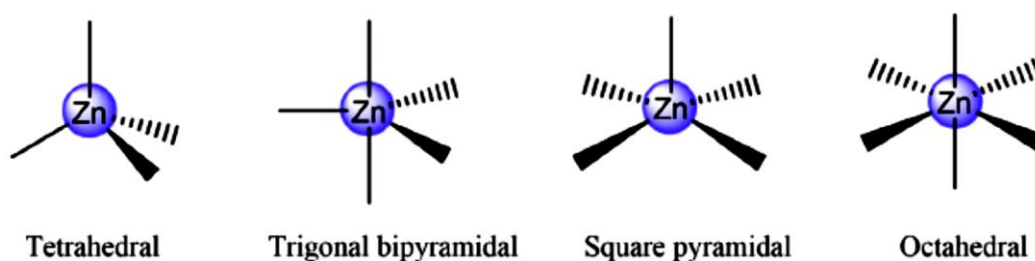


Figure 27: Four typical coordination geometries observed in zinc complexes. Reprinted with permission from Elsevier, from reference.^[175]

As a result of the limited involvement of d-electrons in low-energy charge transfer or metal-centered transitions, the excited states of zinc complexes typically involve ligand-centered (LC) transitions or ligand-to-ligand charge transfer (LLCT) transitions (**Figure 28**). LC transitions predominantly encompass the localized orbitals of the ligands, exhibiting minimal influence from the coordinated metal.

Due to its closed shell d^{10} electronic configuration, the luminescence of zinc complexes mainly arises LC transitions, which can be precisely tuned by modulation of the ligands electronic states. LLCT transitions refer to the transfer of electrons between two orbitals mainly localized on different ligands but connected with the same metal centers.^[176] In most cases these transitions entail multiple mechanisms rather than a single one. Sometimes LLCT, involving the low-lying 4s or 4p empty orbitals of the Zn^{2+} , has been documented in cluster-based zinc complexes.^[177]

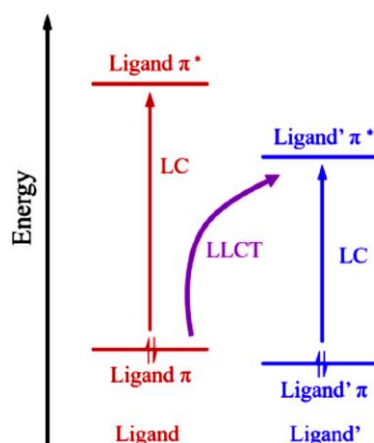


Figure 28: Schematic representation of orbitals and related electronic transitions in zinc complexes. LC: ligand centered; LLCT ligand-to-ligand charge transfer. Reprinted with permission from Elsevier, from reference.^[175]

Typically, zinc complexes display enhanced fluorescence compared to the free ligands. This can be attributed to the improved rigidity of the ligands upon coordination to the metal, resulting in decreased energy dissipation due to bond vibrations.^[178]

Being one of the most abundant transition metals in living systems, zinc is widely present in approximately 10% of all proteins found in the human body.^[179,180] It plays a crucial role in various biological processes, including metabolism, signal transduction and gene expression. Additionally, Zn^{2+} maintains normal physiological function, particularly in the nervous, reproductive, and immune systems, having a vital importance for growth and development.^[181,182] Within cell biology, Zn^{2+} is regarded as a dynamic signalling ion; as a result, its homeostasis is implicated in numerous diseases, such as neurodegenerative disorders (*e.g.*, Alzheimer or stroke), diabetes, cancer and wound healing.^[183]

The introduction of **Zn-DPA** (DPA: dipicolylamine) (**Figure 29**) complexes as luminescent labels marked a significant milestone, paving the way for the design of novel luminescent zinc complexes for molecular imaging.^[175,184] The open chelating ability of these complexes allows zinc to form additional bonds with other ligands, particularly anionic groups like phosphate, carboxylate and histidine.

Apart from DPA, cyclen ligands can selectively bind Zn^{2+} .^[185] The **Zn-cyclen** complex (**Figure 29**) served as an effective probe for early-stage cell apoptosis.^[186]

Keppler *et al.*,^[187] showed how the complexation with Zn^{2+} in **Zn(triapine)Cl₂** (**Figure 29**) appears to stain the nucleoli, whereas the free triapine tends to accumulate in the nuclear membrane and cytoplasm.

The term “salen”, a typical N₂O₂ tetradentate bis-Schiff base ligand typically derives from the combination of salicylaldehyde (sal) and ethylenediamine.^[188] The **Zn-Salen** and **Zn-BTSC** (**Figure 29**) demonstrated efficient uptake by HeLa cells and localising, respectively with the endosomes and the endoplasmatic reticulum (ER).^[189]

Nevertheless, all these complexes do not possess the required photophysical properties, thus showing a significant room for improvement in zinc complexes for bioimaging.

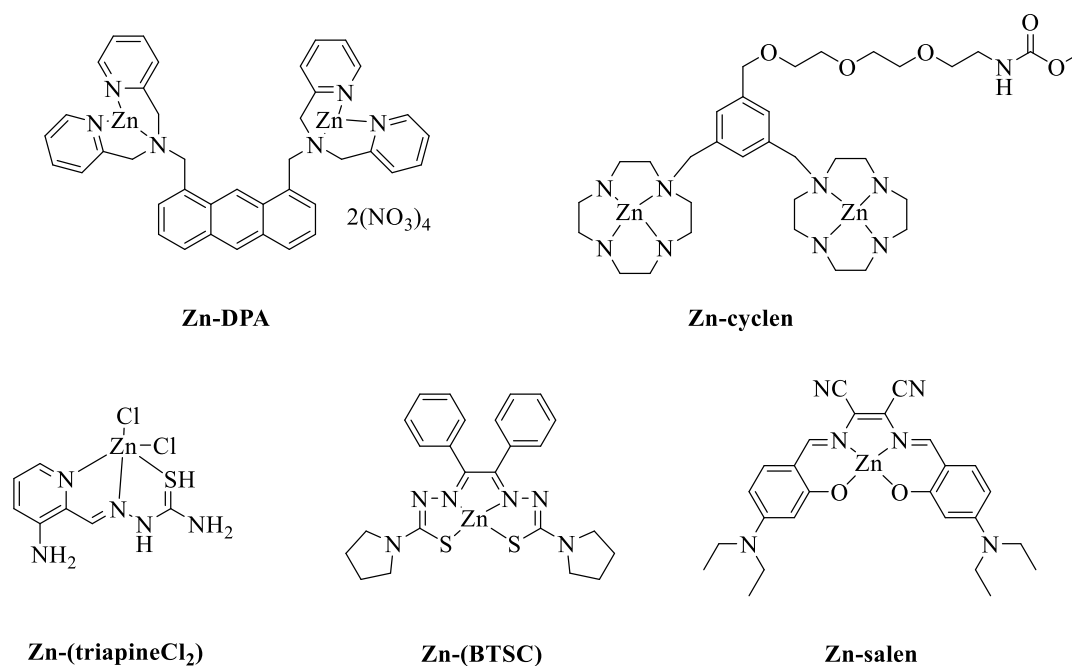


Figure 29: Chemical structures of some Zn-complexes used in bioimaging.

2. Aim of the thesis

Fluorescence imaging is a rapidly growing field of biomedical research, that provides deeper insights into living systems by going beyond morphological cell observation through the use of luminescent molecules. Among the various classes of imaging compounds being investigated, coordination organometallic compounds, that are active in the far-red to near-infrared window, have gathered significant attention.

Hence, this thesis arises from an interest in developing luminescent metal complexes to fulfil this objective. The starting unit used in the synthetic pathway is the dipyrromethene scaffold, which has long been recognized as non-luminescent compound. Nevertheless, by employing various functionalization strategies it is possible to achieve the desired photophysical properties that are required for the probes used in the field of imaging.

The dipyrin skeleton is a very attractive structure because it can be easily obtained through diverse synthetic pathways, offering ample opportunities for post-synthesis modifications. As outlined in **Figure 30**, in this work the α positions (1,9), the β positions (2,3 and 7,8) and the *meso* position (5) will be functionalized. Specifically, various approaches to obtain the target photophysical properties are envisaged.

All these strategies share a common goal: achieving emission within the *biological window*, accompanied by high quantum yields and good stability in different environments. Next, the aim is to proceed with the formation of complexes based on the obtained chelating units with metals that are already present in human body, having a bio-application as purpose.

Due to the interdisciplinarity nature of this project, in addition to the synthesis of the designed molecules, a comprehensive characterization will be conducted, with a focus on their photophysical and biological properties.

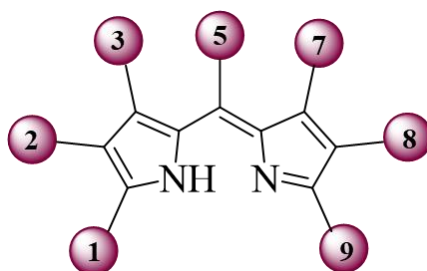


Figure 30: Chemical structure of a generic dipyrromethene scaffold. The highlighted positions indicate the sites that will be functionalized in this thesis.

3. Main Part

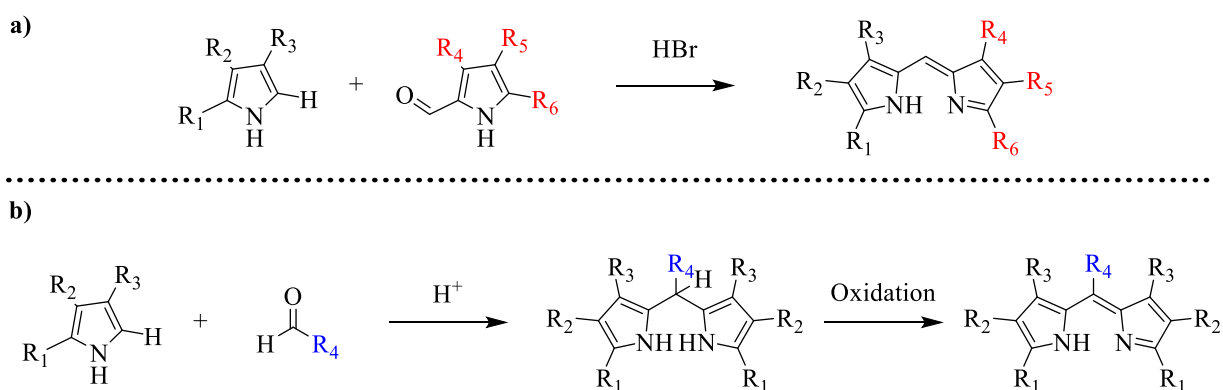
3.1 *Meso*-substituted plain dipyrin ligands

The development of reliable methods for preparing symmetrical and unsymmetrical dipyrins has been one of the most critical advances in dipyrinato chemistry in recent years.^[190]

The MacDonald coupling is an acid-catalyzed condensation of a 2-formyl pyrrole with a 2-unsubstituted pyrrole.^[191] Since it relies upon the reaction of complementary functionalities in the pyrrolic precursors, it is the most convenient method for the preparation of unsymmetrical *meso*-unsubstituted dipyrin (**Scheme 1, panel a**).^[192]

Conversely, much effort has been devoted to the preparation of symmetrical dipyrins, in particular those substituted with aromatic rings at the *meso* position.^[193] At this juncture, the proposed methods range from classical ones to recent breakthroughs, which provide new substitution patterns.^[194]

Direct routes for constructing dipyrins with distinct patterns of *meso* substituents typically begin with dipyrromethanes, as outlined in **Scheme 1 (panel b)**.^[195] The general procedure usually involves the oxidation of *meso* substituted dipyrromethanes to yield dipyrins, which are often stable in their free-base forms, unlike *meso*-unsubstituted dipyrromethanes.^[196]



Scheme 1: Synthetic routes to obtain a) unsymmetrical *meso*-unsubstituted dipyrins through MacDonald coupling^[197] and b) symmetrical *meso*-substituted dipyrins from oxidation of the corresponding dipyrromethanes.^[195]

This two-step method offers the possibility of using unconventional dipyrromethanes as a precursor to obtain corresponding dipyrrens through oxidations; but at the same time, it poses the challenge of avoiding further oligomerization to get dipyrromethenes in isolable quantities.^[198]

A deeper mechanistic investigation of the reaction conditions showed differences in selectivity depending on the concentration, catalyst, solvent, temperature, and reaction time.^[199] Moreover, the rational choice of the starting pyrrole and aldehyde plays a crucial role in the yields of the obtained dipyrromethene.

To increase the selectivity toward the formation of dipyrromethane, it is advisable to: (1) employ substituted pyrrole to eliminate potential coordination site that may lead to oligomerization, (2) raise the steric demand of the aryl aldehyde used to prevent cyclization, and (3) conduct the reaction using mild condition.^[200]

Furthermore, being aware of the synthetic adjustments that increase the rigidity of the dipyrren scaffold, resulting in a better outcome in terms of fluorescence, only aromatic aldehydes with different degrees of steric hindrance were employed to inhibit the rotation at the *meso* position.

In **Figure 31** is depicted the design utilized for the ligands, hereafter referred to as “plain”.

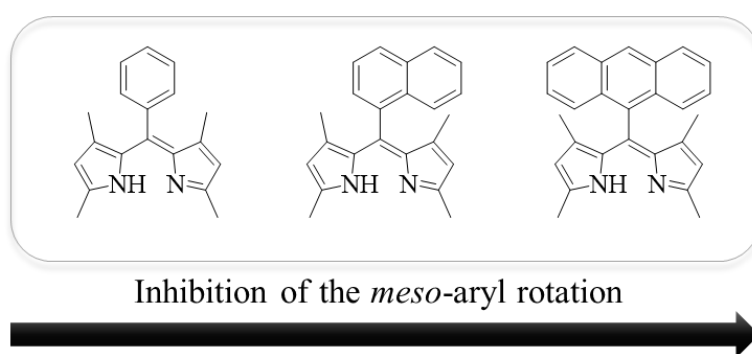
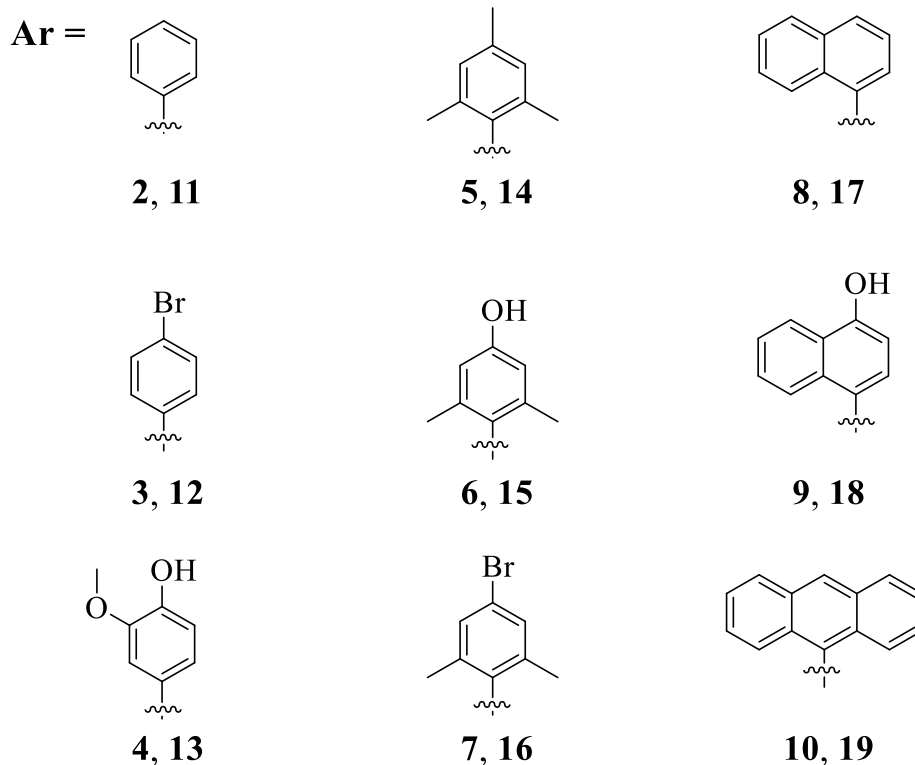
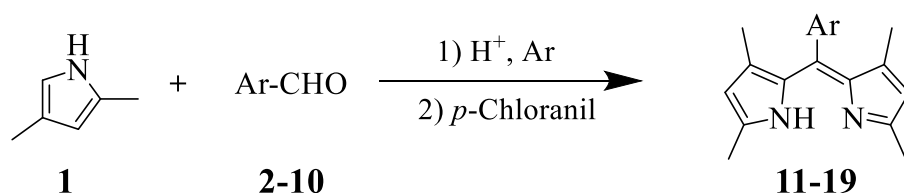


Figure 31: Chemical structures of the plain dipyrromethene scaffolds designed for this work. The critical differences in the aryl groups in *meso* position are capable to hinder the internal rotation enormously.

3.1.1 Synthesis

To enable a high-yielding synthesis route of *meso* substituted dipyrrens, the synthetic strategy employed in this work is the protocol described in **Scheme 1**, developed by Dolphin^[100,201] with some modifications.

The selected starting pyrrole chosen was the 2,4-dimethyl-1*H*-pyrrole **1** and, to ensure the stiffening of the dipyrren core, aromatic aldehydes with different steric hindrance **2-10** have been employed (**Scheme 2**).



Scheme 2: Synthetic scheme for the condensation between 2,4-dimethyl-1*H*-pyrrole **1** and several aromatic aldehydes (**2-10**) to obtain the plain dipyrren ligands (**11-19**). Reaction conditions will be discussed more in detail in the text and tables.

Typically, the most commonly used method for the synthesis of substituted dipyrromethanes is the one reported by Lindsey and co-workers, which involves Lewis acid-mediated reactions.^[202] These catalysts, while promoting efficiently the condensation reaction, they simultaneously lead to an extensive oligomerization of the precursor pyrrole used.^[203] Although pyrrole **1** has only one available α -hydrogen, the polymerization process can still prove to be highly competitive with the formation of dipyrromethane.

For this reason, the initial approach adopted in this work entailed the use of a milder catalyst, such as a solution of hydrochloric acid. Indeed, it was disclosed that the nucleophilic addition of pyrrole to aldehydes could be promoted by electrophilic activation of aldehydes by hydrogen bonds in water.^[204] Thus, using water as solvent afforded the desired dipyrromethane in moderate to good yields, reducing the formation of oligomers because of their limited solubility in such a polar medium.

The reactions for synthesizing dipyrins **11-19** (**Scheme 2**), have been performed multiple times, ranging from 250 mg to a scale-up up to 4 g. In **Table 2** the optimal reaction conditions are presented with varying the aromatic aldehyde in object.

The investigation of the best conditions for obtaining dipyrins in high yields started with benzaldehyde **2**. The oriented synthesis employed dichloromethane/water (2:1) as the reaction medium and a solution of HCl (0.2 M) as the catalytic source.

The optimal conditions required 2.5 equivalents of 2,4-dimethyl-1*H*-pyrrole **1** and one equivalent of benzaldehyde **2**, stirring at room temperature under an argon atmosphere. The starting materials reacted very smoothly within twenty-four hours. The second step, *i.e.*, the oxidation of the obtained dipyrromethane, was carried out *in situ* by adding tetrachloro-1,4-benzoquinone (*p*-chloranil). It promotes the efficient abstraction of the *meso* hydrogen, similar to 2,3-dichloro-5,6-dicyano-1,4-benzoquinone (DDQ), the quinone derivative with the highest reduction potential.^[205] Dehydrogenations with quinone derivatives have found wide application in synthesizing pyrrolic pigment, particularly in converting any reduced porphyrins to the corresponding fully unsaturated ones, and more in general for selective oxidation of organic molecules.^[206] Due to the intrinsic toxicity of DDQ,^[207] enhanced in water because it releases the highly toxic hydrogen cyanide, *p*-chloranil was preferred, even if it is a milder oxidant.

The progression of the reaction was monitored by Thin Layer Chromatography (TLC), indicating the consumption of the dipyrromethane formed in the first step after 7 hours. The

protocol does not require any quenching; the workup consisted of adding water to enhance the separation between the organic and water phases.

Despite the meticulous control and highly mild conditions, other side reactions such as oligomerization and isomerization still took place. As a first purification approach, recrystallization was attempted. However, it was not satisfactory, so purification *via* column chromatography was necessary.

The crude residue was subjected to column chromatography packed with neutral alumina, giving the desired dipyrin **3** in 68 % yield (**Table 2**). It was observed that the reaction can be easily scaled up without loss of reaction yield or selectivity.

The generality of the reaction was investigated using various aromatic aldehydes having different degrees of steric hindrance, as depicted in **Scheme 2**.

The reaction conditions described above have proven to be highly suitable also for 4-bromobenzaldehyde **3**, 4-hydroxy-3-methoxy-benzaldehyde **4**, 2,4,6-trimethyl-benzaldehyde **5** and 4-hydroxy-2,6-dimethylbenzaldehyde **6**, yielding the corresponding dipyrins **12**, **13**, **14** and **15** in high yields, from 62 up to 79% (**Table 2**).

In the specific case of the formation of dipyrromethene **15**, methanol was introduced into the reaction medium to increase the solubility of the starting aldehyde **6**.

The same expedient has been implemented in the synthesis of the dipyrin **13** to ensure homogeneity in the system between pyrrole **1** and 4-hydroxy-3-methoxy-benzaldehyde **4**.

Despite TLC confirming the complete conversion of the starting vanillin **5**, the isolated dipyrin **13** after column chromatography exhibited still moderate yield (37%) but lower in comparison to the ones mentioned above.

This can be ascribed to the effects of the hydroxyl and methoxyl substituents groups in the *ortho* position of the rings, both electron-donating groups (EDGs), which profoundly impact the reaction, resulting in lower yields.

Table 2: Reagents, products, and final yields after the purification for the condensation reaction between 2,4-dimethyl-1*H*-pyrrole (**1**) and aromatic aldehydes (**2-6**). The reactions were carried out using DCM/ H₂O (2:1) as solvent, HCl 0.2 M as catalyst. Reaction time: 24 hours for the first step and 7 hours for second step.

Aldehyde	Product	Yield [%]
2	11	68
3	12	65
4	13	37
5	14	79
6	15	62

The biphasic system optimized, which facilitated high yields and was amenable to scale-up, was not adequate for the condensation between 2,4-dimethyl-1*H*-pyrrole **1** and the more sterically hindered aldehydes **17**, **18** and **19**.

Hence, trifluoroacetic acid (TFA) concentrated, generally adopted for the one-flask methods reported for synthesizing *meso*-substituted dipyrromethane,^[195] was employed.

Thus, treatment of a solution of one equivalent of 1-naphtaldehyde **8** and two and a half equivalents of 2,4-dimethyl-1*H*-pyrrole **1** in dichloromethane, with a catalytic amount of trifluoroacetic acid (0.1 mmol), results in an immediate change of color, from slightly yellow to intense red, and the complete disappearance of the starting aromatic aldehyde in 5 hours (reaction progress monitored *via* TLC). The obtained dipyrromethane intermediate was then oxidized by *p*-Chloranil. The crude product was washed with water and purified by column chromatography, with a stationary phase formed by neutral alumina gel. Dipyrin **17** was isolated in 23% of yield following chromatography, meaning that using TFA significantly diminished the reaction time but concomitantly increased amounts of side-products, which were observed streaking behind the crude spot of the product on TLC analysis.

This method has been applied also to the synthesis of dipyrins **7**, **9** and **10** (see **Table 3**).

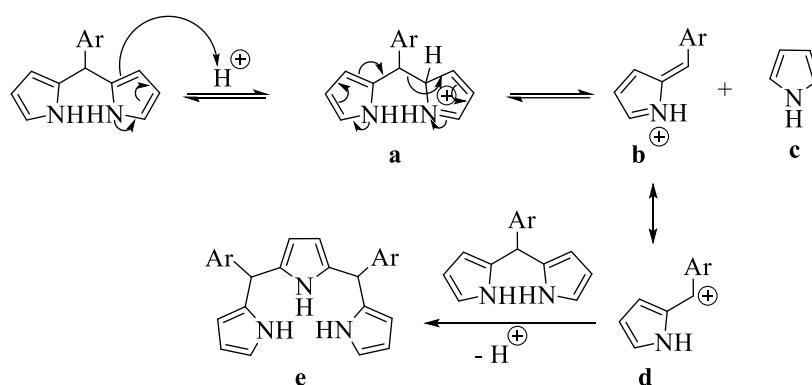
If, on one side, it has been observed a significant drop in the yield of the isolate dipyrins **17** and **18** by using naphthalene derivatives **8** and **9**, on the other side, dipyrin **19** bearing an anthracene residue at *meso* position, was isolated in high yield (78%).

The steric effects certainly play a remarkable role; however, this feature cannot be considered the determining factor. A plausible explanation for this dramatic drop in yield may be due to

the presence of the hydroxyl group in the 4-hydroxy-1-naphthaldehyde **8**, which, as in the case of vanillin, has an electronic effect that provides as an outcome a significant deactivation toward the condensation with pyrrole **1**. The benzene rings fused linearly in naphthalene are stabilized by three canonical resonance structures, which contribute to a variation in the length of the carbon-carbon bonds, suggesting some localization of the double bonds.^[208] Thereby, the aldehyde group could be less prone to undergo reactions.

In addition, the acidity of TFA could have prompted the polymerization of pyrrole more efficiently.^[209] The acid-catalyzed conditions required for the condensation introduce the possibility of scrambling,^[210] which depends mainly on the nature of the *meso* substituents in the dipyrromethane.

The mechanism of scrambling (**Scheme 3**) entails protonation of α -position of pyrrole in a dipyrromethane species (**a**), fragmentation into azafulvene (**b**) and pyrrole (**c**), displacement of the adjacent pyrrole- α -methyl carbenium ion (**d**) and undesired recombination of the resulting fragments (**e**).



Scheme 3: Reaction mechanism of the acid-catalyzed rearrangement (scrambling) of the dipyrromethane scaffold.^[211]

It was observed that the presence of sterically demanding groups at the *meso* position has resulted in less extensive scrambling. The process is complicated to suppress but can be reduced by lowering the reaction rate.^[211] Nevertheless, the possibility of such rearrangement can only partially be ruled out.

The reaction time of the first step, indicated in **Table 3**, refers to the time necessary for the disappearance of the aromatic aldehyde used as a substrate for the condensation and, therefore, the formation of the dipyrromethane intermediate.

Table 3: Reaction conditions and yields for the condensation reaction between 2,4-dimethyl-1*H*-pyrrole **1** and aromatic aldehydes (**7-10**). The reactions were carried out using DCM as solvent and TFA 0.1 mmol as catalyst.

Aldehyde	Reaction time	Product	Yield [%]
7	Step 1: 5 h Step 2: 3 h	16	42
8	Step 1: 5 h Step 2: 3h	17	23
9	Step 1: 7 h Step 2: 3 h	18	15
10	Step 1: 16 h Step 2: 3 h	19	78

Some of the plain dipyrins synthesized, specifically **12**, **13**, **15**, **16** and **18** hold potential coordination sites linked to the aromatic ring in *meso* position, which pave the way for further post-synthetic functionalization, depending on the required target application.

3.1.2 Functionalization with alkyne groups

Halogenated aromatic aldehydes, such as the one appended at the *meso* positions in plain dipyrins **12** and **15**, broaden the scope of the possible functionalization by offering a window for derivatization using transition-metal catalyzed reactions.

Implementing alkynyl groups in the plain dipyrin would enable the potential for a Copper-catalyzed azide-alkyne cycloaddition (CuAAC), in the case of terminal alkynes, and a ruthenium-catalyzed azide-alkyne reaction (RuACC) in the case of internal alkynes, used as substrate. Both are direct methods for accessing several groups in one step.

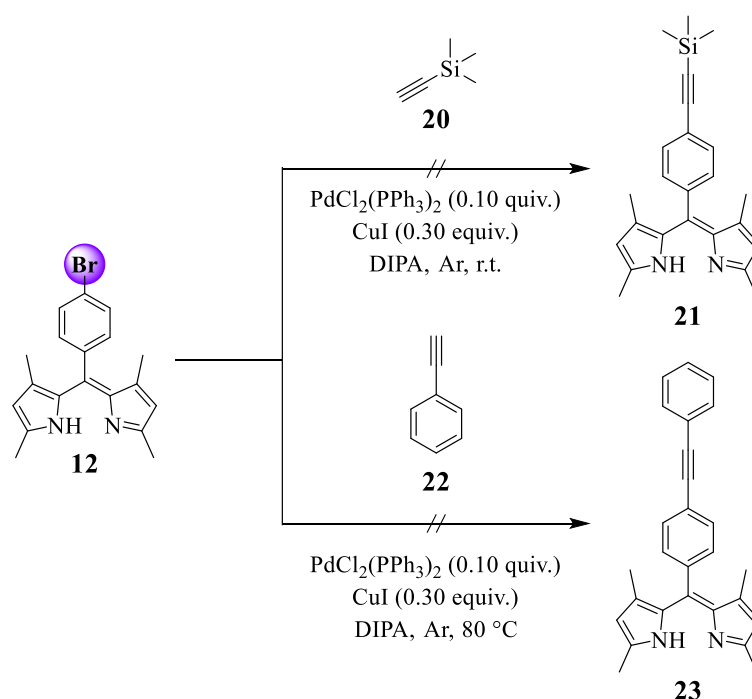
The *meso* functionalized dipyrin **12** was subjected to two different Sonogashira cross-coupling reactions with two different substrates: trimethylsilyl acetylene and ethynylbenzene (**Scheme 4**).

The reaction between one equivalent of **12** and four equivalents of trimethylsilyl acetylene **20** was carried at room temperature, using a palladium source, PdCl₂(PPH₃)₂, as catalyst,

combined with a co-catalytic amount of CuI in a basic solvent, such as dry diisopropylamine (DIPA).

Typically, this type of reaction necessitates an overnight timeframe, approximately sixteen hours. Even if the reaction time was prolonged up to forty-eight hours, no product was formed. Assuming the reaction required higher temperatures, the alkyne substrate was changed to the more robust ethynylbenzene with a boiling point of 143 °C, almost 90°C higher than that one of trimethylsilyl acetylene (53 °C).

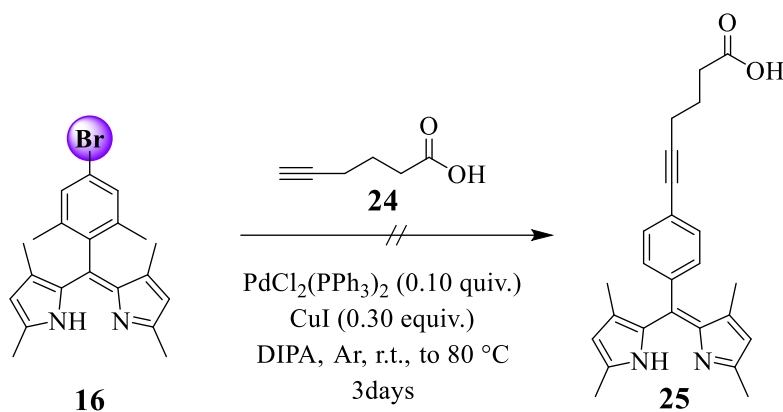
The reaction in **Scheme 4** was first carried out at room temperature. After twenty-four hours, TLC showed no conversion of the starting dipyrin **12**; therefore, the temperature was increased to 80 °C. Despite the efforts, the reaction was unsuccessful, and no product was isolated.



Scheme 4: Attempted Sonogashira cross-coupling reactions of dipyrin **12** with trimethylsilyl acetylene **20** and ethynylbenzene **22** as alkyne substrate to obtain, respectively, dipyrins **21** and **23**.

Concurrently, the other dipyrin having a bromine atom in the structure, ligand **16**, was subjected to a reaction with 5-hexynoic acid **24** (**Scheme 5**). This alkyne is selected based on its potential for further functionalization and the presence of a carboxylic group expected to enhance the molecule solubility in polar solvents.

The reaction was conducted using the same solvent, catalyst, and co-catalyst as before, initially adopting room temperature and heating the reaction temperature to 80 °C. Even so, no conversion of the starting materials was observed and isolating the product **25** was impossible.



Scheme 5: Attempted Sonogashira cross-coupling of dipyrriin **15** with 5-hexynoic acid **24** as alkyne to obtain dipyrriin **25**.

To summarize, the C-C bond formation process between the terminal sp hybridized carbon of the alkyne under examination with the sp² carbon of the aryl halide present in **12** and **16** did not lead to success.

The post-functionalization methodology is a well-documented synthetic approach, supported by numerous examples of cross-coupling reactions performed on BODIPY molecules containing a bromine atom reported in the literature.^[212]

Assuming equal reaction conditions and substrates, the only distinguishing factor between the two systems is the presence of the boron atom coordinated with the nitrogen atoms in the case of BODIPY, which is absent in the case of the free-base dipyrriins **12** and **16**.

Since the Sonogashira cross-coupling involved using a palladium source, such as PdCl₂(PPh₃)₂ as a catalyst, one of the reasonable explanations attributable to the failure of the reactions could be the formation of a dipyrriinato-palladium complex. The complexation of dipyrriins, which will be discussed in more detail in §3.3, requires a base to deprotonate the hydrogen atom statically located between the two nitrogen atoms of the core. Therefore, DIPA, being a basic nucleophilic solvent, may have facilitated this process.

However, what remains unexplained is the fact that no product was isolated during the reactions described in **Schemes 4** and **5**. Indeed, in literature, an homoleptic bis(dipyrrinato) Pd (II) complexes with a similar structure is reported.^[213]

Determining the timeline associated with the formation of the Pd (0) species, which is the active catalyst for the cross-coupling reaction, and the concomitant release of Pd (II), which is the pre-catalyst, but also a potential metal that the dipyrrinato ligands can chelate, is the key to understand the mechanism of this side-reaction better.

3.1.3 Synthesis of water-soluble derivatives

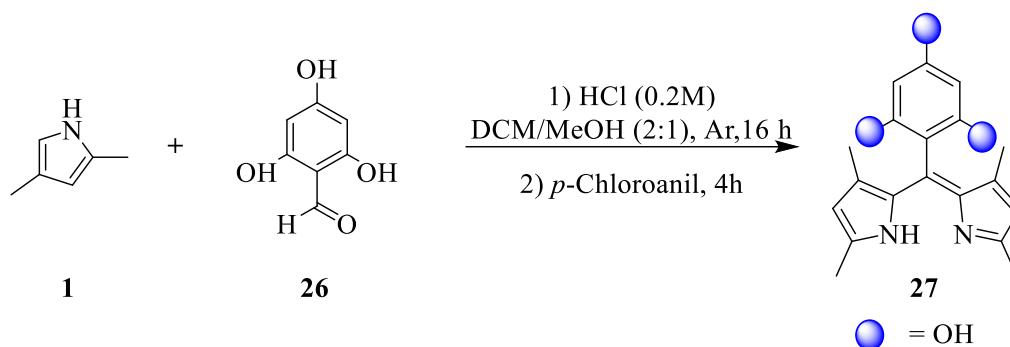
One of the primary limitations of dipyrrin-based scaffolds is their poor solubility in polar solvents, including water. In this context, various post-functionalization studies have emerged to improve water solubility, involving the peripheral incorporation of hydrophilic functionalities that can be grafted into the core.

Based on experimental observation, it has been noted that the introduction of hydroxyl groups in dipyrrins **13**, **15** and **18** (**Scheme 2**) has significantly improved the solubility of these compounds in methanol.

With these observations in hand, 2,4,6-trihydroxybenzaldehyde **26** was chosen as aromatic aldehyde for the condensation with 2,4-dimethyl-1*H*-pyrrole **1** (**Scheme 6**).

As previously reported, the reaction was carried out under an argon atmosphere at room temperature, using a dilute solution of HCl (0.2M) as a catalyst. Methanol was added to the reaction medium to improve the aromatic aldehyde solubility **26**. The second step was the oxidation of the obtained dipyrromethane with *p*-chloranil, which affords the corresponding dipyrrin **27**. Although this technique was highly successful in synthesizing the already reported dipyrrins (**11-19**), some limitations have yet to be encountered in this specific reaction.

The main challenge was the purification of the crude residue. TLC analysis has revealed the presence of several products correlated to several spots. As the molecule in question **27** was not yet reported in the literature, there was uncertainty regarding the relative R_f . To be sure that the product was effectively formed, the crude residue was analysed by mass analysis, which revealed the presence of a peak at 324.1474 m/z, indicative of the compound.



Scheme 6: Condensation reaction between pyrrole **1** and 2,4,6-trihydroxybenzaldehyde **26** to obtain the water-soluble dipyrriin **27**.

The work-up of the reaction mixture was tedious because the reaction crude was soluble in both dichloromethane and water; *ergo*, obtaining a clear phase separation was impossible.

Subsequently, the compound was purified by column chromatography using neutral aluminum oxide gel as stationary phase. Indeed, being more polar than its analogous silica gel,^[214] it was the most effective stationary phase for the other dipyrriins previously purified.

The eluent mixture employed was formed by dichloromethane with a methanol gradient. By increasing the percentage of methanol in the eluent mixture (up to 30%), several fractions remained stacked in the column. For this reason, the polarity of the eluent mixture has been gradually increased, and only when reaching 60% of methanol was it possible to move down the fractions stacked on the column. As expected, several spots were collected and not adequately separated.

Considering the solubility of the crude residue in water, it has been decided to purify the compound through reversed-phase chromatography, assuming that the product, bearing three hydroxyl moieties, could be eluted first. Elution was performed using acetonitrile and methanol as the mobile phase, and the product was isolated as the first spot.

Due to the repeated purifications, the final yield of the compound was only 5%, with an isolated quantity of product of 32 mg.

A more effective strategy could be the use of 2,4,6-trimethoxybenzaldehyde. Since methoxyl groups have lower polarity than their hydroxyl analogues, an easier purification is expected. Once obtained the dipyrriin, the selective cleavage of methoxy-protecting groups next to

hydroxy groups can be achieved using some demethylating agents, such as an acid or a radical hydrogen abstracter.^[215]

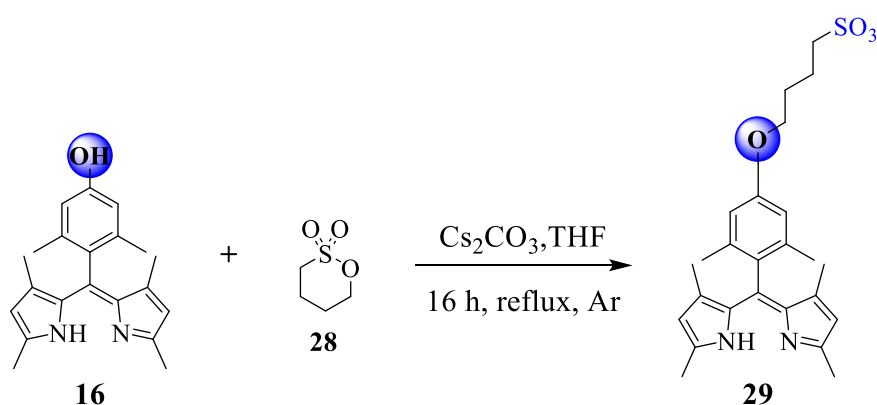
Introducing ionizable hydrophilic groups within the core of hydrophobic molecules can potentially impart an increase in solubility in water.

Among the derivatives employed for the solubilization of dipyrin in water or water-miscible solvents, the sulfonates group have received more consideration.^[216]

The first strategy involved the introduction of an alkyl chain terminating in an SO_3^- group, in dipyrin **16** (**Scheme 7**), through the reaction with 1,4-butane sultone **28**. This is a derivative of 1,4-sultone in which the sulfur atom is cyclically attached to a butane chain.

Due to its strained four-membered ring structure, it is highly reactive and can be opened by nucleophilic attack of the electrophilic carbon attached to the sulfur atom, which is the most reactive center in the molecule due to its high electron deficiency caused by ring strain.^[217]

As outlined in **Scheme 7**, the reaction proceeds through deprotonation of the acidic phenolic hydroxyl group at the dipyrin core **16** with cesium carbonate; thus, the formation of a nucleophilic oxygen atom that can attack the electrophilic carbon atom of the 1,4-butane sultone **28**, resulting in the cleavage of the ring and the formation of the phenolic ether. The reaction was conducted in tetrahydrofuran (THF) and refluxed for 24 hours.

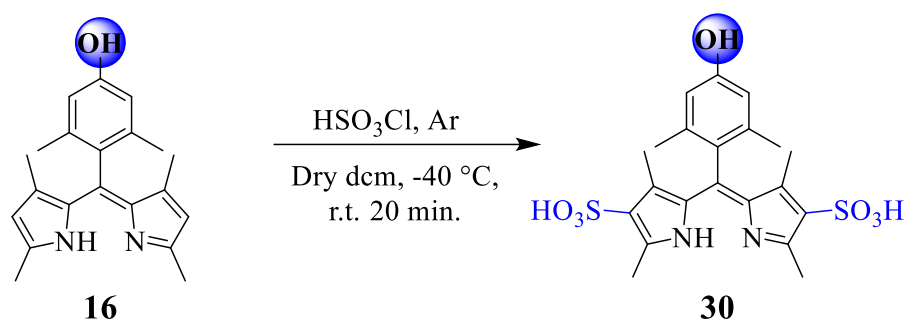


Scheme 7: Synthetic pathway for the sulfo-alkylation reaction of dipyrin **16** promoted by ring-opening of 1,4-butane sultone **28**.

Once at room temperature, cold ethyl acetate was added to the reaction mixture to promote the precipitation of the product, which was isolated as a bright yellow powder with a yield of 35%. Dipyrin **29** was completely soluble in methanol but partially in water. This observation led to

the adoption of another strategy, *i.e.*, introducing sulfonic groups directly into the core of dipyrromethene.

A simple consideration of its mesomeric structures reveals that the core 2- and 8- positions bear the least positive charge, making them susceptible to electrophilic attack.^[218] As such, sulfonate groups were attached directly to the scaffold of dipyririn **16** (Scheme 8).



Scheme 8: Disulfonation of dipyririn **16** to obtain the water-soluble dipyririn **30**.

Disulfonations on dipyrromethene scaffolds tend to proceed efficiently using three and a half equivalents of chlorosulfonic acid (HSO_3Cl) in dry dichloromethane.

An inert atmosphere is required since (HSO_3Cl) is sensitive to moisture, decomposing into hydrogen chloride and sulfuric acid upon contact with water.

According to the literature,^[219] one equivalent of **16** was dissolved in dry dichloromethane under an argon atmosphere, and the obtained solution was cooled to -40°C using an isopropanol/dry ice bath. The sulfonating agent was dissolved in dry dichloromethane and added dropwise over a few minutes to the solution of **16**. After the addition was complete, the cooling bath was removed, and the reaction was allowed to warm up to room temperature and stirred for twenty minutes.

The disulfonate product **30** precipitated out of the dichloromethane solution. The small amount of compound obtained was collected using filtration and dried under vacuum. No chromatography was required, and the procedure afforded an orange-coloured precipitate **30** isolated in 21% yield and completely soluble in water.

3.1.4 Photophysical properties

Dipyrromethene ligands are multifaceted chromophoric systems, even without the complexation of any metal.

To better understand how complexation affects photophysical properties, hereafter is reported the photophysical characterization of the plain dipyrin previously synthesized.

As shown in **Figure 32**, the UV/Vis absorption spectra of the plain ligands **11-13** are dominated by an intense transition between 400 and 550 nm.

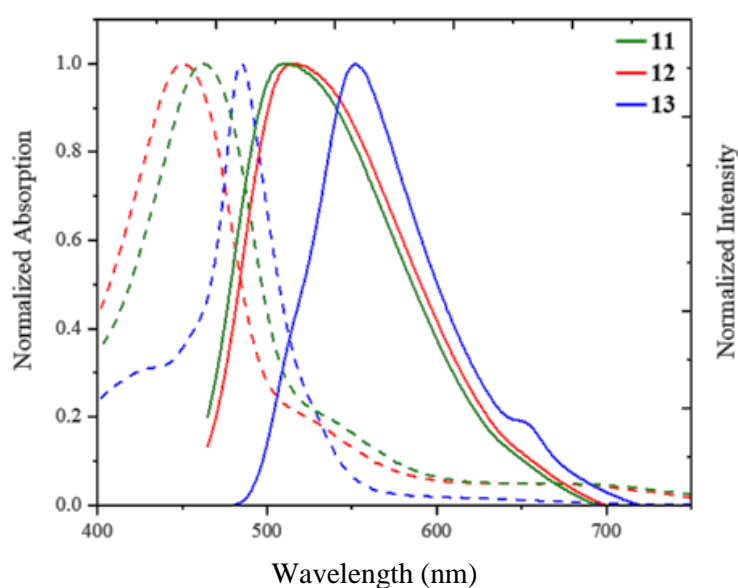


Figure 32: UV/Vis absorption (dashed plot) and emission (solid plot, $\lambda_{exc}=450$ nm) spectra of the plain dipyrins **11-13** in toluene at 20 °C.

The plain *meso* phenyl dipyrin **11** exhibits an absorption peak centered at 463 nm, with a corresponding emission maximum at 510 nm.

The introduction of the bromine atom in position 4' of the phenyl, which is in *para* to the dipyrin **12**, does not result in significant modifications in the absorption and emission profiles, but only a slight hypsochromic shift (see **Table 4**).

A substantial change in the shape of the transition located at 483 nm marks the electronic profile of dipyrin **13**. The presence of 4-hydroxy-2,6-dimethyl phenyl in the *meso* position causes a red-shift in emission, centered at 554 nm, thus resulting in an increase in the Stokes shift compared to the first two exposed plain dipyrins.

Dipyrrin **11** lack substituents in position 2 and 6; therefore, the rotation around the sp^2 carbon atom connecting the two pyrrolic rings leads to a significant decrease in quantum yields, equal to 5%.

In addition to this nonradiative deactivation pathway from the S_1 excited state, the presence of the bromine atom in dipyrrin **12** induces further fluorescence quenching, $\Phi = 2\%$, because of the internal heavy atom effect.^[11]

The presence in the aromatic ring of electron-donating groups, such as hydroxyl and methoxyl, besides inducing a red shift in both absorption and emission spectra, also decreases the fluorescence quantum yield in dipyrrin **13**, $\Phi = 3\%$.

The absorption spectra of the plain dipyrrins **14-16** showed a defined absorption maximum between 450 and 451 nm with fluorescence peaks between 500 and 509 nm (**Figure 33**).

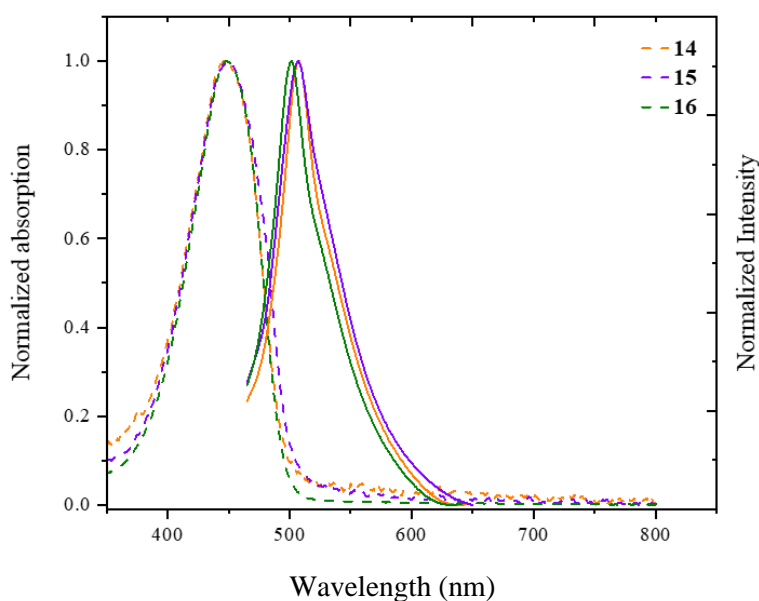


Figure 33: UV/Vis absorption (dashed plot) and emission (solid plot, $\lambda_{exc} = 440$ nm) spectra of the plain dipyrrins **14-16** in toluene at 20°C.

As expected, replacing the phenyl ring at the *meso* position of the dipyrrin core with mesityl group in dipyrrin **14** strongly hinders the internal rotation, increasing the fluorescent quantum yield, $\Phi = 10\%$.

As observed previously, the substitution of the methyl group in position 4' of the aromatic ring with a bromine atom, in the case of dipyrrin **15** and a hydroxyl group for dipyrrin **16**, effect the quantum yields of the compounds, decreasing the fluorescence efficiency (see **Table 4**).

The increase in the extent of the π -electron system of the aromatic rest appended at the *meso* position in dipyrins **17** and **18** bearing a naphthalene residue did not lead to a shift of the absorption and fluorescence spectra to longer wavelengths (**Figure 34**).

A similar consideration applies to dipyrromethene **19** in which the anthracenyl in the *meso* position, in addition to its typical vibrational absorption band, between 310 and 400 nm characteristic of its upper states, exhibits an absorption maximum peak centered at 450 nm.

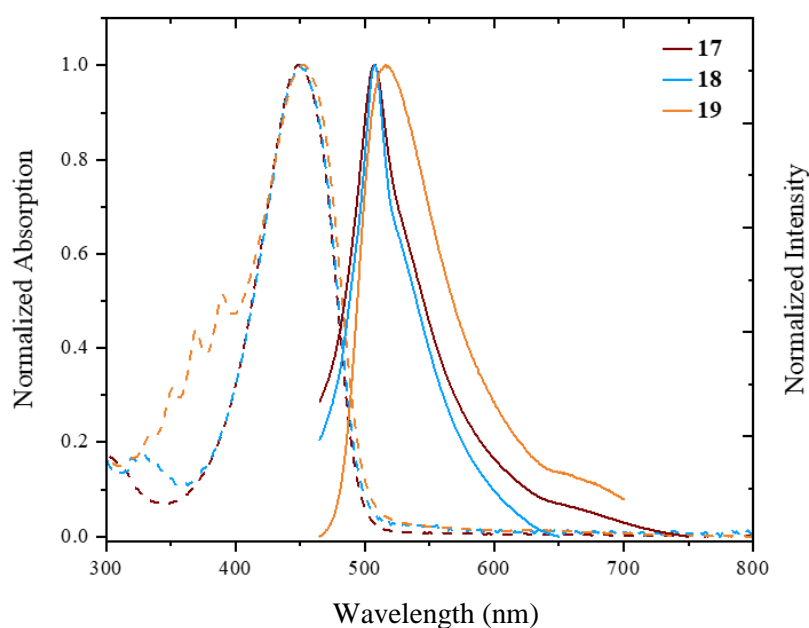


Figure 34: UV/Vis absorption (dashed plot) and emission (solid plot, $\lambda_{exc}=440$ nm) spectra of the plain dipyrins **17-19** in toluene at 20 °C.

Nevertheless, the increase in conjugation induces a bathochromic shift, with an emission at 517 nm. The higher degree of conjugation prompts a modest enhancement of the Φ , from 15 % for **17** to 16% for **19**.

The grafting of an alkyl chain terminating in a sulfonic group into dipyrin **29** marginally affects the photophysical properties compared to the parent molecule **15**. (**Figure 35**). Compared to dipyrin **15**, it shows a similar absorption band and a slight red shift in the emission profile, with a broader vibrational structure and a more minor emission shoulder with a peak situated at 660 nm. It is usually expected that sulfonates groups may cause fluorescence quenching. Even so, the quantum yield of compound **29** in toluene is 12%, slightly higher than its hydroxylated counterpart **15** ($\Phi=8\%$). Although the compound is soluble in water, it was

non-emissive in such a polar medium, therefore the measurements were performed only in toluene.

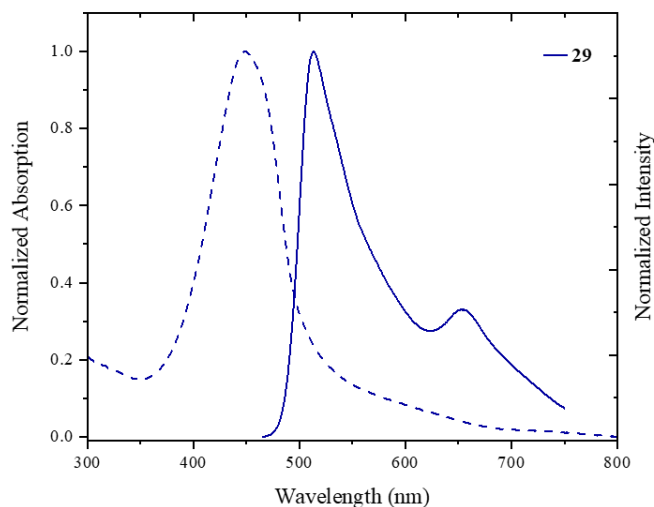


Figure 35: UV/Vis absorption (dashed plot) and emission (solid plot, $\lambda_{\text{exc}}= 450$ nm) spectra of the plain dipyrin **29** in toluene at 20 °C.

In **Table 4** summarized the characteristic photophysical values in spectroscopic toluene obtained for the plain ligands presented so far.

Table 4: Photophysical properties of the plain dipyrins **11-19, 29** in toluene. ^[a]Quantum yields were determined by the reference method, using as reference Ru(bpy)₃Cl₂ in water ($\Phi = 0.028$) ^[b]Exciting with a NanoLED source at 455 nm.

Compound	λ_{abs} [nm]	λ_{em} [nm]	Φ ^[a]	τ ^[b] [ns]
11	463	510	0.05	1.4
12	448	518	0.02	1.6
13	483	554	0.03	1.5
14	450	500	0.10	1.8
15	450	507	0.08	1.7
16	451	509	0.05	1.7
17	448	508	0.15	2.0
18	449	508	0.12	2.0
19	450	517	0.16	2.4
29	449	514	0.12	1.7

3.2 π -expanded dipyrin ligands

Post-modification methods on plain dipyrin frameworks are convenient for preparing α - and β -functionalized dipyrins.^[156]

As previously observed, except for the alkyl-sulfonated dipyrin **29**, the plain ligands characterized in §3.1.3 emit at wavelengths shorter than 650 nm, precluding their use in NIR applications.

One of the strategies widely used to reduce the optical band gaps for dipyrins, thereby pushing the emission to the red, is the extension of the π -conjugation pathway *via* substitution.

The presence of methyl groups in the α position constitutes a good platform for further functionalization of the dipyrin core with aromatic moieties, which can result in a significant red shift in the absorption and emission properties of the dipyrin ligands, owing to the extended π -conjugation.

More specifically, by virtue of their strong nucleophilic character, these methyl groups can be deprotonated under mild conditions. The resultant intermediates will readily add to an electronic-rich aromatic aldehyde, generating a styryl group bearing an aromatic rest (**Figure 36**).

This synthetic procedure, known as Knoevenagel condensation,^[220] has been used to extend the degree of π -electron conjugation in plain dipyrromethene units, having as effect a pronounced bathochromic shift to both absorption and fluorescence spectral maxima.

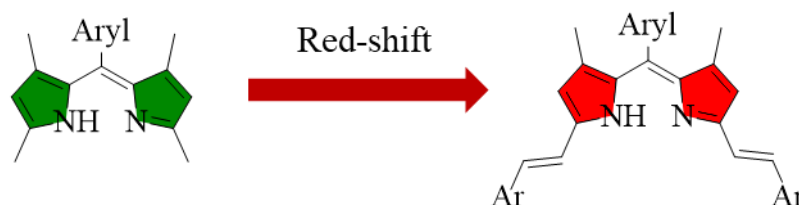


Figure 36: Chemical structure of the π -expanded dipyrromethene scaffold designed to achieve a red-shifted emission.

3.2.1 Knoevenagel condensation: general background

Named after the chemist Emil Knoevenagel in the 1890s,^[220] the eponymous reaction is a modified aldol condensation based on a nucleophilic addition between an aldehyde (or ketone) and an acidic-proton-containing compound in the presence of a basic catalyst, resulting in C=C formation.^[221]

It is one of the imperative and essential reaction in synthetic organic chemistry, which affords the production of various α,β -unsaturated intermediates, like cinnamic acids,^[222] key intermediates for synthesizing natural and therapeutic drugs, polymers, cosmetics and perfumes.^[223] The reaction has been traditionally conducted under homogenous conditions.^[224] With an industrial-level output, there has been an increasing effort to develop efficient and sustainable catalytic conditions.^[225] In recent times, attention has been directed towards the development of heterogeneous catalysts such as zeolites,^[226] metal-organic framework,^[227] ionic liquids, hydrotalcites^[228] and functionalized mesoporous silica,^[229] employed to catalyse the Knoevenagel condensation reaction.

In the pursuit of a deeper understanding of the activation barriers associated with key steps and intermediates, a complete theoretical and free energy profile (**Figure 37**), able to explain the experimental kinetics, has been reported.^[230]

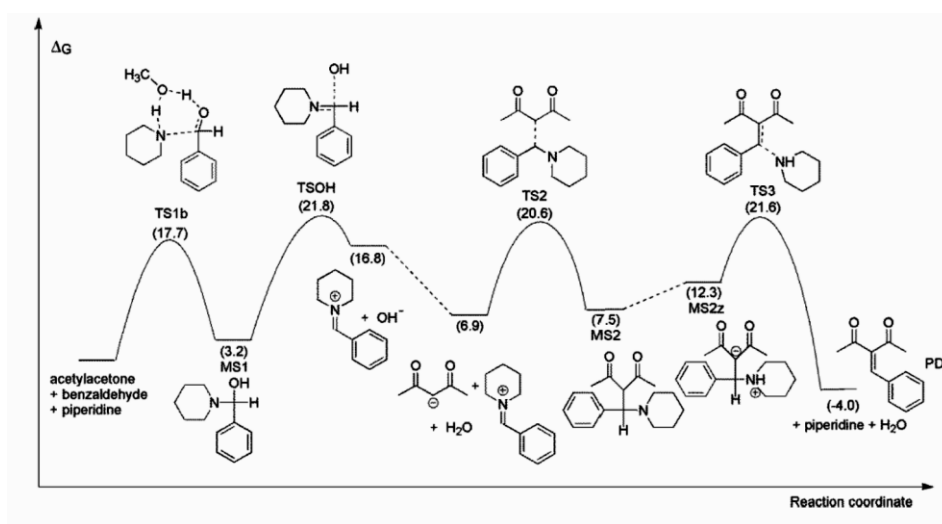


Figure 37: Free energy profile for the acetylacetone reaction with benzaldehyde catalyzed by piperidine. Units in kcal mol⁻¹. The standard state of 1 mol L⁻¹ for solutes and pure solvent for methanol. Reprinted with permission from ACS from E. V. Dalessandro, H.P. Collin, L. G. L. Guimarães, M.S. Valle and J. R. Pliego, *J. Phys., Chem. B*, **2017**, *121*, 5300-5307.^[230]

The kinetics analysis performed in this study revealed that the aromatic aldehyde plays a predominant role; the deprotonation of acetylacetone and its nucleophilic attack on the iminium ions is not the rate-determining step in this reaction.

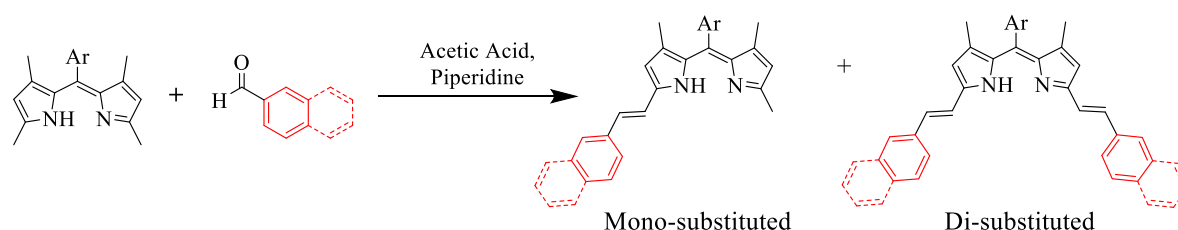
Although the Knoevenagel condensation mechanism for dipyrromethenes (or BODIPY analogues) has never been reported in the literature, mechanistic considerations can be made based on studies conducted on the abovementioned theoretical calculations, shown in **Figure 37**.

Particularly, variations in the final yields are expected by changing the aromatic aldehyde used as reaction substrate.

3.2.2 Synthesis

As anticipated in §3.2, in the presence of a catalyst, the active hydrogens in the methyl groups in the α -position of a dipyrin are deprotonated and can undergo condensation with an aromatic aldehyde. Spontaneous dehydration affords the unsaturated product, resulting in C=C bond formation.^[226]

It is essential to underline that, in each Knoevenagel condensation performed in this work it was observed the formation of the mono- and difunctionalized ligands, as depicted in **Scheme 9**, consistently with the findings reported in the literature.^[125]



Scheme 9: Introduction of styryl-aryl groups in the simple dipyrins by Knoevenagel condensation affording the mono- and disubstituted π -expanded ligands obtained in this work.

Specifically, the starting plain dipyrin was converted entirely into the two different products; however, despite the addition of multiple equivalents of aromatic aldehyde to the reaction mixture, it was not possible to convert the mono-functionalized ligand into the corresponding difunctionalized.

For clarity only the difunctionalized ligands will be highlighted in the following reaction Schemes.

Our interest in developing near-infrared emissive dipyrin dyes has seen us explore several aromatic aldehydes, each having a different structure and steric hindrance, to modulate the outcome in terms of fluorescent properties and selectivity for various pursuits.

3.2.2.1 Expansion *via* classic condensation

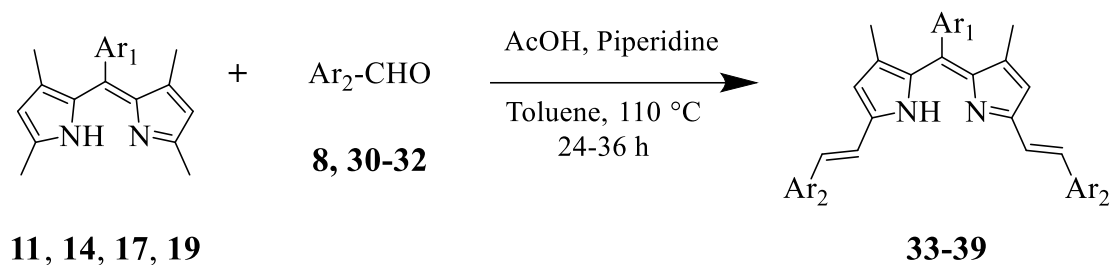
The initial approach utilized for the expansion of the π -conjugation of the plain dipyrins **11**, **14**, **17**, **19** involved the conventional method.^[125]

As outlined in **Scheme 10**, the endothermic reactions were conducted in dry toluene under an argon atmosphere. Being a condensation, water was formed as a co-product, when the activated methylene groups of the dipyrin reacted with the carbonyl group of the aromatic aldehyde. Water loss is a critical step in creating the carbon-carbon double bond of the α,β -unsaturated product. Aiming to remove water quantitatively, a Dean-Stark apparatus was attached to the reaction flask and the air condenser. The water in toluene boiled from an azeotrope (b.p. 87°C); subsequently, the azeotropic vapours reached the reflux condenser, cooled down, and then they were collected in the neck of the Dean-Stark apparatus. The water was distilled and accumulated in the trap, while the toluene returned to the reaction flask to continue boiling. The reactions were refluxed for 24-36 hours with a catalytic amount of piperidine and acetic acid. Specifically, piperidine is used as a base to deprotonate the methylene groups of the plain dipyrin, which increases its reactivity towards the carbonyl compound. On the other hand, acetic acid is used as a catalyst to increase the reaction rate. It can protonate the carbonyl group of the aromatic aldehyde, making it more susceptible to attack by the methylene groups of the nucleophile.

According to a general procedure,^[125] π -extended dipyrin **33** was obtained by condensation of naphthalene-2-carbaldehyde **8** with plain dipyrin **11**.

A control TLC after 24 hours showed complete conversion of the starting dipyrromethene **11** and the formation of two spots: a more polar blue one, indicative of the difunctionalized product, and a purple one of the monofunctionalized compound.

Despite the number of equivalents of aldehyde added, up to six, the monofunctionalized product was not converted.



	Ar ₁	Ar ₂	yield
33			36 %
34			27 %
35			30 %
36			10 %
37			26 %
38			33 %
39			45 %

Scheme 10: Knoevenagel condensation between plain dipyrroles (**11,14,17,19**) and aromatic aldehydes (**8,30-32**) to obtain π -expanded ligands (**33-39**).

The reaction proved to be relatively straightforward; the primary issue associated with this type of functionalization was the purification. The two obtained products, mono- and difunctionalized, have a substantially comparable polarity. The optimal strategy for the purification was using a very long column packed with neutral alumina gel and a nonpolar eluent, such as cyclohexane; this resulted in very long purification times. The product was a bright violet powder with a 36% yield.

Aware of the importance of choosing the meso-phenyl substituent, plain dipyrins **12** and **13** were not further functionalized, as they lack substituents in positions 2 and 6 of the aromatic ring.

Therefore, the functionalization of dipyrromethene **14** was subsequently carried out.

In this case, the procedural setup also involved using a Dean-Stark apparatus to remove the water formed from the condensation reaction and thus shift the equilibrium towards the products. Small quantities of piperidine (0.1 mmol) and acetic acid (0.2 mmol) created a catalytic system that helped in improving the yield and selectivity of the desired product.

Despite the different electrophilic character of the aromatic aldehydes **8**, **30-32** employed for expanding the conjugation of dipyrin **14**, the conversion of the starting dipyrromethene occurred in a comparable time for each one, within twenty-four to thirty-six hours. From a synthetic point of view, the same considerations made for the π -expanded dipyrromethene **33** are also valid for **34** and **35**, isolated with yields of 27% and 30 %, respectively.

Whether the substrate was 2-naphthaldehyde **8** or 4-methoxy-benzaldehyde **30**, the formation of the mono- and difunctionalized products was observed, along with other byproducts. The purification, in this case, was also carried out using pure cyclohexane as the eluent solvent.

The reaction with 5-(hydroxymethyl)-furan-2-carbaldehyde **31** proved to be more complicated; in this specific case, the condensation led to multiple products: control TLC of the crude reaction mixture showed seven highly coloured spots. Since the π -expanded ligand **36** has not been reported in the literature, each spot was collected. Due to the presence of highly polar substituents, the eluent mixture used for the column chromatography was dichloromethane with 10% of methanol. As the spots were very close, purification had to be repeated three times. This accounts for the low obtained yield (10%).

The condensation of 9-phenanthrenecarbaldehyde **32** and plain dipyrin **14** was substantially characterized by the same aspects as the previous reported reactions. In this case, the mono-

functionalized product was also formed. Purification by column chromatography led to the isolation of the product **37** with a 26% of yield, consistent with the others previously described.

The methyl groups in position 1 and 9 of the simple ligand **17** having an anthracene rest appended at *meso* position were converted into the π -expanded ligand **38** after twenty-four hours of reflux in dry toluene with 2-naphthaldehyde **8**, under an argon atmosphere (**Scheme 10**). As expected, the reaction led to mono- and bi-functionalization, providing a final yield of the desired compound **38** of 33%, in line with those reported in this work.

Finally, also dipyrromethene **19**, bearing an anthracene residue in the *meso* position, was subjected to condensation with 2-naphthaldehyde **8** (**Scheme 10**). The reaction was carried out as previously described; the main difference to underlining lies in the final yield. The product **39** was isolated with a yield of 45%, the highest value obtained for the Knoevenagel condensation described in this work. The carbonyl group involved in the reaction, specifically the one in the 2-naphthaldehyde **8**, has already been previously used, so it is reasonable to affirm that there is no significant variation in electrophilicity. What is different is the *meso*-anthracene in the dipyrin core, which may have influenced the electronics of the methyl groups subjected to condensation in some way.

3.2.2.2 Expansion *via* microwave assisted condensation

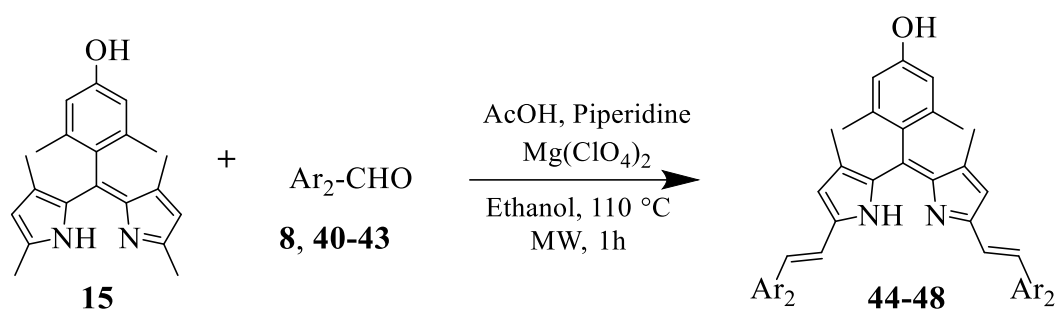
As the strategic design aims to balance good quantum yields with modest solubility properties, the expansion of the plain ligand **15**, bearing a 4-hydroxy-2,6-dimethyl-aryl moiety at the *meso* position, was achieved.

Based on a pros and cons analysis, the Knoevenagel condensation on dipyrin **15** was conducted in a microwave (MW) reactor to enhance the reaction yields and achieve greater output. Microwave irradiation is often used to improve the rates for classical organic reactions.^[231]

As outlined in **Scheme 11**, the reactions were carried out in ethanol in the presence of a catalytic amount of the Lewis acid $\text{Mg}(\text{ClO}_4)_2$, which has been reported as a salt displaying remarkable catalytic activity in such types condensation.^[229] The application of MW energy has been superior to conventional heating, resulting in a conversion of the starting material in just one hour. The fast conversion, however, resulted in the formation of numerous byproducts,

presumably due to the microwave heating leading to a reduction in activation energy for other side reactions.

Going more in detail, the expansion of the π -system of dipyrin **15** with 2-naphthaldehyde **8** proved to be comparable to the different Knoevenagel reactions presented so far, resulting in a yield of 27% for the compound **44**. Introducing a hydroxyl group into the aromatic aldehyde, precisely 1-hydroxy-2-naphthaldehyde **40**, provoked a significant decrease in yield, specifically to 10% **45**, due to the exhaustive formation of other byproducts.



	Ar ₂	yield
44		27 %
45		12 %
46		31 %
47		13 %
48		10 %

Scheme 11: Microwave-assisted Knoevenagel condensation between plain dipyrin (**15**) and aromatic aldehydes (**8**, **40-43**) to obtain π -expanded ligands (**44-48**).

Moreover, having a comparable polarity, the purification was carried out several times. The best way to purify this compound **45** was through an automatic column chromatographic packed with alumina gel. The higher operating pressure of the system, coupled with the ability to slowly increase the gradient of the polar solvent, methanol in this case, makes it the optimal way to obtain a pure compound.

The utilization of aromatic aldehydes formed by condensed heterocycles showed different effects in terms of final yield.

Using 1-*H*-indole-5-carbaldehyde **40** as a carbonyl substrate for the Knoevenagel condensation with dipyrin **15** affords the final disubstituted π -expanded ligand with a yield of 31%. Generally speaking, indoles are known to have more pronounced acidic properties than naphthalene derivatives.^[232] This could have facilitated deprotonation and hence greater reactivity in the nucleophilic attack of the methyl groups present in the dipyrin substrate.

On the other hand, employing benzo[*b*]thiophene-2-carbaldehyde **41** as an aromatic aldehyde caused a decrease in the final yield of the compound **47**. The thiophene ring, being directly conjugated to the carbonyl group, could have rendered the latter less reactive towards the nucleophilic attack of the methyl groups.

The sulfur atom in the thiophene can also form a strong bond with the hydrogen atom of the methyl groups in the dipyrin **15**, forming a stable intermediate that may not readily undergo further reactions.^[233] These factors could have contributed to a lowered yield of the desired product. In addition to the low selectivity in forming the difunctionalized expanded ligand, it should be emphasized that purifications *via* column chromatography usually impact the percentage yields of the pure obtained product.

The morpholino group attached in position 4 to the aromatic ring in the 4-morpholinobenzaldehyde **43** exerts an electron-donating effect. The presence of the nitrogen with a lone pair of electrons, which can donate electron density to the benzaldehyde, makes the morpholino group an electron-donating group (EDG), but at the same time, the ring less electrophilic, thus causing a low reaction yield, 10%, for compound **48**. In this latter case, the crude residue was also subjected to purification by column chromatography, so the compound loss due to this technique should also be considered.

3.2.3 Photophysical properties

The π -expanded dipyrrens obtained were then characterized from a photophysical point of view in toluene.

The normalized absorption spectrum of the π -extended ligand **30** (**Figure 38**) displays an intense band centered at 360 nm, attributable to the electronic transitions localized on the vinyl-naphthyl moiety attached to the α -positions of the dipyrren core, which are absent in the absorption spectrum of the derivative simple plain ligand **11**.

The extension of the π -conjugation results in a clear and conspicuous bathochromic shift of both absorption and emission profile, which exhibit maxima values at, respectively, 581 and 645 nm (see also **Table 5**).

As the aromatic ring in the meso position of the π -expanded dipyrromethene ligands is a simple unsubstituted phenyl, rotation around the bond is facilitated as expected. Thus, the quantum yield is low ($\Phi = 8\%$). Despite the occurrence of several nonradiative processes, the measured lifetime of the fluorophore is 4.2 ns.

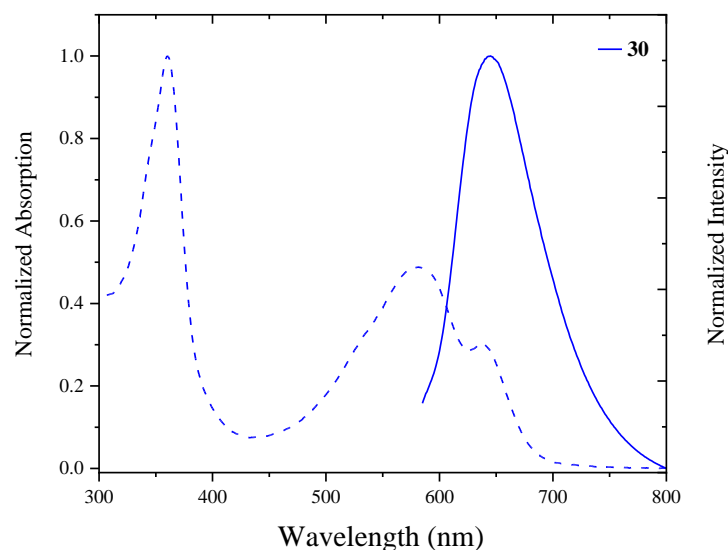


Figure 38: UV/Vis absorption (dashed plot) and emission (solid plot, $\lambda_{\text{exc}} = 560$ nm) spectra of π -expanded ligand **30** in toluene at 20 °C.

The diverse conjugation of the electron-rich aromatic aldehydes employed for the expansion of the plain ligand **14** result in a definite effect on their photophysical properties.

The structural difference between the π -expanded dipyrrens **33** and **34** lies in the presence of 2- and 6-mesityl groups in the aromatic rest situated at the *meso* position of the dipyrromethene core.

This replacement does not affect electronic absorption and emission profiles of compound **34**, which remain almost unaltered (**Figure 39**) but impinges on the emission efficiency, specifically fluorescence quantum yields, increasing up to $\Phi = 15\%$. The absorption profile of the π -expanded dipyrren **35** exhibits a more intense band between 320-400 nm, attributed to transitions localized on the vinyl methoxy group present in α -positions and another band, less intense, ranging from 490 and 650 attributed to the $\pi \rightarrow \pi^*$ transition localized on the dipyrromethene core.

Albeit the conjugation of the group utilized for expanding the π -system of the chromophoric unit is reduced for **35**, the methoxy substituent placed at the *para* position on the benzene ring is classified as an electron-donor group, according to Hammett equation.^[234]

This effect shifts the emission profile toward longer wavelengths, with a maximum of 645 nm. Both π -expanded ligands show a highly intense violet colour in toluene solutions.

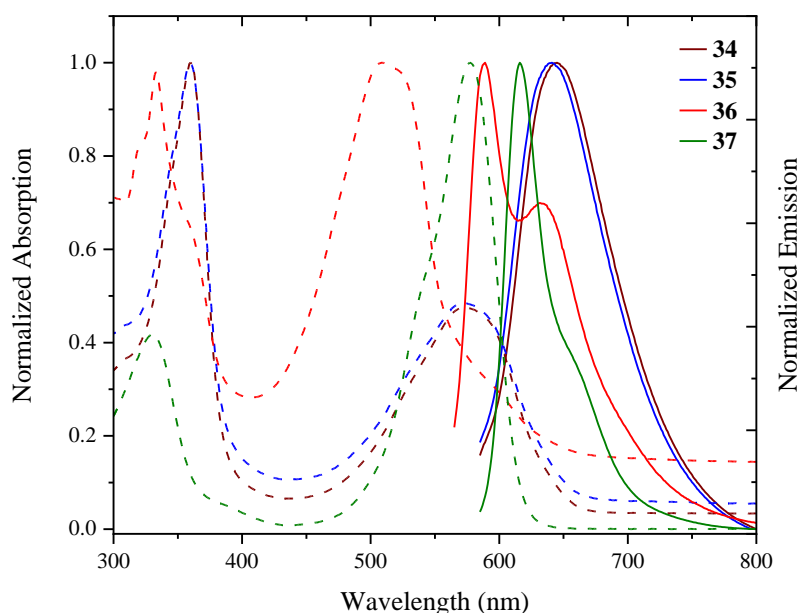


Figure 39: UV/Vis absorption (dashed plot) and emission (solid plot, $\lambda_{\text{exc}} = 550$ nm for **36** and $\lambda_{\text{exc}} = 585$ nm for **34, 35** and **37**) spectra of π -expanded ligands **34-37** in toluene at 20 °C.

The π -expanded ligand **36** is a result of the Knoevenagel condensation between the plain ligand **14** and 5-(hydroxymethyl)-furan-2-carbaldehyde **31**.

This group is distinguishable in the absorption spectrum (red dashed plot in **Figure 39**) with a slightly different shape than the styryl-naphthyl moiety. The extension of the conjugation of the core through the insertion of the vinyl-hydroxymethyl-furanyl groups results in an absorption band located at 511 nm, entailing a bathochromic shift compared to the plain ligand **14** but a dramatical hypsochromic shift compared to expanded ligands **34** and **35**.

The same considerations apply to the emission profile, characterized by a narrower band, with a maximum of 589 nm and an emission shoulder centered at 650 nm. The reduced conjugation in the system shows emission at a lower wavelength than the naphthalene residue.

Remarkably, adding an extra aromatic ring to the conjugated aromatic system in **37** did not produce the expected result. More precisely, it has been hypothesized that replacing the vinyl-naphthyl group with an analogous phenanthrene-based could have further destabilized the expanded dipyrromethene molecular orbitals **37**, thus, inducing a bathochromic shift in the electronic spectrum. The absorption profile of **37** (green dashed plot, **Figure 39**) remained essentially unchanged in comparison to **34** (wine dashed plot, **Figure 39**), even though with a surprisingly reduced intensity of the phenanthrene absorption band located between 300-400 nm and an increase in the absorption band of the dipyrromethene core, in the range of 480-650 nm. On the other hand, the emission profile is characterized by a significantly narrower bandwidth, with a maximum peak shifted towards lower wavelengths, 616 nm.

The results obtained from the expansion of the plain dipyrin **14** show that the styryl-naphthyl groups present in the π -extended dipyrin **34** induced superior longer wavelength characteristics compared to the styryl-methoxy groups present the π -extended dipyrin **35** (see **Table 5**).

A lower-wavelength emission profile defines the π -expanded ligand **36**, with a peak at 589 nm, and, concurrently, the best solubility in methanol, owing to the presence of hydroxyl groups in the pendant moieties.

Further investigation is required to fully understand why the fused tricyclic system that characterizes phenanthrene has not significantly altered the molecule molecular orbitals **37**, causing a red shift in the electronic spectra. It cannot be ruled out that phenomena of aggregation or other factors may be concealed in the small shoulder that can be observed (green solid plot, **Figure 39**) at approximately 680 nm through careful observation.

The absorption (dashed plot) and emission (solid plot) spectra of the π -extended dipyrromethene ligand **38** in toluene are shown in **Figure 40**.

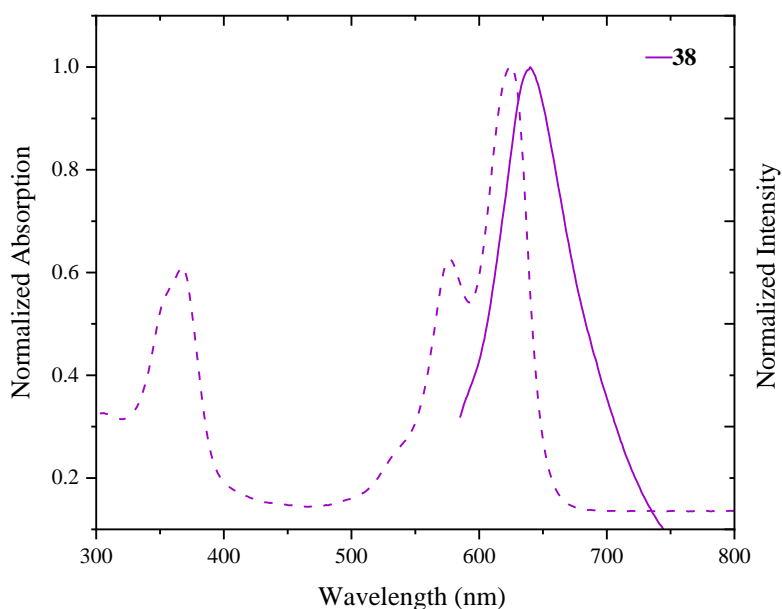


Figure 40: UV/Vis absorption (dashed plot) and emission (solid plot, $\lambda_{\text{exc}}=585$ nm) spectra of π -expanded ligand **38** in toluene at 20 °C.

The absorption profile shows two bands, the typical one localized on the vinyl-naphthyl groups and a second one between 500 and 700 nm arising from the transitions localized on the dipyrinato scaffold.

Compared to the other expanded ligand investigated, we can notice a small absorption shoulder at a lower wavelength that falls back before developing a second peak at higher intensities and longer wavelengths, *i.e.*, 625 nm. It is, therefore, possible that the naphthalene group present in the *meso* position of the chromophoric unit, in addition to causing a shift at lower energies in the absorption, may also have caused a change in shape.

A consistent bathochromic shift is also observed in the emission profile, which peaks at 640 nm. The excited-state population decays with a lifetime $\tau=5.1$ ns. Surprisingly, the quantum yield of the fluorophore **38** is limited to 4%.

The photophysical properties of the π -extended ligand **39** were investigated in toluene.

As it can be observed in **Figure 41**, the molecule containing an anthracenyl group at the *meso* position of the dipyrinato unit shows features comparable to those of the compound **38**.

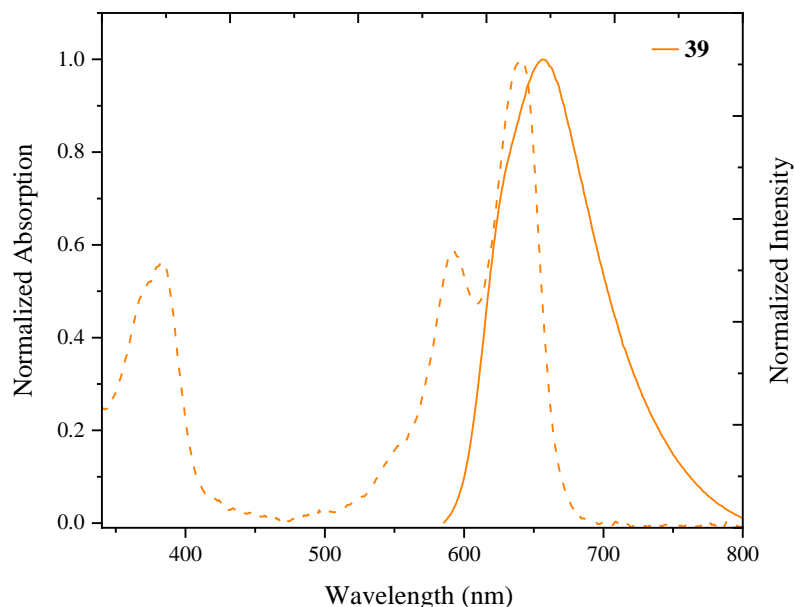


Figure 41: UV/Vis absorption (dashed plot) and emission (solid plot, $\lambda_{\text{exc}}=585$ nm) spectra of π -expanded ligand **39** in toluene at 20°C.

A further shift toward the red region can also be noticed, with an emission centered at 656 nm, proceeding up to 800 nm. The quantum yield of **39**, compared to **38**, increased to $\Phi=12\%$, with a reduced lifetime of 2.3 ns.

The absorption and emission spectra of the π -expanded dipyrins **44** and **45** in toluene are shown in **Figure 42**.

They are both derived from the simple ligand **15** extended through the insertion of styryl-naphthyl groups which contain an additional hydroxyl group substituent **45**.

Although this difference may appear minimal, the immediate link of the hydroxyl group, present on the naphthalene ring with the vinyl set, alters the electronic cloud of the conjugated system.

As represented in **Figure 42**, the absorption spectrum of the π -extended dipyrin **44** displays the characteristic structured band of the naphthyl vinyl moiety in the range of 300-400 nm, which appears to be more intense and narrower in comparison to the $\pi \rightarrow \pi^*$ transition and its

vibronic coupling localised on the dipyrin, between 450 and 650 nm. For the π -expanded dipyrin **45**, we can observe a reversal of the trend: a more intense and narrower transition ascribed to the absorption of the dipyrromethene ligand (450-650 nm) and a fainter band localized on the vinyl naphththyl moiety (300-400 nm).

However, the emission profiles are identical, even though it is evident that a decrease in the quantum yield and relative lifetime ($\Phi = 11\%$, $\tau = 4.1$ ns for **44** and $\Phi = 6\%$, $\tau = 4.1$ ns for **45**) due to the hydroxyl group.

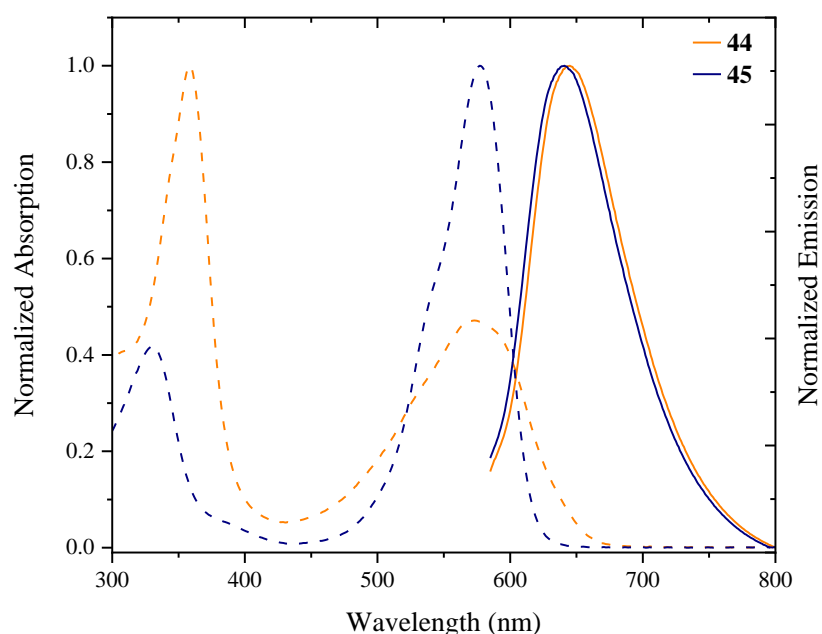


Figure 42: UV/Vis absorption (dashed plot) and emission (solid plot, $\lambda_{\text{exc}} = 585$ nm) spectra of π -expanded ligands **44** and **45** in toluene at 20 °C.

A heteroatom in a fused aromatic system usually significantly influences the π -cloud of the main chromophore, modifying the final optical properties.

The derivatization of the plain ligand **15** with five-membered heteroatom cyclic moieties fused with an additional aryl resulted in the formation of the π -extended ligands **46** and **47**.

For the former, a nitrogen atom is bonded to carbon atoms in the heterocycle; the transitions involving the nonbonding electrons have properties similar to those of the $\pi \rightarrow \pi^*$ transition.

The nonbonding orbital is perpendicular to the ring plane, allowing it to overlap the π -orbitals on the adjacent atoms.

This explains why compound **46** shows an absorption band between 300-400 nm (**Figure 43**), which resembles the diagnostic band localized on the vinyl-naphthyl moiety, previously observed and a similar band situated in the range 500-700 nm due to the transition localized on the expanded dipyrin.

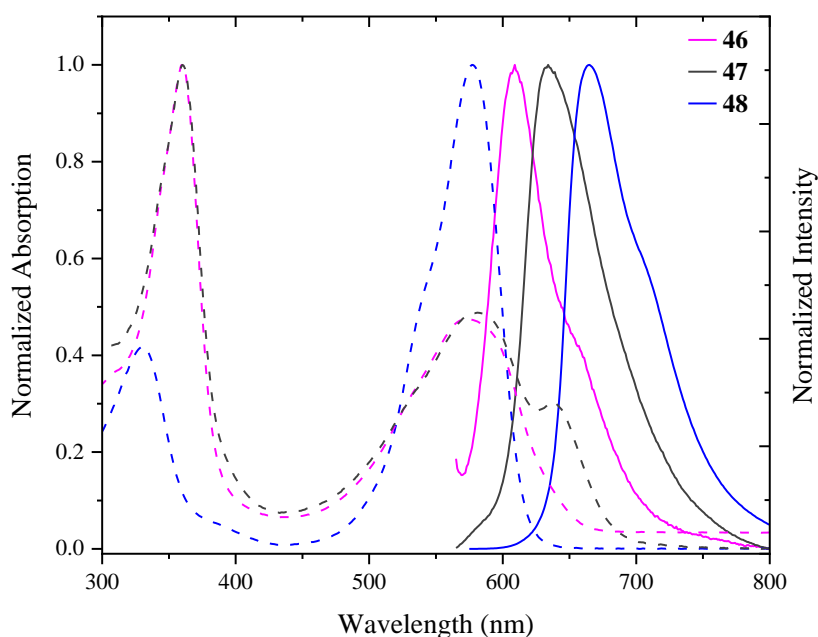


Figure 43: UV/Vis absorption (dashed plot) and emission (solid plot, $\lambda_{\text{exc}}=585$ nm) spectra of π -expanded ligands **46-48** in toluene at 20 °C.

The same reasoning can be extended to the π -expanded dipyrin **47**, bearing vinyl-benzo[*b*]thiophen-2'-yl groups in α -positions. The electron-donating role of the sulfur in the latter is evident in the emission spectrum, which is red-shifted compared to the indole analogue **46**.

Indeed, the emission maximum for compound **46** is 609 nm, while for compound **47** set at 635 nm. The measured quantum yields are identical, $\Phi=0.05$ for both, *ditto* for the lifetimes of the excited state, ca. 2.8 ns for both (see **Table 5**).

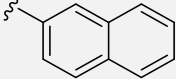
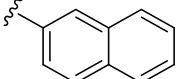
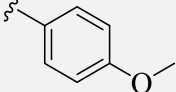
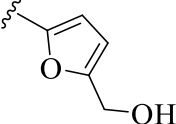
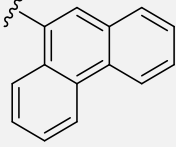
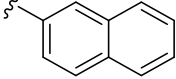
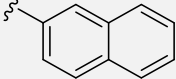
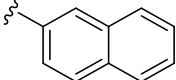
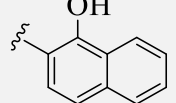
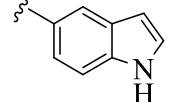
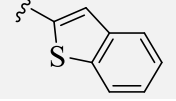
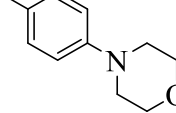
It should be considered that the heteroatoms are placed in different positions within the ring, which can dictate other interactions, peculiar electronic transitions and, thus, more complicated deactivation pathways.

In this latest set of π -expanded ligands, depicted in **Scheme 11**, compound **48**, resulting from the expansion of the plain ligand **15** with 4-morpholinobenzaldehyde **43**, is the one with the longest wavelength emission, centered at 665 nm (blue solid plot in **Figure 43**).

Morpholine is an organic heterocyclic compound consisting of a 6-membered ring with oxygen and a nitrogen atom. The latter, connected in *para* position to the aryl group attached through a styryl moiety to the dipyrin (**1**), can exert a significant electron-donating effect, effectively destabilizing the π -electron cloud of the dipyrin core, thus migrating the emission up to 800 nm.

The quantum yield of compound **48** is also classified as superior, $\Phi = 0.20$. On the other hand, the reduction of the HOMO-LUMO gap offers as an upshot the decrease in the average time of the excited state lifetime of the compound, with a value of $\tau = 2$ ns for the π -extended ligand **48** (**Table 5**).

Table 5: Photophysical properties of the π -expanded ligands **30**, **34-37**, **41-47** in toluene at 20°C.^[a]Quantum yields were determined by the relative method, using as reference cresyl violet in methanol ($\Phi = 0.54$)^[b]Exciting with a NanoLED source at 570 nm

Compound	Aromatic residue attached to the vinyl moiety	λ_{abs} [nm]	λ_{em} [nm]	Φ ^[a]	τ ^[b] [ns]
33		581	645	0.08	4.2
34		576	645	0.16	4.1
35		574	641	0.15	3.7
36		511	589	0.09	4.1
37		580	616	0.12	3.6
38		576	645	0.11	4.1
39		641	656	0.12	2.3
44		625	640	0.04	5.1
45		580	641	0.06	2.4
46		580	609	0.05	2.8
47		582	635	0.05	2.9
48		557	665	0.20	2.5

3.3 Homoleptic bis(dipyrrinato)Zn^{II} complexes

Once the ligands were obtained, the formation of homoleptic complexes was carried out.

It is widely acknowledged that, upon deprotonation, the pyrrolic nitrogen atoms in dipyrrinato ligands can coordinate various metals.^[118]

In particular, the coordination with Zn^{II}, a d¹⁰ metal with total valence electrons and a +2 charge, will form an 18-electron complex. The central zinc atom is tetracoordinated to the two nitrogen atoms present in each dipyrrinato ligand, thus filling the coordination sphere, adopting a tetrahedral geometry schematized in **Figure 44**, depicting the homoleptic complexes investigated in this work.

Specifically, some of the plain ligands described in §3.2 (blue unit **D**, on the left in **Figure 44**) and a couple of π -extended ligands described in §3.3 (red unit **D π** , on the right in **Figure 44**) were used to build several homoleptic bis (dipyrrinato) Zn^{II} complexes.

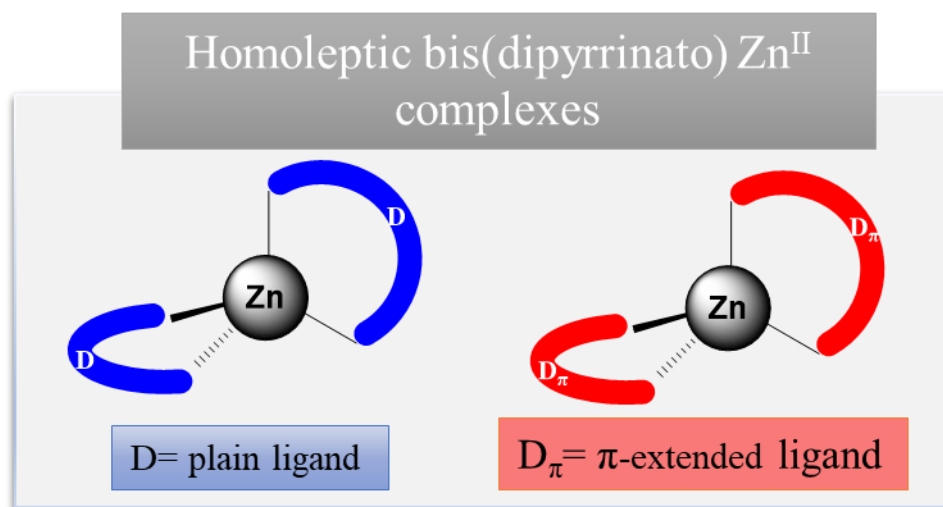
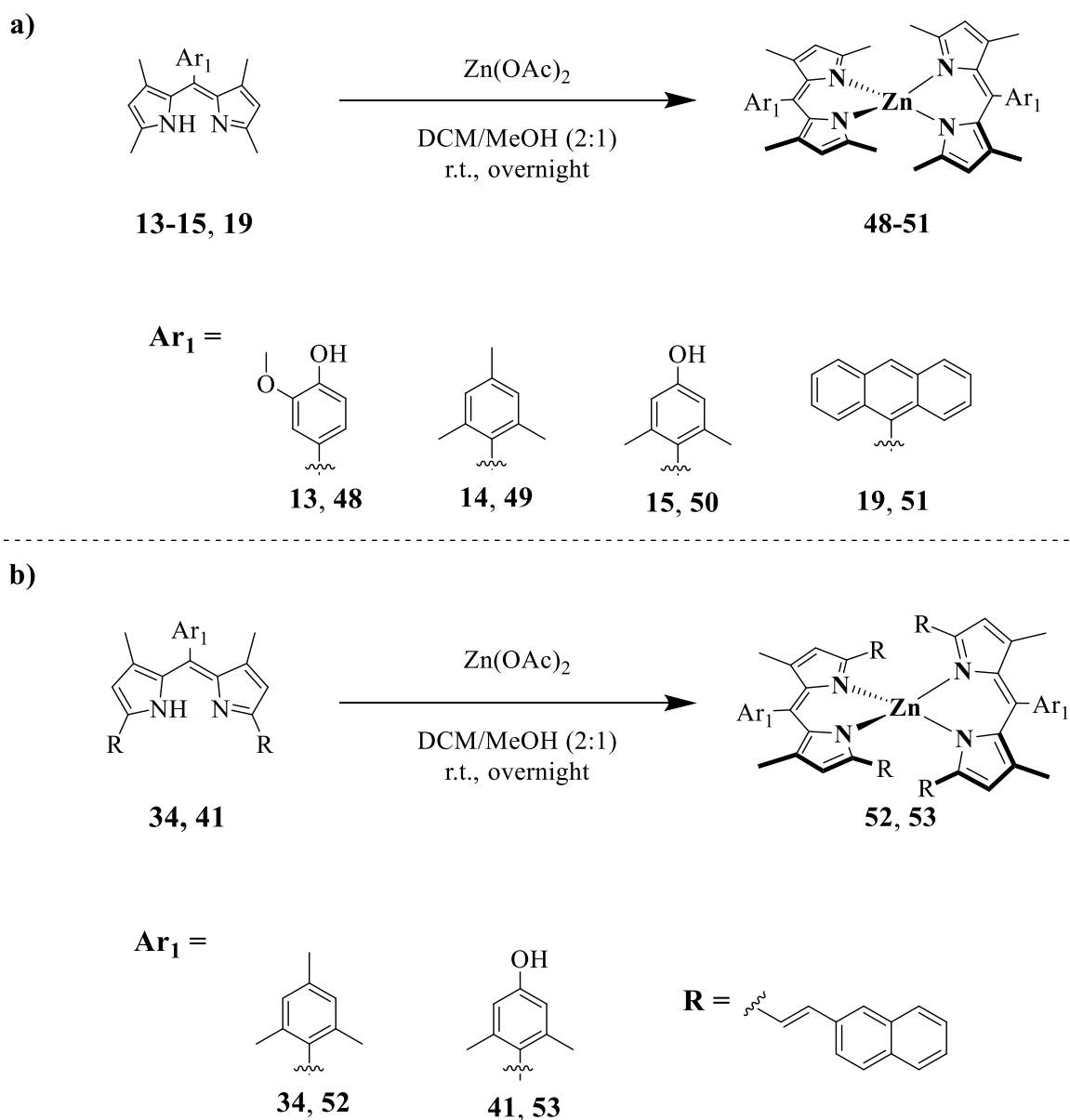


Figure 44: Schematic representation of the homoleptic bis(dipyrrinato) Zn^{II} complexes synthesized and investigated in this work. On the left are presented the homoleptic derivatives constituting of plain dipyrrin ligands (**D**, in blue); on the right are shown the homoleptic counterparts formed by the π -extended ligands (**D π** , in red).

3.3.1 Synthesis

The formation of homoleptic complexes was a simple procedure, which occurred at room temperature and was used both for the plain dipyrin ligands (in this case **13-15, 19**, Scheme **12a**) and for the ligands with a π -expanded conjugation (specifically **34,41**, Scheme **12b**).



Scheme 12: Synthetic method to obtain the homoleptic bis(dipyrinato) Zn^{II} complexes (**48-53**) investigated in this work. **a)** complexation of plain ligands (**13-15,19**) with Zn(OAc)_2 to obtain the complexes (**48-51**) and **b)** complexation of π -expanded ligands (**34,41**) with Zn(OAc)_2 to obtain the complexes (**52,53**).

According to a well-established literature procedure,^[235] a concentrated dichloromethane solution of ligand was mixed with a methanolic solution of the divalent metal ion Zn^{II} as its acetate, yielding the corresponding highly colored metal complexes (**Scheme 12**).

After stirring overnight, the solvent was reduced, and the colorful solid was filtered and rinsed with cold methanol. The homoleptic bis(dipyrrinato)Zn^{II} complexes **48-51** formed by the simple ligands were recrystallized and isolated, with yields ranging from 40% to 60%. In the reaction medium, *i.e.*, dichloromethane/methanol (2:1), they showed a light orange color and weak green luminescence under UV irradiation.

Conversely, complexation of π -expanded ligands **34** and **41** resulted in blue intense solution turning into weak red luminescence upon UV irradiation. After recrystallization, the resultant homoleptic bis(dipyrrinato)Zn^{II} complexes **52** and **53** were isolated with yields between 73% and 75%.

The different electronic structures did not lead to any synthetic variations. On the other hand, as aforesaid, the colors of the two sets of homoleptic complexes are very different, thereby suggesting, as expected, different photophysical properties.

3.3.2 Photophysical properties

The spectroscopic properties of the six homoleptic bis(dipyrrinato)Zn^{II} complexes **48-53** in toluene are summarized in **Table 6**, and their absorption, excitation and emission spectra are shown in **Figures 45** and **46**.

The most important feature of the absorption spectra of the complexes **48-51** is an intense broad absorption band between 425-525 nm, attributed to the ¹ π - π^* transition of the dipyrin core, as already reported for this type of complexes.^[99]

The absorption maxima, emission wavelengths and decay constants reported in **Table 6** are in accordance with the values already reported for the complexes **49**^[118] and **51**^[150]. For the latter, as shown in **Figure 45**, there is an additional absorption between 350 and 400 nm, attributed to the ¹ π - π^* anthracenyl moiety in the *meso* position.

As expected, the electronic profiles of the complexes resemble those of the corresponding free base dipyrrens, suggesting the absence of transitions involving the metal center, as expected.

However, the lowest-energy absorption band of the simple free ligands is red-shifted upon complexation with Zn^{II} : the maximum absorption in toluene shifts by approximately $0.542 \cdot 10^3 \text{ cm}^{-1}$, from 483 nm in the plain dipyrren **13** to 496 nm in the relative homoleptic complex **48**; the absorption peak of dipyrren **15** undergoes a more pronounced shift, of around $1.897 \cdot 10^3 \text{ cm}^{-1}$, from 450 nm to 492 nm in the resultant homoleptic complex **50**.^[236]

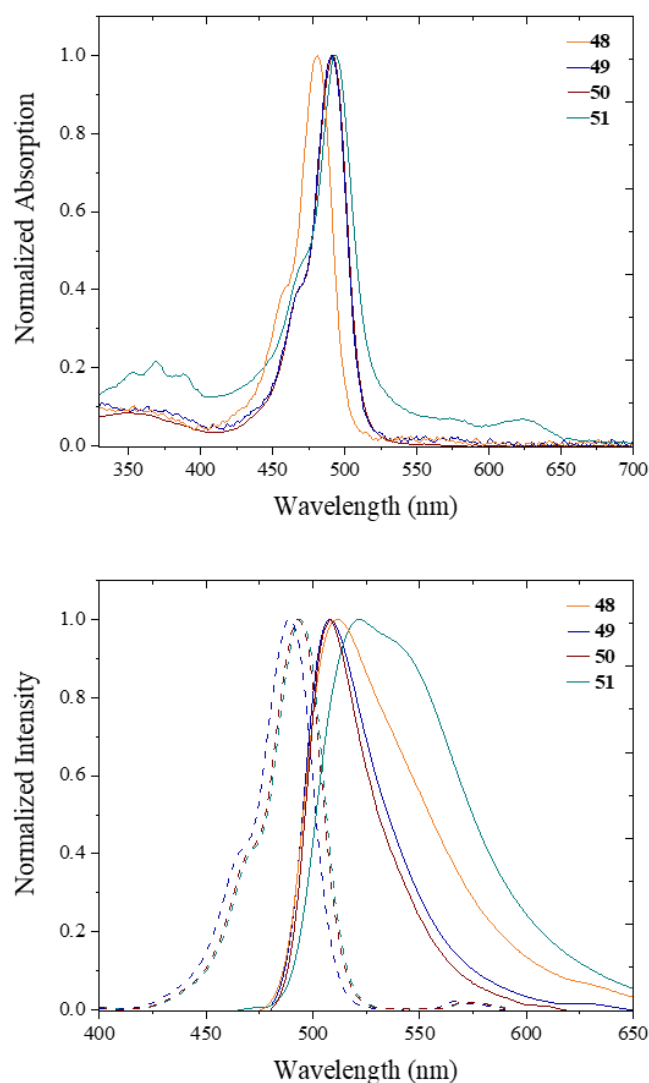


Figure 45: UV/Vis absorption (top), excitation (dashed plot, $\lambda_{em} = 570 \text{ nm}$) and emission (solid plot, $\lambda_{exc} = 450 \text{ nm}$) (bottom) spectra for homoleptic bis(dipyrrinato) Zn^{II} complexes **48-51** in toluene at 20 °C.

This effect is not so pronounced in the emission spectra, as reported in **Table 6**. For steric reasons, it can be inferred that the phenyl moiety in the *meso* position is approximately perpendicular to the plane of the dipyrin. Consequently, it is not in full conjugation with the pyrrolic system, and its substituents minimally influence the π -cloud of the dipyrin.

This explains the close similarity of the electronic spectra of the homoleptic complexes **48-51**, as shown in **Figure 45**, made from plain ligands bearing different aryl groups in the *meso* position.

On the other hand, it can be observed how the steric demand of the *meso*-aryl group significantly affects the accessibility of nonradiative decay pathways.^[116] Thus, as underlined in **Table 6**, the fluorescence quantum yields and lifetimes values increase as the aromatic ring rotation is increasingly inhibited. Predictably, the excitation spectra (dashed plot in **Figure 45**) of the homoleptic complexes have the same spectral shape and appearance as the absorption spectra.

Similarly, the electronic properties of the homoleptic complexes **52** and **53**, shown in **Figure 46**, are comparable with their analogous free-base ligands **34** and **41**.

The absorption spectra recorded in toluene show two intense bands, which are assigned to the transition localized on the vinylnaphthyl moieties in the range 325-425 nm and to the $^1\pi\text{-}\pi^*$ transition of the π -extended dipyrin units, between 525-650 nm.

The analytical data collected suggested that the *meso*-aryl groups of the π -extended chromophores constituting the complexes have little effect on the energy of the ground and excited electronic states of the dipyrin but contribute to a differentiation of the radiative and nonradiative paths in the final complexes.

The structured emissive profiles arising from this $\pi\text{-}\pi^*$ state are very similar among ligands and relative complexes, even though the chelation with Zn^{II} caused a rigidification of the system, thus enhancing the fluorescence quantum yields of the final complexes, in comparison to the non-chelated ligands (see **Table 6**).

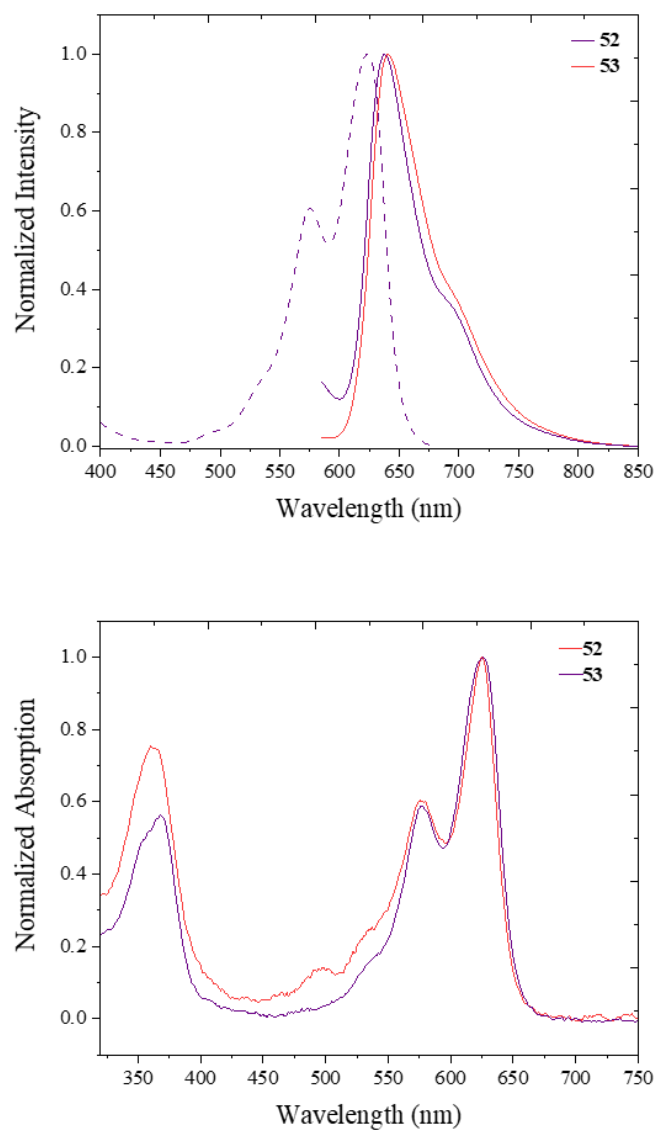


Figure 46: UV/Vis absorption (top), excitation (dashed plot, $\lambda_{em} = 700$ nm) and emission (solid plot, $\lambda_{exc} = 570$ nm) (bottom) spectra for homoleptic bis(dipyrrinato) Zn^{II} complexes **52-53** in toluene at $20^{\circ}C$.

Table 6: Photophysical properties of homoleptic bis(dipyrrinato)Zn^{II} complexes **48-53** in toluene.

^[a]Quantum yields were determined by the reference method, using as reference Ru(bpy)₃Cl₂ in water ($\Phi = 0.028$, 22 °C) and ^[b]cresyl violet in methanol ($\Phi = 0.54$, 22 °C). ^[c]Exciting with a NanoLED source at 455 nm for compounds **48-51** and ^[d]by using NanoLED source at 570 nm for compounds **52-53**.

Complex	λ_{abs} [nm]	λ_{em} [nm]	Φ [a, b]	τ [c, d] [ns]	k_r (10 ⁷) [s ⁻¹]	k_{nr} (10 ⁷) [s ⁻¹]
48	496	512	0.13 ^[a]	2.2 ^[c]	3.9	27.3
49	491	508	0.18 ^[a]	2.5 ^[c]	5.7	25.5
50	492	508	0.14 ^[a]	2.8 ^[c]	4.4	26.8
51	494	522	0.16 ^[a]	2.3 ^[c]	4.9	26.2
52	625	641	0.24 ^[b]	3.9 ^[d]	7.6	23.7
53	626	637	0.23 ^[b]	4.2 ^[d]	7.3	23.9

Photophysical measurements of the complexes (**48-53**) were not performed in dimethylsulfoxide (DMSO) or in any polar solvents. As thoroughly explained in §1.7.1, photoexcitation of these chromophores results in one electron transfer which generates a charge-separated state (CS), known to be stabilized in polar solvents.

The solvent significantly influences the energy difference between the locally excited state of the chromophore and the charge transfer state.

As highlighted in the Jablonski diagram depicted in **Figure 47**, upon irradiation, $\lambda_{\text{exc}} = 470$ nm, the electrons present in the homoleptic complexes are excited from the singlet ground electronic level S^0 -[L-Zn-L] to the highest excited state S^1 -[L-Zn-L].

In non-polar solvents, which have low dielectric constants and weak intermolecular interactions, the solvation energy provided by the solvent molecules is insufficient to stabilize the charge-separated state.^[237,238]

As a result, the SBCT $[L^+-Zn-L^-]$ state is located at higher energy and not effectively stabilized; thus, the excited molecule, through vibronic relaxation (VR) and /or redistribution pathways, populate the first excited state S^1 [L-Zn-L], emitting photons *via* fluorescence emission while returning to the ground state.^[236]

In polar solvents the SBCT $[L^+-Zn-L^-]$ experiences stabilization primarily due to the presence of solvent molecules with higher dielectric constant and permanent dipoles which allow the

solvation of the CS because of the stronger molecular interactions.^[124] The greater solvation energy facilitates the stabilization of the SBCT $[L^+-Zn-L^-]$ to the point where it becomes the lowest energy excited state.

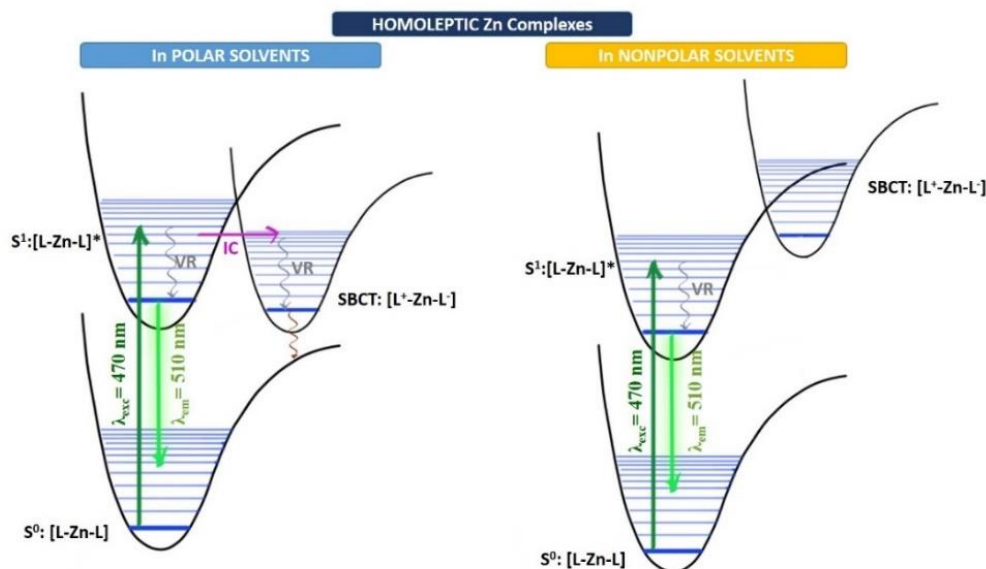


Figure 47: Qualitative Jablonski diagram for the involved photophysical processes in homoleptic bis (dipyrrinato) Zn (II) complexes in polar and non-polar solvents. (VR: vibrational relaxation; IC: internal conversion). Reprinted with permission from R. Tabone, D. Feser, E. D. Lemma, U. Schepers, C. Bizzarri, *Front. Chem.* **2021**, 9:754420.

Thus, the excited molecule reaching the $S^1[L-Zn-L]$ state is capable of dissipating part of the absorbed energy through internal conversion (IC) with the sequential population of the CS. As a consequence, the emission associated with this state undergoes a red-shift and becomes less efficient. As the solvent polarity is increased, the SBCT state becomes progressively more stable and inefficient emission takes over.

3.4 Heteroleptic bis(dipyrrinato)Zn^{II} complexes

Preceding studies have revealed how dissymmetry, *i.e.*, utilizing two distinct dipyrrinato ligands in the same molecule, improves the fluorescence quantum efficiencies of these types of complexes in polar solvents.^[239]

Expanding upon these findings, we have developed chromophoric systems of heteroleptic nature. **Figure 48** illustrates the design of the heteroleptic bis(dipyrrinato)Zn^{II} complexes investigated in this work.

In **Figure 48**, the blue units (**D**) represent the plain ligands described in §3.2, and the red units (**D_π**) stand for the π -extended ligands described in §3.3. We expect they will display a distorted tetrahedral geometry consistent with the geometry observed in similar dissymmetric bis(dipyrrinato)Zn^{II} complexes.

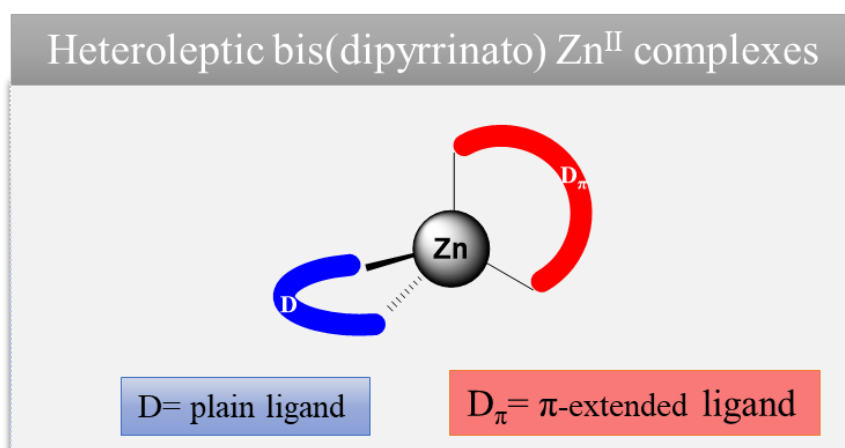


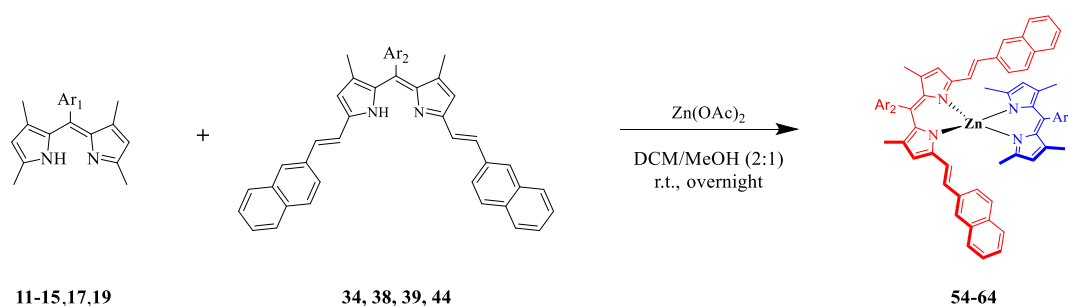
Figure 48: Schematic representation of the heteroleptic bis(dipyrrinato)Zn^{II} complexes synthesized and investigated in this work. They are composed of a plain dipyrrin ligand (**D**, in blue) and a π -extended ligand (**D_π**, in red).

3.4.1 Synthesis

In this work, eleven heteroleptic bis(dipyrinato)Zn^{II} complexes have been synthesized, each consisting of one plain and one π -expanded dipyrromethene ligands.

According to the general procedure outlined in **Scheme 13**, the dissymmetric complexes were obtained by combining one equivalent of a plain dipyrin ligand **11-15**, **17**, **19** with one equivalent of a π -extended ligand **34,38,39,44** and zinc diacetate Zn(OAc)₂ at room temperature.

The desired complexation process is in competition with the formation of the homoleptic complexes of the respective plain and π -extended ligands; thereby, the heteroleptic complexes were purified by column chromatography with yields ranging from 18% up to 40%.



	54	55	56	57	58	59	60	61	62	63	64
Ar ₁ :											
Ar ₂ :											

Scheme 13: Synthetic scheme to obtain the heteroleptic bis (dipyrinato) Zn^{II} complexes **54-64** investigated in this work. Different plain ligands **11-15**, **17**, **19** were chelated with π -extended ligands **34**, **38**, **39**, **44** through the insertion of Zn^{II} as a central metal.

In solution all the complexes display a highly intense blue color and, upon UV irradiation, they exhibit a red fluorescence. However, the intensity of this fluorescence varies significantly among the complexes, and it is also dependent on the type of solvent used.

3.4.2 Photophysical properties

The photophysical properties of the heteroleptic bis(dipyrrinato)Zn^{II} complexes were explored in both a weakly polar solvent, such as toluene (PhMe) and a polar aprotic solvent, such as dimethylsulfoxide (DMSO). The numerical data, including quantum yield, lifetime, radiative and nonradiative constants in both solvents, are listed in **Table 7**.

The electronic absorption spectra of the heteroleptic complexes **54-64** are largely similar. Based on the photophysical analyses presented so far, it can be asserted that the absorption spectra of the heteroleptic complexes are the summation of the bands found in the simple and π -expanded ligands.

As shown in **Figure 49**, the UV/Vis spectra of the heteroleptic complexes **54-56** in DMSO feature three main electronic bands.

The first broad energy band, localized in the range between 300-400 nm, is assigned to the electronic transitions localised on the naphthyl vinyl moiety present in the π -extended dipyrrin **34**, which is more intense for complex **55** ($\epsilon = 4.21 \cdot 10^4 \text{ cm}^{-1}\text{M}^{-1}$). There are two singlet ligand centred transitions (¹LC) localised on the two different dipyrrins. The intraligand transition on the plain dipyrrins **11-13** is between 450-550 nm.

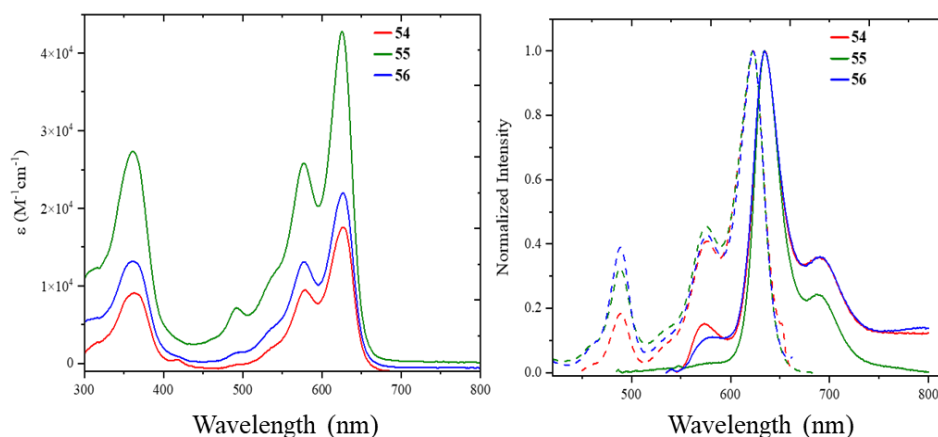


Figure 49: UV/Vis absorption spectrum with molar absorptivity coefficient (ϵ) (left); excitation (dashed plot, $\lambda_{\text{exc}} = 710 \text{ nm}$) and emission (solid plot, $\lambda_{\text{em}} = 470 \text{ nm}$) (right) spectra of heteroleptic bis(dipyrrinato) Zn^{II} complexes **54-56** in DMSO at 20 °C.

It is not well-defined; indeed, the extinction molar coefficient undergoes a slight decrease but then it increases until it reaches a peak at ca. 630 nm, present with a shoulder at ca. 570 nm giving rise to the band originated from the $\pi \rightarrow \pi^*$ transition localised on the π -extended dipyrin **34**. As observed for the homoleptic complexes, the Zn^{II} centre, being a d^{10} metal, does not participate in any transition.

The excitation profiles of the heteroleptic complexes **54-56** recorded in DMSO (dashed plots in **Figure 49**) clearly define the two bands ascribed to the ^1LC localised on the plain and expanded unit forming the chelate. The emission profiles resemble those of the π -expanded ligand **34**, with a far-red emission centred around 635 nm and a lower intensity shoulder in the near-infrared region up to 800 nm.

The disappearance of the emission band of the plain ligand is due to a quantitative intramolecular and interligand energy transfer from the plain dipyrins to the expanded,^[240] achieving large pseudo-Stokes shifts (ca. 4590 cm^{-1}) for complexes **54-56** (see **Table 7**).

The electronic spectra of the heteroleptic complexes **54-56** in toluene are almost comparable to those reported in DMSO, except for a slight bathochromic shift of the emission maxima in the former solvent (see **Table 2**).

The substantial difference, as expected, lies in the quantum yields, which increase significantly in toluene. For instance, the weak fluorescence efficiencies measured in DMSO ($\Phi = 4\%$ for **54**, 8% for **55** and 5% for **56**), increase in toluene ($\Phi = 20\%$ for **54**, 14% for **55** and 18% for **56**).

Upon examination of **Scheme 13**, it can be observed that the aryl groups located at the *meso* position of the simple dipyrin **11-13** forming the complexes **54-56** lack groups that impede rotation around the ring, thereby introducing an additional nonradiative decay, resulting in quantum yields values of 20% in toluene, which is still relatively low compared to the achievable yields with these systems.^[241]

Additionally, in the plain dipyrin **12** forming the heteroleptic complexes **55**, the presence of the bromine atom in position 4 to the phenyl ring in *meso* position might lead to the quenching of fluorescence due to several mechanisms induced by the heavy atom effect.^[11]

Analogously, the presence of a methoxy and a hydroxyl group in the aryl group at the *meso* position of the plain dipyrin **13**, being both electron-donating groups, may induce an additional quenching effect in the fluorescence efficiency of the heteroleptic complex **56**. The solvent

polarity exerts a significant role also in the excited state lifetimes, resulting in an increase from 3 ns (in DMSO) up to 4.5 ns (in PhMe) for the heteroleptic complexes **54-56**.

The second set of heteroleptic bis(dipyrrinato)Zn^{II} complexes that are going to be investigated is composed of the same chromophoric unit, the π -extended dipyrin **34** and simple ligands (**14,15,17,19**), whose steric hindrance increases, going from **57** to **60**.

The UV/Vis absorption profiles of the heteroleptic complexes in DMSO, depicted in **Figure 50**, are dominated by the usual three transition bands localised on the vinyl-naphthyl moieties of the π -extended unit at ca. 360 nm and the two ligand-centered transition localized on the plain ligand (450-550 nm) and on the π -extended ligand (550-700 nm) forming the complexes. Nonetheless, significant differences can be observed in the intensities of the extinction coefficients.

The additional hydroxyl group in position 4 to the 2,6-dimethylphenyl substituent present in the plain ligand **15** (see **Scheme 13**) forming the heteroleptic complex **58** causes a slight increase of the molar absorption coefficient (at 625nm, $\epsilon = 1.83 \cdot 10^4 \text{ cm}^{-1}\text{M}^{-1}$ for **58** in comparison to $\epsilon = 1.74 \cdot 10^4 \text{ cm}^{-1}\text{M}^{-1}$ for **57**). Both emission maxima are centered at 635 nm, with a second emission shoulder up to 800 nm.

The presence of the 2,4-dimethyl groups attached to the aryl appended to the *meso* position hinders the rotation. This leads to a remarkable boost in emission efficiency. The quantum yields measured for the heteroleptic complexes **57** and **58** are 44% and 46% in DMSO, and, as expected, they show a substantial rise in toluene, up to 71% and 63%, respectively. The fluorescence lifetimes for both complexes are ca. 3.0 ns (see **Table 7**).

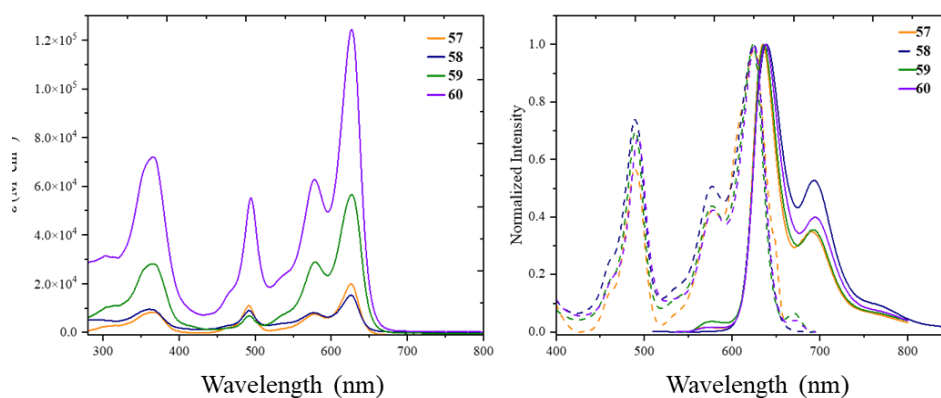


Figure 50: UV/Vis absorption spectrum with molar absorptivity coefficient (ϵ) (left); excitation (dashed plot, $\lambda_{\text{exc}} = 710 \text{ nm}$) and emission (solid plot, $\lambda_{\text{em}} = 470 \text{ nm}$) (right) spectra of heteroleptic bis(dipyrrinato)Zn^{II} complexes (**57-60**) in DMSO at 20 °C.

The heteroleptic complex **59**, bearing a naphthyl moiety in the *meso* position of the plain dipyrin forming the chelate, displays a first intense electronic band in the UV/Vis spectrum in DMSO (**Figure 50**), centred at 367 with $\epsilon = 2.41 \cdot 10^4 \text{ cm}^{-1}\text{M}^{-1}$.

The singlet ligand-centred (^1LC) $\pi \rightarrow \pi^*$ transition localised on the plain dipyrin at 493 nm exhibits an extinction coefficient of $0.72 \cdot 10^4 \text{ cm}^{-1}\text{M}^{-1}$.

The most intense absorption, $\epsilon = 5.64 \cdot 10^4 \text{ cm}^{-1}\text{M}^{-1}$ at 627 nm, is attributable to the $\pi \rightarrow \pi^*$ transition localised on the π -expanded dipyrin, as for all heteroleptic complexes.

The emission profile portrayed in **Figure 50** is identical to those already discussed, with an emission maximum of 636 nm. The lifetime measured in DMSO, $\tau = 3.1 \text{ ns}$, is lower than that measured in toluene, $\tau = 4.6 \text{ ns}$ (see **Table 7**). Despite the presence of the sterically hindered naphthyl group in the *meso* position, the quantum yields measured for this complex are 25% in DMSO and 33% in PhMe.

The final heteroleptic complex **60** of the set illustrated in **Figure 50**, is comprised of the π -extended dipyrin **34** and the simple dipyrin **19** with an anthracenyl moiety appended in *meso* position (see **Scheme 7**).

The incorporation of this highly chromophoric unit in the system results in a significant enhancement of the molar absorption coefficient (e.g., $\epsilon = 7.73 \cdot 10^4 \text{ cm}^{-1}\text{M}^{-1}$ at 364 nm, $\epsilon = 5.41 \cdot 10^4 \text{ cm}^{-1}\text{M}^{-1}$ at 493 nm and $\epsilon = 12.2 \cdot 10^4 \text{ cm}^{-1}\text{M}^{-1}$ at 627 nm).

The diagnostic absorption band attributable to the $^1\pi \pi^*$ transition of the anthracene subunit, which was observed in both ligands **19** (**Figure 34**) and its relative homoleptic complex **51** (**Figure 45**) appears to be overlapped by the band localised on the vinyl naphthyl groups. Despite having the same shape, the emissive profile of the heteroleptic complex **60** displays a slight shift, with a peak located at 639 nm.

The lifetime of the excited species **60** in DMSO, $\tau = 3.6 \text{ ns}$, is slightly lower than those measured in toluene, $\tau = 4.2 \text{ ns}$. Likewise, the quantum yield calculated in toluene, up to 55%, experiences a decline in DMSO, up to 37% (see **Table 7**).

The heteroleptic bis(dipyrinato) Zn^{II} complex **61** differs from the hitherto **58** only by the presence of the additional hydroxyl group in para position of the aryl ring featured in the π -expanded ligand **44** composing it (**Scheme 7**).

As can be discerned from **Figure 51**, despite this slight variation in the chromophoric unit constituting the heteroleptic complex **61**, the electronic spectra in DMSO display an analogous pattern.

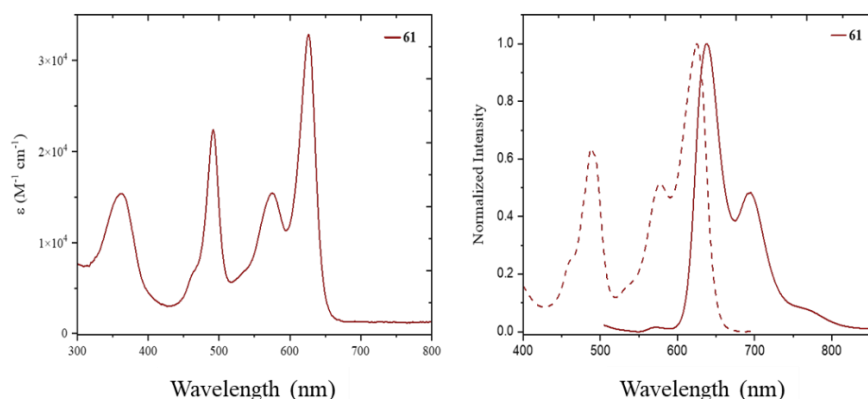


Figure 51: UV/Vis absorption spectrum with molar absorptivity coefficient (ϵ) (left); excitation (dashed plot, $\lambda_{\text{exc}} = 710$ nm) and emission (solid plot, $\lambda_{\text{em}} = 470$ nm) spectra of heteroleptic bis(dipyrrinato)Zn^{II} complex **61** in DMSO at 20 °C.

Rather instead, a dissimilarity is observed regarding the strength of both absorption and emission of the complex.

Specifically, the molar absorption coefficients measured for compound **61** are significantly increased, in comparison to **58**, for each of the three characteristic absorption bands, such as $\epsilon = 1.54 \cdot 10^4 \text{ cm}^{-1}\text{M}^{-1}$ at 361 nm, $\epsilon = 2.24 \cdot 10^4 \text{ cm}^{-1}\text{M}^{-1}$ at 493 nm and $\epsilon = 3.28 \cdot 10^4 \text{ cm}^{-1}\text{M}^{-1}$ at 627 nm (see **Table 7**).

Within the same arrangement exhibited from the other complexes, there is a distinct analogy between the excitation (dashed plot in **Figure 51**) and the absorption spectra. The emission spectrum, originating exclusively from the π -extended ligand **44**, manifests a maximum peak at 640 nm (vs 636 nm for **58**) with the usual shoulder extending up to 800 nm.

Predictably, the extra electron-donating hydroxyl group induces a quench of the fluorescence efficiency resulting in a decrease of the quantum yield of approximately 10% in DMSO ($\Phi = 46\%$ for **58** and 38% for **61**) and around 20% in PhMe ($\Phi = 63\%$ for **58** and 45% for **61**).

In **Figure 52**, the absorption, excitation, and emission spectra in DMSO are shown for the heteroleptic bis(dipyrrinato)Zn^{II} complexes **62** and **63**, both made up of the π -extended dipyrin **38**, bearing a naphthyl ring at *meso* position. The absorption profile of both complexes has an

identical shape, *albeit* the shorter wavelength band is marked by a drastic increase of extinction coefficient for compound **63** (e.g., $\epsilon = 5.61 \cdot 10^4 \text{ cm}^{-1}\text{M}^{-1}$ at 361 nm) (see **Table 7**).

The simple dipyrin forming this complex incorporates the anthracenyl moiety at the *meso* position, which was previously witnessed to absorb in this region strongly. Therefore, for this reason, it shows a pronounced difference in intensity.

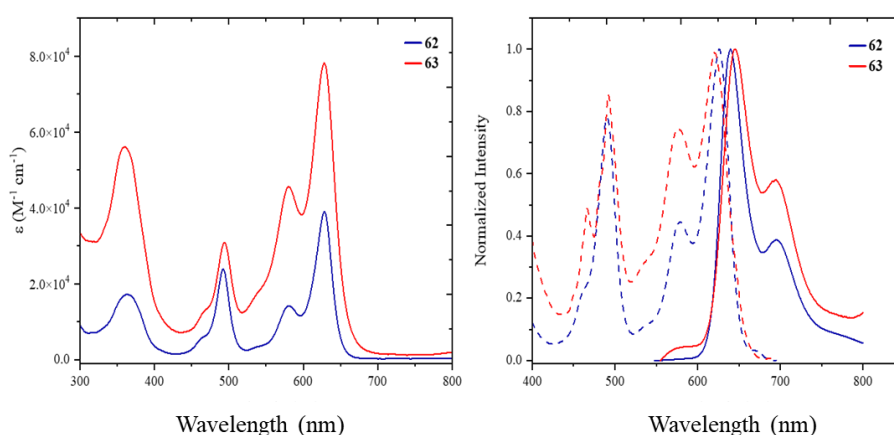


Figure 52: UV/Vis absorption spectrum with molar absorptivity coefficient (ϵ) (left); excitation (dashed plot, $\lambda_{\text{exc}} = 710 \text{ nm}$) and emission (solid plot, $\lambda_{\text{em}} = 570 \text{ nm}$) (right) spectra of heteroleptic bis(dipyrinato) Zn^{II} complexes **62-63** in DMSO at 20 °C.

The characteristic band between 450-550 nm, assigned to the (^1LC) $\pi \rightarrow \pi^*$ transition localised on the plain dipyrin, appears to be similar, even though the simple dipyrin forming the complex **62** features the naphthyl group instead.

A notable distinction lies in the absorption band occurring in the long-wavelength region. The latter, associated with the $\pi \rightarrow \pi^*$ transition localised on the expanded dipyrin, is striking different for the two complexes. As reported in **Table 7**, the values measured for the heteroleptic complexes **62** and **63** are remarkably different (*i.e.*, $\epsilon = 3.89 \cdot 10^4$ and $7.81 \cdot 10^4 \text{ cm}^{-1}\text{M}^{-1}$, respectively at 628 nm).

Consequently, it can be hypothesized that the electronic effects of this low-energy band are not solely determined by the shared chromophoric unit **38** but are also influenced by the interaction with the plain dipyrin.

The emission of the heteroleptic complex **62** is centred at 640 nm, while the maximum peak observed in the emission of the heteroleptic complex **63** is located at 644 nm. In toluene, the

quantum yields for both complexes range around 38%, while they significantly decrease in DMSO.

The considerable steric hindrance inherent in the structure can reasonably account for the formation of aggregates in a polar aprotic solvent such as DMSO. As a result, the quantum efficiency decreases significantly, displaying a value of 14% with **62**, which is further diminished with the addition of more steric hindrance in **63**, $\Phi = 5\%$ (see **Table 7**).

The presence of two anthracenyl groups, one in the π -expanded ligand **39** and the other in the plain ligand **19**, is evident in the absorption spectrum of the resultant heteroleptic bis(dipyrrinato)Zn^{II} complex (**64**), shown in **Figure 53**.

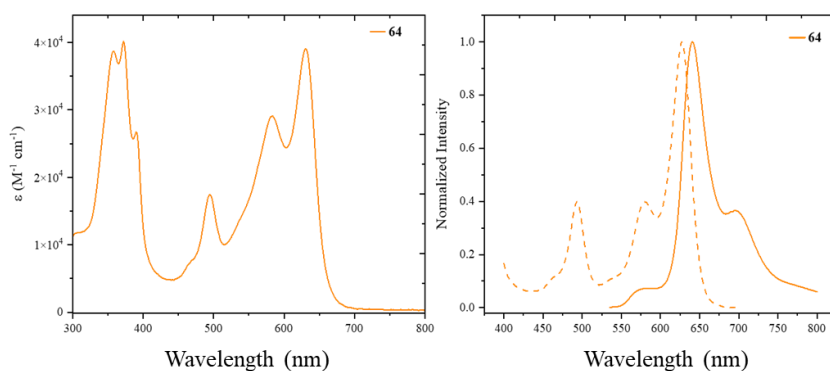


Figure 53: UV/Vis absorption spectrum with molar absorptivity coefficient (ϵ) (left); excitation (dashed plot, $\lambda_{\text{em}} = 710$ nm) and emission (solid plot, $\lambda_{\text{exc}} = 470$ nm) (right) spectra of heteroleptic bis(dipyrrinato) Zn^{II} complex **64** in DMSO at 20 °C.

The highest energy absorption band, with an $\epsilon = 4.10 \cdot 10^4 \text{ cm}^{-1}$, reflects the characteristic band of anthracene.^[150] The ligand centered transition localized on the plain dipyrrin at 494 nm is fairly distinct.

In contrast, the one localized on the π -expanded unit, between 550-700 nm, appears elevated above the baseline, presumably because of aggregation processes. Centered at 641 nm, the fluorescence is connotated by a quantum yield of 14% in toluene and only 7% in DMSO (see **Table 7**).

As stated before, this drastic decrease can be ascribed to the formation of aggregates in polar solvents because of the aromatic bulkiness of the system.

Table 7: Photophysical properties of the heteroleptic bis(dipyrrinato)Zn^{II} complexes (**54-64**) in DMSO and PhMe. ^[a] Measured in DMSO and ^[b] in toluene. ^[c] Quantum yields were determined by the relative method, using cresyl violet ($\Phi = 0.54$ in MeOH, 22 °C) and ^[d] zinc-phthalocyanine ($\Phi = 0.45$ in PrOH, 22 °C). ^[e] Exciting with a NanoLED source at 570 nm.

Complex	$\lambda_{\text{abs}}^{\text{[a]}}$ [nm] (ϵ [10^4 $\text{M}^{-1}\text{cm}^{-1}$])	λ_{em} [nm]	$\Delta\nu$ [cm^{-1}] (<i>Pseudo</i> $\Delta\nu$ [10^3 cm^{-1}])	Φ [c, d]	τ [ns] [10^7 s^{-1}]	k_r [10^7 s^{-1}]	k_{nr} [10^7 s^{-1}]
54	368 (0.60) 492 (0.20) 627 (1.87)	634 ^[a]	0.29 (4.59) ^[a]	0.04 ^[a, c] 0.07 ^[a, d]	3.3 ^[a]	2.0 ^[a]	28.2 ^[a]
		638 ^[b]	0.22 (4.61) ^[b]	0.20 ^[b, c] 0.25 ^[b, d]	3.5 ^[b]	7.1 ^[b]	21.4 ^[b]
55	359 (2.84) 492 (0.65) 630 (4.2)	635 ^[a]	0.28 (4.53) ^[a]	0.08 ^[a, c] 0.07 ^[a, d]	3.2 ^[a]	2.6 ^[a]	28.6 ^[a]
		641 ^[b]	0.31 (4.81) ^[b]	0.14 ^[b, c] 0.12 ^[b, d]	4.5 ^[b]	3.2 ^[b]	19.0 ^[b]
56	366 (1.27) 491 (0.72) 626 (1.28)	634 ^[a]	0.20 (4.59) ^[a]	0.05 ^[a, c] 0.07 ^[a, d]	3.0 ^[a]	1.8 ^[a]	31.5 ^[a]
		635 ^[b]	0.17 (4.42) ^[b]	0.18 ^[b, c] 0.16 ^[b, d]	4.0 ^[b]	4.5 ^[b]	20.5 ^[b]
57	366 (0.54) 491 (0.60) 627 (1.74)	635 ^[a]	0.20 (4.62) ^[a]	0.44 ^[a, c] 0.51 ^[a, d]	3.1 ^[a]	14.2 ^[a]	18.1 ^[a]
		638 ^[b]	0.30 (4.61) ^[b]	0.71 ^[b, c] 0.69 ^[b, d]	3.5 ^[b]	20.3 ^[b]	8.3 ^[b]
58	360 (0.55) 492 (0.55) 625 (1.83)	636 ^[a]	0.27 (4.62) ^[a]	0.46 ^[a, c] 0.49 ^[a, d]	2.6 ^[a]	17.0 ^[a]	20.0 ^[a]
		634 ^[b]	0.32 (4.56) ^[b]	0.63 ^[b, c] 0.59 ^[b, d]	3.8 ^[b]	16.6 ^[b]	9.7 ^[b]
59	367 (2.41) 493 (0.72) 627 (5.64)	636 ^[a]	0.22 (4.56) ^[a]	0.25 ^[a, c] 0.17 ^[a, d]	3.1 ^[a]	3.3 ^[a]	28.9 ^[a]
		639 ^[b]	0.24(4.59) ^[b]	0.33 ^[b, c] 0.39 ^[b, d]	4.6 ^[b]	7.2 ^[b]	14.4 ^[b]
60	364 (7.73) 493 (5.41) 628 (12.2)	639 ^[a]	0.27 (4.63) ^[a]	0.37 ^[a, c] 0.36 ^[a, d]	3.6 ^[a]	10.3 ^[a]	17.3 ^[a]
		641 ^[b]	0.21(4.51) ^[b]	0.55 ^[b, c] 0.51 ^[b, d]	4.2 ^[b]	13.1 ^[b]	10.7 ^[b]
61	361 (1.54) 493 (2.24) 627 (3.28)	640 ^[a]	0.32 (4.66) ^[a]	0.38 ^[a, c] 0.42 ^[a, d]	3.2 ^[a]	11.9 ^[a]	19.4 ^[a]
		636 ^[b]	0.20 (4.53) ^[b]	0.45 ^[b, c] 0.41 ^[b, d]	3.9 ^[b]	11.5 ^[b]	14.1 ^[b]
62	361 (1.70) 493 (2.4) 628 (3.89)	640 ^[a]	0.29 (4.65) ^[a]	0.14 ^[a, c] 0.15 ^[a, d]	2.2 ^[a]	5.4 ^[a]	29.0 ^[a]
		639 ^[b]	0.25 (4.55) ^[b]	0.35 ^[b, c] 0.31 ^[b, d]	3.8 ^[b]	9.0 ^[b]	16.5 ^[b]
63	360 (5.61) 493 (3.0) 628 (7.81)	644 ^[a]	0.39 (4.75) ^[a]	0.05 ^[a, c] 0.06 ^[a, d]	1.3 ^[a]	6.0 ^[a]	70.0 ^[a]
		646 ^[b]	0.25 (4.64) ^[b]	0.38 ^[b, c] 0.41 ^[b, d]	2.2 ^[b]	1.7 ^[b]	43.7 ^[b]
64	373 (4.10) 494 (1.7) 631 (3.90)	641 ^[a]	0.24 (4.64) ^[a]	0.07 ^[a, c] 0.08 ^[a, d]	3.2 ^[a]	2.6 ^[a]	28.7 ^[a]
		636 ^[b]	0.17 (4.63) ^[b]	0.14 ^[b, c] 0.11 ^[b, d]	5.0 ^[b]	2.9 ^[b]	17.0 ^[b]

3.4.3 Photophysical properties at 77 K

The characteristics arising from the transitions localized on the plain and π -expanded ligands are evident in the absorption and excitation spectra, obtained in both DMSO and PhMe, of the heteroleptic bis(dipyrrinato)Zn^{II} complexes **54-64**. In contrast, the corresponding emission profiles solely reflects that of the π -expanded ligands forming the complexes.

As can be observed in **Figure 54**, by changing the excitation wavelength, the emission profile of the heteroleptic bis(dipyrrinato)Zn^{II} complex **57** remains largely unchanged.

Upon excitation on the (¹LC) $\pi \rightarrow \pi^*$ localized on the plain dipyrrin **14** constituting the complex, thus at 470 nm, the emission profile generated (red profile, **Figure 54**) presents a small peak between 500 and 525 nm, which resembles the emission peak observed for the plain dipyrrin **14** in toluene (**Figure 33**, §3.1.4). Nevertheless, its intensity is negligible compared to the more prominent band peaking at 635 nm, which is characteristic of the π -expanded ligand **34**. It is possible to detect this small emissive band because the analysis is conducted in the weakly polar toluene. Indeed, there is no trace of this minor emission peak in the emission profile of the same complex recorded in DMSO (**Figure 49**, §3.4.2) even though it was also generated by excitation localized on the plain dipyrrin.

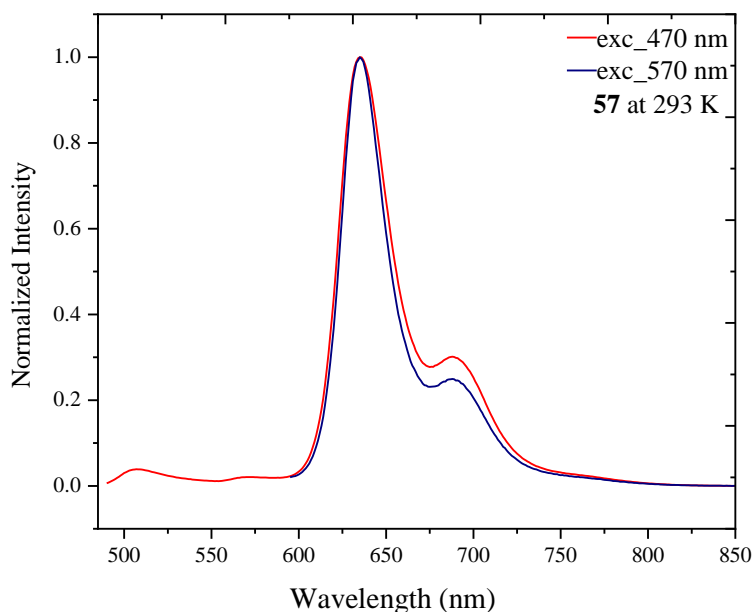


Figure 54: Emission spectra of the heteroleptic bis(dipyrrinato)Zn^{II} complex **57** in toluene at 293 K (20 °C). The red emissive profile was recorded by exciting on the (¹LC) $\pi \rightarrow \pi^*$ localized on the plain dipyrrin **14** forming the complex ($\lambda_{\text{exc}} = 470$ nm, $\lambda_{\text{em}} = 485$ to 800 nm). The blue emissive profile was recorded by exciting on (¹LC) $\pi \rightarrow \pi^*$ localized on the π -expanded dipyrrin **34** forming the complex ($\lambda_{\text{exc}} = 570$ nm, $\lambda_{\text{em}} = 485$ to 800 nm).

Upon excitation on the (^1LC) $\pi\rightarrow\pi^*$ localized on the π -expanded dipyrin **34**, thus at 570 nm, as the emission is collected at longer wavelength (blue profile, **Figure 54**), the small emissive bump at higher intensity is not visible, however the emissive peak remains unaltered.

The same emission profile for the heteroleptic complex **57** is obtained in toluene at 77 K (blue profile, **Figure 55**). On the other hand, upon excitation at 470 nm at this cryogenic temperature (red profile, **Figure 55**), the emission spectrum displays additional bands. The lower temperature restricts the molecular motion and vibration, leading to narrower spectral features. Therefore, the small emissive band between 500-520 nm, ascribable to the emission of the plain dipyrin **14**, showed higher resolution and better distinction.

In addition, minor bands can be observed between 560-600 nm and another distinct peak between 600 and 625 nm. However, these features are much less intense compared to the dominant band arising from 600 to 850 nm, exhibiting two well-defined peaks at 635 nm and ca. 700 nm, originated as usual by the π -expanded ligand.

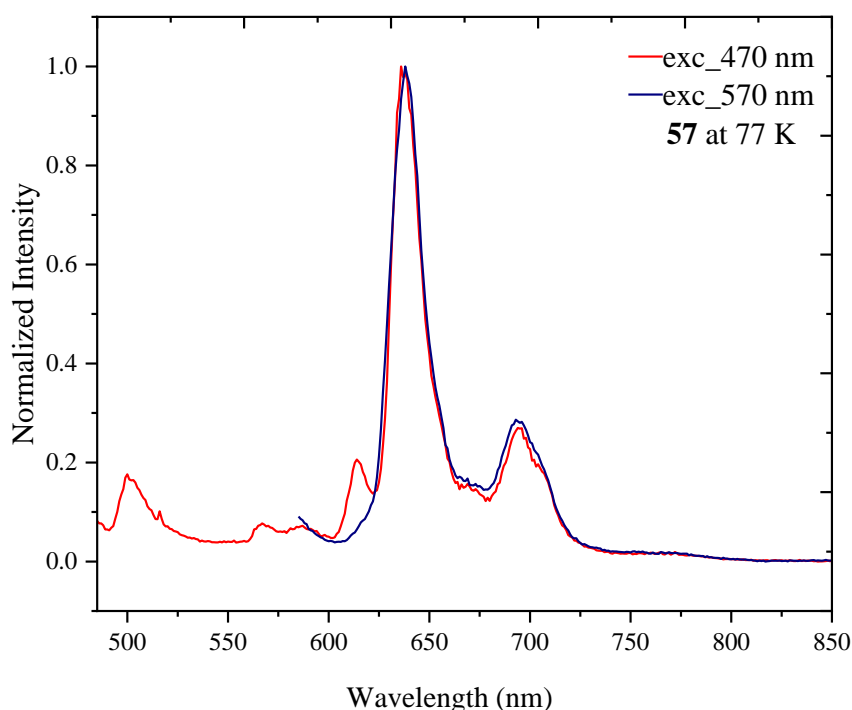


Figure 55: Emission spectra of the heteroleptic bis(dipyrinato)Zn^{II} complex **57** in toluene at 77 K (-196 °C). The red emissive profile was recorded by exciting on the (^1LC) $\pi\rightarrow\pi^*$ localized on the plain dipyrin **14** forming the complex ($\lambda_{\text{exc}}=470$ nm, $\lambda_{\text{em}}=485$ to 800 nm). The blue emissive profile was recorded by exciting on (^1LC) $\pi\rightarrow\pi^*$ localized on the π -expanded dipyrin **34** forming the complex ($\lambda_{\text{exc}}=570$ nm, $\lambda_{\text{em}}=485$ to 800 nm).

Nishihara *et al.*^[242] suggested that the dissymmetric complexes, such as **57**, undergo quantitative energy transfer from the plain dipyrinato ligand to the π -expanded dipyrinato ligand.

As highlighted in the Jablonski diagram depicted in **Figure 56**, upon excitation at shorter wavelength, $\lambda_{\text{exc}} = 470 \text{ nm}$, the electrons present in the heteroleptic complexes are excited from the singlet ground electronic level S^0 -[L_p-Zn-L _{π}] to the highest excited state 1L_pC -[L_p*-Zn-L _{π}] of the plain dipyrin. Hence, from this state occurs a rapid interligand nonradiative transition, which, after dissipating energy through vibronic relaxation (VR) and/or redistribution pathways, populate the lower excited state $^1L_{\pi}C$ -[L_p-Zn-L _{π} *] of the π -expanded dipyrin emitting photons *via* fluorescence emission while returning to the ground state. Irrespective of the shorter or longer excitation wavelength, only the emission at lower energies ($\lambda_{\text{em}} = 635 \text{ nm}$) is detected. This occurs in both polar and nonpolar solvents.

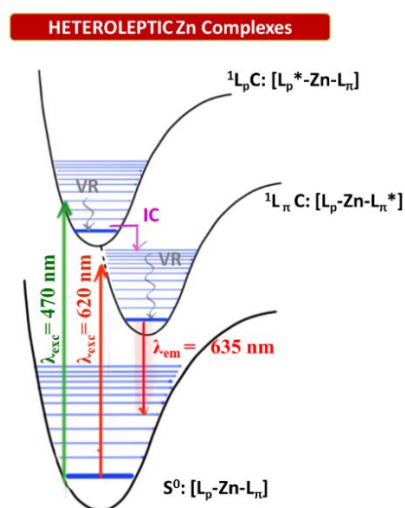


Figure 56: Qualitative Jablonski diagram for the involved photophysical processes in heteroleptic bis(dipyrinato)Zn^{II} complexes upon excitation at different λ . (VR: vibrational relaxation; 1L_pC : singlet excited state centered on the plain dipyrin; $^1L_{\pi}C$: singlet excited state centered on the π -extended dipyrin; IC: internal conversion plus subsequent VR). Reprinted with permission from R. Tabone, D. Feser, E. D. Lemma, U. Schepers, C. Bizzarri, *Front. Chem.* **2021**, 9:754420.

In the context of molecular systems, energy transfer refers to the process by which energy is transferred from one entity to another.^[243] In this case the donor unit is the plain dipyrin, while the acceptor moiety is the π -expanded ligand. There are several energy transfers that can occur through various mechanism. Efforts have been made in this work to understand the type of energy transfer that take place within these particular architectures. However, in-depth investigations are still required and for this reason not reported.

3.4.4 Transient absorption spectroscopy

To gain a better understanding of the dynamics occurring after photoexcitation, the steady-state measurements reported in this work have been complemented by transient absorption spectroscopy conducted by Dr. Julia Leier and M.Sc. Pascal Rauthe, both working in the group of Prof. Dr. Andreas Neil Unterreiner (KIT, Molecular Physical Chemistry Group).

The bis(dipyrrinato)Zn^{II} complexes represent an intramolecular donor-acceptor system which give rise to an additional state through an intramolecular charge transfer (CT), which is sensitive to intermolecular environmental influences.

Broadband transient absorption (TA) measurements coupled with early sub-picosecond dynamics studies of some homoleptic bis(dipyrrinato)Zn^{II} complexes revealed the presence of an ultrafast component, that could be attributed to a CT excited state in the nonpolar cyclohexane.^[125]

Typically, this state is not favorable in nonpolar solvents,^[244,245] suggesting other mechanisms like intramolecular vibrational redistribution (IVR) and/or intersystem crossing (ISC)

To gather further insights in this regard, the displacement of the excited state channels of the homoleptic complexes caused by the change of polarity was investigated by fs-broadband absorption spectroscopy in different solvents, such as dichloromethane, acetonitrile, and ethanol.^[246]

Efforts were made to explore indications of the CT state signature within the spectral range of 350 and 1400 nm. However, apart from the ultrashort dynamics, no indication was found.

Steady-state measurements showed how the coordination of the ligand with the zinc atom induce modifications in its photophysical properties, particularly with respect to quantum yield (§3.3 and 3.4).

Thus, TA spectroscopy was used to compare the dynamics of some heteroleptic complexes with those probed for the forming ligand.

As depicted in **Figure 57**, upon excitation at 625 nm the ground state undergoes depopulation, resulting in a small ground-state bleach (GSB) at 360 nm, which turns in a positive band up to 540 nm.

This presents an isosbestic point at 488 nm, clearly distinguishable only within 1 ps, which can be attributed to an intramolecular charge transfer, more pronounced in dichloromethane.^[246]

A more intense GSB is observable between 444-655 nm, because of the decrease of the absorbance of the ground state caused by depletion of molecules during the excitation process.

Additionally, between 655 nm and 750 nm stimulated emission (SE) is visible superimposed on an excited state absorption (ESA).

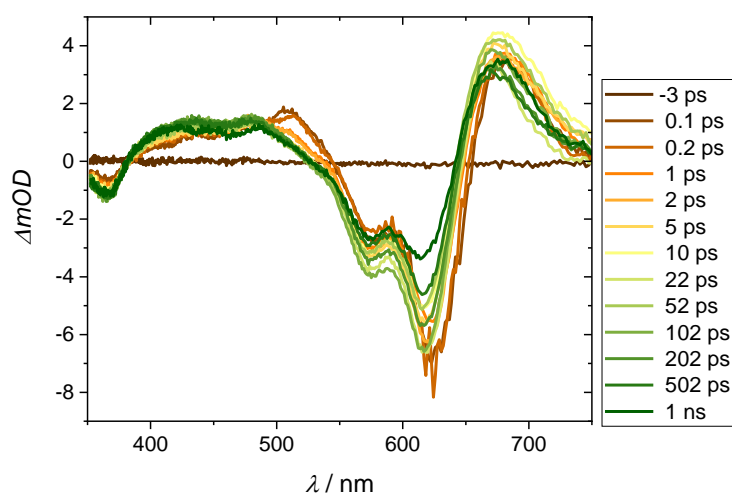


Figure 57: Transient absorption spectroscopy of the heteroleptic bis(dipyrrinato)Zn^{II} complex **57** in toluene after photoexcitation at 625 nm at different delay times. E = 0.42 μJ, OD_{625 nm} = 0.39

Analogous dynamics can be observed in the heteroleptic complex **60** (Figure 58).

The isosbestic point at 535 nm represents a strong indication of S₀→S₁ dynamics, however, especially in the early time frame (within 1 ps) it can be observed at around 510 nm a deviation that can be attributed to a CT, IVR or ISC.

The GSB state between 550-650 nm precedes the positive absorption that occurs between 660-750 nm.

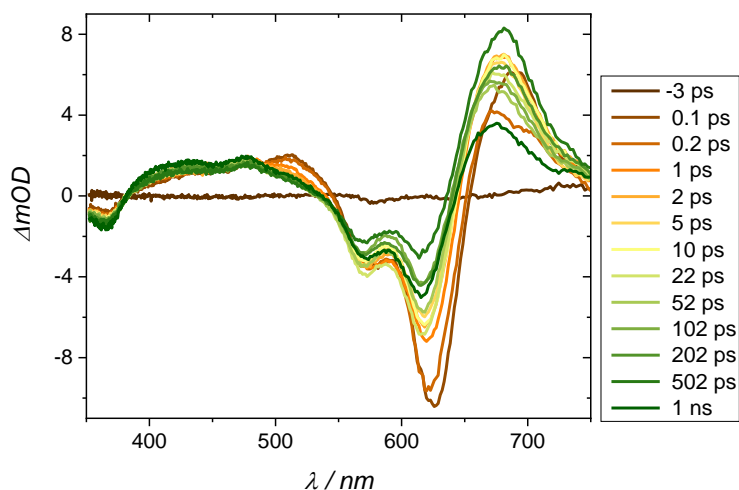


Figure 58: Transient absorption spectroscopy of the heteroleptic bis(dipyrrinato)Zn^{II} complex **60** in toluene after photoexcitation at 625 nm at different delay times. E = 0.42 μJ, OD_{625 nm} = 0.51

Similarly to the observation for complex **60**, the TA spectra of the heteroleptic complex **64** show a deviation at ca. 510 nm at delay times of 1 ps or less that can be due to a CT. As one can see in **Figure 59**, it is more pronounced for complex **64**. There is no doubt that this ultrafast feature is clearly identified at the earliest time scale of 1 ps.

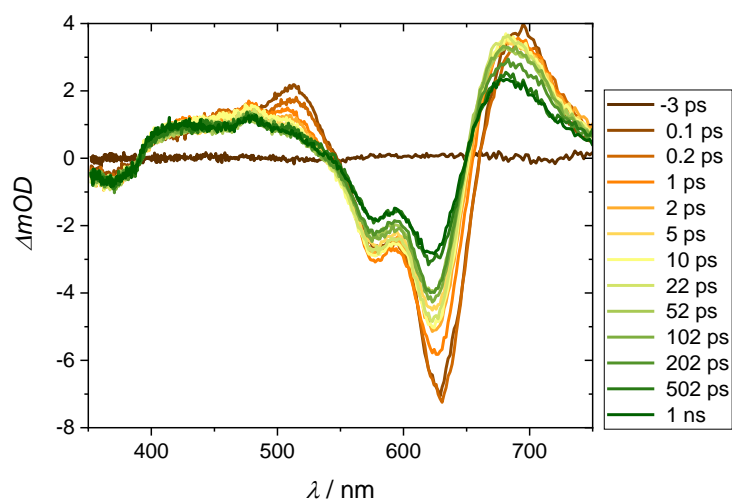


Figure 59: Transient absorption spectroscopy of the heteroleptic bis(dipyrrinato)Zn^{II} complex **64** in toluene after photoexcitation at 625 nm at different delay times. E = 0.42 μJ, OD_{625 nm} = 0.38.

As mentioned above, wavelengths have been probed from 350 to 1400 nm,^[246] but no further transitions could be identified in the solvents EtOH, DCM, MeCN and CHX.

Perhaps, similar NIR experiment in toluene would be a good system to test the complexes **57**, **60** and **64**.

As briefly mentioned above, one could alternatively interpret the band around 510 nm as IVR, which is solvent-independent, or as ISC where the resulting triplet population is hidden under the strong singlet dynamics between 400 and 500 nm.

Hereafter the single transient spectra of the complexes **57**, **60** and **64** in toluene are reported (**Figures 60, 61, 62**). All of them were selected based on the peak maximum. In the specific case of complex **64**, the peak exhibits a slight redshift.

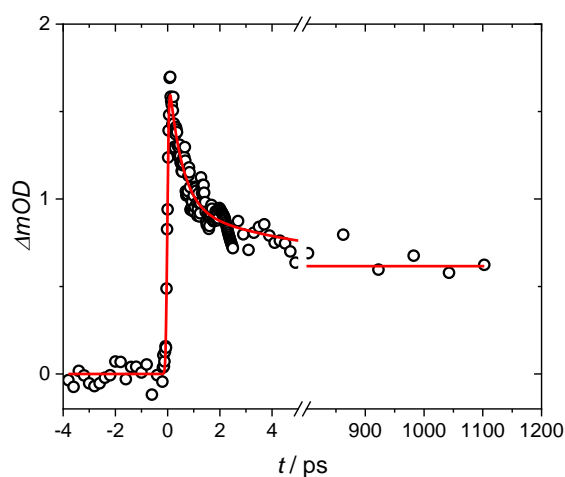


Figure 60: Single transient of the heteroleptic bis(dipyrrinato)Zn^{II} complex **57** in toluene after photoexcitation at 625 nm.

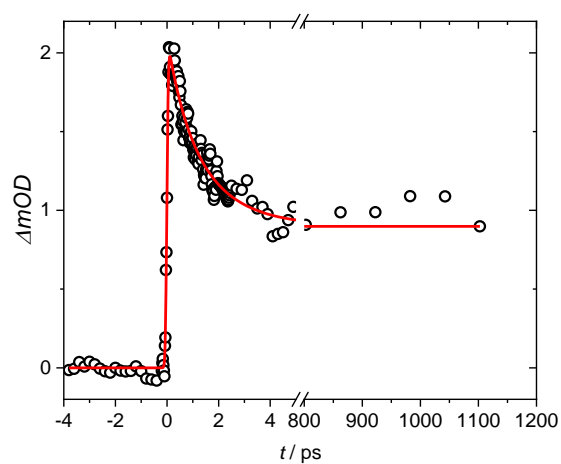


Figure 61: Single transient of the heteroleptic bis(dipyrrinato)Zn^{II} complex **60** in toluene after photoexcitation at 625 nm.

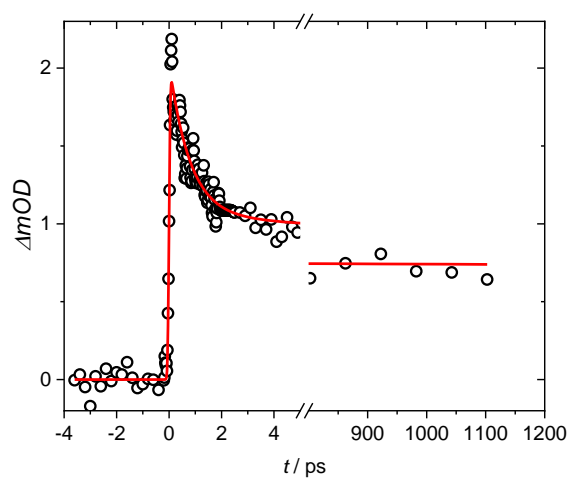


Figure 62: Single transient of the heteroleptic bis(dipyrrinato)Zn^{II} complex **64** in toluene after photoexcitation at 625 nm.

It is possible to determine the time resolution of the experiment via Equation 1.

$$\Delta A(t) = g(t) * B. \quad (1)$$

The transient response ΔA (ΔOD) is a convolution of the instrumental response $g(t)$ and a second input B . $g(t)$ is an error-function which describes the transient response and is for determination of the experimental time resolution τ_0 .

$$g(t) = \frac{1}{2} \left(1 + \operatorname{erf} \left[\sqrt{4 \cdot \ln(2)} \frac{t}{\tau_0} \right] \right). \quad (2)$$

The convolution can be simplified with a multiplication. B describes the relaxation dynamics after excitation, which is expressed as a sum of exponential functions. It includes the time constants τ_i of the excited state dynamics i and the respective amplitude $A_i(\lambda_{\text{probe}})$.

Thus, the analysis of the single transients depicted in **Figures 60-62**, was performed using the equation reported below (Equation 3).

$$f(x) = \frac{1}{2} \left(1 + \operatorname{erf} \left(\sqrt{4 \cdot \ln(2)} \cdot \frac{x - x_0}{t_0} \right) \right) \cdot \sum_{i=1}^3 A_i \cdot e^{-\frac{x-x_0}{\tau_i}} \quad (3)$$

In **Table 8**, the obtained lifetimes with the multiexponential fit-function (3) are reported.

As it can be observed from **Table 8**, the acquired τ_1 value for complexes **57** is equal to 0.51 ps, while for complexes **60** and **64** are more similar, respectively $\tau_1 = 0.75$ ps and $\tau_1 = 0.79$. It can be assumed that this lifetime is associate to an ISC or a charge transfer.

On the other hand, the attained τ_2 values are significantly different among the three complexes **57**, **60** and **64**. (**Table 8**). It is supposed that these lifetime values are associated to vibrational relaxation processes.

Table 8: Lifetime constants of the heteroleptic bis(dipyrrinato) Zn^{II} complexes **57**, **60**, **64** in toluene calculated from the fit function (Equation 1).

Complex	τ_1 [ps]	τ_2 [ps]
57	0.51	5.6
60	0.75	1.7
64	0.79	26.7

It will also be interesting to see TA spectra in DMSO as solvent where typically lower fluorescence quantum yields compared to the solvent toluene are observed. In any case, these promising results show that more experiments and analyses are needed for a final assessment of the ultrafast processes involved.

3.5 π -extended bulky pyrroles

Another approach to further increase the π -conjugation of the dipyrin systems relies on using already extended pyrroles as building blocks.

Thus, as depicted in **Figure 63**, the replacement of the methyl groups presents in the pyrrolic precursor used as starting material for the dipyrromethenes presented so far in this work, namely the 2,4-dimethyl-1*H*-pyrrole, with more sterically demanding groups, may lead to advantageous modification of the system.



Figure 63: Schematic representation of the substitution of the methyl groups present in the 2,4-dimethyl-1*H*-pyrrole with more bulky substituents to obtain an aryl-expanded building block, thereby achieving a further bathochromic shift in the photophysical properties of the resultant dipyrin scaffold.

Post-functionalization processes, such as the Knoevenagel condensation described in §3.2, undoubtedly allows for a wide range of substituents.

At the same time, in terms of reaction efficiency, commencing with pre-functionalized pyrroles may enable dipyrin synthesis with optimal photophysical properties, all accomplished within a single stage.

Consequently, this would lead to expedited processes and, ideally, increased final yields, given the decreased number of reaction steps.

3.5.1 Synthesis

Aiming at achieving a near-infrared emission, along with a stiffening of the system, the commercially available 2,4-diphenyl-1*H*-pyrrole **65** was selected as starting material for synthesizing the conformationally restricted π -extended dipyrin **66**.

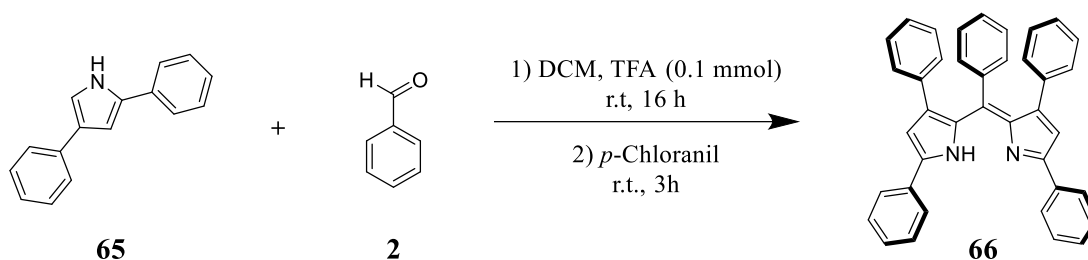
Due to the already high steric hindrance provided by the pyrrolic precursor, benzaldehyde **2** was chosen as the reagent, giving a phenyl substituent at the *meso* position of the dipyrin.

According to the general procedure,^[247] already discussed in §3.1, two and a half equivalents of 2,4-diphenyl-1*H*-pyrrole **65** and one equivalent of benzaldehyde **2** were dissolved in dichloromethane (**Scheme 14**).

The addition of some drops of TFA (0.1 mmol) resulted in an immediate change of color of the reaction mixture from light blue to intense turquoise. After confirming the complete conversion of the benzaldehyde **2** through TLC, *p*-chloranil was added to carry out the dehydrogenation of the dipyrromethane formed as an intermediate.

The crude residue was purified *via* column chromatography packed with neutral alumina gel to afford the resulting dipyrin **66** as a light violet solid with a yield of 54 %, which is perfectly in line with the value reported in the literature.^[248]

The 2,4,5,7,9 pentaphenyl-dipyrin **66** showed a bright pink fluorescence under UV irradiation in the solid state.



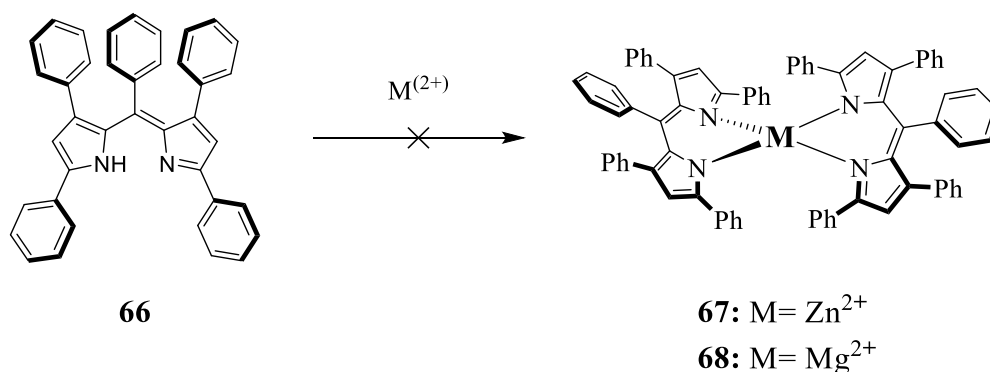
Scheme 14: Synthetic scheme for the condensation reaction between 2,4-diphenyl-1*H*-pyrrole **65** and benzaldehyde **2** to obtain dipyrin **66**.

3.5.2 Complexation

Considering the substantial extent of conjugation in the chromophoric system ascribable to the presence of the five phenyl groups, dipyrin **66** was not further functionalized and subjected to complexation (**Scheme 15**) using different conditions, listed in **Table 9**.

Following the procedure previously reported for the synthesis of the homoleptic complexes in §3.3,^[236] a methanolic solution of $\text{Zn}(\text{OAc})_2$ was added to a solution of dipyrin **66** in dichloromethane; however, after 24 hours, no conversion of the starting material was observed (Entry 1, **Table 9**).

Assuming that a higher temperature could facilitate the complexation, the synthesis was repeated using the same metal precursor, $\text{Zn}(\text{OAc})_2$, but changing the solvent, such as dimethylformamide (DMF) (Entry 2, **Table 9**). Despite the higher temperature, 80 °C, the reaction was also unsuccessful in this case.



Scheme 15: Synthetic scheme of the attempted complexations of ligand **66** to obtain the homoleptic Zn^{II} complex **67** and Mg^{2+} complex **68**. Reagents and conditions are detailed in **Table 9**.

Hence, we sought a theoretical explanation considering these experimental results. Spectroscopic studies reported in the literature have elucidated the mechanism leading to the formation of homoleptic bis(dipyrinato) Zn^{II} complexes.^[72]

The initial stage involves the chelation of one dipyrinato unit by the zinc, which retains an acetate as an ancillary ligand, resulting in a formally heteroleptic complex as an intermediate.

Then, occurs an exchange of the ancillary acetate ligand with another dipyrinato unit, thereby forming the homoleptic Zn^{II} complex. It may be foreshadowed that the zinc connected to the acetate ligand cannot reach the two nitrogen atoms of the dipyrin core **66** because of the two phenyl groups at positions 2 and 8.

To confirm this hypothesis, the complexation reaction was repeated, employing DMF again as a solvent but using two different metal precursors, such as $\text{Zn}(\text{NO}_3)_2$ (Entry 3, **Table 9**) and ZnBr_2 (Entry 4, **Table 9**). In both cases, the formation of the complex was not detected.

To assess whether the unsuccessful complexation could be due to the dimension of the Zn^{2+} (ionic radius = 74 pm)^[249] or to other aspects, it was decided to carry out the complexation of dipyrin **66** with another element having a comparable size, such as Mg^{2+} (ionic radii= 79 pm)^[249] which is known to be coordinated by the dipyrinato ligands.^[72]

The reaction was carried out in DMF using $Mg(ClO_4)_2$ as metal salt (Entry 5, **Table 9**). Similarly, in this instance as well, no conversion of the starting material was observed.

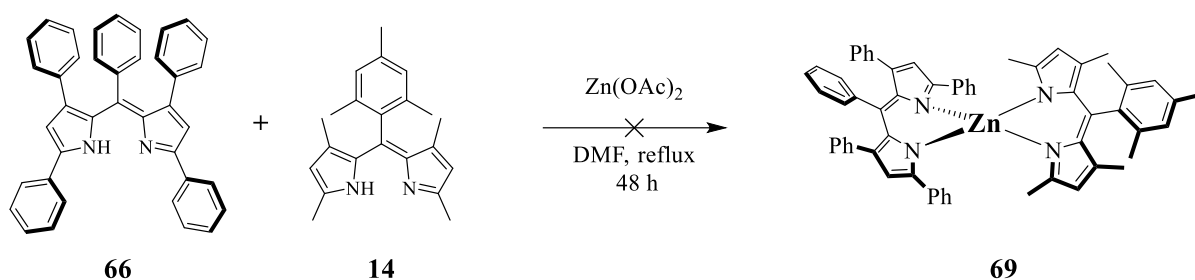
Table 9: Reagents and conditions for the complexation of the dipyrin **66** outlined in **Scheme 15**. Each reaction was carried out for 24 hours. No product was detected in each different attempt.

Entry	Metal precursor	Solvent	Temperature
1	$Zn(OAc)_2$	DCM/MeOH (2:1)	25 °C
2	$Zn(OAc)_2$	DMF	80 °C
3	$Zn(NO_3)_2$	DMF	80 °C
4	$ZnBr_2$	DMF	80 °C
5	$Mg(ClO_4)_2$	DMF	80 °C

These results suggested that the issue could be linked to the phenyl groups at positions 2 and 8 of the two dipyrins.

According to X-Ray crystallographic studies reported in the literature for compound **66**,^[250] the peripheral phenyl groups are arranged in a propeller-like conformation, causing substantial steric congestion in the system.

To diminish the overcrowding, as outlined in **Scheme 16**, the π -expanded ligand **66** reacted with the plain dipyrin **14** in DMF in the presence of $Zn(OAc)_2$ to obtain the heteroleptic derivative **69**.



Scheme 16: Synthetic scheme of the attempted complexation of ligand **66** and the plain dipyrin **14** with Zn(OAc)_2 to obtain the heteroleptic complex **69**.

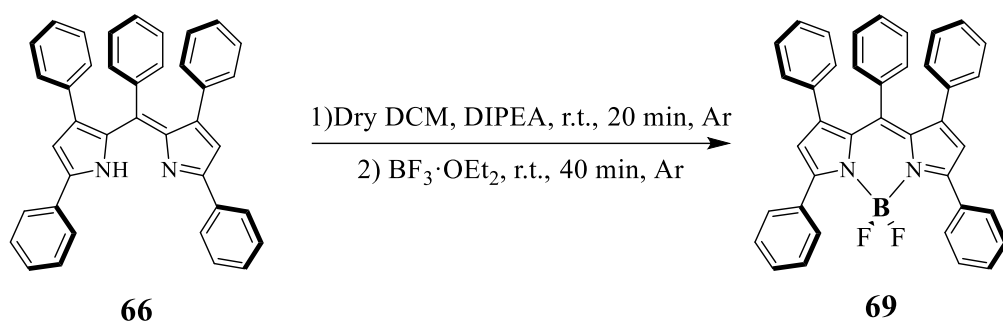
This precursor was preferred this time since it is widely established in dipyrin that metal chlorides do not form heteroleptic dipyrin complexes as readily as metal acetates or acetylacetonates.^[72]

Despite the reaction being prolonged for forty-eight hours, no formation of compound **69** was observed. It was isolated the homoleptic complex of the dipyrin **14**, having the same structure of the complex **49** reported in §3.3.1.

Based on the failures encountered in attempting to synthesize the above-mentioned bis(dipyrinato) homoleptic and heteroleptic complexes, it was decided to proceed with the complexation of the ligand **66** with boron difluoride.

As depicted in **Scheme 17**, according to a well-established literature procedure,^[219] under an argon atmosphere, *N,N*-diisopropylethylamine was added to a solution of dipyrin **66** in dry dichloromethane and stirred for twenty minutes.

Subsequently, boron trifluoride diethyl etherate ($\text{BF}_3 \cdot \text{OEt}_2$) was added to the reaction mixture, resulting in an intense bright red luminescence under UV irradiation.



Scheme 17: Synthetic scheme for the complexation of ligand **66** with $\text{BF}_3 \cdot \text{OEt}_2$ to obtain the BODIPY **69**.

The crude residue was processed *via* column chromatography to afford the BODIPY derivative **69** as a blue powder, with 81% of yield. Like its precursor **66**, also BODIPY **69**, upon UV irradiation, exhibited luminescence in the solid state, emitting a deep red color.

3.5.3 Photophysical properties

A comparison of the emission spectra generated by the π -extended ligand **66** and the corresponding BODIPY **69** in DMSO is shown below (**Figure 64**).

The emission profile of compound **66** displays a small initial hump which is not observed in **69**. The shape of the two bands is slightly different; however, what sets them apart is a considerable bathochromic shift of ca. 800 cm^{-1} induced by the boron difluoride presence in BODIPY **69**, which exhibits an emission from 565 nm up to 800 nm with a maximum at 651 nm.

Although its maximum is 616 nm, the emission profile of the free-base ligand **66** extends up to 800 nm.

The quantum yield measured for ligand **66** in DMSO solution is equal to 17%. In the same conditions, the inclusion of the boron difluoride group in the structure guarantees remarkable fluorescence, $\Phi = 0.54$ for **69** (**Table 10**). Interestingly, the quantum yield of the BODIPY **69** increases tremendously in the solid state, $\Phi = 0.96$ on a spin-coated film.^[251]

The quantum yield measured for ligand **66** in DMSO solution is equal to 17%.

In the same conditions, the inclusion of the boron difluoride group in the structure guarantees remarkable fluorescence, $\Phi = 0.54$ for **69** (**Table 10**). Interestingly, the quantum yield of the BODIPY **69** increases tremendously in the solid state, $\Phi = 0.96$ on a spin-coated film.^[251]

The lifetimes of both species are roughly the same, $\tau = 3.2$ and 4.0 , respectively, for **66** and **69**.

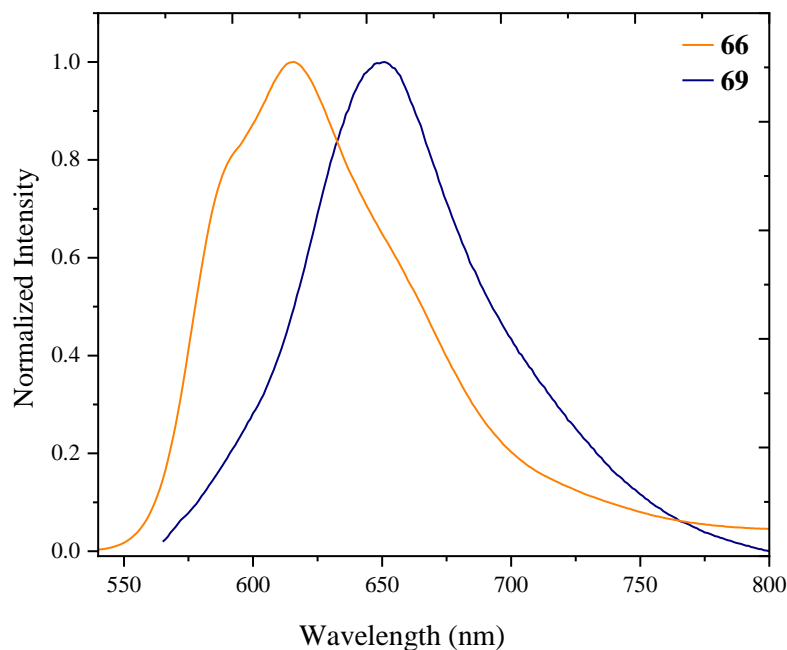


Figure 64: Emission spectra of π -extended dipyrin **66** ($\lambda_{\text{exc}} = 520$ nm) and BODIPY **69** ($\lambda_{\text{exc}} = 540$ nm) in DMSO at 20 °C.

Table 10: Photophysical properties of π -extended dipyrin **66** and BODIPY **69** in DMSO at 20 °C. ^[a]Quantum yields were determined by the relative method, using cresyl violet ($\Phi = 0.54$ in MeOH, 22 °C). ^[b] Exciting with a NanoLED source at 570 nm.

Compound	λ_{abs} [nm]	λ_{em} [nm]	Φ ^[a]	τ ^[b] [ns]
66	541	616	0.17	3.2
69	560	654	0.54	4.0

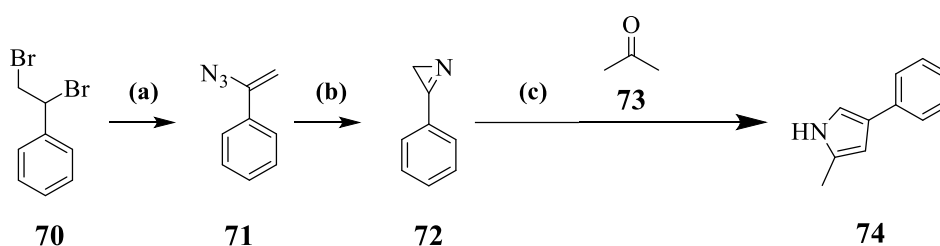
3.5.4 Synthesis of 2-methyl-4-phenyl-1*H*-pyrrole

Considering the failures encountered during the complexation of the dipyrin **66**, selecting a building-block pyrrole with intermediates properties was preferred, differing from those utilized thus far, *e.g.*, **1** and **65**.

In particular, it was envisioned a perfect balance of the characteristics required in 2-methyl-4-phenyl-1*H*-pyrrole **74**. This specific one features a phenyl group at position 4, which contributes to an extended conjugation of the system and further enhances its rigidity. Additionally, the methyl group at position 2 has been previously observed to be amenable to functionalization, specifically through Knoevenagel condensation.

By employing this approach, the inclusion of a phenyl ring and vinyl aryl moieties at positions, respectively 4,8 and 2,9, in the resultant dipyrin ensures both a red shift in the photophysical properties and, at the same time, being flexible, facilitates the complexation with another dipyrromethene unit.

The synthesis of pyrrole **74** was carried out following a multi-step procedure reported in the literature and outlined in **Scheme 18**.^[252,253]



Scheme 18: Multi-step synthesis for the preparation of 2-methyl-4-phenyl-1*H*-pyrrole **74** starting from (1,2-bromomethyl) benzene. (a) NaN₃, DMF, Ar, r.t. overnight. (b) Dry toluene, Ar, reflux overnight. (c) NaH, DMSO, Ar, r.t. overnight.

The first step was an S_N2 reaction between (1,2-bromomethyl) benzene **70** and an excess of sodium azide (NaN₃) in anhydrous DMF under an argon atmosphere.

The initial substitution predominantly occurred at the secondary carbon of compound **70** due to transition state stabilization.

The reaction mixture was stirred under an inert atmosphere, at room temperature, for eighteen hours, forming (1-azidovinyl) benzene **71** as a brown oil. The ¹H-NMR spectrum showed the purity of the compound, which was then directly engaged in the following step without any further purification.

Compound **71** was dissolved in dry toluene under an inert atmosphere to induce its thermal arrangement into the 3-phenyl-2*H*-azirine **72**. After 30 minutes, TLC analysis showed the complete conversion of **72**; the solvent was evaporated under reduced pressure to obtain a brown oil.

The crude residue was purified *via* column chromatography, using silica gel as the stationary phase and cyclohexane/dichloromethane as eluent mixture. However, ¹H-NMR and high-resolution mass spectroscopy did not detect the presence of the product. Instead, the proton peaks resemble those observed for the azidovinyl precursor **71**.

The pronounced ring strain of 2*H*-azirines contributes to the elevated chemical reactivity of these three-membered ring compounds consisting of a C-N double bond, but at the same time, renders them extremely unstable.^[254]

Hence, although column chromatography was the indicated method for the purification of the compound, after three different attempts, it was considered that the 3-phenyl-2*H*-azirine **72** could decompose during the purification process.

Given the thermal stability issues, it was decided to investigate a one-pot reaction. Thus, (1-azidovinyl) benzene **71** was dissolved in anhydrous DMSO under an argon atmosphere and heated up to 100 °C.

Once confirmed by TLC analysis of the complete conversion of compound **71**, the reaction mixture was first allowed to cool down to room temperature and then cooled to 0°C. Sodium hydride (NaH) was gradually added, and after a few minutes, acetone **73** was introduced into the reaction mixture, which was stirred at room temperature overnight.

TLC analysis showed different spots, including a luminescent one, possibly attributed to the product (the R_f value for this compound was not reported in the literature).

Therefore, after the work-up, the crude residue was processed with column chromatography and all the fractions were collected, but none provided the expected mass or ¹H-NMR signals. The reaction, as well as the purification, was repeated multiple times but without success.

Some methods reported for the synthesis of 2-methyl-4-phenyl-1*H*-pyrrole **74** include a rhodium-catalyzed hydroformylation of propargylamines for the formation of β-aryl pyrroles^[255] or a transannulation of N-sulfonyl-1,2,3-triazoles with vinyl ether^[256].

It is also possible to achieve a cyclocondensation of enones with aminoacetonitrile, which furnishes 3,4-dihydro-2*H*-pyrrole-2-carbonitriles that can be converted to 2,4-disubstituted pyrroles by microwave-induced dehydrocyanation.^[257]

These methods were not considered due to their high cost and considerable safety risks. Nevertheless, through careful retrosynthetic analysis, alternative strategies can be considered to obtain the desired product.

3.6 Aza-dipyrinato ligands

To attain a red-shift absorption and emission of the dipyrin, one of the most atom-effective methods is to replace the methine carbon atom at the *meso* position with an imino moiety (**Figure 65**).^[258,259]

This ring modification affords the closely related family of aza-dipyrin. The electronegative aza-N-atom lowers the HOMO-LUMO energy gap, thus resulting in a red-shifted emission from the azadipyrins.^[260]

Thus, the focus was shifted towards obtaining inherently red-emissive ligands by incorporating a nitrogen atom within the structure, as depicted in **Figure 65**.

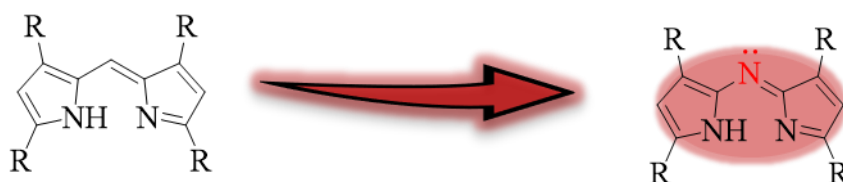


Figure 65: Schematic representation of replacing the C-methine atoms present in the dipyrin with an aza-N atom to obtain the corresponding aza-dipyrin.

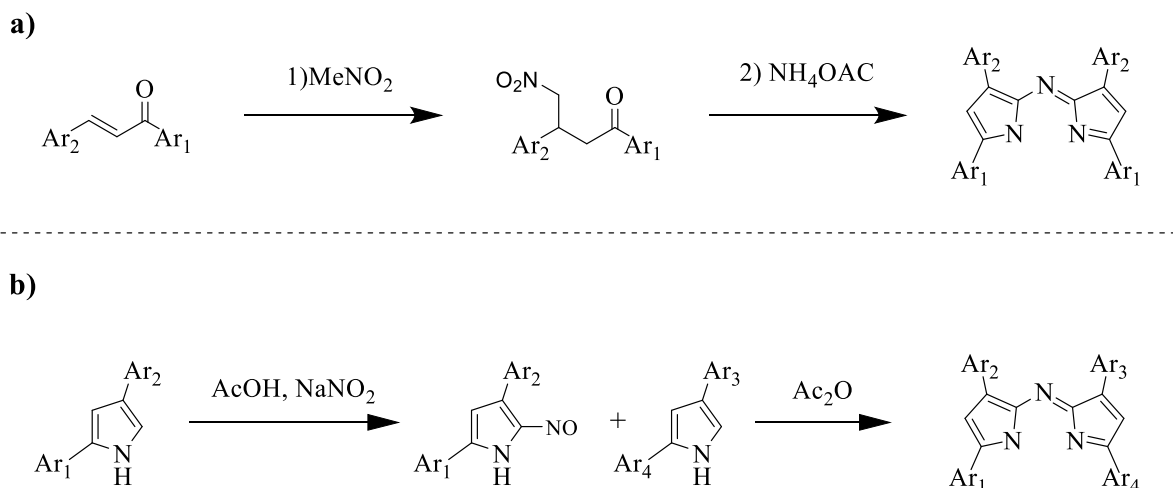
Over the years, two major synthetic routes have been established to prepare azadipyrromethenes, as reported in **Scheme 19**. Both strategies rely on the use of nitro-intermediates to create the aza-structure.

The first method was developed by O'Shea *et al.*^[261] and it is based on α,β -unsaturated ketones converted in the first stage into their corresponding nitro-butanone derivatives, which are cyclized after condensation with an ammonium source, usually ammonium acetate (**Scheme 19a**).

This strategy allows for the synthesis of symmetrical azadipyrromethenes. In contrast, the second method (**Scheme 19b**), proposed by Carreira *et al.*^[262] provides a versatile design platform for the synthesis of both symmetrical and unsymmetrical azadipyrromethenes using pyrroles as building blocks. This technique involves using sodium nitrite to convert the first pyrrole molecule. The 5-nitroso derivative obtained undergoes a cross-condensation with a

second molecule of pyrrole, which can be either the same or different from the first one, through the addition of acetic anhydrides, leading to the formation of the desired azadipyrromethene.

Both methods were used in this work.



Scheme 19: Synthetic methods to obtain **a)** symmetric tetra-substituted azadipyrromethenes starting from α , β -unsaturated ketones and **b)** unsymmetrical tetra-substituted azadipyrromethenes starting from a pyrrole building block.

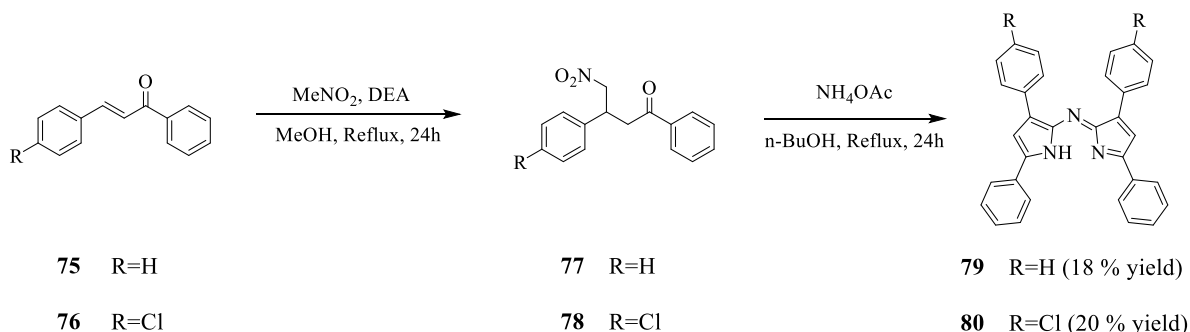
3.6.1 Synthesis from α , β -unsaturated ketones

The starting point of the synthesis was the Michael addition of nitromethane MeNO_2 to the commercially available chalcones **75** and **76**, followed by the formation of the tetra-aryl-azadipyrromethenes **79** and **80** (**Scheme 20**).

Following the general protocol,^[263] the aforementioned diaryl α,β unsaturated ketones were subjected to reflux with diethyl amine (DEA) in ethanol.

The electron-withdrawing nitro group makes the adjacent methylene hydrogens in the nitromethane acidic enough to form the nitromethanide anion when reacted with DEA. Once the carbanion, which acts as a nucleophilic Michael donor, attacked the electrophilic β -carbon

atom present in **75** and **76**, yielded the 1,3-diaryl-4-nitrobutan-1-ones **77** and **78**, as yellow oil residues.



Scheme 20: Synthetic scheme to obtain the aza-dipyrrins **79** and **80** starting from the commercially available chalcones **75** and **76**.

The obtained Michael adducts were treated with an excess of ammonium acetate in *n*-butanol for twenty-four hours. The crude residue was then concentrated to a few milliliters.

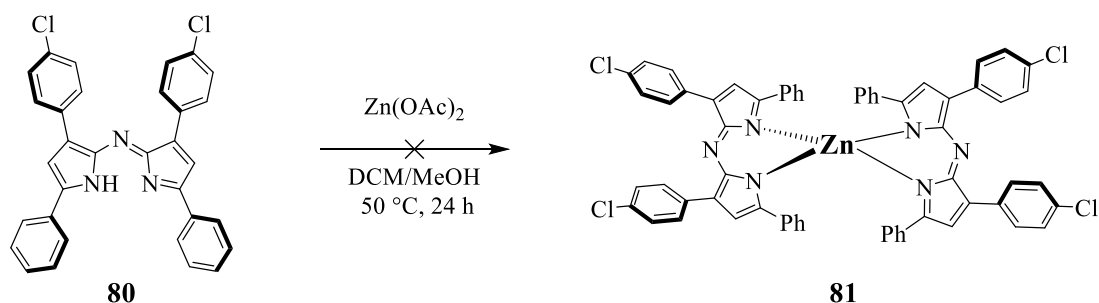
The formed precipitates were filtered and washed with ethanol, giving the target azadipyrrromethenes **79** and **80** as a blue and violet powder, respectively. Subsequently, a complexation attempt was carried out.

The literature has already reported the homoleptic bis(azadipyrrinato)Zn^{II} complex formed by the azadipyrrromethene **79**.^[264] It showed absorption maxima ranging between 593-596 nm in different solvents, specifically $\lambda_{\text{abs}} = 593$ in CH₂Cl₂, $\lambda_{\text{abs}} = 590$ in EtOH, $\lambda_{\text{abs}} = 596$ in PhMe. Nevertheless, Palma *et al.*^[264] did not detail the emission values as they observed that the complex was not fluorescent.

Due to its potential for further conjugation, as it contains two chlorine atoms in two of its four phenyl groups attached to the core, the aza-dipyrrin **80** was subjected to complexation with Zn²⁺.

According to the established procedure described for the complexation of **79**,^[263] the azadipyrrromethene **80** was dissolved in dichloromethane and added to a solution of Zn(OAc)₂ in methanol (**Scheme 21**).

The reaction was carried out overnight at 50 °C in a crimp-vessel vial. TLC analysis indicated no conversion of the starting material.



Scheme 21: Attempted complexation of the aza-dipyrrin **80** with $\text{Zn}(\text{OAc})_2$ to obtain the homoleptic bis(azadipyrinato) complex **81**.

This outcome was unsurprising, considering the previous attempts on the similar π -extended dipyrrin **66**. From a synthetic perspective, the nitrogen atom in *meso* should not display differences in the complexation processes.

No further attempts of complexation were made for this ligand, as its boron difluoride complex is already reported in the literature.^[265]

Instead, preliminary investigations were carried out to gain insights into the photophysical properties of compound **80**, which have not been documented in the literature.

The electronic spectra of the free-base aza-dipyrrin **80** in spectroscopic DMSO are displayed in **Figure 66**. Installing the nitrogen atom in the *meso* position proved to be an optimal strategy to shift the $^1\pi\text{-}\pi^*$ transition localized on the dipyrrin core at lower energy.

The latter raises a broad band between 500-650 nm, with a maximum of 596 nm (dash plot, **Figure 66**). The emission profile (solid plot, **Figure 66**) displays a broad band ranging from 600 to 800 nm, characterized by a peak at 642 nm.

Upon comparison with the emission profile of the aryl *meso* corresponding ligand **66** (§3.5.3, **Figure 64**), it becomes evident that the electron-donating aza group induces a bathochromic spectral shift from 616 nm for **66** to 642 nm for **80**, quantified as $6.57 \times 10^2 \text{ cm}^{-1}$.

It should be considered that the two structures being compared, precisely **66** and **80**, do not differ only by a single atom. The former **66** contains a phenyl group at the *meso* position, while

the latter **80** incorporated two chlorine atoms in its structure, which, being electron-withdrawing groups, will undoubtedly impact the photophysical properties.

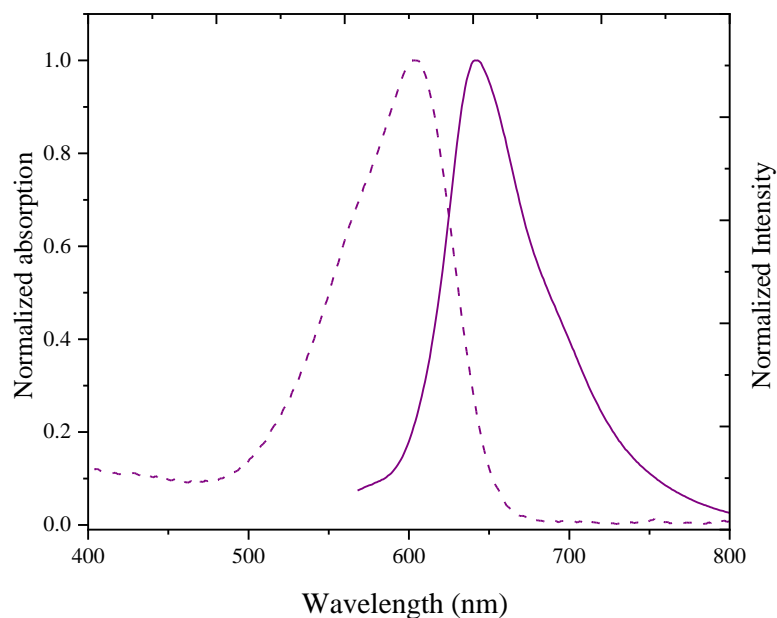


Figure 66: UV/Vis (dashed plot) and emission (solid plot, $\lambda_{\text{exc}} = 550 \text{ nm}$) spectra of the aza-dipyrrin **80** in DMSO at 20 °C.

Nevertheless, this preliminary study highlights how the interplay between the electronegative effect of the N-atom on the LUMO energy and the increased contribution of the peripheral aryl rings in shaping the HOMO-LUMO energy gap originates the combination of electronic effects that results in the observed red-shift. The fine-tuning of the electronic characteristics of the substituents on the aryl groups could further amplify this energy gap.

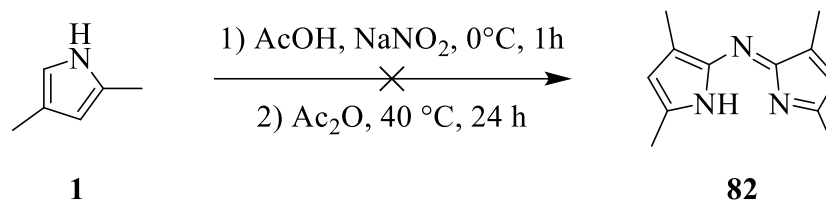
The fluorescence lifetime for the π -extended azadipyrrin **80** in DMSO is 3.5 ns with a $\Phi = 0.12$ (**Table 11**).

Table 11: Photophysical properties of π -extended dipyrin **66** previously reported and the π -extended azadipyrrin **80** in spectroscopic DMSO at 20 °C. ^[a]Quantum yields were determined by the relative method, using cresyl violet ($\Phi = 0.54$ in MeOH, 22°C). ^[b] Exciting with a NanoLED source at 570 nm.

Compound	λ_{abs} [nm]	λ_{em} [nm]	Φ ^[a]	τ ^[b] [ns]
66	541	616	0.17	3.2
80	596	642	0.12	3.5

3.6.2 Synthesis from pyrrole building blocks

The red shift observed in the π -extended azadipyrrin **80** has prompted the exploration of another system containing the *meso* nitrogen atom. Specifically, it was selected as target for our synthesis compound **82**, depicted in **Scheme 22**.



Scheme 22: Synthetic scheme for obtaining the azadipyrrin **82** starting from the 2,4-dimethyl-1*H*-pyrrole **1**.

According to the literature procedure,^[262] 2,4-dimethyl-1*H*-pyrrole **1** was dissolved in glacial acetic acid. After a few minutes, the system was cooled to 0°C through an ice bath and four equivalents of sodium nitrite (NaNO₂) were added to the reaction mixture, which immediately changed color from orange to yellow.

Extreme caution must be exercised during this step. NaNO₂ should be added carefully, not inhaling the resultant fumes. Subsequently, a solution composed of another equivalent of pyrrole **1** in acetic anhydride was added to the reaction mixture, which was heated at 40 °C for twenty-four hours. TLC analysis showed the presence of the starting material along with two additional spots, one orange and black.

The first spot could correspond to the desired product, while the second, located on the TLC baseline, might be attributed to polymer materials. As a result, after work-up, the second fraction was separated and purified *via* column chromatography. However, the product was not identified.

The reaction was repeated multiple times, varying the temperature, order of addition and reaction times. Based on these experimental observations, this method cannot lead to the formation of the aza-dipyrrin **82**.

This protocol is reported only for pyrroles with aromatic substituents, and the specific reaction outlined in **Scheme 22** has never been reported in the literature.

In this regard, an explanation has yet to be provided regarding the unsuitability of this reaction for pyrroles lacking bulky substituents.

Different methodologies need to be considered for the synthesis of the synthon **82**, which could potentially allow for the incorporation of up to four styryl aryl groups *via* Knoevenagel condensation. ^[266] The obtained tetrasteryl azadipyrrin, never reported in the literature so far, could pave the way for enhanced near-infrared emission.

3.7 Benzo[*a*]- and [*b*]-fused dipyrrens: strategy

In the molecular design of dyes with narrow HOMO-LUMO gap, it is crucial to decrease the LUMO level of the molecule while moderately increasing the HOMO level to enhance stability toward air oxidation.

To achieve this, the π -conjugation of the dipyrren core can be extended through annulations of aromatic rings to the pyrrole unit.^[267,268]

Two distinct isomeric structures can be identified depending on which bond of the entire dipyrren is involved in the aromatic ring fusion, specifically [*a*]-annulated or [*b*]-annulated dipyrrens (**Figure 67**).

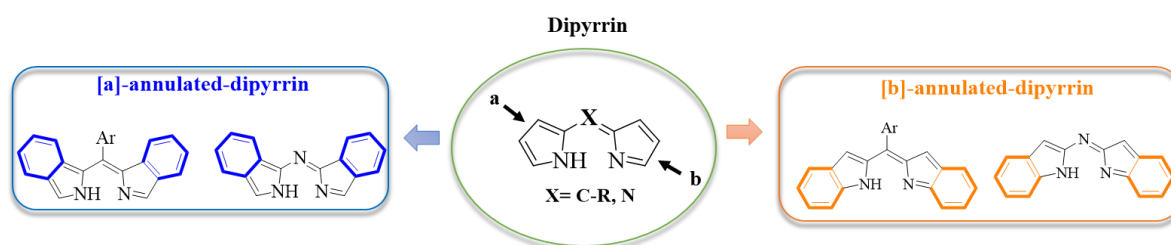


Figure 67: Generic structures of [*a*]- and [*b*]-annulated dipyrrens investigated in this work.

The DFT calculations unveiled that the ring fusion at the [*a*]-bond in the dipyrren skeleton increases the HOMO level, while the ring fusion at the [*b*]-bond results in a lowered LUMO.^[269]

In studying fully ring-fused planar π -conjugated dipyrrens derivatives, this work examined all four systems depicted in **Figure 67**.

The atom located at the *meso* position can be either a carbon (X=C-R) or a nitrogen (X=N), leading to a clear differentiation between carbon-benzofused, with a focus on *meso*-aryl functionalized scaffolds and aza-benzofused dipyrrens.

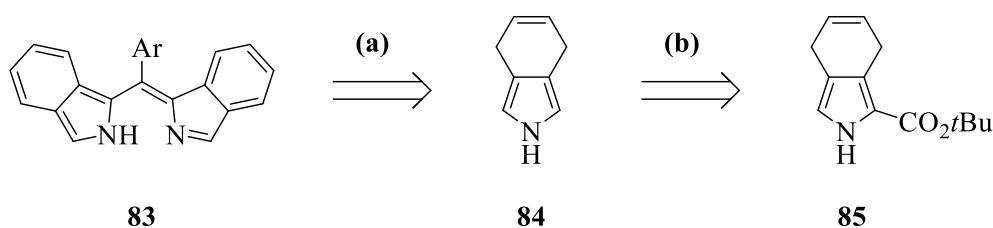
Each of them has involved distinct synthetic approaches, yielding different results.

3.7.1 Benzo[*a*]fused systems with aryl groups in *meso* position

The straightforward application of the standard porphyrin chemistry methods, such as the condensation of an appropriate pyrrole with aromatic aldehydes, already discussed in §3.1, is not feasible with 2*H*-isoindoles due to the unstable transient nature of this progenitor pyrrole.^[270]

Referring to the chemistry of the tetrabenzoporphyrins, one of the most employed methods to mitigate this instability involves using 4,7-dihydroisoindole derivatives, which undergo aromatisation after the assembly of the porphyrin macrocycle.^[271]

Considering this method, it seemed reasonable that the condensation of 4,7-dihydro-2*H*-isoindole **84** with an aromatic aldehyde could yield the benzofused system **83** under acidic conditions, followed by oxidation (**Scheme 23**).



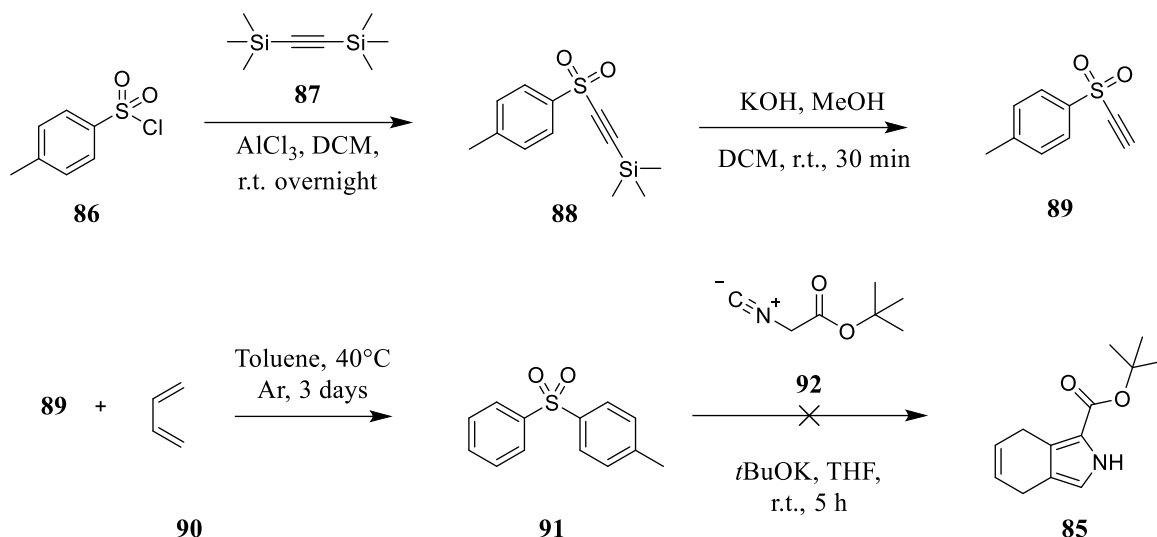
Scheme 23: Retrosynthetic pathway for the benzo[*a*]fused system **83** having an aromatic rest at *meso*-position starting from 4,7-dihydro-2*H*-isoindole **84**. (a) Condensation reaction with an aromatic aldehyde under acidic conditions and subsequent oxidation with *p*-chloranil; (b) TFA, KOH, reflux, 30 min.

According to a literature protocol,^[272] the synthesis of tert-butyl 4,7-dihydro-2*H*-isoindole-1-carboxylate **85** started from 4-methylbenzenesulfonylchloride **86**, which is commercially available (**Scheme 24**).

This, through forming an aluminocyclopropene intermediate species,^[273] was converted into the silane derivative **88**, which after deprotection afforded *p*-toluenesulfonylacetylene **89**. The sulfone substituent activates the adjacent π -system^[274] thus rendering compound **89** an excellent dienophile for the Diels Alder reaction with 1,3-butadiene **90**.

The cycloaddition was conducted in a crimped vial to avoid the evaporation of the diene from the reaction mixture. After three days of stirring, TLC analysis showed the complete conversion of the starting dienophile.

Thus, compound **91** was isolated by recrystallization. The last step entailed the formation of the dihydro-2*H*-isoindole derivative through the reaction with the isocyanoacetate derivative **92**.



Scheme 24: Multi-step synthetic pathway for the synthesis of *tert*-butyl 4,7-dihydro-2*H*-isoindole-1-carboxylate **85** starting from 4-methylbenzenesulfonylchloride **86**.

This protocol relies on a modified Barton-Zard chemistry,^[275] wherein the unsaturated sulfone **91** replacing the conventional nitro-olefins,^[276] reacts with *tert*-butyl 2-isocyanoacetate **92**, forming compound **85**.

Although the reaction was expected to proceed under straightforward conditions, difficulties were encountered during the purifications, preventing the attainment of the desired product.

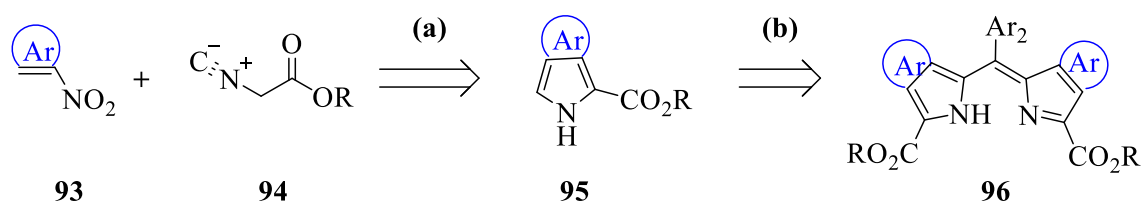
The crude residue was processed two times through column chromatography, using alumina gel as stationary phase for the first time and silica gel as for the second time. The mass peak corresponding to the product, detected in the crude reaction mixture, was not observed in any of the fractions collected after the column. Therefore, the only plausible explanation is that the product decomposed during the purification process.

The followed literature procedure^[271] mentioned the instability of compound **85** at room temperature, which rapidly darkens like the other electron-rich β -substituted pyrroles, thereby justifying the absence of NMR spectra recorded. Nevertheless, they claimed to successfully isolate the product after chromatography, which proved to be relatively stable when stored in

the refrigerator. Consequently, the multi-step procedure was repeated a second time. Each step proved to be straightforward, with yields of approximately 70 %. However, even in this second attempt, the purification of the product, this time through recrystallization, did not yield the product. The reaction could be further optimized, perhaps by carefully reconsidering the purification procedure.

Hence, it was decided to synthesize isoindoles as a precursor for the benzo[*a*]fused dipyrin using the route depicted in **Scheme 25**, where the key chemical event is an extension of the Barton-Zard reaction between aromatic nitro-compounds with α -isocyanoesters in the presence of a base.^[277,278] Since the double bonds substituted with nitro groups in polycyclic aromatic compounds have an alkene character, they behave as nitroalkene toward the carbanion derived from the isocyanoacetate derivative to give substituted pyrroles in good yields.

Thus, the base-catalyzed addition of an α -isocyanoacetate derivative, such as compound **94**, to a polycyclic aromatic nitroalkene **93**, followed by cyclisation, would give the pyrrole fused with one or more aromatic rings, like compound **95**. The latter provides the starting point for the synthesis of benzo[*a*]fused dipyrin, such as the generic **96**, after condensation with an aromatic aldehyde.

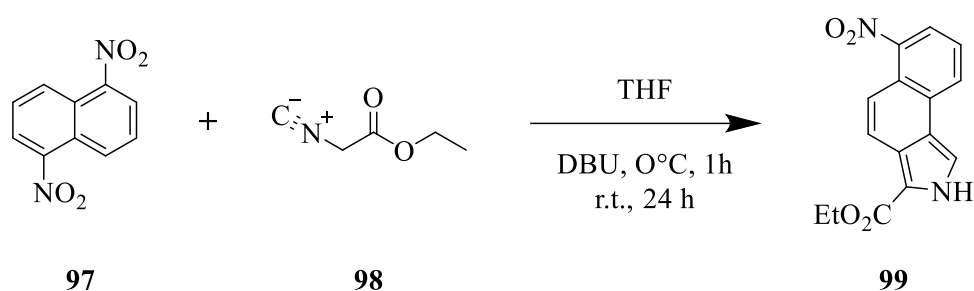


Scheme 25: Retrosynthetic pathway employed for the benzo[*a*]fused dipyrins having an aromatic rest at *meso*-position synthesized in this work. (a) Barton-Zard reaction between polycyclic nitroaromatic alkenes with α -isocyanoesters in the presence of a base. (b) Condensation with an aromatic aldehyde under acidic conditions followed by oxidation.

According to a literature procedure,^[279] the commercially available 1,5-dinitronaphthalene **97** dissolved in tetrahydrofuran (THF) was reacted with two equivalents of ethyl 2-isocyanoacetate **98**.

Once the system was ensured at 0°C, 1,8-diazabicyclo-[5.4.0]-undec-7-ene (DBU) was added dropwise to the reaction mixture, changing color from grey to dark red. The addition of the base needs to be done with extreme caution because it leads to the formation of the nitronate anion, which causes the generation of vapors due to the exothermic nature of the reaction.

After one hour, the reaction mixture changed color from dark red to black, attesting the cyclisation of the anion onto the isocyanate group, leading to the formation of the pyrroline intermediate. Subsequently, the reaction mixture was allowed to stir at room temperature for additional twenty-four hours (**Scheme 26**). After work-up, purification *via* column chromatography using silica gel as a stationary phase, afforded compound **99** as a bright yellow powder, with 38 % of yield. This value is perfectly in line with the one reported in the literature.^[279]



Scheme 26: Synthetic route for annulated pyrrole **99** by reaction of 1,5-dinitronaphthalene **97** and ethyl 2-isocyanoacetate **98**.

The annulated pyrrole **99** was used as starting material for the condensation with benzaldehyde **2** (**Scheme 27**).

In the absence of literature references specific to compound **100**, the reaction was tackled by drawing upon similar conditions employed in the synthesis of related benzo-fused porphyrin.^[270]

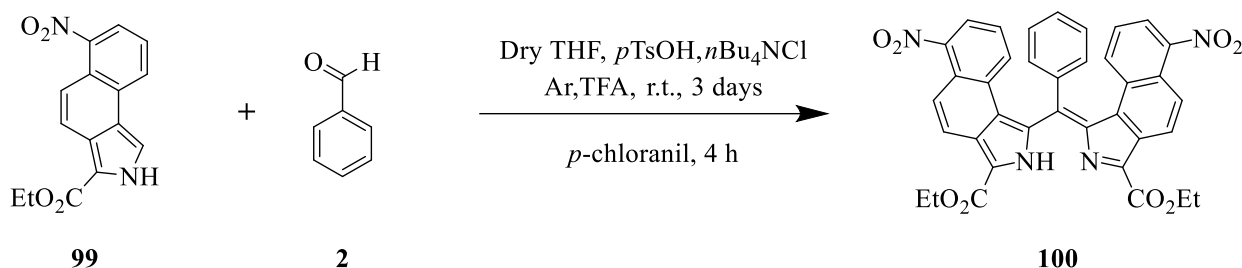
In an anhydrous system, purged with argon, compounds **2** and **99** were dissolved in dry THF in the presence of a catalytic amount of TFA (0.1 mmol).

Although the annulated pyrrole **99** possesses only one hydrogen in α , the polymerization is favored over the condensation due to the significant steric hindrance of the aromatic fused ring in the structure. Thereby, anhydrous tetrabutylammonium chloride was added to improve the formation of the dipyrromethane. This highly hygroscopic salt works as a water scavenger, thus hypothetically suppressing tar-alike products formation and other possible side reactions at the double bond.

Additionally, *p*-toluenesulfonic acid was incorporated into the system as a complementary catalyst to augment the effects of the TFA, but also by virtue of its hygroscopic nature.

After approximately three hours of stirring, the reaction mixture turned from yellow to orange, with an intense green luminescence under UV irradiation. After twenty-four hours of reaction, TLC analysis attested to the presence of a new spot in addition to those corresponding to the starting materials. A few drops of TFA were added to the reaction mixture to enhance the conversion, which was left stirring for additional two days at room temperature. After this time, the spot corresponding to the starting compound **99** appeared less intense but still visible in the TLC plate.

Nevertheless, it was decided to perform the oxidation by adding *p*-chloranil to the reaction mixture.



Scheme 27: Condensation reaction between the annulate pyrrole **99** and benzaldehyde **2** in dry THF to obtain the benzo[*a*]fused dipyrin **100**.

The crude residue was then purified with column chromatography packed with silica gel. The first fraction eluted, corresponding to the new spot, was analyzed. High-resolution mass spectroscopy revealed the presence of a significant peak at 654.58 *m/z*, corresponding to compound **100**.

Despite this, ¹H-NMR spectroscopy indicated the presence of one extra peak, integrating 1 proton at ca. 7.5 ppm, not accounted for the designed structure and not assignable to any solvents. The crystallization process has not yielded crystals suitable for X-Ray diffraction yet. Once the structure of this novel compound is acquired, it will enable further insights into the geometric arrangement of the molecule.

The benzo[*a*]fused dipyrin **100** was isolated with a yield of only 12%, and the starting annulated pyrrole **99** was collected as the second and last fraction. Its purity was confirmed by ¹H-NMR and mass spectroscopy.

The reaction was then repeated using different conditions, described in **Table 12**. The stoichiometric ratio between the starting materials remained unchanged, specifically one equivalent of **2** and two equivalents of **99**.

Considering that the formation of similar benzofused BODIPY is typically conducted in dichloromethane, our investigation started with this solvent. After twenty-four hours at room temperature, no conversion of the starting material was observed through TLC analysis. Therefore, the temperature was increased until reflux (Entry 1, **Table 12**). After seventy-two hours, no product was detected.

It was supposed that a further temperature increase could then diminish the activation energy of the reaction, thus facilitating the condensation. However, the reaction conducted in toluene did not lead to the conversion of the starting material after twenty-four hours at 80 °C (Entry 2, **Table 12**) and at 110 °C for seventy-two hours (Entry 3, **Table 12**).

In both cases, the formation of multiple byproducts was observed, but none corresponded to the desired product **99**. Returning to the starting system seemed reasonable, but increasing the temperature (Entry 4, **Table 12**). However, no significant changes were observed.

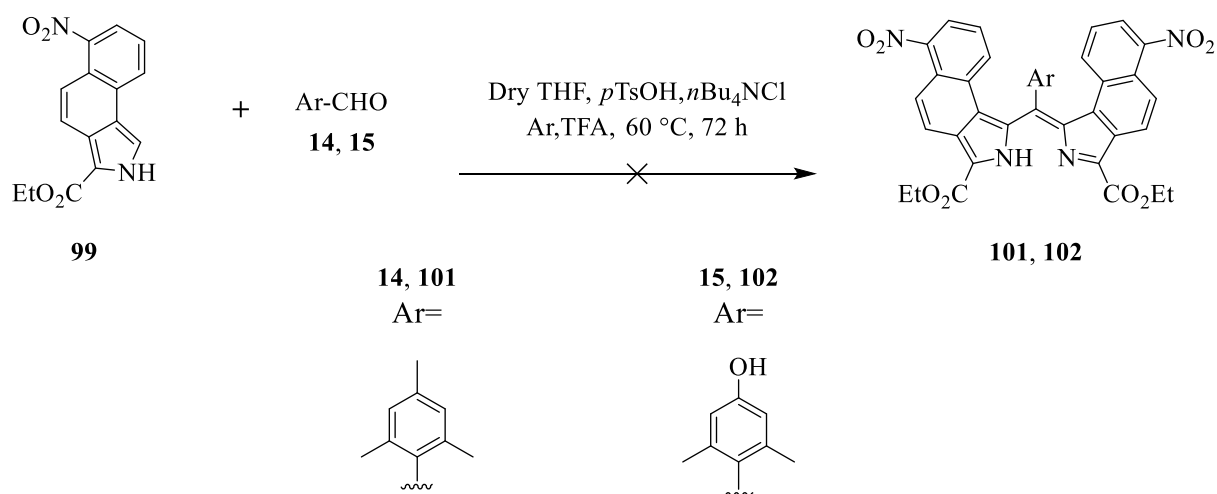
Table 12: Screening conditions for the synthesis depicted in **Scheme 27**.

Entry	Solvent	Temperature	Time	Product 99
1	DCM	25-40 °C	72 h	Not detected
2	Toluene	80 °C	24 h	Not detected
3	Toluene	110 °C	72 h	Not detected
4	THF	60 °C	72 h	10 %

This preliminary screening is limited to a few solvents, and further in-depth studies are required. Nevertheless, based on these investigations, it can be stated that the initial conditions outlined in **Scheme 27** yield the most favourable results.

To diversify the aromatic substituents at the *meso* position of the new benzofused system developed, the benzofused pyrrole **99** was subjected to a condensation reaction with two different aromatic aldehydes, such as the 2,4,6-trimethylbenzaldehyde **14** and the 4-hydroxy,2-6 dimethylbenzaldehyde **15**.

Based on the results reported in **Table 12**, the condensation reaction shown in **Scheme 28** was conducted in dry THF initially at room temperature. After twenty-four hours, no conversion of the starting material **99** was observed; for this reason, the temperature was increased up to 70 °C and additional few drops of TFA were added to the reaction mixture. Nevertheless, prolonging the reaction for another forty-eight hours under reflux did not form the desired product. Therefore, the reaction was stopped without proceeding with the oxidation to recover the starting pyrrole **99**. The increased steric hindrance dictated by the presence of the methyl groups at position 2- and 6- in the aromatic aldehydes **14** and **15** probably posed a challenge for condensation with the aldehyde high steric hindered pyrrole **99**. In literature, an example of naphtha[1,2-*c*] pyrrole is condensed with naphthyl and pyrenyl groups appended at the *meso*-positions of the corresponding BODIPY scaffolds.^[280] They stated a successful condensation occurring at ca. 140 °C in an oven without solvent. However, considering these reaction conditions too harsh, the protocol was not replicated.



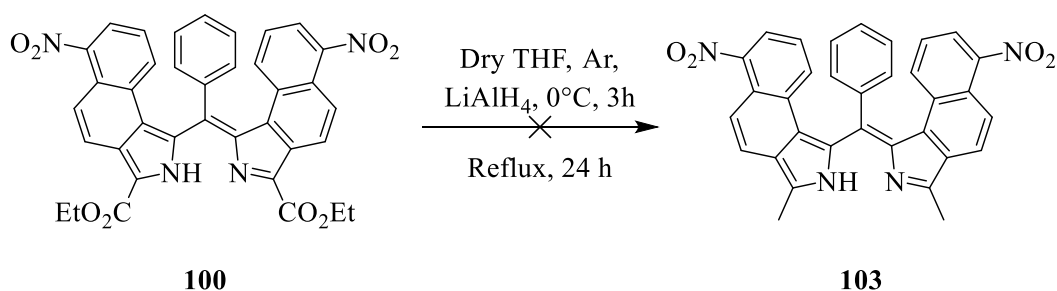
Scheme 28: Attempts of condensation reactions between the annulate pyrrole **99** and the aromatic aldehydes **14** and **15** to obtain the benzo[*a*]fused dipyrins **101** and **102**.

Once the benzo[*a*]fused dipyrin **100** was obtained, the aim was to remove the ester moiety attached to the α positions of the nitrogen atoms to facilitate the incorporation of other functional groups and extend the conjugation of the system. In this case, the specific reaction outlined in **Scheme 29** was not reported in the literature, so it was attempted to adapt it from the analogous porphyrin scaffolds.

According to the literature procedure,^[279] one equivalent of compound **100** was dissolved in dry THF under an argon atmosphere. Once the system was cooled to 0°C through an ice bath, five equivalents of lithium aluminium hydride (LiAlH₄) was added and allowed to react at that temperature for three hours. Subsequently, the system was refluxed for sixteen hours. The reaction mixture changed color, from yellow to intense orange, along with the appearance of a new spot, in addition to the starting material **100**.

The reaction mixture was refluxed for additional eight hours. After twenty-four hours, TLC analysis still showed the presence of starting material; nevertheless, it was decided to stop the synthesis and quench the reaction by adding a saturated solution of sodium sulfate (Na₂SO₄) until the release of gaseous hydrogen was stopped. After the work-up, the crude residue was subject to automatic column chromatography packed with silica gel.

However, the isolated fraction corresponding to the TLC spot, did not exhibit the diagnostic mass and the ¹H-NMR peaks of the expected product **103**. No further investigations were conducted.



Scheme 29: Attempt to reduce the ethoxycarbonyl groups at the α -position in the benzo[*a*]fused dipyrin **100** with LiAlH₄ to obtain the corresponding methyl groups in **103**.

Due to the low yield of the benzo[*a*]fused dipyrin **100**, it was preferred to explore the optimal conditions for the reduction of the esters functionalities the annulated pyrrole **99** instead (**Scheme 30**).

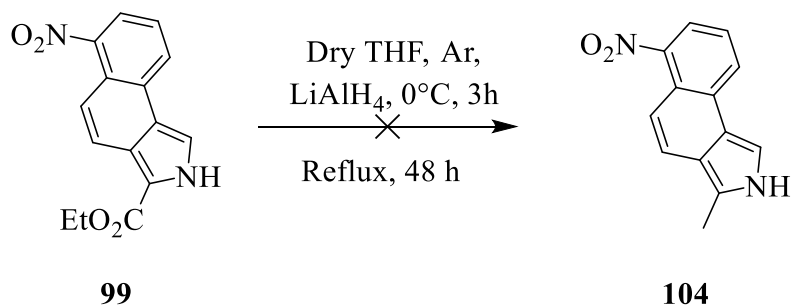
Fresh LiAlH₄ (new batch, never opened before) was employed to ensure utmost dryness. Using dried glassware and under a generous flux of argon gas, compound **99** was dissolved in dry THF. LiAlH₄ (4 equivalents, new batch, never opened before) was employed to ensure utmost dryness and thus added at 0°C in ten minutes.

After approximately one hour, the reaction was allowed to stir at room temperature and then refluxed for sixteen hours. TLC analysis still showed the presence of the starting material in the reaction mixture; thus, other two equivalents of reducing agent, LiAlH₄, was added to the refluxed system until the starting material was converted. Also, the reaction mixture changed from yellow to orange in this case. After quenching the reaction with a saturated solution of Na₂SO₄, a rapid celite plug eluting with ethyl acetate was performed, according to a literature procedure.^[281]

So, the material was processed with column chromatography, collecting two fractions: a new spot, yielding an orange powder and the starting material **99**. The new spot was characterized with NMR spectroscopy.

Interestingly, the peaks corresponding to the ester groups, specifically the quartet at 4.40 ppm (2 H of the -CH₂) and the singlet at 1.41 ppm (3H of the -CH₃), remained unchanged. Instead, the reduction occurred in the nitro group located in the aromatic ring. This is evident from the appearance of a broad peak at ca. 4.5 ppm, integrating two hydrogens.

Thus, the -NO₂ group was reduced in the amino group -NH₂.



Scheme 30: Attempt for the reduction of the ethoxycarbonyl groups at the α -position in the annulated pyrrole **99** with LiAlH₄ to obtain the corresponding methyl group in **104**.

To further broaden the scope of our investigation and overcome the limitations imposed by the presence of the nitro groups, the synthesis of the isoindole derivative **107**, starting from 1-nitronaphthalene **105**, was performed.

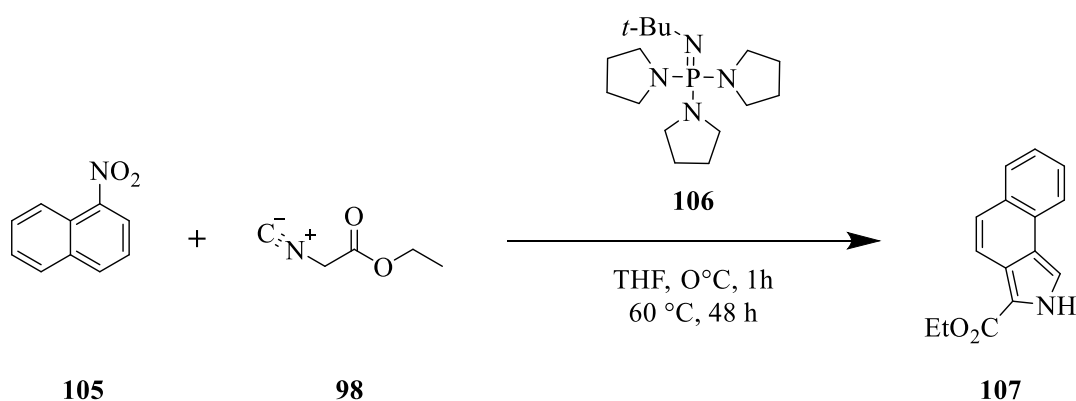
Previous studies have demonstrated how the presence of an additional nitro group, such as in 1,5-dinitronaphthalene **96**, imparts greater reactivity toward this type of synthesis than the simple 1-nitronaphthalene **105**.

For this reason, the reaction depicted in **Scheme 31** involved the use of the phosphazene base **103**, which, being a stronger base, was found to be more efficient compared to the commonly used DBU.^[282]

Specifically, *N*-*tert*-butyl-1,1,1-tri(pyrrolidine-1-yl)-15-phosphanimine **106** was added dropwise at 0°C to a solution of **105** and **98** dissolved in dry THF under an argon atmosphere. After one hour, the reaction was allowed to reach room temperature and then refluxed at 60 °C for forty-eight hours. After standard work-up, the crude residue was subjected to column chromatography packed with silica gel.

The product was isolated as a grey powder, showing an intense turquoise luminescence upon UV irradiation, both in a solid state and solution.

The obtained compound **107** was crystallized by simple evaporation from a concentrated dichloromethane solution, with a yield of only 12 %, according to the values reported in the literature.^[279]



Scheme 31: Synthetic route for the annulated pyrrole **107** by reaction of 1-nitronaphthalene **105** and ethyl 2-isocyanoacetate **98** in the presence of a phosphazene base **106** through an extension of the Barton-Zard reaction.

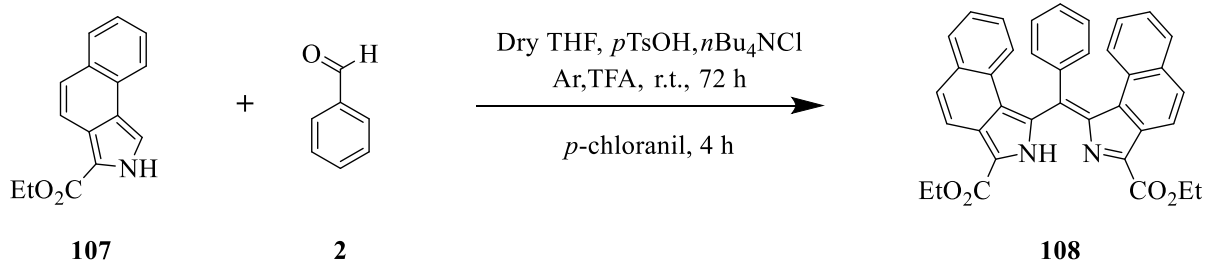
The reaction was repeated using DBU as a base, resulting in a 5% product yield. Therefore, the employment of base **106** is crucial for enabling this type of synthesis, *albeit* it has a considerably higher cost than the former base employed.

By adopting the same conditions illustrated in **Scheme 27**, benzaldehyde **2** and the annulate pyrrole **107** were dissolved in dry THF under an inert atmosphere (**Scheme 32**).

Catalytic amounts of TFA, *p*-toluenesulfonic acid and anhydrous tetrabutylammonium chloride were added to the reaction mixture, stirring for seventy-two hours.

Similarly to what was observed during the reaction of the nitro-analogous compound **100**, complete conversion of the starting material **107** was not achieved. Instead, different from what was reported for compound **100**, TLC analysis showed the presence of eight spots in this specific reaction.

Thus, it proceeded with the oxidation using *p*-chloranil, which occurred in four hours. The purification process was very tedious and complicated because the spots were quite close to each other. Consequently, more than single-column chromatography was needed to isolate each spot.



Scheme 32: Condensation reaction between the annulate pyrrole **107** and benzaldehyde **2** in dry THF to obtain the benzo[*a*]fused dipyrin **108**.

The interpretation of the ¹H-NMR spectrum of each fraction collected from the first column did not provide unequivocal results.

In contrast, the high-resolution mass spectroscopy confirmed the presence of a peak corresponding to the targeted compound **108**, specifically at 564.40 m/z in the second fraction.

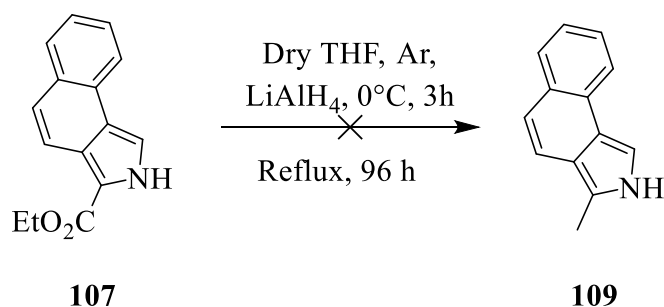
This was subjected to column chromatography, packed with alumina gel. High-resolution mass spectroscopy determined the presence of the desired mass-peak in the first fraction, corresponding to the first spot. It appeared as a violet powder, green luminescent in DCM solution.

Despite the clean mass spectrum, the $^1\text{H-NMR}$ analysis in different solvents did not reveal a pure compound.

Based on the findings observed, it is reasonable to confirm the presence of the product, although further details are needed to give an overall view. Currently, crystallization of the compounds is also being pursued, using different techniques to obtain more specific information.

Since the annulated pyrrole **107** lacks any competing functionalities, such as the nitro group in the related compound **99**, it was used for exploring the reduction of the ester group in α -position to the nitrogen atom.

According to the literature procedure,^[283] under an argon atmosphere, the annulated pyrrole **107** was dissolved in dry THF and, once the system was cooled down to 0°C , six equivalents of LiAlH_4 were added (**Scheme 33**).



Scheme 33: Attempt for the reduction of the ethoxycarbonyl groups at the α -position in **107** with LiAlH_4 to obtain the corresponding methyl group in **109**.

After this time, the reaction mixture was then allowed to reach room temperature, and subsequently it was refluxed for ninety-six hours. A change of color was observed, from a dark grey to a bright pink solution; however, TLC analysis revealed the presence of the starting material with a new spot. Thus, after quenching the reaction with a saturated solution of Na_2SO_4 and processing the organic phase through a celite plug eluting with ethyl acetate, the crude residue was purified *via* column chromatography.

The second fraction collected from the column, corresponding to the new spot displayed a faint, aromatic signal region in the $^1\text{H-NMR}$ spectrum.

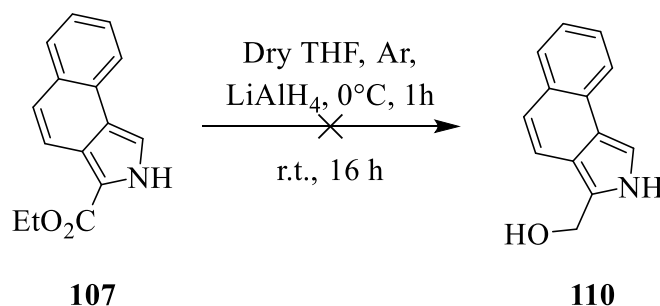
Aside from this apparent discrepancy given by the absence of aromatic peaks, the mass spectrum did not exhibit the peak corresponding to the target structure **109**. Upon analysis of the mass fragmentation, it remained unclear what type of compound may have been formed. Nonetheless, recovering from the column the pure starting material **107** was possible. Hence, the recovered isoindole derivative **107** was reused in the reaction outlined in **Scheme 33**.

The reducing agent induces the reduction from ester to alcohol. According to findings reported in the literature^[279] the intermediate **110**, once formed, undergoes the bond cleavage to methyl at higher temperature.

The reaction (**Scheme 33**) was carried out following the same procedure as earlier mentioned, but in this case, after the first hour at 0°C , the system was allowed to stir at room temperature without reflux. However, it was not possible to isolate the desired product as no conversion of the starting material occurred.

As stated above, the specific reaction outlined in **Scheme 33**, employing the indicated starting **107** is not reported in the literature. As such, it is predictable to observe a different output.

Nonetheless, the protocols used for similar compounds,^[284-286] which should, in principle, enable drawing parallels, described the same procedure performed in this work several times but unsuccessfully.



Scheme 34: Attempt to reduce the ethoxycarbonyl groups at the α -position in **107** with LiAlH_4 to obtain the corresponding alcohol group in **110**.

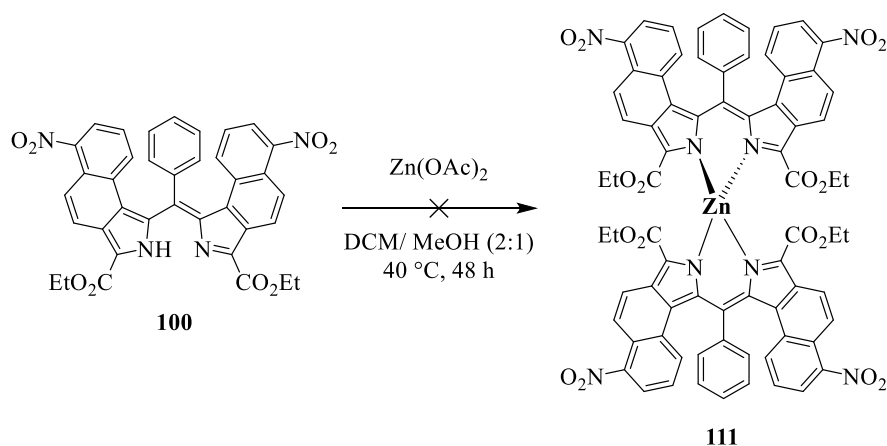
The interest in obtaining the methyl groups in α to the nitrogen atoms composing the core of the benzo [*a*]fused dipyrrens **100** and **108** stemmed from a post-functionalization design, precisely the intention of incorporating functional groups into the system through Knoevenagel condensation.

Taking into account the results shown until now in this work, this strategy, accurately described in §3.2, proved to be the most effective for extending the π -conjugation while simultaneously allowing the complexation of the dipyrriato ligand with different metals. The aromatic styryl moieties attached to the acidic methyl group do not hinder the complexation process, unlike the rigid aryl groups directly linked in the same position, as described in §3.5. Therefore, considering these reaction attempts, different synthetic strategies can be envisaged to achieve the same target.

The benzo [*a*]fused dipyrrens **100** and **108** were subjected to complexation.

According to the procedure already described in §3.4, two equivalents of **100** were dissolved in dichloromethane; a methanolic solution of one equivalent of $\text{Zn}(\text{OAc})_2$ was added to the reaction mixture, which was stirred at room temperature overnight (**Scheme 35**).

Since TLC analysis showed no product conversion, the temperature was increased up to 40 °C. However, after additional twenty-four hours, no product was detected.



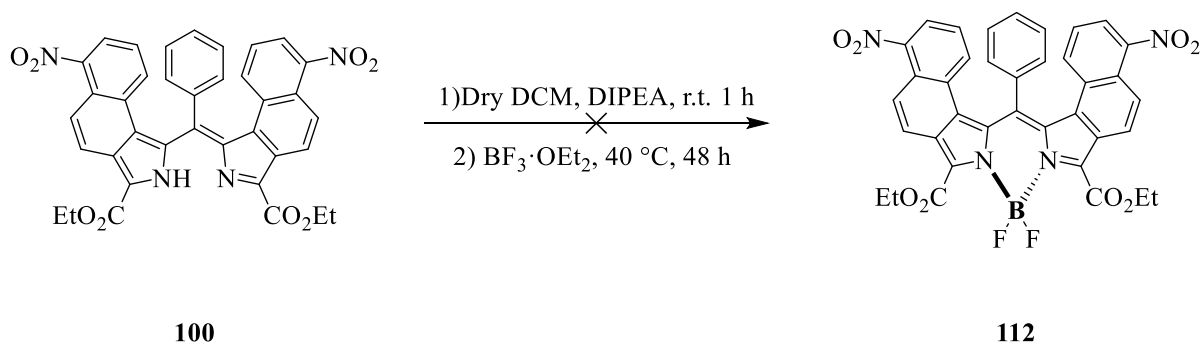
Scheme 35: Synthetic scheme for the attempted complexation reaction of the benzo [*a*]fused dipyrren **100** with $\text{Zn}(\text{OAc})_2$ in DCM at 40 °C to obtain the homoleptic complex **111**.

Simultaneously, it was carried out the complexation with boron difluoride (**Scheme 36**).

Following the same protocol outlined in §3.5.2, N,N-Diisopropylethylamine was added to a solution of benzo [*a*]fused dipyrin **100** in dry dichloromethane and stirred for one hour under an inert atmosphere. Afterwards, (BF₃·OEt₂) was added to the reaction mixture, causing an intensification of the green, the initial reaction color.

The reaction was carried out for two days at 40 °C. TLC analysis attested to the presence of multiple spots; thus, the reaction was stopped, and after workup, the crude residue was subject to purification *via* column chromatography.

The desired product was not obtained from any of the collected fractions.

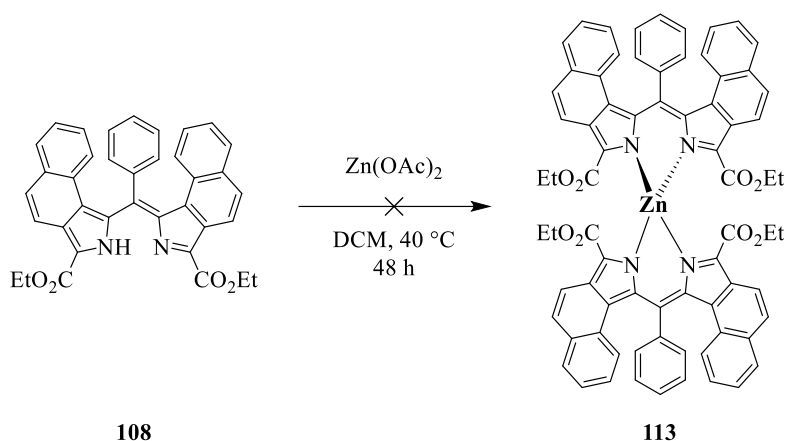


Scheme 36: Synthetic scheme for the attempted complexation reaction of the benzo [*a*]fused dipyrin **100** with BF₃·OEt₂ to obtain the BODIPY **112**.

Analogously, two equivalents of **108** dissolved in dichloromethane were added to a methanolic solution of Zn(OAc)₂ and stirred for forty-eight hours at 40 °C (**Scheme 37**).

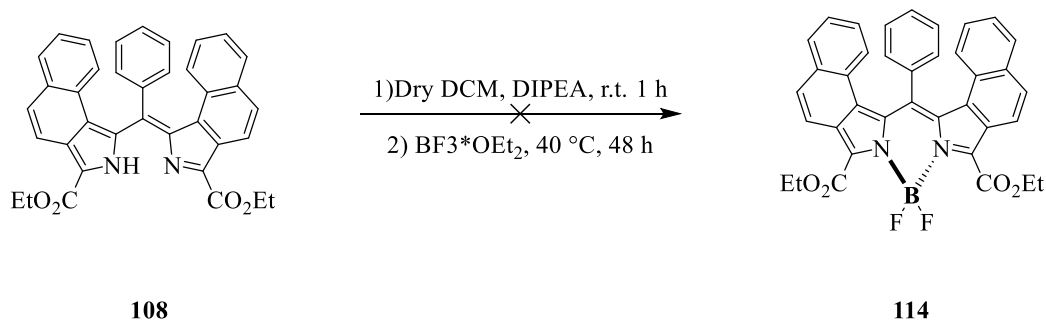
In control TLC, there was no trace of the starting material, so after the removal of the solvent, the crude residue was purified through column chromatography.

Despite this, the NMR and mass analyses of each collected fraction revealed the absence of the desired product.



Scheme 37: Synthetic scheme for the attempted complexation reaction of the benzo[*a*]fused dipyrin **108** with Zn(OAc)_2 in DCM at 40°C to obtain the homoleptic complex **113**.

Similar to what was observed for compound **100**, the complexation of **108** with boron difluoride did not yield the desired product **114** (**Scheme 38**).



Scheme 38: Synthetic scheme for the attempted complexation reaction of the C-benzo[*a*]fused dipyrin **108** with Zn(OAc)_2 in DCM at 40°C to obtain the BODIPY **114**.

Although elevated temperatures were not employed, an important factor to consider, it is still unclear why the complexation, especially with boron difluoride, did not occur. Filatov *et al.*^[287] reported a complexation *in situ* by adding Zn(OAc)_2 to a solution of the analogous free-base 5-(4-methoxycarbonylphenyl)-1,9-di(ethoxycarbonyl)dinaphtho[2,3-*b,g*]dipyrromethene in DMF. The reaction needs to be repeated under these particular conditions. Ongoing investigations are underway to determine whether the two-novel benzo[*a*]fused dipyrins **100** and **108** adopt the specific conformation illustrated in the previous schemes or if the steric hindrance has led to the formation of different isomers which inhibit the complexation.

3.7.2 Benzo[*a*]fused systems with an imine in *meso* position

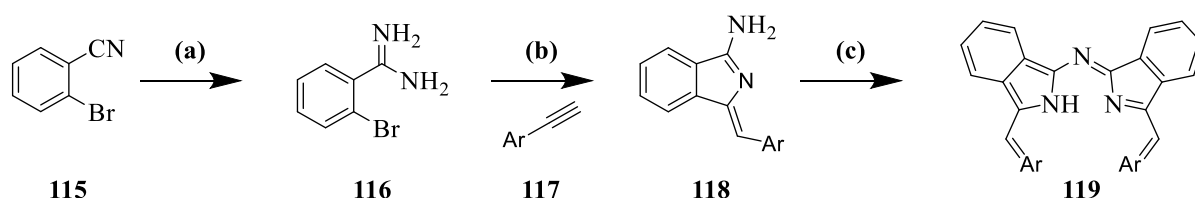
The synthesis of aza-diisoindolmethines reported in the literature starts from phthalonitrile derivatives.^[262]

According to the Lukyanets' method^[288] described in **Scheme 39**, the synthesis entails nitrile cascade reactions, where the final step leads to the formation of a dimeric intermediate, the generic benzo[*a*]-fused azadipyrin **119**. In the first step, the nitrile group is converted into amidine.

This can be achieved using various methodologies, including exchange reactions of halodiazirines,^[289] conversion to tris(trimethylsilyl)amidines,^[290] or preparation of amidine salts by reaction of nitriles with ammonium salts in the presence of ammonia.^[291]

The second step is the conversion of the benzamidine derivative **116** into the aryl-aminoindolene **118** through a domino reaction involving a domino (copper-free) Sonogashira coupling with an appropriate aryl alkyne **117** and cycloisomerization under heating.^[292]

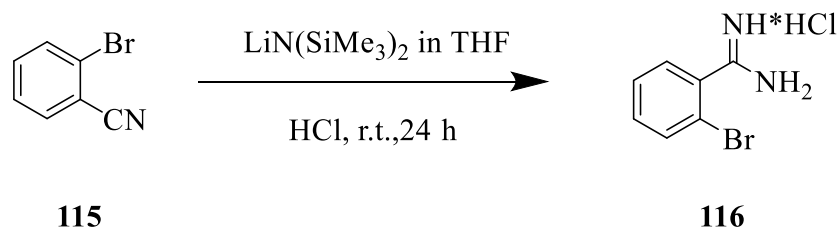
The transformation from **118** into **119** is initiated by a reduction step mediated by formamide, according to the Leuckart-Wallack reaction process.^[293]



Scheme 39: Synthetic pathway to obtain the benzo [*a*]fused azadipyrin synthon **118** according to Lukyanets' method.^[288] (a) Conversion of amidine from nitrile derivatives^[289–291] (b) domino Cu-free Sonogashira coupling with an aryl compound **117** and consequent cycloisomerization.^[292] (c) Leuckart-Wallack condensation with formaldehyde.^[293]

Following the method reported by Dalai *et al.*^[294] for the conversion of the nitrile group to tris(trimethylsilyl)amidines, a solution of 2-bromobenzonitrile **115** in dry THF was added to a solution of lithium bis(trimethylsilyl)amide $\text{LiN}(\text{SiMe}_3)_2$ (1 M in dry THF).

The reaction mixture was stirred at room temperature for four hours (**Scheme 40**).

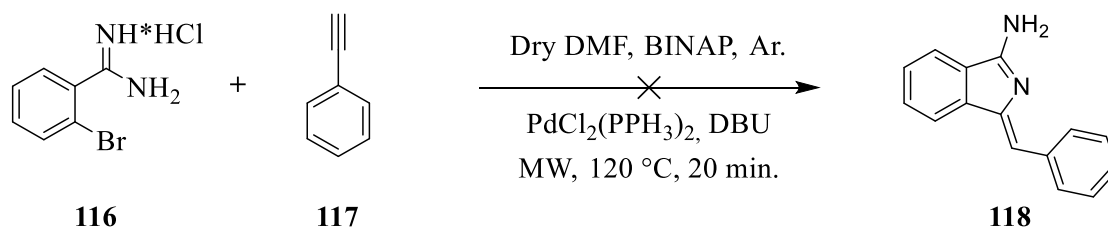


Scheme 40: Synthetic scheme for converting 2-bromobenzonitrile **115** into the 2-bromobenzimidamide hydrochloride **116** by treatment with LiHDMS followed by HCl workup.

After this time, the system was cooled to 0°C , and a solution of HCl (5M in isopropanol) was added to the reaction mixture, which was stirred for additional twenty hours. The precipitate formed was recrystallized to yield the 2-bromobenzimidamide hydrochloride salt **116** as a white solid, with a 54 % yield.

Thus, it was employed in the second step of the synthesis, which involved the reaction described in **Scheme 41**.

According to the literature procedure,^[292] a mixture of compound **116**, 2,2'-bis(diphenylphosphino)-1,1'-binaphthyl (BINAP) and bis(triphenylphosphine)palladium(II) dichloride $\text{PdCl}_2(\text{PPh}_3)_2$ was sealed in a microwave vessel and purged with argon.



Scheme 41: Synthetic attempt for the microwave-assisted Cu-free Sonogashira coupling-cycloisomerization domino reaction from the 2-bromobenzimidamide hydrochloride salt **116** to obtain (Z)-1-benzylidene-1H-isoindol-3-amine **118**.

Then, a solution of phenylacetylene **117** in dry DMF was added to the reaction mixture with DBU. The reaction mixture was purged with argon for five minutes and then irradiated in a microwave reactor at 120 °C for twenty minutes.

The formation of the product was not observed. It is considered appropriate to repeat the reaction by changing the Pd source or consider to use a co-catalysator.

3.7.3 Benzo[*b*]fused systems with aryl groups in *meso* position

Indole has a bicyclic structure consisting of a benzene fused with a pyrrole ring; therefore, in principle can be perceived as a benzannulated pyrrole.

This consideration led to the condensation reactions depicted in **Scheme 42**.

It was thus hypothesized that 3-methyl-1*H*-indole **117** could also undergo a condensation reaction with an aromatic aldehyde to yield the resultant benzo [*b*]fused dipyrin. An initial condensation attempt occurred between indole **117** and benzaldehyde **2** in dichloromethane at 40 °C.

In contrast to the findings observed for pyrroles **1** in §3.1.1 and **66** in §3.5.1, the condensation reaction did not proceed in dichloromethane.

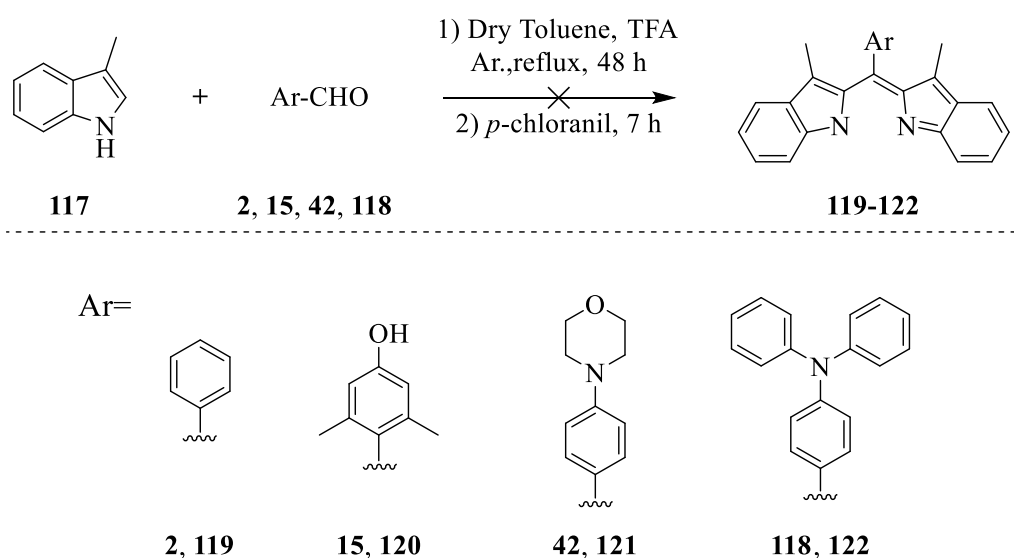
Recognizing the potential difficulty laid by the aromaticity of indole, this system was abandoned, and was chosen a solvent that allows for higher reaction temperatures to be employed.

As outlined in **Scheme 42**, indole **117** and benzaldehyde **2** were dissolved in dry toluene under an argon atmosphere in the presence of TFA as a catalyst. The reaction was refluxed for forty-eight hours. TLC analysis confirmed the conversion of the starting benzaldehyde **2** and the concurrent formation of various reaction products.

After the workup, purification was carried out using column chromatography. A dichloromethane gradient with a significant percentage of methanol had to be used to isolate all the fractions.

None of the analyzed fractions showed the corresponding mass of the product.

To verify the purpose of the reaction, the scope was broadened by using different aldehydes with different degrees of electrophilicity (**Scheme 42**). In each reaction performed, the conversion of the starting material was observed, resulting in the formation of several spots on TLC, many of which exhibited high luminescence. Nevertheless, solubility issues hampered the purification process, and none of the collected fractions yielded the desired benzo [*b*]fused dipyrrens **119-122**.



Scheme 42: Attempts for the condensation reaction between 3-methyl-1*H*-indole **117** and different aromatic aldehydes to obtain the benzo [*b*]fused dipyrrens **119-122**.

3.7.4 Benzo [*b*]fused system with aza group in *meso* position

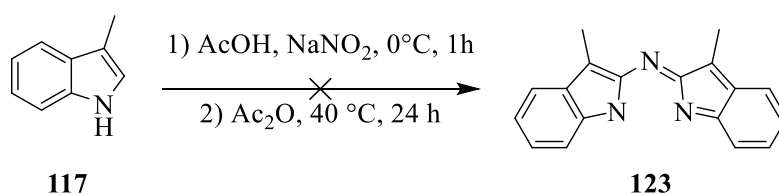
In connection, 3-methyl-1*H*-indole **117** was subjected to the procedure developed by Carreira *et al.* ^[262] detailed in §3.6.

Although compound **123** has not been documented in the literature, it was conceived that the increased conjugation in the starting indole **123** could render it amenable to this type of reaction, unlike the simple pyrrole **1** reported in §3.6.2.

As outlined in **Scheme 43**, sodium nitrite was added at 0°C to a solution of **117** dissolved in glacial acetic acid. It was observed that an intense change of color from pale yellow to red.

After approximately one hour, another equivalent of **117** dissolved in acetic anhydride was incorporated into the reaction mixture, which was heated at 40 °C for twenty-four hours. TLC analysis of the crude reaction mixture, which turned color to intense blue, showed the conversion of the starting material and the presence of multiple spots.

Therefore, the crude residue was subjected to column chromatography packed on alumina gel. The target benzo[*b*]fused aza-dipyrrin **123** was not found in any collected fractions.



Scheme 43: Synthetic scheme for obtaining the benzo[*b*]fused aza-dipyrrin **123** starting from 3-methyl-1*H*-indole **117**.

3.8 Applications in bio-imaging

The remarkable photophysical properties showed by the heteroleptic bis(dipyrinato)Zn^{II} complexes described in §3.4, such as their emission up to 800 nm, perfectly fitting in the *biological window*, supported by their enhanced quantum yields in DMSO and exceptional stabilities, envisaged their great potential for utilisation in bioimaging applications.

In this paragraph are presented the results obtained in collaboration with M.Sc. Dominik Feser and Prof. Ute Schepers (Institute of Functional Interfaces, KIT) (§3.8.1, 3.8.3), Dr. Enrico Lemma (Zoological Institute, Cell and Neurobiology, KIT) (§3.8.3), Dr. Sergiy Afonin and Prof. Anne Ulrich (Biochemistry and Molecular Biophysics, KIT) (§3.8.4).

3.8.1 Cell viability tests

One of the distinguishing factors that sets biomaterials apart from any other material is their ability to interact with human tissues without causing significant harm.^[295] There are many ways in which materials and tissues can interact, potentially affecting their coexistence. These interactions generally fall under the broad topic of “biocompatibility”, which is a crucial aspect to consider when developing new compounds intended for biological applications.

The term biocompatibility is widely used in the field of biomaterials science, but there remains a significant level of uncertainty regarding its precise definition and the underlying mechanisms.^[296] There are several definitions associated to the above-mentioned term, leading to different paradigms. However, none of these provide a universal definition that can be applied to all materials.

Since our study is still in its initial stage and it has not included yet the implementation of our tailor-made probes in more sophisticated systems, considering Dorland’s definition appears to be reasonable in this context, which states that biocompatibility is “*the quality of not having toxic or injurious effects on biological systems*”.^[297] This definition does not consider the potential interaction between the host tissue and the compound under analysis. Nevertheless, as mentioned before, in this context is adequately suitable.

Cell viability and proliferation rates are reliable indicators of cell health, and various *in vitro* assays, based on these parameters, are commonly used to assess the cytotoxicity of a specific compound.^[298] Colorimetric assays are widely utilised and can be conducted explicitly on

adherent and suspended cell lines. These assays operate by measuring the intensity response of a biochemical marker: specific reagents form coloured products depending on the viability of cells, allowing the colorimetric measurement of cell viability using a spectrophotometer.^[299]

The MTT assay was employed in this work. First described by Mosmann,^[300] the (3-(4,5-dimethylthiazol-2-yl)-2'-5'-diphenyltetrazolium bromide (MTT), is an enzyme-test based on the determination of specific functions, predominantly mitochondrial dehydrogenases^[300] and succinate dehydrogenase^[301,302] which are detectable only in the metabolically active cells. MTT assays were carried out using HeLa and HepG2 cell lines. They are both immortal cancer cell lines but originate from different tissues: the first from the cervical and the second from liver cells.

In this study the values of cell viability will not be evaluated by comparison with other systems, as standardization is not feasible in this regard. Instead, our focus will be on evaluating the values obtained within the compounds analyzed and, if applicable, making a comparison among them.

In **Table 13** are reported the cell viability values measured for HeLa and HepG2 cells incubated with the plain dipyrrens **11-15**, **17**, **19** for 72 hours in four different concentrations, ranging from 1 μ M to 7.5 μ M.

Compounds **11-13** exhibit good viability values (**Table 13**), which gradually decrease as the concentration increases, ranging from ca. 90% to 60%.

The plain dipyrren **14** shows a more pronounced decrease, halving the cell viability values from 81 % at 1 μ M to approximately 46 % at 7.5 μ M. Dipyrren **15** is the least toxic, with viability values exceeding 100 %, indicating cellular proliferation. On the contrary, dipyrren **17** displays the highest toxicity, with viability values dropping to 9% in HeLa cells. Interestingly, in HepG2 cells, the highest concentration of the same compound, **17**, retained 36 % of cell viability. The plain dipyrren **19** displays low biocompatibility, 50 %, already at 1 μ M, although it experiences only slight decreases as the concentration rises.

Drawing an accurate correlation between these values and the structures of the plain dipyrrens investigated could be speculative and not precise. Nonetheless, it can be underlined that the most biocompatible plain dipyrren examined is the **15**, bearing the 4-hydroxy-3-methoxy-phenyl group at the *meso* position; thus, the hydroxyl group may have played a role in this regard.

Conversely, the most cytotoxic plain dipyrrens, **17** and **19**, consist of a naphthyl and an anthracenyl group at the *meso* position. Therefore, extra-aromatic rings could potentially have introduced additional toxicity to the system.

Table 13: Percentage values of cell viability and relative standard deviation measured through MTT assays for HeLa and HepG2 cells after 72 hours of incubation with solutions of the plain ligands **11-15**, **17,19** in DMSO at different concentrations.

Plain Ligand	Cell viability % HeLa Cells				Cell viability % HepG2 Cells			
	1 μ M	2.5 μ M	5 μ M	7.5 μ M	1 μ M	2.5 μ M	5 μ M	7.5 μ M
11	88.7 \pm 4.2	87.9 \pm 6.0	87.8 \pm 3.1	77.2 \pm 4.1	90.7 \pm 3.0	90.7 \pm 3.0	88.6 \pm 9.6	86.1 \pm 7.9
12	86.9 \pm 1.7	82.5 \pm 3.2	74.6 \pm 3.9	60.9 \pm 2.3	74.0 \pm 0.6	74.0 \pm 0.6	83.5 \pm 6.2	74.1 \pm 2.8
13	86.7 \pm 2.3	87.6 \pm 0.7	83.4 \pm 3.5	80.1 \pm 6.3	86.8 \pm 3.8	86.8 \pm 3.8	86.4 \pm 6.9	74.4 \pm 6.6
14	81.8 \pm 8.3	67.6 \pm 11.5	58.1 \pm 0.2	46.1 \pm 1.9	81.8 \pm 8.3	78.8 \pm 4.3	58.1 \pm 0.2	46.1 \pm 1.9
15	130.6 \pm 3.8	126.5 \pm 2.7	122.2 \pm 4.3	103.7 \pm 2.1	95.8 \pm 4.8	95.8 \pm 4.8	98.5 \pm 2.3	92.3 \pm 3.3
17	73.0 \pm 3.7	43.8 \pm 5.3	16.1 \pm 2.9	9.7 \pm 1.8	76.8 \pm 6.4	76.8 \pm 6.4	41.7 \pm 4.0	35.9 \pm 1.8
19	50.7 \pm 6.7	50.6 \pm 6.7	43.7 \pm 0.2	38.5 \pm 0.3	69.8 \pm 2.1	69.8 \pm 2.1	49.7 \pm 2.5	42.6 \pm 2.3

Analogously, in **Table 14** are reported the cell viability values measured for HeLa and HepG2 cells incubated with the π -expanded dipyrrens **34**, **38**, **39**, and **44** for 72 hours in four different concentrations from 1 μ M to 7.5 μ M.

The π -expanded ligand **34** shows good cell viability values across all concentration ranges and in both cell lines. Paradoxically, compound **38**, derived from the expansion of dipyrren **17**, previously observed as one of the most toxic plain dipyrrens, turns out to be the least harmful, with biocompatibility values up to 98% at 7.5 μ M. The π -expanded ligand **39** manifests more pronounced toxicity in both cell lines. Similar to **15**, its corresponding functionalised π -expanded dipyrren **44** demonstrated good biocompatibility values, from 8% to 73 % in both cell lines.

In this case, providing explanations regarding a potential correlation between structure-biocompatibility/cytotoxicity would also be speculative. It would be interesting to investigate

the mechanism by which some dipyrrens inhibit vital cellular processes compared to others. However, this study is beyond the scope of this thesis.

Table 14: Percentage values of cell viability and relative standard deviation measured through MTT assays for HeLa and HepG2 cells after 72 hours of incubation with solutions of the π -expanded ligands **34**, **38**, **39**, **44** in DMSO at different concentrations.

Expanded Ligands	Cell viability % HeLa Cells				Cell viability % HepG2 Cells			
	1 μ M	2.5 μ M	5 μ M	7.5 μ M	1 μ M	2.5 μ M	5 μ M	7.5 μ M
34	80.3 \pm 2.6	74.8 \pm 1.8	64.9 \pm 2.5	68.9 \pm 3.2	81.5 \pm 2.3	75.3 \pm 4.9	68.5 \pm 3.6	75.9 \pm 5.6
38	100.5 \pm 1.5	93.1 \pm 0.8	96.7 \pm 4.9	98.7 \pm 5.9	80.8 \pm 4.5	85.8 \pm 4.9	89.6 \pm 3.1	85.3 \pm 4.8
39	51.9 \pm 1.2	37.6 \pm 1.5	33.0 \pm 1.8	29.2 \pm 3.7	52.7 \pm 3.9	50.7 \pm 3.2	42.9 \pm 2.2	33.5 \pm 7.5
44	80.4 \pm 4.1	79.5 \pm 2.5	74.8 \pm 1.3	73.1 \pm 3.2	87.4 \pm 1.4	85.3 \pm 1.2	80.1 \pm 1.3	78.5 \pm 2.8

Once the biocompatibility of the ligands was determined, the same measurements were carried out for the corresponding heteroleptic complexes.

Hereafter are reported the cell viability values measured for HeLa (**Table 15**) and HepG2 (**Table 16**) cells incubated with the heteroleptic bis(dipyrrinato)Zn^{II} complexes **54-64** for 72 hours in six different concentrations from 1 μ M to 20 μ M.

In **Table 15**, one feature that stands out is the remarkably high biocompatibility of the values reported among all the investigated complexes. Except for complex **54**, showing increased toxicity at 20 μ M, all the other compounds at the same concentration exhibit biocompatibility values up to 77%.

The survival rate of HeLa cells treated with complexes solution with a concentration equal to 10 μ M decreases but remains exceptionally high, from 114 % for compound **58** to 72 % for compound **54**. As expected, the biocompatibility values are significantly increased at lower compound concentrations, such as 1 and 2.5 μ M, often exceeding 100 %.

Table 15: Percentage values of cell viability and relative standard deviation measured through MTT assays for HeLa cells after 24 hours of incubation with solutions of the heteroleptic bis(dipyrrinato)Zn^{II} complexes **54-64** in DMSO at different concentrations.

Heteroleptic complexes	Cell viability % HeLa Cells					
	1 μ M	2.5 μ M	5 μ M	7.5 μ M	10 μ M	20 μ M
54	100.6 \pm 1.2	93.1 \pm 0.9	82.8 \pm 4.2	74.2 \pm 3.9	71.6 \pm 3.6	53.4 \pm 2.9
55	82.1 \pm 2.9	86.1 \pm 3.5	81.1 \pm 3.5	82.3 \pm 4.2	93.3 \pm 2.5	93.1 \pm 2.9
56	113.1 \pm 2.4	107.7 \pm 7.5	103.4 \pm 3.1	87.8 \pm 4.3	89.5 \pm 1.9	77.3 \pm 1.2
57	111.7 \pm 2.8	110.0 \pm 2.8	84.7 \pm 3.7	100 \pm 2.6	93.0 \pm 1.3	84.1 \pm 1.1
58	129.4 \pm 7.2	139.1 \pm 8.5	123.5 \pm 9.1	117.3 \pm 5.4	114.0 \pm 5.4	97.0 \pm 4.8
59	99.1 \pm 7.8	93.4 \pm 2.9	86.0 \pm 1.0	90.0 \pm 2.5	93.3 \pm 2.5	93.1 \pm 2.9
60	88.8 \pm 0.8	84.7 \pm 1.4	86.7 \pm 3.1	84.2 \pm 2.8	96.9 \pm 1.9	92.1 \pm 1.9
61	96.6 \pm 1.8	99.9 \pm 5.2	99.7 \pm 1.9	97.6 \pm 2.7	94.2 \pm 1.8	88.5 \pm 0.4
62	100.9 \pm 4.3	93.3 \pm 2.7	80.3 \pm 1.5	70.1 \pm 3.5	96.9 \pm 1.9	92.1 \pm 1.9
63	82.2 \pm 9.1	87.9 \pm 3.5	83.7 \pm 1.0	80.0 \pm 1.5	90.7 \pm 1.9	87.7 \pm 0.7
64	97.2 \pm 3.3	96.5 \pm 1.8	96.9 \pm 1.8	94.4 \pm 3.1	93.1 \pm 2.4	86.9 \pm 3.8

A similar trend is also observed with the HepG2 cell line (**Table 16**). One notable exception is the heteroleptic complex **62**, which is the most toxic for this cell line, while retaining a compatibility value of 67 % at 20 μ M.

Table 16: Percentage values of cell viability and relative standard deviation measured through MTT assays for HePG2 cells after 24 hours of incubation with solutions of the heteroleptic bis(dipyrrinato)Zn^{II} complexes **54-64** in DMSO at different concentrations.

Heteroleptic complexes	Cell viability % HepG2 Cells					
	1 μ M	2.5 μ M	5 μ M	7.5 μ M	10 μ M	20 μ M
54	104.2 \pm 4.0	100.9 \pm 2.6	91.5 \pm 8.8	89.9 \pm 2.3	84.5 \pm 5.9	83.9 \pm 2.7
55	79.6 \pm 4.5	82.6 \pm 3.3	79.2 \pm 3.0	84.1 \pm 4.7	89.2 \pm 2.0	98.9 \pm 3.6
56	95.2 \pm 4.3	108.2 \pm 5.9	102.3 \pm 2.8	103.6 \pm 4.5	99.2 \pm 3.4	91.6 \pm 2.0
57	124.2 \pm 4.3	120.1 \pm 2.7	107.9 \pm 2.8	103.6 \pm 4.5	101.4 \pm 1.6	95.7 \pm 1.1
58	99.3 \pm 6.6	100.5 \pm 3.7	88.6 \pm 5.5	86.9 \pm 5.7	86.9 \pm 2.8	75.3 \pm 3.4
59	84.5 \pm 5.1	83.8 \pm 2.2	84.7 \pm 0.5	81.9 \pm 6.6	82.3 \pm 2.1	81.1 \pm 1.6
60	87.4 \pm 2.2	86.7 \pm 3.4	87.4 \pm 3.9	85.8 \pm 6.2	90.6 \pm 9.2	93.9 \pm 3.7
61	107.3 \pm 2.6	115.1 \pm 4.8	110.8 \pm 3.6	108.4 \pm 2.7	109.44 \pm 3.7	99.2 \pm 3.5
62	87.3 \pm 2.5	93.6 \pm 1.8	82.9 \pm 2.6	81.4 \pm 3.4	71.7 \pm 5.4	67.0 \pm 7.1
63	72.9 \pm 3.1	78.7 \pm 3.0	79.3 \pm 4.4	81.0 \pm 4.1	94.2 \pm 3.3	90.7 \pm 1.1
64	108.9 \pm 2.2	97.4 \pm 4.5	76.6 \pm 1.2	95.0 \pm 5.8	96.4 \pm 1.7	89.0 \pm 3.9

The most significant finding of these tests is the clear distinction between the ligands, either plain or π -expanded and the corresponding heteroleptic complexes. The higher biocompatibility of the complexes compared to the ligands highlights the positive impact of the central metal zinc, which further confirms its intrinsic compatibility as an essential element in the human body.^[180]

Furthermore, the stability of the heteroleptic complexes in highly polar medium, such as the cellular environment, is validated. Indeed, if the heteroleptic complexes were unstable, the recorded compatibility values would be comparable to those reported for the ligands in **Tables 13 and 14**.

Nevertheless, these colorimetric assays present intrinsic limitations correlated to external factors that may impact the outcome.^[298] Therefore, it should be regarded as a screening tool that can provide a basic understanding.

3.8.2 Photophysical insights

Once the biocompatibility of the complexes was confirmed, the focus of our investigation shifted to five specific heteroleptic bis(dipyrrinato)Zn^{II} complexes, whose structures are depicted in **Figure 68**.

They were selected based on their highest quantum yields in DMSO, specifically $\Phi = 44\%$ for **57**, 46% for **58**, 51% for **60** and 38% for **61**. Despite having a quantum yield of only 5%, for the reasons deeply explained in §3.4.2, the heteroleptic complex **56** was included in this selection due to its high solubility in methanol, attributed to the presence of the methoxyl and hydroxyl groups in the structure. Thus, it was deemed appropriate to investigate whether the higher hydrophilicity could compensate for the lower quantum yield in DMSO.

Predicting the microscopy of cells incubated with a dye involves understanding the properties of the dye and its interaction with the cells. Therefore, specific analyses were conducted to closely mimic the photophysical properties of the complexes in the cells environment before proceeding with cell microscopy.

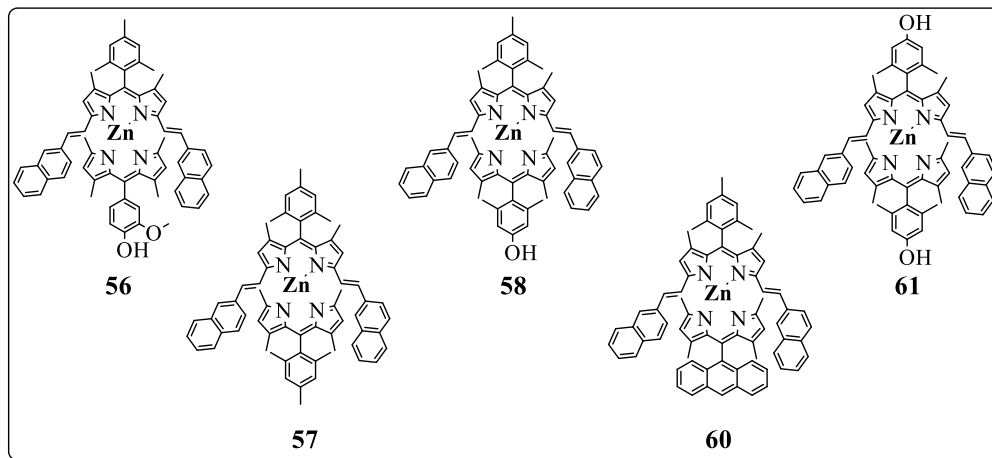


Figure 68: Chemical structures of the heteroleptic bis(dipyrrinato)Zn^{II} complexes **56**, **57**, **58**, **60**, **61** chosen for a deeper investigation of the photophysical properties for their exploitation in bioimaging.

The absorption, excitation and emission spectra recorded in DMSO at 20 °C are shown in **Figure 69**. As previously mentioned in §3.4.2, these profiles exhibit a similar pattern across the various heteroleptic complexes. The noteworthy properties to highlight, particularly for their relevance in bioimaging, are the prominent emission maxima falling within the range of

634 nm to 640 nm and the large *pseudo*-Stokes shift up to $4.66 \cdot 10^3 \text{ cm}^{-1}$, which is an appealing feature in this type of application.

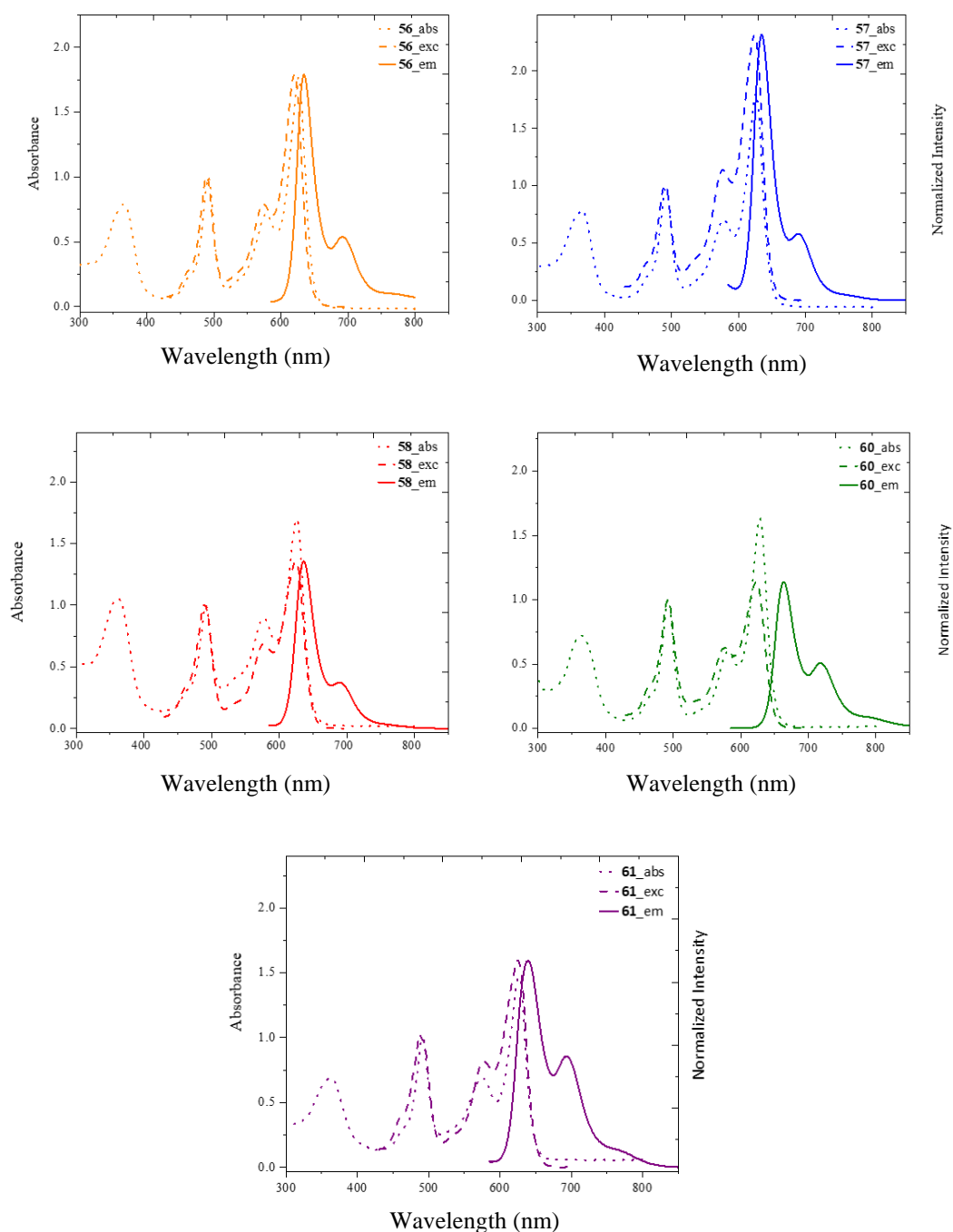


Figure 69: UV/Vis absorption (dotted plot), excitation (dashed plot, $\lambda_{\text{exc}} = 710 \text{ nm}$) and emission (solid plot, $\lambda_{\text{em}} = 570 \text{ nm}$) spectra of the heteroleptic bis(dipyrrinato) Zn^{II} complexes **56**, **57**, **58**, **60**, **61** in spectroscopic DMSO at $20 \text{ }^\circ\text{C}$. Reprinted from R. Tabone, D. Feser, E. D. Lemma, U. Schepers, C. Bizzarri, *Front. Chem.* **2021**, 9:754420.

To further confirm the excitation wavelength independency of the emissive state of the selected heteroleptic complexes, the lifetime of the heteroleptic bis(dipyrrinato) Zn^{II} complexes **56**, **57**, **58**, **60**, **61** were measured by Time-Correlated Single Photon Counting (TCSPC), by using

three different excitation wavelengths (455, 570 and 625 nm) (**Figure 70**). The baseline shows variations depending on the excitation laser wavelength because of the signal/noise ratio differences arising from scattering and other sources.

However, the single exponential decay curves remain unaffected by changing the excitation wavelength of the NanoLED source employed.

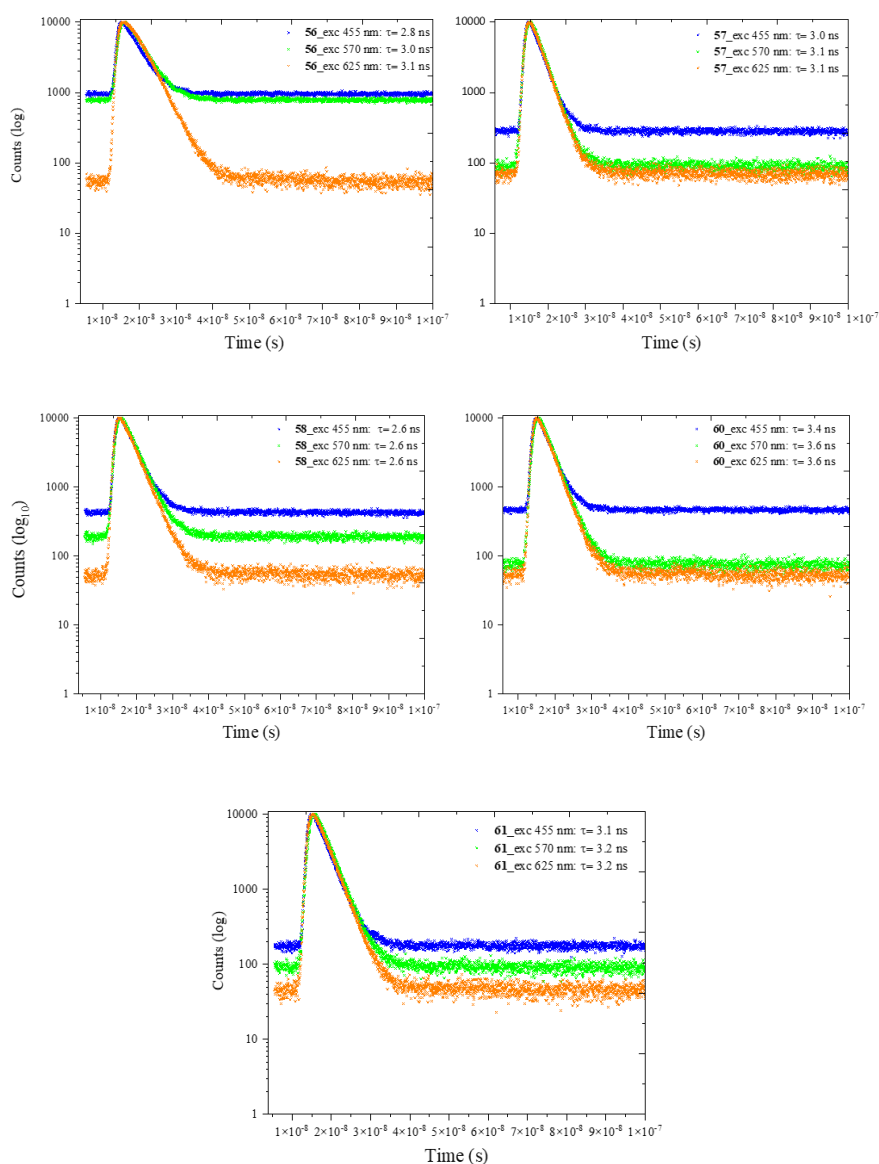


Figure 70: Fluorescence lifetimes of the heteroleptic bis(dipyrrinato)Zn^{II} complexes **56**, **57**, **58**, **60**, **61** in DMSO measured by TCSPC, exciting with NanoLED source at three different excitation wavelengths (λ_{exc} 455, 570, 625 nm). Reprinted from R. Tabone, D. Feser, E. D. Lemma, U. Schepers, C. Bizzarri, *Front. Chem.* **2021**, 9:754420.

The cell culture environment encompasses the various conditions established through specific laboratory protocols to support their growth, proliferation, and maintenance. Nutrients play a vital role in supporting the growth and metabolic activities of cells. Specific cell culture media such as DMEM (Dulbecco's Modified Eagle's Medium) are utilised to meet the nutritional requirements of cells.

As outlined in **Figure 71a**, the absorption profiles of the investigated heteroleptic bis(dipyrrinato) Zn^{II} complexes **56**, **57**, **58**, **60**, **61** in DMEM experience an increase in the intensity of the bands at 300-400 nm, localised on the vinyl naphthyl moieties, and the bands at 550-700 nm due to the ¹ π - π transition localised on the π -expanded unit. The corresponding emission profile, shown in **Figure 71b**, shows a peak that remains almost at the same position as that measured in DMSO (**Figure 69**). However, variations in the emission shoulder around 700 nm appear less intense and, in compound **61** (violet plot, **Figure 71b**), is notably hypsochromically shifted.

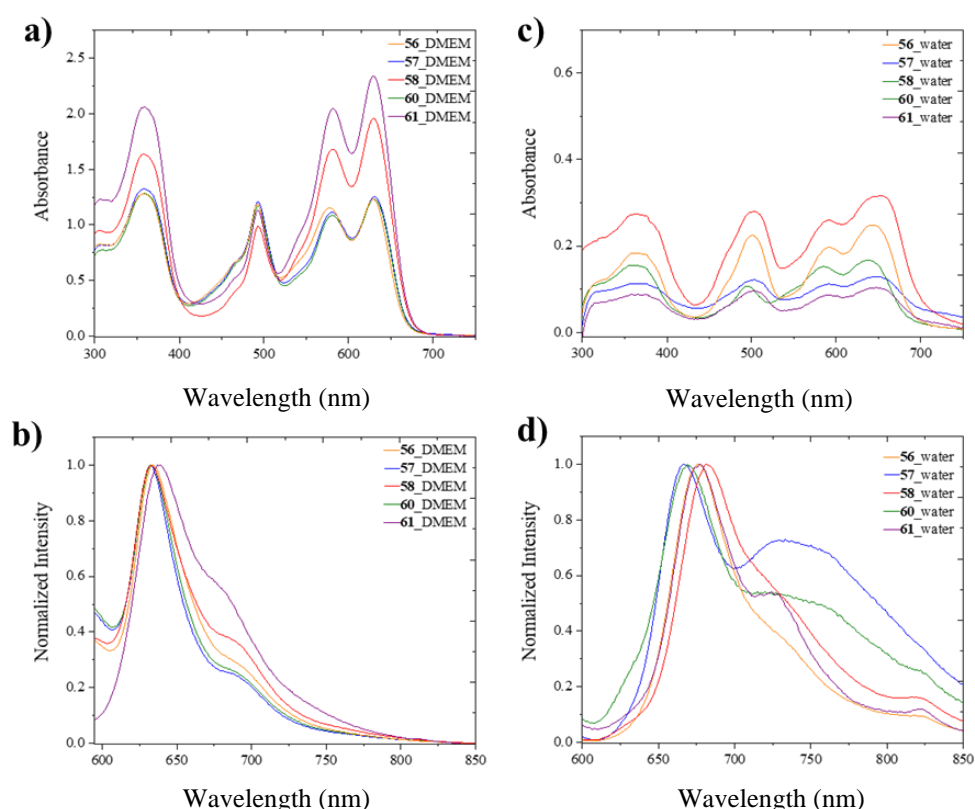


Figure 71: Photophysics of the heteroleptic bis(dipyrrinato)Zn^{II} complexes in DMEM and water. (a) UV/Vis absorption and (b) emission ($\lambda_{\text{exc}} = 570$ nm) spectra of complexes **56**, **57**, **58**, **60**, **61** (20 μM in DMSO) in DMEM (Dulbecco Modified Eagle Medium, supplemented with 10% of FCS). (c) UV/Vis absorption and (b) emission ($\lambda_{\text{exc}} = 570$ nm) spectra of complexes **56**, **57**, **58**, **60**, **61** (20 μM in DMSO) in distilled water. Reprinted from R. Tabone, D. Feser, E. D. Lemma, U. Schepers, C. Bizzarri, *Front. Chem.* **2021**, 9:754420.

Since DMEM is formulated to contain a balanced combination of essential nutrients, including carbohydrates, proteins, lipids, vitamins, minerals and amino acids, insoluble aggregates may have formed, leading to the quenched quantum yield experienced by the complexes, as reported in **Table 17**.

Water is the predominant solvent within cells, essential for maintaining cellular homeostasis and facilitating various biological processes.

The absorption profiles the investigated heteroleptic bis(dipyrrinato) Zn^{II} complexes **56**, **57**, **58**, **60**, **61** in water, reported in **Figure 71c**, display broadening of the characteristic bands, which have lower and comparable intensities.

Similarly to what was observed in DMEM, the corresponding emission profiles in **Figure 71d** manifest alterations concerning the emission shoulder at around 700 nm, with noticeably higher intensity observed for compounds **57** and **60**. Complex **61** retains its typical morphology, with an additional tiny peak observed at approximately 825 nm. The broadening of the emissive profile is the result of fluctuations in the solvation shell structure of the water surrounding the complex molecules.

The complexes-water interactions affect the electronic transitions and energy levels, leading to an observable shift of the maximum emission of all the complexes shift toward longer wavelength with emission maxima at about 670 nm (**Table 17**). The quantum yield of the complexes in water is dramatically decreased, registering values of around 1%. (**Table 17**).

Table 17: Photophysical properties of the heteroleptic bis(dipyrrinato) Zn^{II} complexes **56**, **57**, **58**, **60**, **61** in ^[a] DMEM and ^[b] water. ^[c] Quantum yields were determined by the relative method, using cresyl violet ($\Phi = 0.54$ in MeOH, 22°C).^[303]

Complex	λ_{em} [nm]	$\Phi^{[c]}$ (%)
56	635 ^[a] , 676 ^[b]	1.0 ^[a] , 0.6 ^[b]
57	633 ^[a] , 666 ^[b]	1.9 ^[a] , 0.8 ^[b]
58	634 ^[a] , 681 ^[b]	2.0 ^[a] , 1.7 ^[b]
60	637 ^[a] , 669 ^[b]	1.6 ^[a] , 0.6 ^[b]
61	636 ^[a] , 677 ^[b]	3.1 ^[a] , 0.8 ^[b]

The pH of the cell culture medium is carefully regulated and maintained at a physiological level, usually around pH 7.4, using a buffer system and a standard gas mixture of 5% of CO₂ in the incubator. However, the pH can vary in the cellular environment depending on the organelle or cellular compartment.

For this reason, the absorption spectra of the investigated heteroleptic bis(dipyrrinato) Zn^{II} complexes **56**, **57**, **58**, **60**, and **61** were measured at acidic pH values of 3.3 and 5.0. As can be noticed in **Figure 72**, the absorption bands display variations in intensity, but they show the characteristic profile which was reported so far.

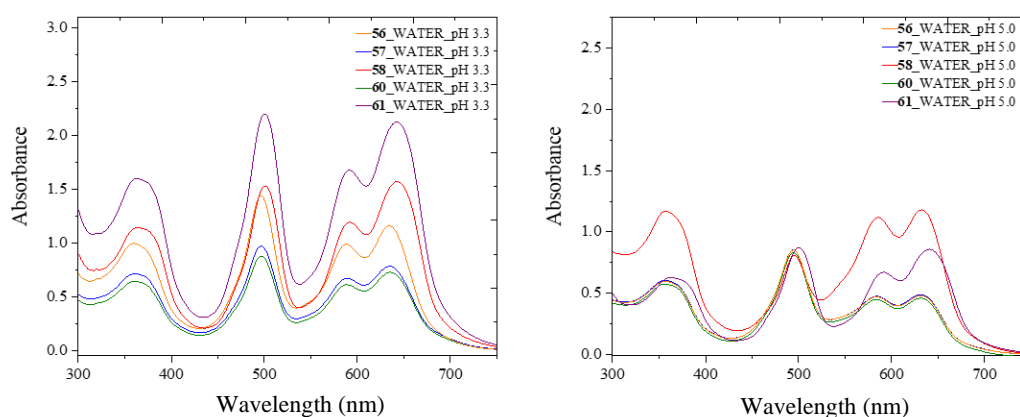


Figure 72: UV/Vis absorption spectra of the heteroleptic bis(dipyrrinato) Zn^{II} complexes **56**, **57**, **58**, **60**, **61** (20 μ M in DMSO) in water at different pH (3.3 and 5.0). The pH was adjusted by using some drops of HCl.

The temperature at which cells are cultivated is another essential factor to consider. Using a CO₂ incubator equipped with specific controlled chambers, besides regulating the humidity and the carbon dioxide levels, ensures constant temperature maintenance at 37 °C.

The choice of 37 °C as the standard temperature for cell culture is based on its close resemblance to the normal body temperature of humans. The effect of the temperature on the emissive properties of the complexes was therefore tested.

As depicted in **Figure 73**, the temperature increase from 20°C to 50°C results in a reduction in the intensity of the emission peaks and their associated shoulders at longer wavelengths for the heteroleptic bis(dipyrrinato) Zn^{II} complexes **56**, **58**, **60**, **61**. Remarkably, complex **57** preserves the same intensity, throughout the temperature variations, with a perfect overlapping pattern observed.

The decrease in fluorescence as the temperature rises is a common phenomenon due to the enhanced efficiency of the nonradiative processes caused by thermal agitation, such as collisions with solvent molecules, intramolecular vibrations, and rotations.

Nevertheless, the heteroleptic complexes demonstrate high luminescence even at 50 °C. (**Figure 73**).

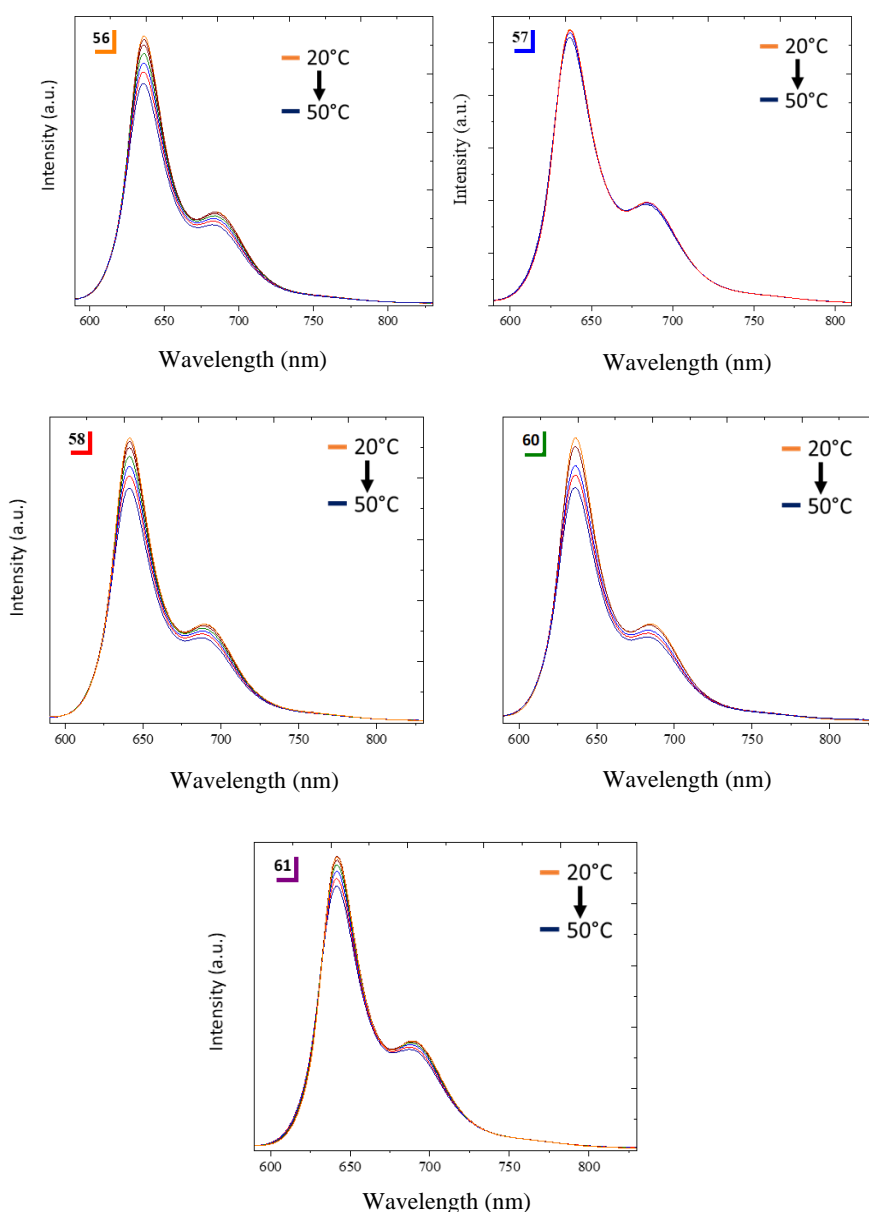


Figure 73: Emission spectra of the heteroleptic bis(dipyrrinato) Zn^{II} complexes **56**, **57**, **58**, **60**, **61** in DMSO ($\lambda_{\text{exc}} = 570$ nm) recorded from 20°C to 50 °C (5°C of intervals in between). Reprinted from R. Tabone, D. Feser, E. D. Lemma, U. Schepers, C. Bizzarri, *Front. Chem.* **2021**, 9:754420.

3.8.3 Confocal microscopy of the heteroleptic bis(dipyrrinato) Zn^{II} complexes

To assess their cell permeability, two different cell lines, specifically NIH3T3 (panel 1, **Figure 74**) and MCF7 (panel 2, **Figure 74**), were incubated with the heteroleptic bis(dipyrrinato) Zn^{II} complexes **56**, **57**, **58**, **60**, **61** without any further staining (**Figure 74**).

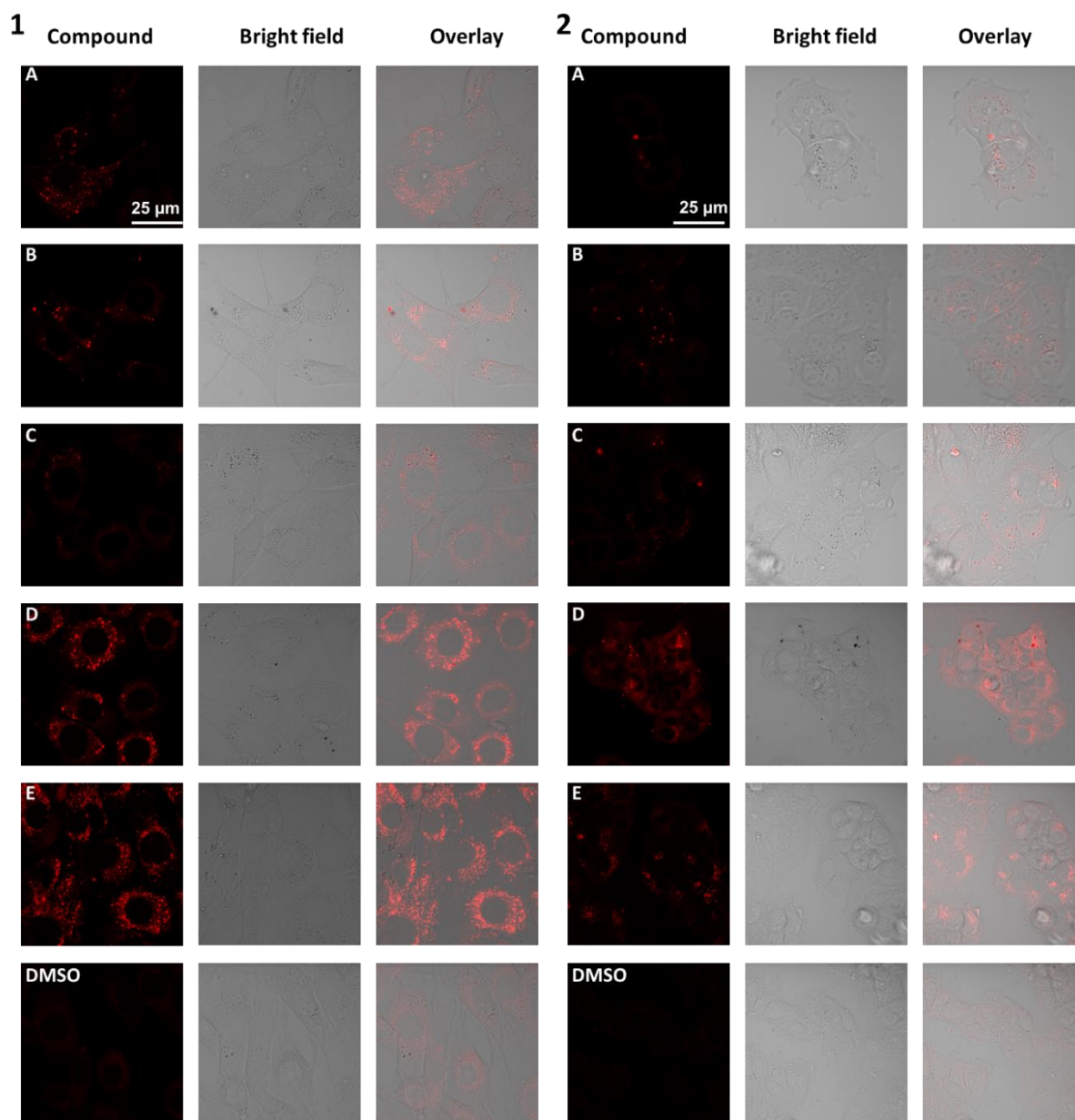


Figure 74: Cellular uptake of the heteroleptic bis(dipyrrinato) Zn^{II} complexes **56**, **57**, **58**, **60**, **61** (20μM) (A:**57**, B:**60**, C:**56**, D:**58**, E:**61**) in NIH3T3 cells (panel 1) and MCF7 cells (panel 2) without further staining. Intracellular accumulation was detected using fluorescence confocal microscopy (Zeiss LSM800, Objective: C-Apo 40x 1.2 Water Immersion) $\lambda_{exc} = 488\text{nm}$, $\lambda_{em} 550\text{-}700\text{nm}$. Scalebar: 25μm. Reprinted from R. Tabone, D. Feser, E. D. Lemma, U. Schepers, C. Bizzarri, *Front. Chem.* **2021**, 9:754420.

The first three complexes, specifically A:**57**, B:**60** and C:**56**, shown in panel 1 (**Figure 74**), display a weak luminescence in the embryonic fibroblast cell line NIH3T3.

The confocal laser microscopy shows a comparable outcome despite the higher quantum yield of complexes **57** and **60** (around 40 %) compared to complex **56** (5%) in DMSO. This suggests that the improved solubility of complex **56** leads to a better uptake, thereby compensating for its lower quantum yield in polar solvents.

As proof of this, the last two complexes, specifically D:**58** and E:**61**, shown in panel 1 (**Figure 74**), despite having quantum yields up to 40 %, similar to compounds **57** and **60** (§3.4.2, **Table 7**), they contain hydroxyl groups in their structure (**Figure 68**) and therefore show better cellular uptake because of their higher solubility in polar media.

Similarly, complexes **57**, **60** and **56** display weak luminescence in the human breast cancer cell line MCF7 (A, B, and C in panel 2, **Figure 74**). Likewise, the better uptake previously demonstrated by complexes **57** and **58** is also confirmed with this different cell line. However, as seen in D:**58** and E:**61** (panel 2, **Figure 74**), the pictures appear less sharp.

This variation is not necessarily related to the complexes under examination but rather to the cell line characteristics used. Cancer cell lines, such as MCF7, are typically immortalised, meaning they can continuously divide and reproduce; therefore, uncontrolled growth can result in a dense and clumped picture.

Since the heteroleptic complexes **58** and **61** manifest the highest ability to cross the cell membrane and effectively accumulate within the cellular environment, their uptakes at different concentrations in NIH3T3 and MCF7 cell lines were investigated.

Complex **58** shows a weak fluorescence signal at 1 μM in both cell lines (**Figure 75**). However, between 10 μM and 20 μM there is no substantial difference in the intensities, so both concentrations can potentially be used for microscopy measurements.

On the contrary, complex **61** displays low intensity at both 1 μM and 10 μM (**Figure 76**), suggesting the use of a concentration of at least 20 μM for this type of test.

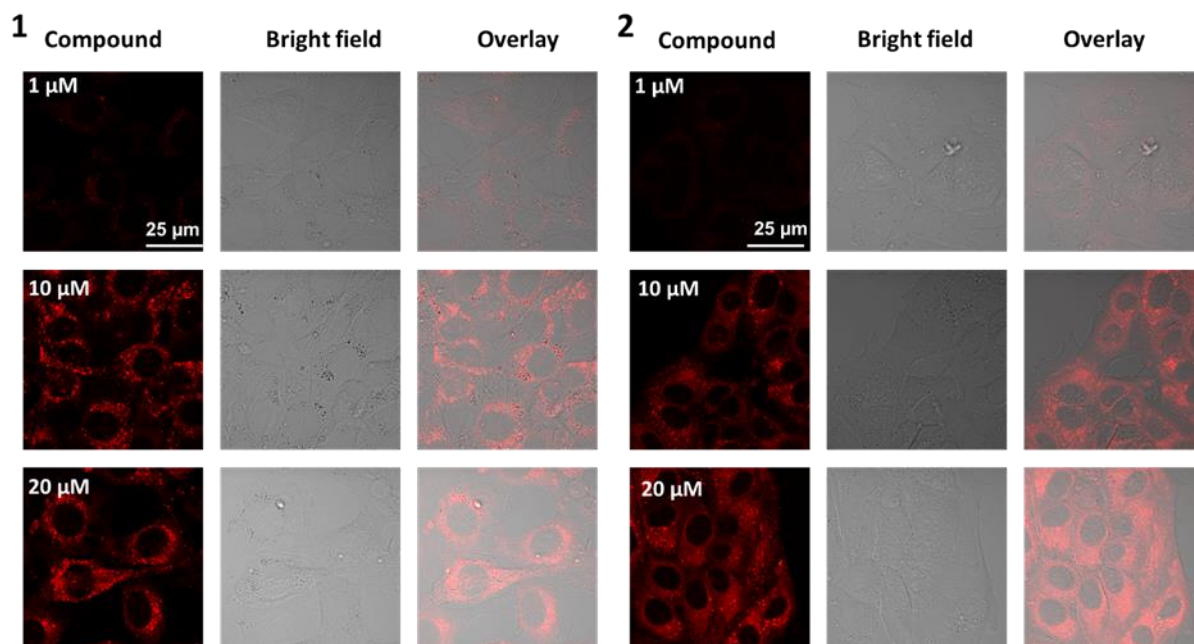


Figure 75: Cellular uptake of the heteroleptic bis(dipyrrinato) Zn^{II} complex **58** at different concentrations (1-10-20 μM) in NIH3T3 cells (panel 1) and MCF7 cells (panel 2) without further staining. Intracellular accumulation was detected using fluorescence confocal microscopy (Zeiss LSM800, Objective: C-Apo 40x 1.2 Water Immersion) $\lambda_{\text{exc}} = 488 \text{ nm}$, $\lambda_{\text{em}} 550\text{-}700 \text{ nm}$. Scalebar: 25 μm . Reprinted from R. Tabone, D. Feser, E. D. Lemma, U. Schepers, C. Bizzarri, *Front. Chem.* **2021**, 9:754420.

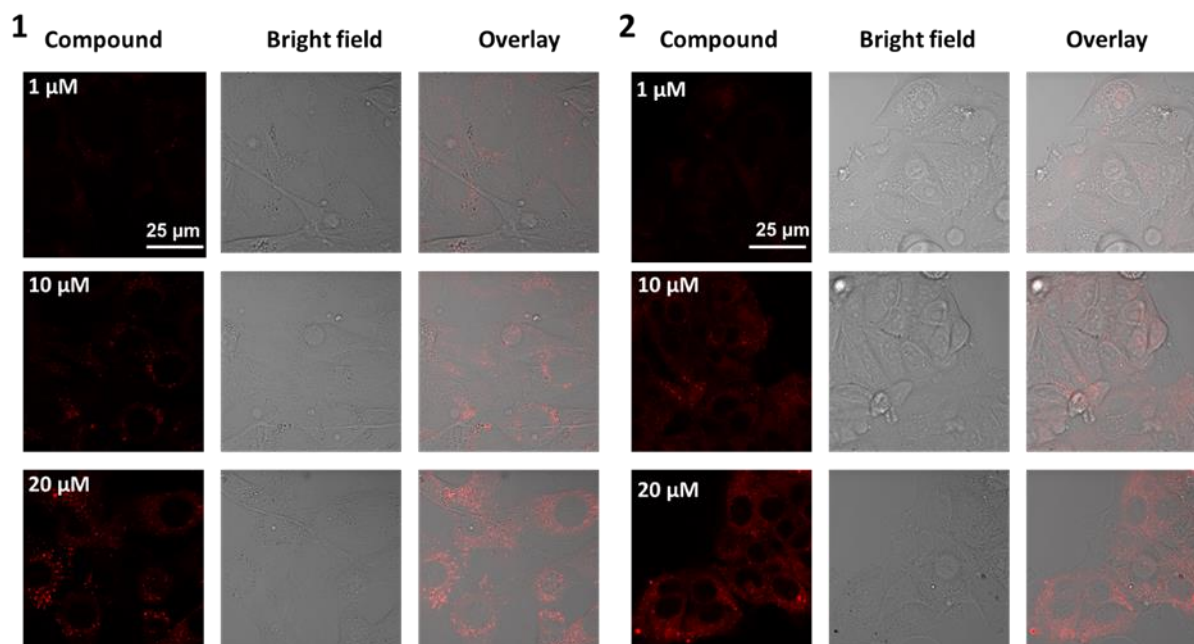


Figure 76: Cellular uptake of the heteroleptic bis(dipyrrinato) Zn^{II} complex **61** at different concentrations (1-10-20 μM) in NIH3T3 cells (panel 1) and MCF7 cells (panel 2) without further staining. Intracellular accumulation was detected using fluorescence confocal microscopy (Zeiss LSM800, Objective: C-Apo 40x 1.2 Water Immersion) $\lambda_{\text{exc}} = 488 \text{ nm}$, $\lambda_{\text{em}} 550\text{-}700 \text{ nm}$. Scalebar: 25 μm . Reprinted from R. Tabone, D. Feser, E. D. Lemma, U. Schepers, C. Bizzarri, *Front. Chem.* **2021**, 9:754420.

Counterstaining experiments with Hoechst 33342 and MitoTracker™ Green were conducted in HeLa cells (**Figure 77**) and NHDF cells (**Figure 78**) to understand the localisation of the heteroleptic complexes within the cell.

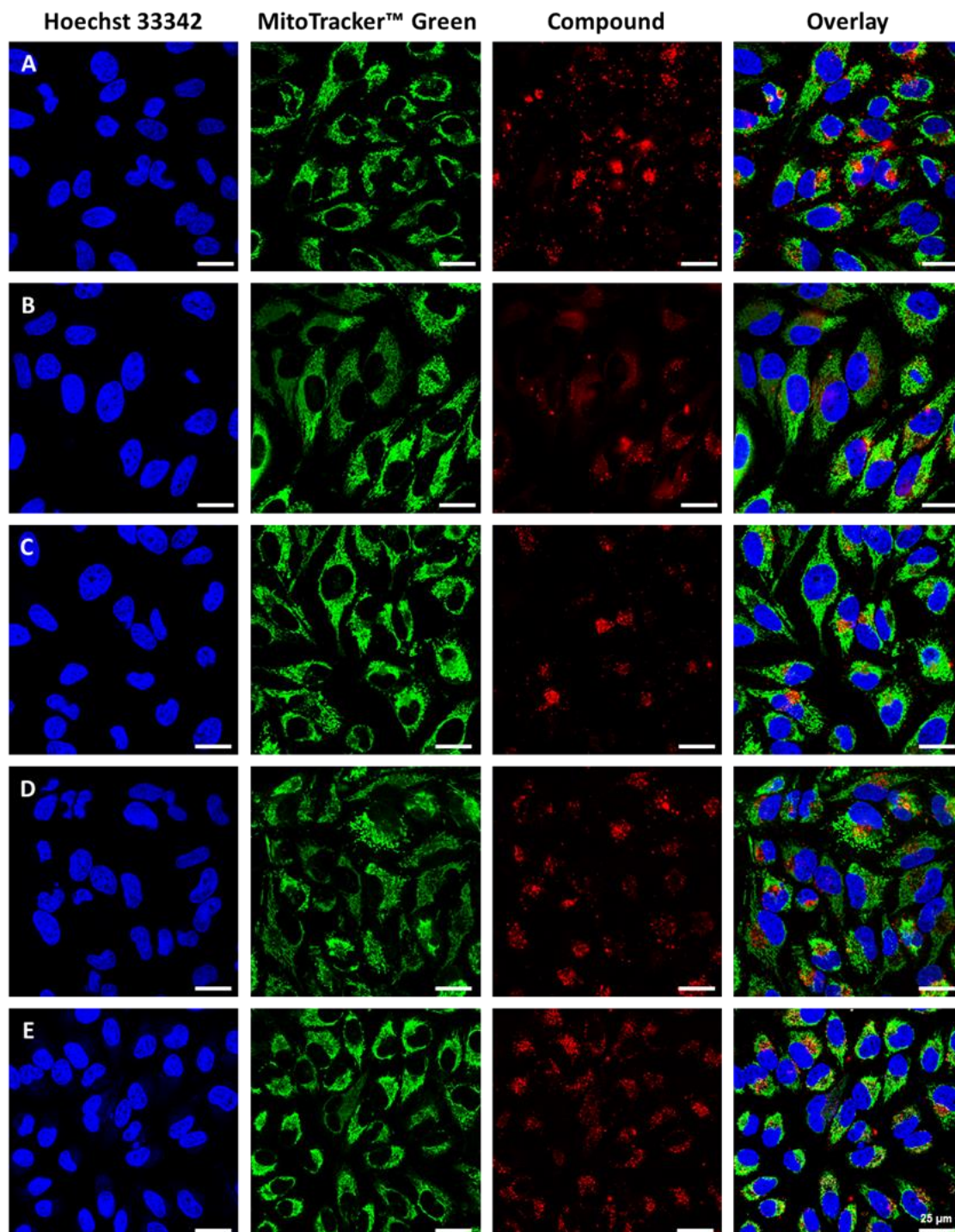


Figure 77: Cellular uptake of the heteroleptic bis(dipyrrinato) Zn^{II} complexes **56**, **57**, **58**, **60**, **61** ($20\mu M$) (A:**57**, B:**60**, C:**56**, D:**58**, E:**61**) in HeLa cells with MitoTracker™ Green. Intracellular accumulation was detected using fluorescence confocal microscopy (Leica Stellaris, Objective: HC PL APO CS2 63x/1.40 OIL). From left to right: Hoechst 33342 ($\lambda_{exc}= 405$ nm, $\lambda_{em}= 414-462$ nm); MitoTracker™ Green ($\lambda_{exc}= 488$ nm, $\lambda_{em}= 494-545$ nm); compounds **56**, **57**, **58**, **60**, **61** ($\lambda_{exc} = 630$ nm, $\lambda_{em} = 640-750$ nm). Scale bars $25\ \mu m$. Reprinted from R. Tabone, D. Feser, E. D. Lemma, U. Schepers, C. Bizzarri, *Front. Chem.* **2021**, 9:754420.

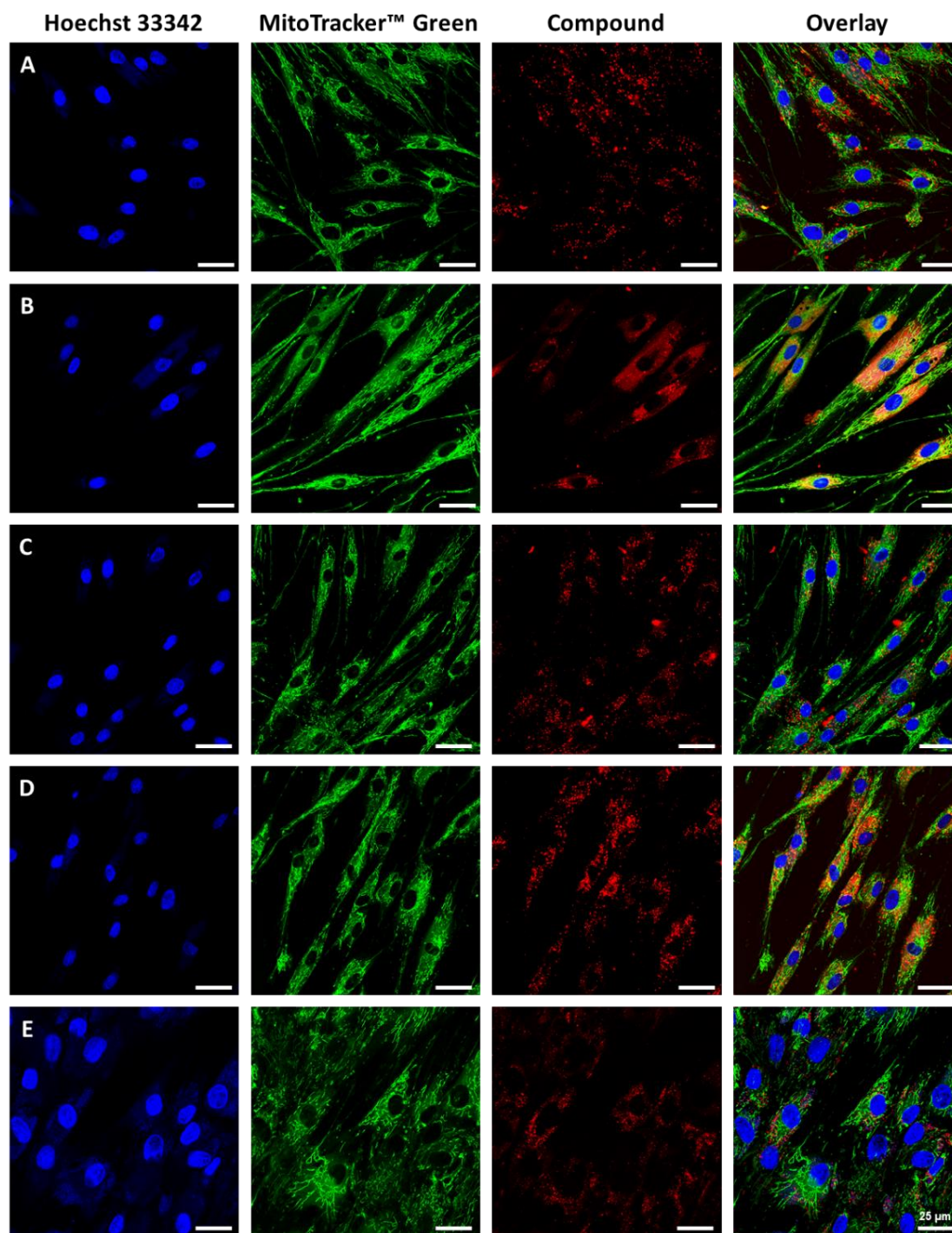


Figure 78: Cellular uptake of the heteroleptic bis(dipyrrinato) Zn^{II} complexes **56**, **57**, **58**, **60**, **61** (20 μM) (A:**57**, B:**60**, C:**56**, D:**58**, E:**61**) in NHDF cells with MitoTracker™ Green. Intracellular accumulation was detected using fluorescence confocal microscopy (Leica Stellaris, Objective: HC PL APO CS2 63x/1.40 OIL). From left to right: Hoechst 33342 (λ_{exc} = 405 nm, λ_{em} = 414-4462 nm); MitoTracker™ Green (λ_{exc} = 488 nm, λ_{em} = 494-545 nm); compounds **56**, **57**, **58**, **60**, **61** (λ_{exc} = 630 nm, λ_{em} = 640-750 nm). Scale bars 25 μm. Reprinted from R. Tabone, D. Feser, E. D. Lemma, U. Schepers, C. Bizzarri, *Front. Chem.* **2021**, 9:754420.

Based on the microscopy images in both cell lines (**Figures 77** and **78**), the distribution of the heteroleptic bis(dipyrrinato) Zn^{II} complexes **56-58**, **60**, and **61** inside the nucleus can be certainly ruled out. There is no observed co-localization with Hoechst 33342, which is known to stain the nuclei of living and fixed cells by binding the minor groove of the double-stranded DNA with a preference for the sequences rich in adenine and thymine.^[304]

Upon closer examination of **Figure 77**, it can also be observed that there is no co-localization in the mitochondria of the HeLa cells. The overlay of the fluorescence generated by the MitoTracker Green and the compound does not exhibit any merge. The red dots distinguish the compound in the superimposition, located outside the nucleus, sometimes forming aggregates, especially in A:**57** and B:**60** (**Figure 77**).

The change of the cell line (**Figure 78**) does not show significant differences, except for the different morphology of the Normal Human Dermal Fibroblast Cells (NHDF). With a flattened appearance, the elongated, spindle-shaped cells provide the same information obtained before, indicating no localisation in the mitochondria. However, microscopy pictures B:**56** and D:**58** show a better cellular uptake for the complexes into the cells, while in images A:**57**, C:**56** and E:**61**, the complexes appear as aggregates.

As detailed in the caption of **Figures 77** and **78**, MitoTrackerTM Green was excited at 488 nm, while the complexes were excited at 630 nm.

To investigate the possible excitation of the heteroleptic complexes at shorter wavelengths (§3.4.3), MitoTrackerTM Blue (excited at 405 nm) was used as a mitochondrial stain, while the complexes **56,57**, **58**, **60**, **61** were excited at 488 nm. As shown in **Figure 79**, consistent with the previous finding, no co-localization with mitochondria is also evident in the NIH3T3 cells. A localisation outside the nucleus was observed, especially in the microscopy images D:**58** E:**61**.

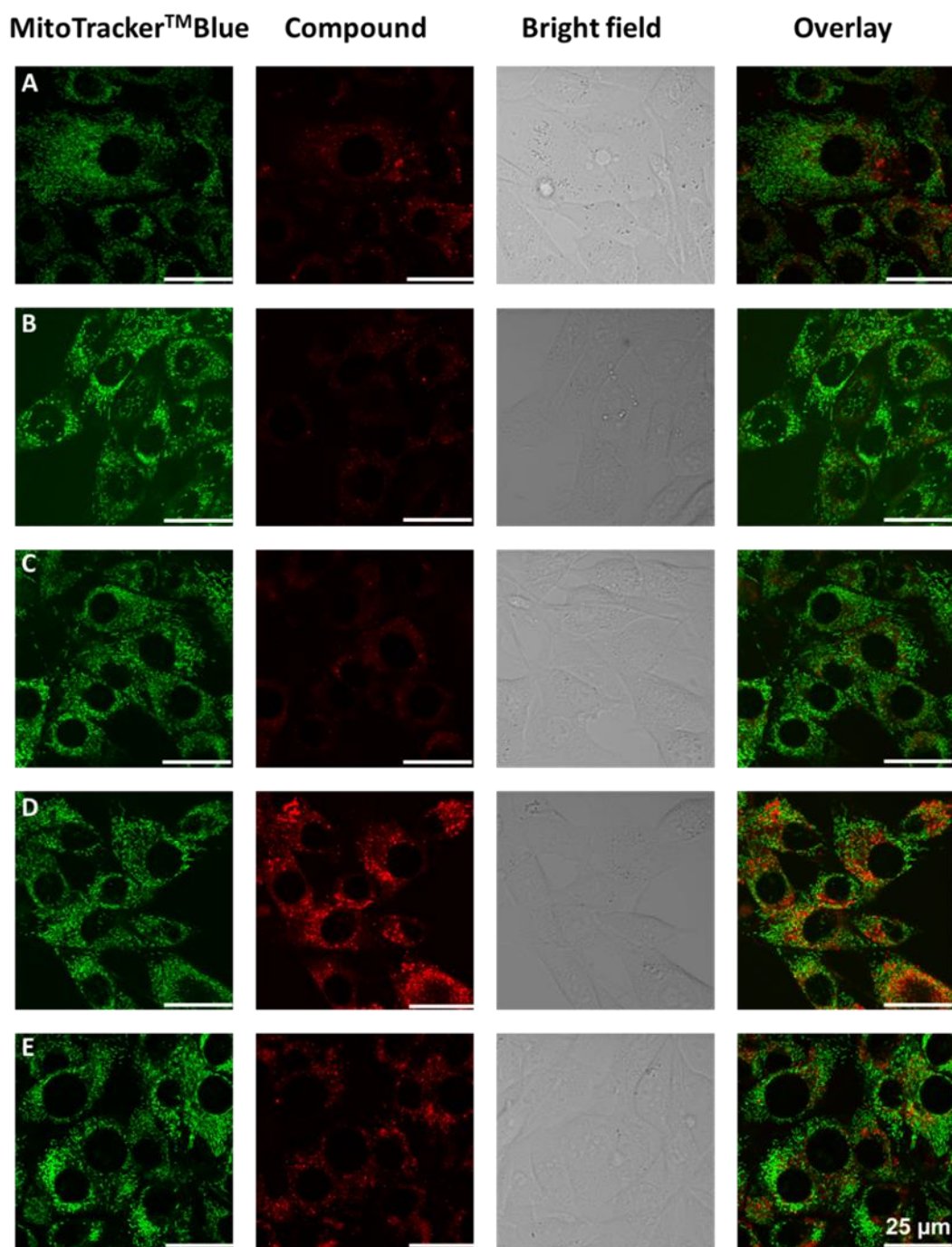


Figure 79: Cellular uptake of the heteroleptic bis(dipyrrinato) Zn^{II} complexes **56**, **57**, **58**, **60**, **61** (20 μM) (A:**57**, B:**60**, C:**56**, D:**58**, E:**61**) in NIH3T3 cells with MitoTracker™ Blue. Intracellular accumulation was detected using fluorescence confocal microscopy (Zeiss LSM800, Objective: C-Apo 40x 1.2 Water Immersion). From left to right: MitoTracker™ Blue ($\lambda_{exc}=405$ nm, λ_{em} 410-500 nm); compounds **56**, **57**, **58**, **60**, **61** ($\lambda_{exc}=488$ nm, $\lambda_{em}=550-700$ nm). Scale bars 25 μm. Reprinted from R. Tabone, D. Feser, E. D. Lemma, U. Schepers, C. Bizzarri, *Front. Chem.* **2021**, 9:754420.

Presuming a distribution of the complexes within a cellular compartment, co-staining experiments were conducted using LysoTracker™ Green. Based on the overlay shown in **Figure 80**, the co-localization of the heteroleptic bis(dipyrrinato) Zn^{II} complexes (A:**60**, B:**56**) with the lysotracker is not observed.

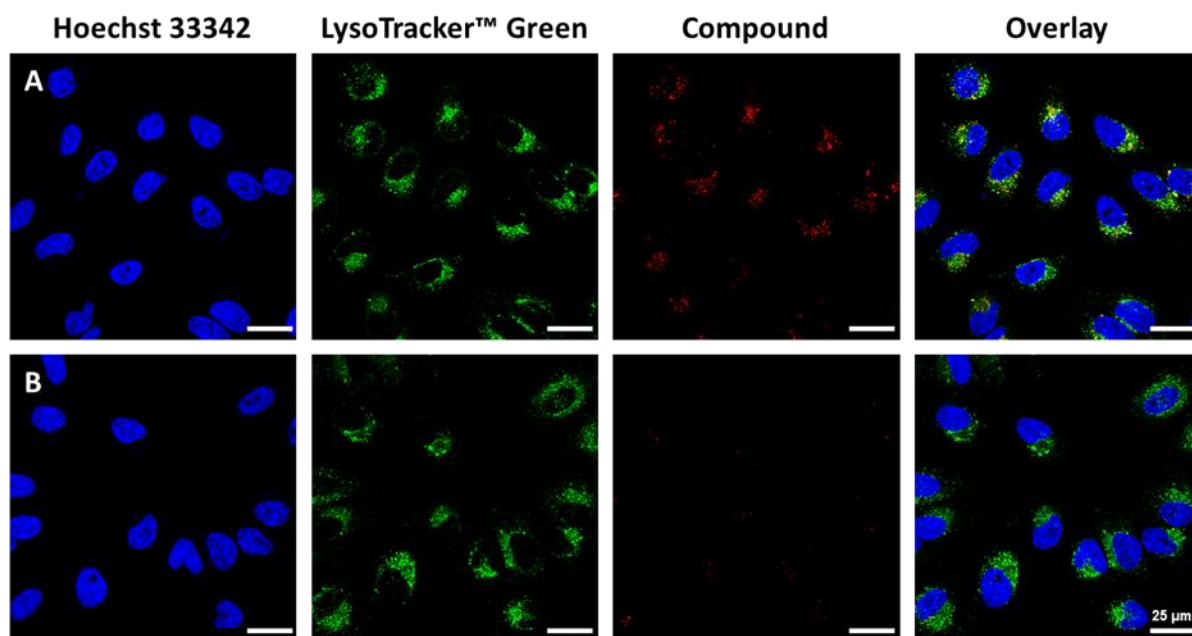


Figure 80: Cellular uptake of the heteroleptic bis(dipyrrinato) Zn^{II} complexes **60** and **56** (A:**60**, B:**56**) in HeLa cells with LysoTracker™ Green. Intracellular accumulation was detected using fluorescence confocal microscopy (Leica Stellaris, Objective: HC PL APO CS2 63x/1.40 OIL). From left to right: Hoechst 33342 ($\lambda_{exc}=405$ nm, $\lambda_{em}=414-462$ nm); LysoTracker™ Green ($\lambda_{exc}=488$ nm, $\lambda_{em}=494-545$ nm); compounds **56**, **60** ($\lambda_{exc}=630$ nm, $\lambda_{em}=640-750$ nm). Scale bars 25 μ m. Reprinted from R. Tabone, D. Feser, E. D. Lemma, U. Schepers, C. Bizzarri, *Front. Chem.* **2021**, 9:754420.

In contrast, precise localisation of the complexes **57**, **58** and **61** within the lysosomes is observed in **Figure 81**; moving from A to C, an apparent increase in the overlay (yellow signal on the image due to green and red overlapping). The Pearson coefficient is a static metric computed on the covariance of the intensities (and their standard deviations) of the two channels^[305]: the one with the LysoTracker™ Green and the one with the heteroleptic bis(dipyrrinato) Zn^{II} complexes **57**, **58** and **61**.

Therefore, the Pearson coefficient was calculated to quantify the degree of co-localization, resulting in 0.24 for **57**, 0.60 for **58** and 0.85 for **61**. This increase in co-localization, which can also be visually observed by the increasing yellow color in the detail view images outlined in

Figure 81, is presumably due to the addition of hydroxyl groups in the structure of the complex, thereby promoting a greater uptake into the cell.

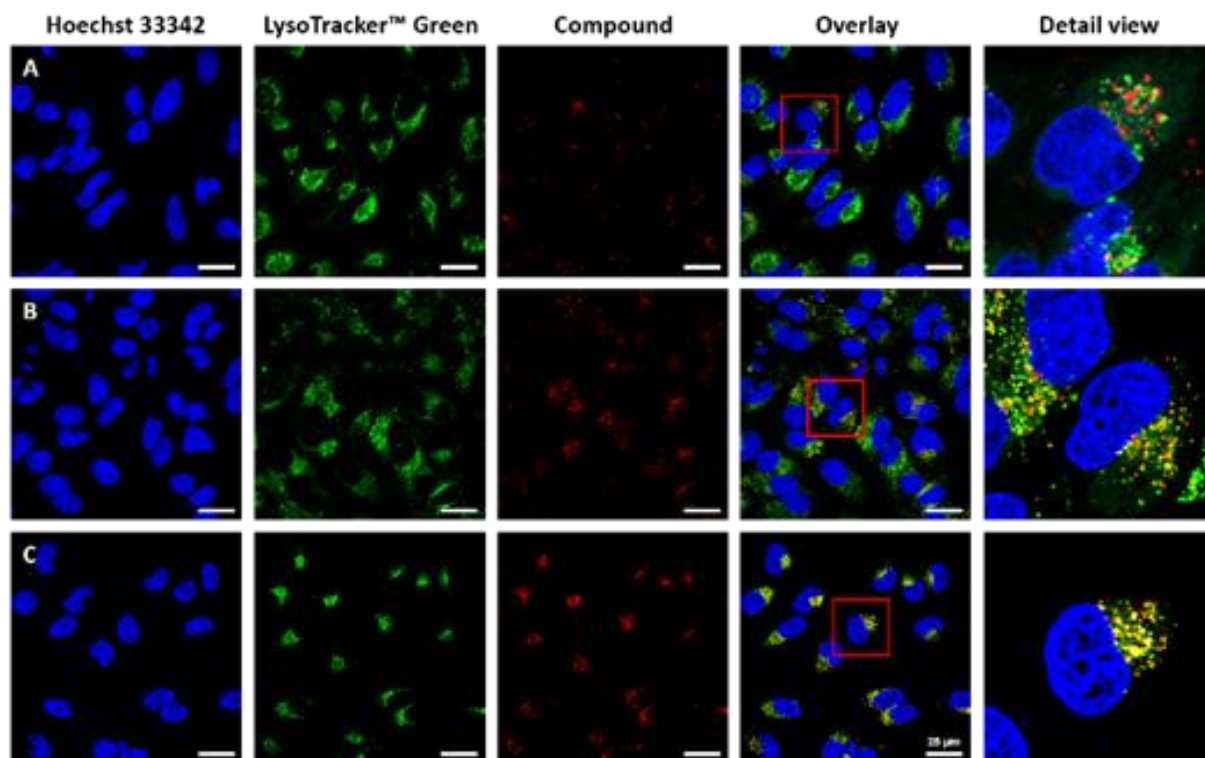


Figure 81: Cellular uptake of the heteroleptic bis(dipyrrinato) Zn^{II} complexes **57**, **58**, **61** in HeLa cells (A: **57**, B: **58**, C: **61**). For co-staining of nuclei and endosomes, cells were treated with Hoechst 33342 ($\lambda_{exc}=405$ nm, $\lambda_{em}=414-462$ nm), LysoTracker™ Green ($\lambda_{exc}=488$ nm, $\lambda_{em} 494-545$ nm); and Hoechst 33342, compounds **57**, **58**, **61** ($\lambda_{exc} =630$ nm, $\lambda_{em} =640-750$ nm). Intracellular accumulation of the complexes was detected with fluorescence confocal microscopy using a Leica Stellaris 5 with a white light laser. The overlay is the merged image of the single-channel fluorescence images. Scale bars: 25 μ m. Reprinted from R. Tabone, D. Feser, E. D. Lemma, U. Schepers, C. Bizzarri, *Front. Chem.* 2021, 9:754420.

To test the possibility of exciting the compound at a lower wavelength, as observed for the MytoTracker™ blue (**Figure 79**), an additional co-staining experiment was conducted using LysoTracker™ blue (excited at 402 nm), (**Figure 82**).

By exciting the heteroleptic bis(dipyrrinato) Zn^{II} complexes **56**, **57**, **58**, **60** and **61**, it is observable a fluorescence signal for all of them, with increased intensity, as expected, for the complexes D:**58** and E:**61**. Through the detailed view, highlighted in **Figure 82**, of the NIH3T3 cell, incubated with the complexes, it is possible to observe the localisation of the compounds within the lysosomal/endosomal compartment.

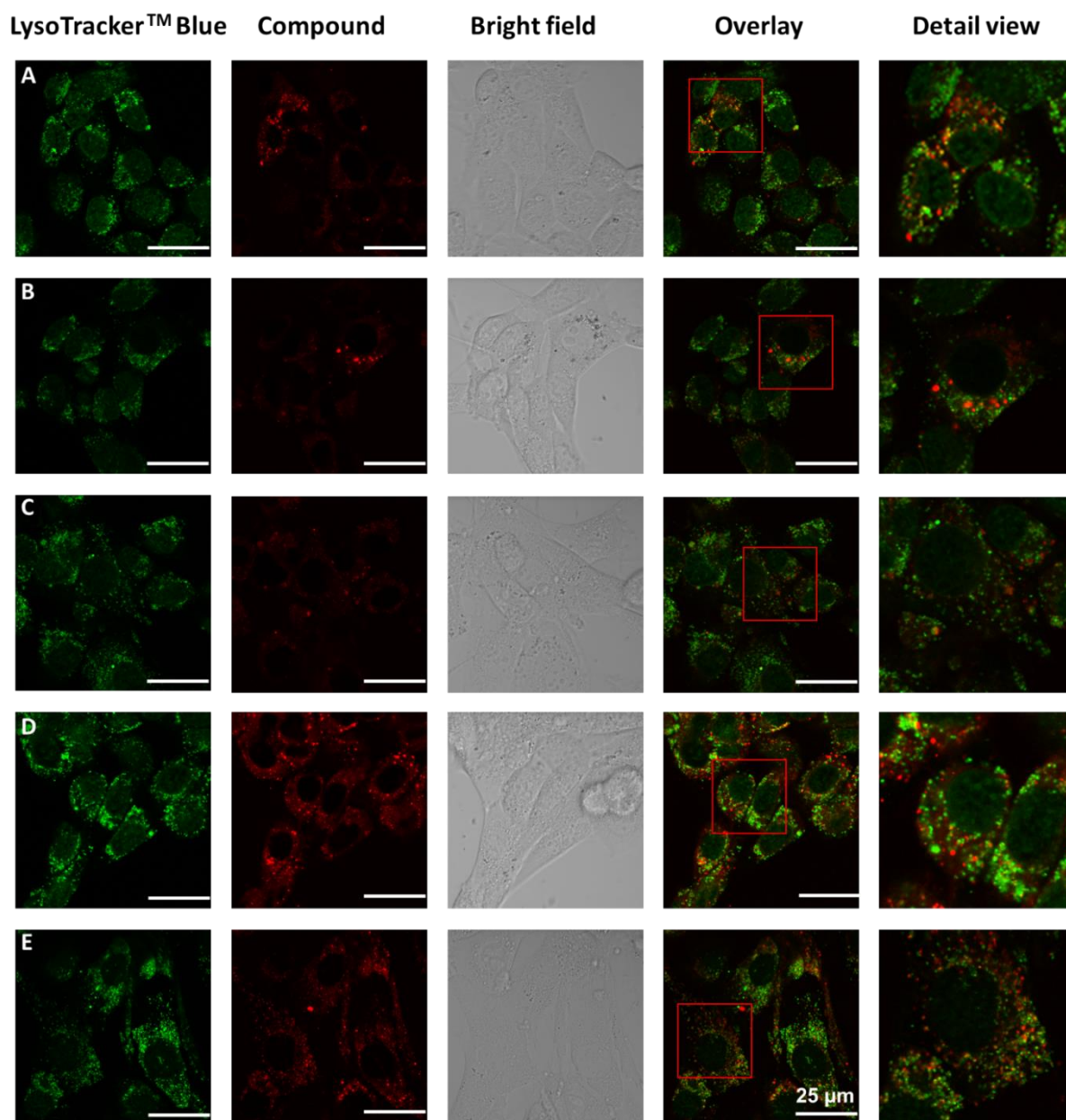


Figure 82: Cellular uptake of the heteroleptic bis(dipyrrinato) Zn^{II} complexes **56**, **57**, **58**, **60**, **61** (20 μM) (A:**57**, B:**60**, C:**56**, D:**58**, E:**61**) in NIH3T3 cells with LysoTracker™ Blue. Intracellular accumulation was detected using fluorescence confocal microscopy imaging parameters for the compounds (Zeiss LSM800, Objective: C-Apo 40x 1.2 Water Immersion). From left to right: LysoTracker™ Blue ($\lambda_{exc}=402$ nm, λ_{em} 410-500 nm); compounds **56**, **57**, **58**, **60**, **61** ($\lambda_{exc}=488$ nm, $\lambda_{em}=550-700$ nm). Scale bars 25 μm. Reprinted from R. Tabone, D. Feser, E. D. Lemma, U. Schepers, C. Bizzarri, *Front. Chem.* **2021**, 9:754420.

All the samples analysed by microscopy and reported so far are prepared by simply incubating the complexes within the cell culture for 24 hours without additional treatments. We can exclude passive transport as a means of uptake because the complexes are too large for such a process. Instead, we consider endocytosis more plausible.^[306,307]

The complexes, probably internalised into the cells through endocytic mechanisms, became enclosed within a membrane-bound vesicle and once engulfed, reached the lysosomes and co-localised there. Nonetheless, these are only assumptions; to further investigate the processes of cellular uptake of the heteroleptic complexes, more comprehensive studies need to be conducted.

As outlined in **Figure 83**, the heteroleptic complex **61** is completely internalised within the NIH3T3 cells after 6 hours of incubation. After this time frame, the sample was fixed *via* crosslinking fixative procedure with paraformaldehyde, and after 24 hours of incubation, it still showed high fluorescence (**Figure 83d**).

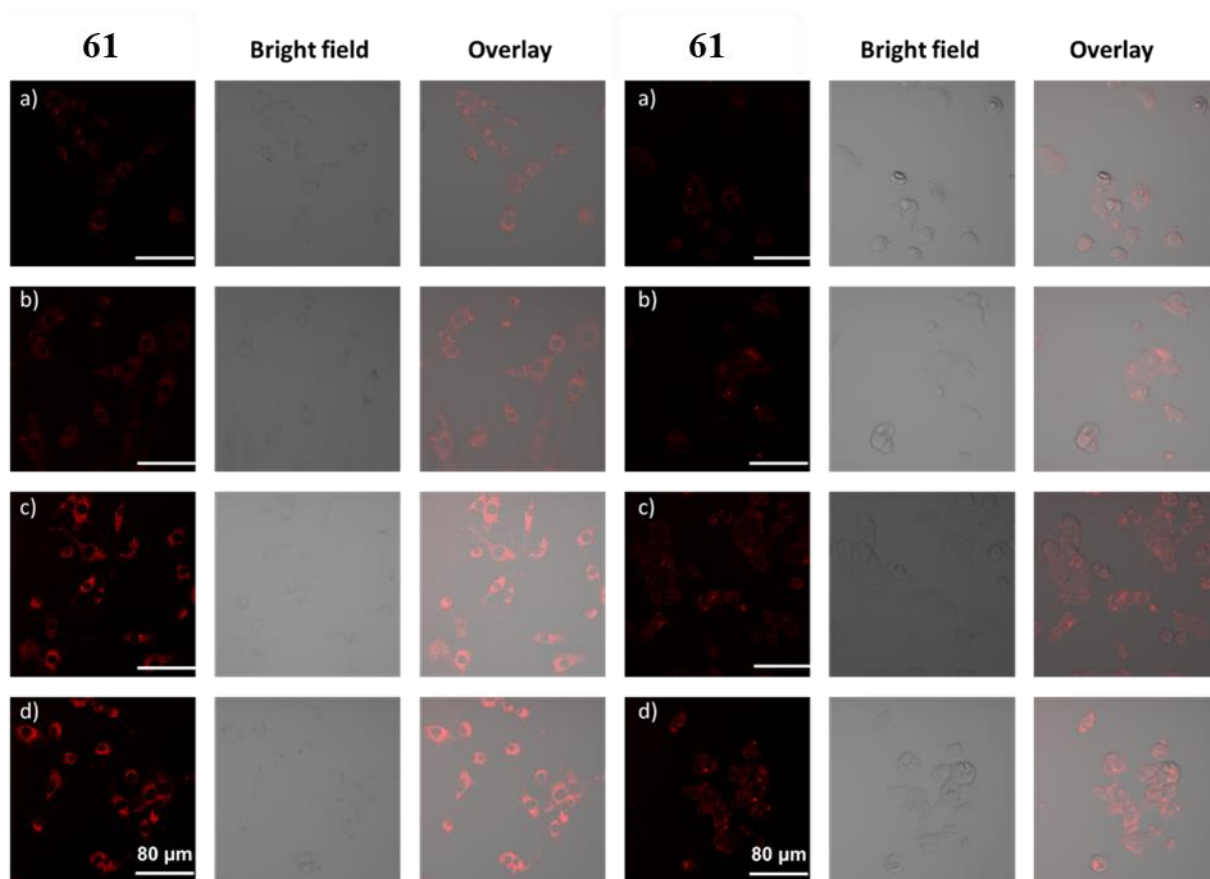


Figure 83: Cellular uptake of the heteroleptic bis (dipyrrinato) Zn^{II} complex **61** ($20\mu M$) in NIH3T3 cells (panel 1) and MCF7 cells (panel 2) over time (a: 0.5 h; b: 1.5 h; c: 6 h) and post-fixation (d). After 6 h, samples were fixed, incubated for 24 h, and imaged (d). Intracellular accumulation was detected using fluorescence confocal microscopy (Zeiss LSM800, Objective: PLN-Apo 20x 0.8 AIR) ($\lambda_{exc} = 488\text{ nm}$, $\lambda_{em} 550\text{-}700\text{ nm}$). Scalebar: 80 μm . Reprinted from R. Tabone, D. Feser, E. D. Lemma, U. Schepers, C. Bizzarri, *Front. Chem.* **2021**, 9:754420.

To further assess the behaviour of complex **61** on fixed cells, co-staining experiments were performed. DAPI was used for nuclear labelling, while actin staining was employed to visualise the cytoskeleton. As observed in **Figure 84**, the heteroleptic bis(dipyrrinato) Zn^{II} complex **61** shows a pronounced and persistent fluorescence signal in the merged image, even after fixation.

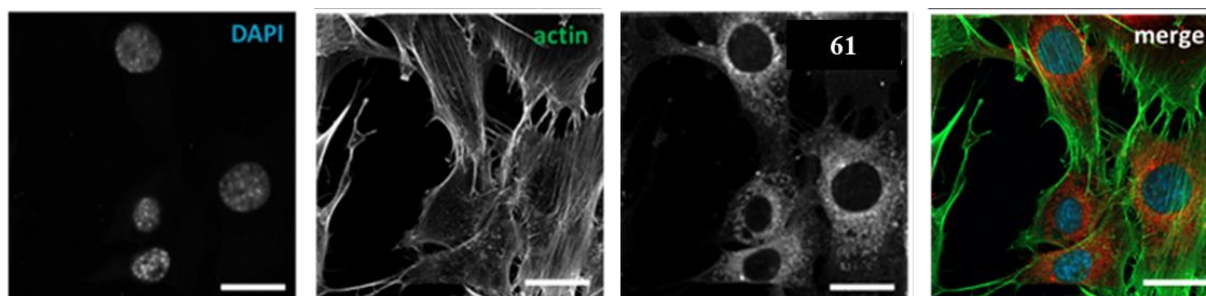


Figure 84: Post-fixation immunochemical staining of nuclei and actin cytoskeleton of NIH3T3 cells treated with the heteroleptic bis (dipyrrinato) Zn^{II} complex **61** (20 μ M). Cells were treated with DAPI (λ_{exc} =405 nm, λ_{em} 410-470 nm), Actin (λ_{exc} =488 nm, λ_{em} 490-535 nm), compound **61** (λ_{exc} =640 nm, λ_{em} =656-700 nm).

Immunochemical investigations were conducted to explore the feasibility of exciting the sample at different wavelengths in fixed cells.

In the first sequence of images (**Figure 85**), NIH3T3 cells incubated with DAPI, actin and complexes **61** were excited at 488 nm, with emission collected between 550-700 nm.

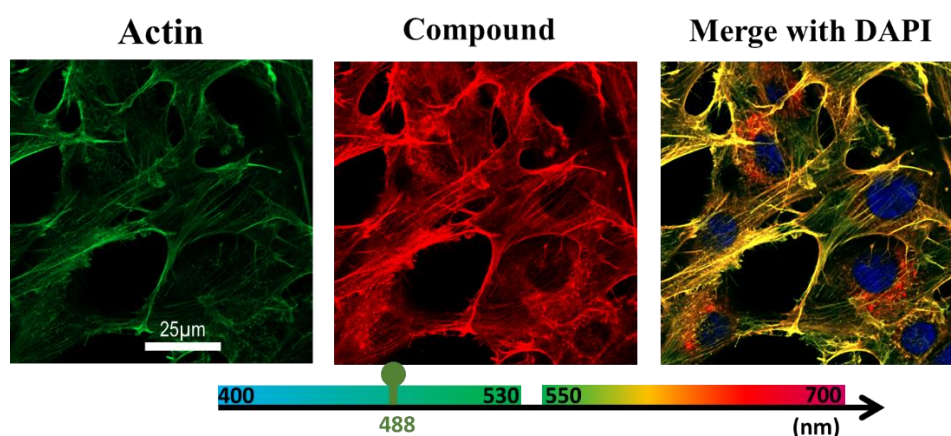


Figure 85: Post-fixation immunochemical staining of nuclei and actin cytoskeleton of NIH3T3 cells treated with the heteroleptic bis(dipyrrinato) Zn complex **61** (20 μ M). Cells were treated with Actin (λ_{exc} =488 nm, λ_{em} 490-535 nm). No further excitation was performed.

Due to the concurrent signal detection from actin, the merged image displays yellow (overlap between green and red).

However, there is also a distinct portion in the image that does not overlap with actin, the red spots, attributed to the heteroleptic bis(dipyrrinato) Zn^{II} complex **61**. Owing to its significant *pseudo*-Stokes, such as $4.66 \cdot 10^3 \text{ cm}^{-1}$ (§3.4.2, **Table 7**), even exciting at 488 nm, it is possible to observe emissions up to 700 nm.

Instead, in **Figure 86** the confocal laser microscopy experiment entailed the use of two different excitation wavelengths: 488 nm and 640 nm. Although a portion of fluorescence photons emitted by complex **61** (which emission profile starts at 600 nm), however the fluorescence signal remains remarkably strong.

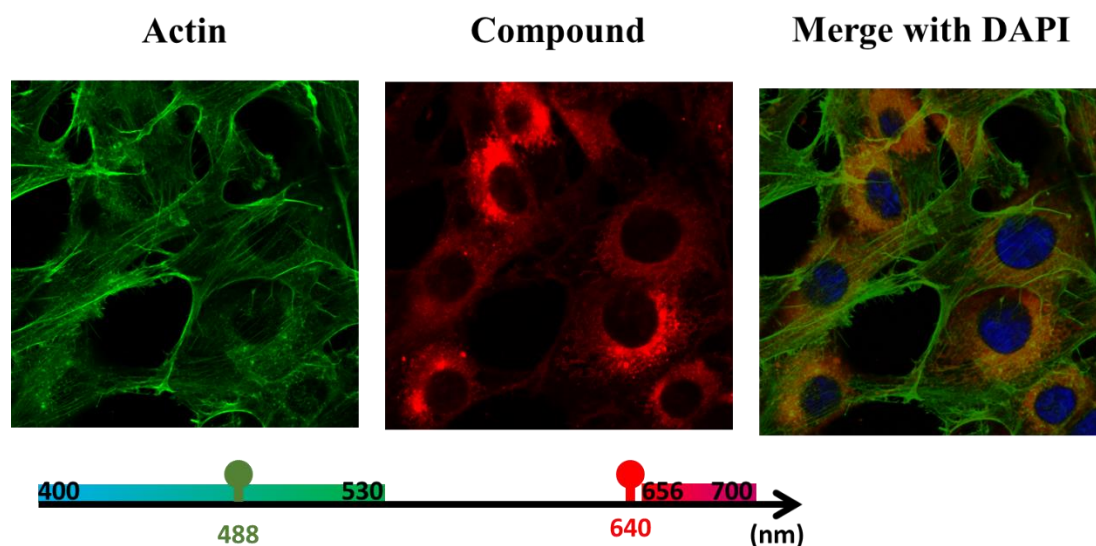


Figure 86: Post-fixation immunochemical staining of nuclei and actin cytoskeleton of NIH3T3 cells treated with the heteroleptic bis(dipyrrinato) Zn^{II} complex **61** (20 μ M). Cells were treated with Actin (λ_{exc} =488 nm, λ_{em} 490-535 nm). In this case, compound **61** was further excited (λ_{exc} =640 nm, λ_{em} =656-700 nm).

3.8.4 Encapsulation in liposomes

The solubility of bulky fluorophores with extensive aromatic systems poses a significant challenge in polar environments, such as cellular ones. This limitation hinders their cellular uptake, thereby rendering these fluorophores unsuitable for cellular imaging, despite their excellent photophysical properties (see §3.4.2).

Nonetheless, solubility obstacles can be potentially overcome by incorporating these fluorophores into various drug delivery systems, such as polymerosomes, micelles, solid lipid nanoparticles or liposomes. The latter is perhaps the most well-explored system in the pharmacology of hydrophobic, poorly soluble drugs.

From the physical chemistry viewpoint, phospholipid liposomal formulations are self-assembled colloidal structures composed of vesicles with one or several phospholipid bilayers, typically 100-400 nm in size. Liposomal suspensions offer a promising drug delivery solution by providing a suitable environment for encapsulating both polar and lipophilic types of molecules.

Thus, the heteroleptic bis(dipyrrinato)Zn^{II} complexes **55**, **60**, **62**, **63** and **64**, whose structures are reported in **Figure 87**, were entrapped in supposedly unilamellar liposomes with the lipid composition of DSPC/DSPG/cholesterol (25:75:10 mol%).

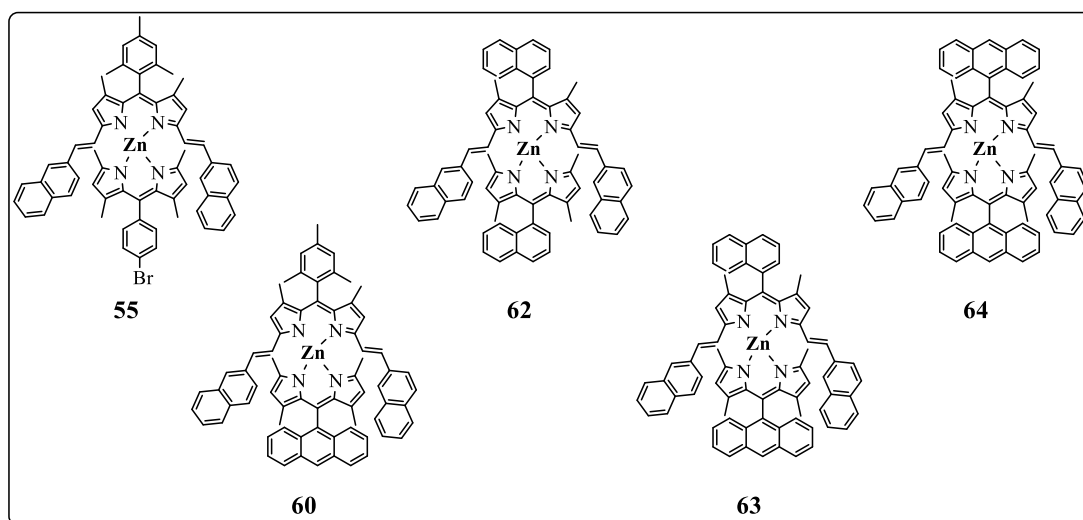


Figure 87: Chemical structures of the heteroleptic bis(dipyrrinato)Zn^{II} complexes **55**, **60**, **62**, **63** and **64** encapsulated in liposomes.

Complex-loaded liposomes were prepared by co-dissolving compounds of interest, one at a time, with lipids in MeOH/CHCl₃ (2:1, v:v) mixture, followed by N₂-flow removal of organic solvents and drying the mixtures *in vacuo* overnight. Dry mixtures were re-hydrated with Phosphate Buffer Saline (=PBS: 137 mM NaCl, 10 mM phosphate buffer, pH 7.4) by incubation for 30 min at 60°C and homogenized by 6 freeze/thaw cycles (liq. N₂/ water bath 60°C, vortexing). 2 mM (total lipid) multilamellar vesicles (MLV) obtained this way were thereafter extruded through polycarbonate membranes with pores of 200 nm *i.e.* at 60°C, providing the desired large unilamellar vesicles (LUV) with bilayers enriched with **55**, **60**, **62**, **63** or **64**.

3.8.4.2 Photophysical properties in liposomes

The absorption spectra of the encapsulated heteroleptic bis(dipyrrinato)Zn^{II} complexes **55**, **60**, **62**, **63** and **64** in PBS are shown in **Figure 88**.

One of the first noticeable features is undoubtedly the absorption profile of complex **55** (red plot, **Figure 88**), which, at an equivalent concentration, exhibits higher absorption. Despite a slightly raised baseline, the three peculiar absorption bands display clear and distinct contours. Compared to **55**, the absorption profile of complex **62** manifests a less pronounced band ranging from 300 nm to 400 nm, attributed to the electronic transitions localized on the naphthyl vinyl moieties present in the chromophoric unit. Nevertheless, its intensity rivals that of the other complexes **60**, **63** and **64**.

Among the complexes, there are differences in the intraligand transition (¹LC) localized on the plain dipyrins. These bands appear more intense and broadened for complexes **55** and **62**, ranging from 450 and 550 nm and less sharply defined for complexes **60**, **63** and **64**. They can be discerned within a considerably narrower range.

As outlined in **Figure 87**, complex **62** is composed of the plain dipyrin **17**, bearing a naphthyl group at the *meso* position. In contrast, the plain dipyrin in complexes **60**, **63** and **64** is compound **19**, having an anthracenyl group at the same position. The increasing steric hindrance may have caused stronger interactions with the hydrophobic parts of the lipid molecules that compose LUVs, thereby leading to this observed narrower and less intense absorption band.

The third absorption bands, arising from the $^1\pi\rightarrow\pi^*$ transition localized on the π -expanded dipyrrens forming the heteroleptic complexes, manifest a similar pattern. Despite the higher intensity of the complexes **55** and **62**, the profiles of all the complexes remain largely similar.

As outlined in **Table 18**, compared to the measurements conducted in DMSO (§3.4.2), a bathochromic shift can be observed for all the heteroleptic complexes, when in liposomes.

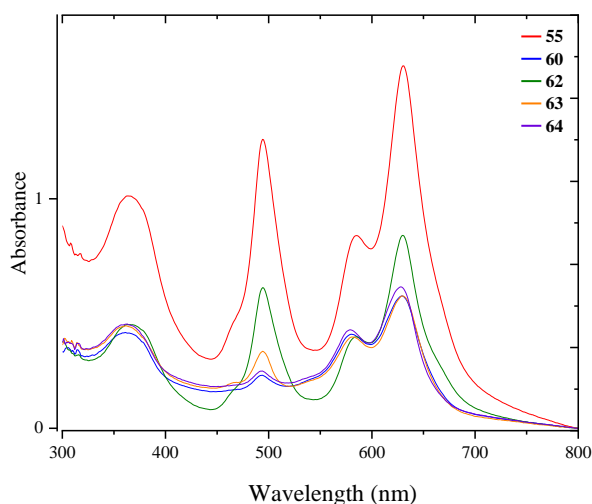


Figure 88: UV/Vis absorption spectra of the heteroleptic bis(dipyrrinato) Zn^{II} complexes **55**, **60**, **62**, **63**, **64** in DMSO solution ($1\mu M$) encapsulated in liposomes ($1\mu M$) in PBS solution.

Nevertheless, the notable redshift is observed in the emission of all complexes (**Figure 88**, **Table 18**). It suggests location in the hydrophobic bilayer core rather than in any polar surroundings. Complex **60** display a peak at 635 nm, with an emission shoulder at approximately 700 nm. The emission maxima of complexes **55**, **64** and **63** are located between 642-644 nm.

The heteroleptic complex **62** shows an emission profile characterized by a peak centered at 644 nm and a significantly more intense emission shoulder than to the other complexes. Once embedded in liposomes, the heteroleptic complex **60**, which already exhibits a remarkable quantum yield in DMSO, decreases slightly (to 28%).

Instead, complex **55** undergoes a slight increase, reaching $\Phi=15\%$, while the quantum yield of complex **62** and **64** undergo a more substantial enhancement to, respectively, 20% and 16% (**Table 18**). Incorporating into liposomes proves to be highly effective in doubling the quantum yield of complex **60** to 15%. Furthermore, the entrapment in liposomes has led to an extension

of the lifetimes of the heteroleptic bis(dipyrrinato)Zn^{II} complexes **55**, **60**, **62**, **63**, **64**, as outlined in **Table 18**. By creating a controlled microenvironment in which the mobility of the species is restricted, like in the gel-phase phospholipid bilayers, the nonradiative pathway could be reduced, thus explaining the increase in the fluorescence lifetime.

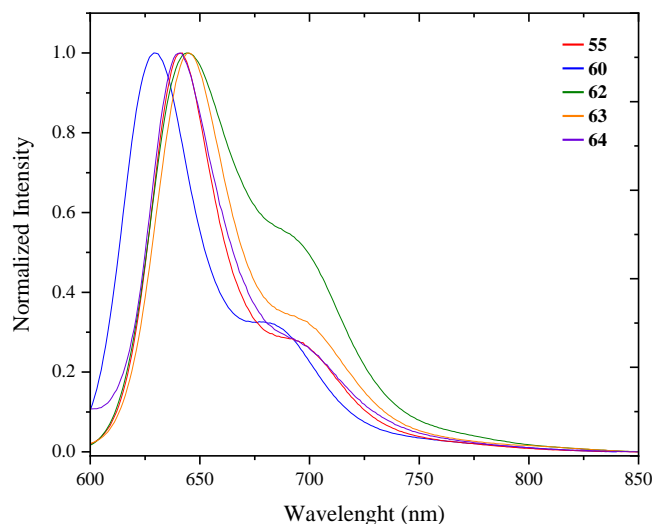


Figure 89: Emission spectra ($\lambda_{exc} = 570$ nm) of the heteroleptic bis(dipyrrinato)Zn^{II} complexes **55**, **60**, **62**, **63**, **64** in DMSO solution (1 μ M) encapsulated in liposomes (1 μ M) in PBS solution.

Table 18: Photophysical properties of the heteroleptic bis(dipyrrinato)Zn^{II} complexes (**55**, **60**, **62**, **63**, **64**) in ^[a]DMSO solution (1 μ M) and ^[b] encapsulated in liposomes (1 μ M) in PBS solution. ^[c] Quantum yields were determined by the relative method, using cresyl violet ($\Phi = 0.54$ in MeOH, 22 °C). ^[d] Quantum yields were determined by integrating sphere ^[e] Exciting with a NanoLED source at 570 nm.

Complex	$\lambda_{abs}^{[a]}$ [nm]	λ_{em} [nm]	Φ [c, d]	τ [e] [ns]
55	625 ^[a]	634 ^[a]	0.12 ^[a, c]	3.2 ^[a]
	629 ^[b]	642 ^[b]	0.15 ^[b, d]	4.2 ^[b]
60	626 ^[a]	638 ^[a]	0.36 ^[a, c]	2.6 ^[a]
	630 ^[b]	635 ^[b]	0.28 ^[b, d]	3.4 ^[b]
62	628 ^[a]	640 ^[a]	0.15 ^[a, c]	2.2 ^[a]
	629 ^[b]	644 ^[b]	0.20 ^[b, d]	3.5 ^[b]
63	627 ^[a]	640 ^[a]	0.08 ^[a, c]	1.3 ^[a]
	630 ^[b]	645 ^[b]	0.16 ^[b, d]	2.7 ^[b]
64	626 ^[a]	640 ^[a]	0.08 ^[a, c]	3.2 ^[a]
	628 ^[b]	643 ^[b]	0.15 ^[b, d]	4.7 ^[b]

3.8.4.3 Confocal laser microscopy

Interaction with live cells without liposomes

As a starting point of the investigation, compounds **60** and **62** have been co-incubated with the non-confluent HeLa and NHDF cells. The complexes without liposomes, in the form of DMSO solution (20 μ M) have been added, incubated for twenty-four hours and imaged with the Hoechst 33342 and Mitotraker™ Green, as co-staining dyes. As seen in the representative **Figures 90** and **91**, below, irrespective of the cell line, only minimal signal from **60** and **62** is visible above the red background fluorescence.

The red signal spots correspond to the complexes signals, which is non-uniform, non-specific and in most cases, it is stemming outside the cells. Probably because of the formation of the large aggregates formed by complexes **60** and **62** in DMSO dilution.

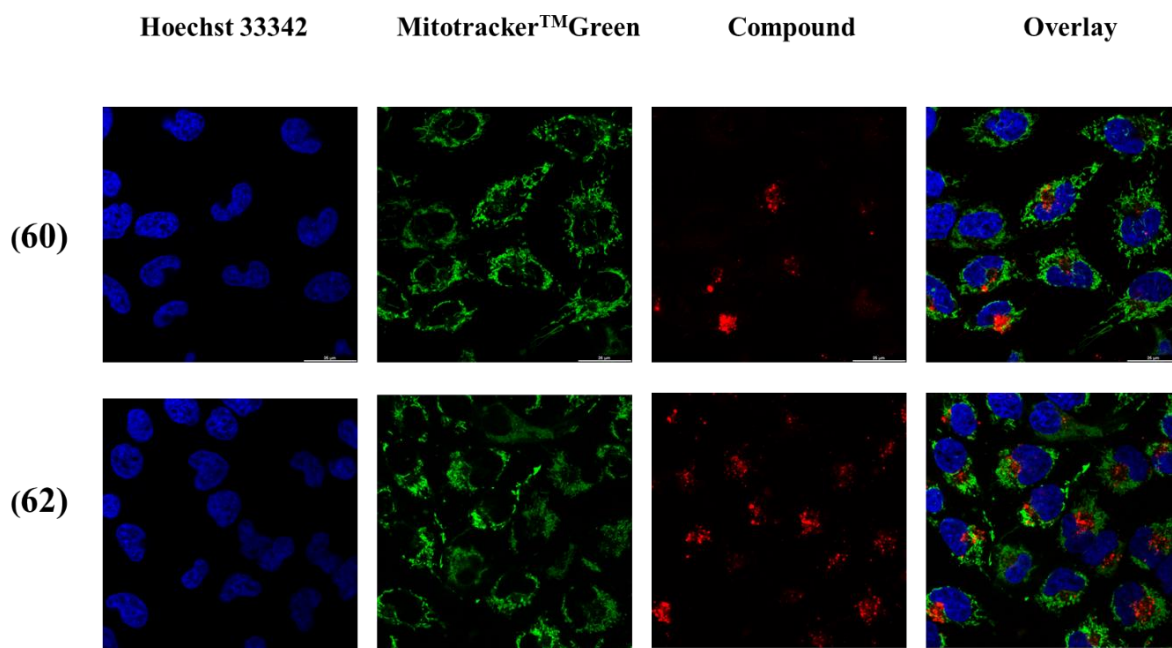


Figure 90: Cellular uptake of heteroleptic bis(dipyrrinato)Zn^{II} complexes **60** and **62** in HeLa cells with MitoTracker™ Green. Intracellular accumulation was detected by using fluorescence confocal microscopy (Leica Stellaris, Objective: HC PL APO CS2 63x/1.40 OIL). From left to right: Hoechst 33342 (λ_{exc} =405 nm, λ_{em} = 414-462 nm); MitoTracker™ Green (λ_{exc} =488 nm, λ_{em} 494-545 nm); compounds **60,62** (λ_{exc} =630 nm, λ_{em} =640-750 nm). Scale bars 25 μ m.

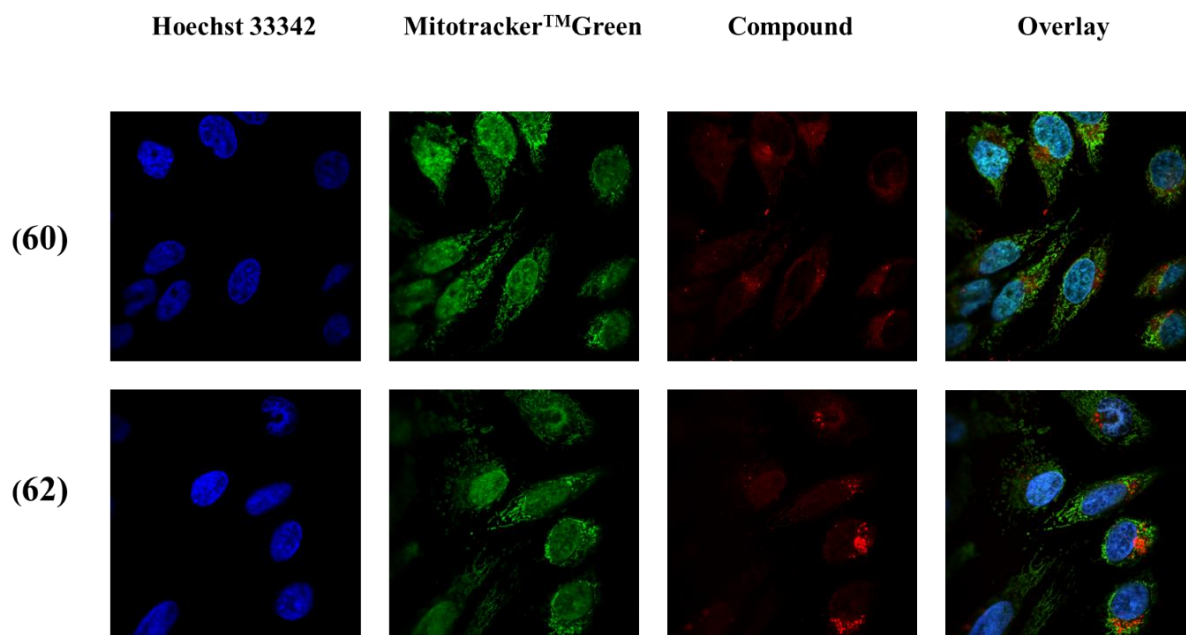


Figure 91: Cellular uptake of heteroleptic bis(dipyrrinato)Zn^{II} complexes **60** and **62** in NHDF cells with MitoTracker™ Green. Intracellular accumulation was detected by using fluorescence confocal microscopy (Leica Stellaris, Objective: HC PL APO CS2 63x/1.40 OIL). From left to right: Hoechst 33342 ($\lambda_{exc}=405$ nm, $\lambda_{em}=414-462$ nm); MitoTracker™ Green ($\lambda_{exc}=488$ nm, $\lambda_{em} 494-545$ nm); compounds **60,62** ($\lambda_{exc} =630$ nm, $\lambda_{em} =640-750$ nm). Scale bars 25 μ m.

Interaction with live cells as liposomal formulation

In addition to the above-described composition (specifically DPSC/DSPG/Chol), liposomes containing the heteroleptic bis(dipyrrinato)Zn^{II} complexes **55**, **60**, **62**, **63**, **64** and lipids with low melting temperatures (POPC/POPG/Chol) were used.

The former lipidic composition provides lipid bilayers which are normally in the so-called “gel lamellar phase”, while the latter are in the “fluid lamellar phase”. Gel-phase bilayers exhibit greater rigidity, with rotational and lateral diffusion coefficients approximately one order magnitude lower compared to those in the fluid state.

The mobility of lipid plays a crucial role in imparting rigidity, as was observed in the different photophysical properties exhibited by the complexes in comparison to the lipid-embedded ones in §3.8.4.2.

Besides, the gel-state bilayers are more biostable and preferred in the *in vivo* applications, due to their enhanced circulation lifetime and reduced clearance rate.

Thus, staining experiments of the complexes, enclosed within two different lipid formulations, such as fluid and gel, in HeLa cells, were performed.

Already after one hour of co-incubation into HeLa cells, distinct punctuate signals in the cytoplasm, close to the plasma membrane, could be observed (**Figure 92**).

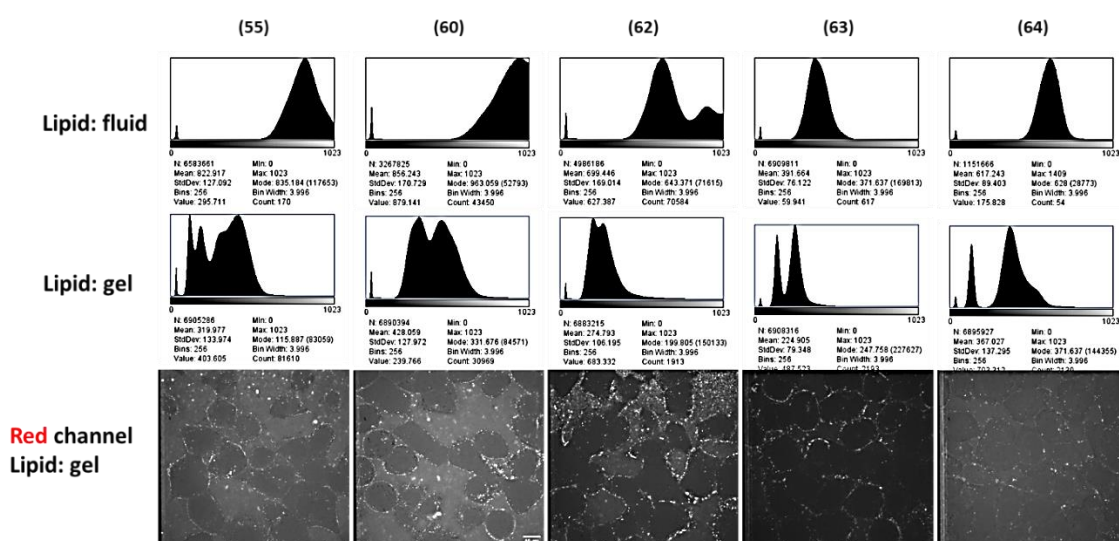


Figure 92: Cellular uptake of the heteroleptic bis(dipyrrinato)Zn^{II} complexes **55**, **60**, **62**, **63**, **64** in liposomes of varying fluidity after short-time incubation (1 h) with HeLa cells. Intracellular accumulation was detected by using a spinning disk confocal imaging (Objective: 64x/1.40 OIL). Top and middle: corresponding fluorescence intensity histograms of individual pixels. Bottom individual confocal planes without brightness/contrast adjustment. No co-staining was added. (λ_{exc} =630 nm, λ_{em} =640-750 nm). Scale bars 10 μ m.

The incubation time was then extended to twenty-four hours, allowing for a longer interaction between the complexes under investigations and the cells.

The cellular uptake of the heteroleptic bis(dipyrrinato)Zn^{II} complexes **55**, **60**, **62**, **63**, **64** after twenty-four hours of co-incubation with HeLa cells by altering the lipid composition was investigated, as depicted in **Figures 93** and **94**.

Generally, brighter fluorescent spots, primarily located in the periplasmic region, were observed in the fluid large unilamellar vesicles (LUVs), as shown in **Figure 93**.

When comparing complexes **55**, **60**, **62**, **63** within the same bilayer phase, the variation in signal intensity can be correlated to the differences in their quantum yields (§3.8.4.2, Table 1).

As such, complex **60** shows the highest intensity after twenty-four hours of incubation.

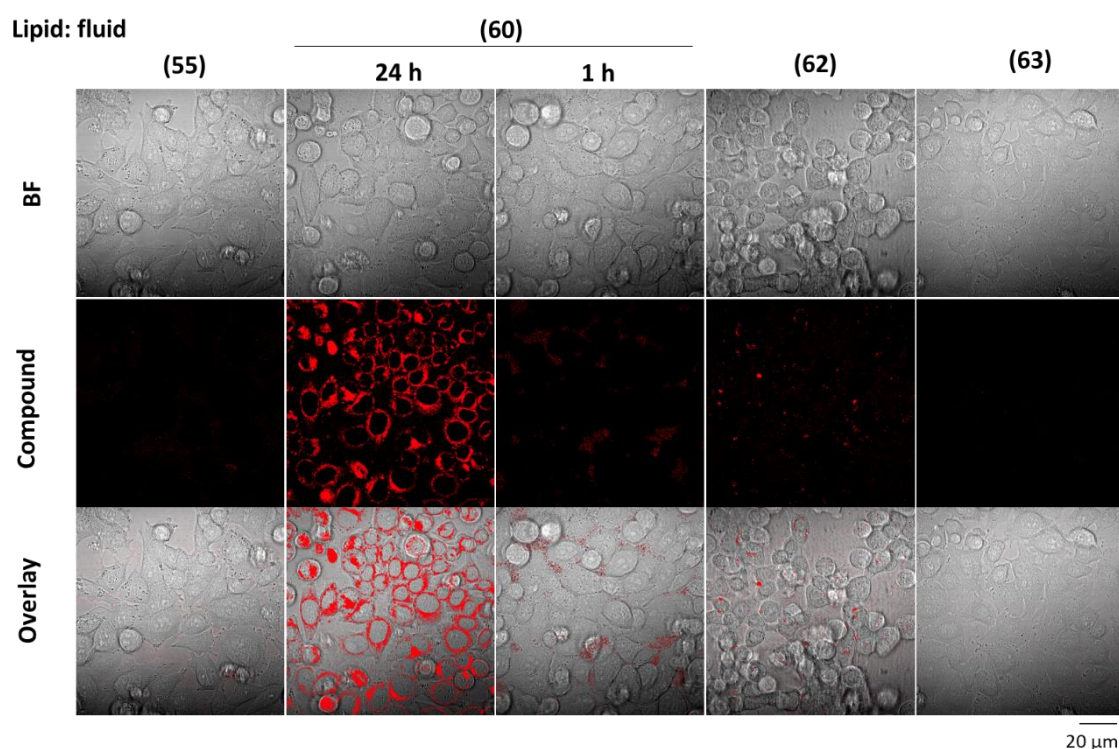


Figure 93: Cellular uptake of the heteroleptic bis(dipyrrinato)Zn^{II} complexes **55**, **60**, **62**, **63** in fluid liposomes of varying fluidity after long-time incubation (24 h) with HeLa cells. Intracellular accumulation was detected using light sheet confocal fluorescence microscopy (Zeiss LSM 880 Airyscan, Objective: 63x/1.40 OIL, λ_{exc} =630 nm, λ_{em} =640-750 nm). BF – bright field image. No co-staining was applied. (λ_{exc} =630 nm, λ_{em} =640-750 nm). Scale bar 20 μ m.

Significantly reduced signal was observed for the complexes in the fluid state liposomes, presumably due to the decreased metabolic stability of these lipid formulations. There were no principal differences in the intracellular distribution, indicating that the liposomal formulation plays a predominant role in the cell uptake.

However, co-applying the liposomal formulation for twenty-four hours changed the staining pattern.

The sharper intensity of complex **60** is retained also in the gel-phase lipid composition, as it can be observed in **Figure 94**. Conversely from what observed for the fluid liposomes, a considerable fluorescence intensity is observed even from complexes **62**, and, at lower intensities, from complexes **63** and **64**.

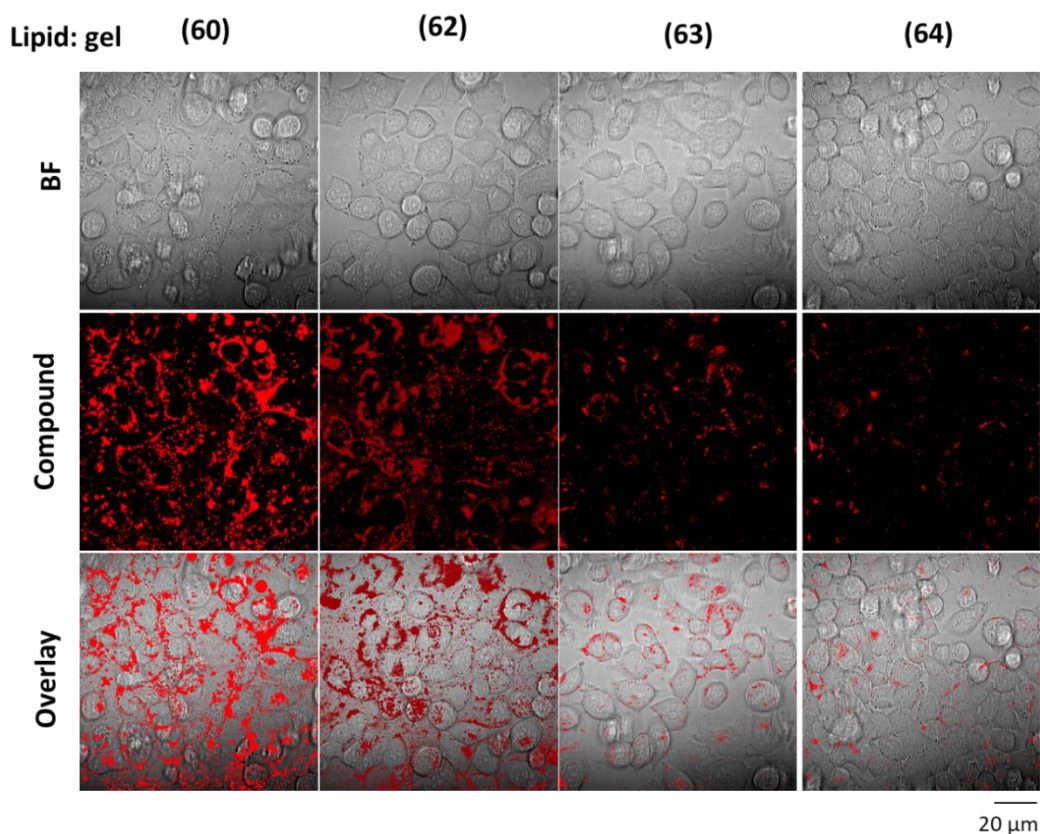


Figure 94: Cellular uptake of the heteroleptic bis(dipyrrinato)Zn^{II} complexes **60**, **62**, **63**, **64** in gel liposomes of varying fluidity after long-time incubation (24 h) with HeLa cells. Intracellular accumulation was detected using light sheet confocal fluorescence microscopy (Zeiss LSM 880 Airyscan, Objective: 63x/1.40 OIL, λ_{exc} =630 nm, λ_{em} =640-750 nm). BF – bright field image. No co-staining was applied. (λ_{exc} =630 nm, λ_{em} =640-750 nm). Scale bar 20 μ m.

Upon closer examination of twenty-four hours exposure of the best performing complex **60** (**Figure 95**), several differences can be observed.

The majority of fluorescent signal is located inside the cells in the fluid bilayer formulation. Though, it appears to be more enhanced in vesicular-like perinuclear structures, with a significant amount of signal remaining in the cytoplasm.

Interestingly, there is no observable overaccumulation at the plasma membrane, which contrasts with the previously reported interaction of fluorescently labelled liposomes that often enter the cells through fusion with the plasma membrane.^[308]

Regardless of the bilayer fluidity, the liposomal formulations containing complex **60** appear to enter the cells *via* vesicular trafficking pathways.

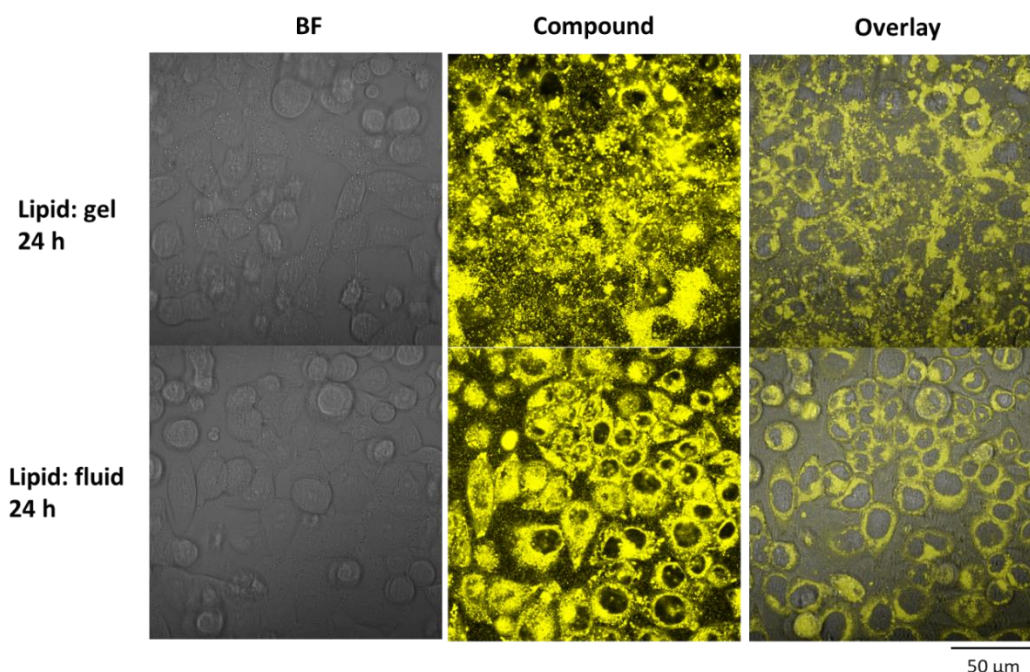


Figure 95: Cellular uptake of the heteroleptic bis(dipyrrinato)Zn^{II} complex **60** in liposomes of varying fluidity after long-time incubation (24 h) with HeLa cells. Intracellular accumulation was detected using light sheet confocal fluorescence microscopy (Zeiss LSM 880 Airyscan, Objective: 63x/1.40 OIL, λ_{exc} =630 nm, λ_{em} =640-750 nm). BF – bright field image. No co-staining was applied. (λ_{exc} =630 nm, λ_{em} =640-750 nm). Scale bar 50 μm.

Hence, the approach of encapsulating the complexes within liposomes has proven to enhance the uptake efficiency of the heteroleptic bis(dipyrrinato)Zn^{II} complexes **55**, **60**, **62**, **63**, **64**, resulting in a good cellular staining of HeLa cells.

Further investigations are ongoing, along with tests on animals.

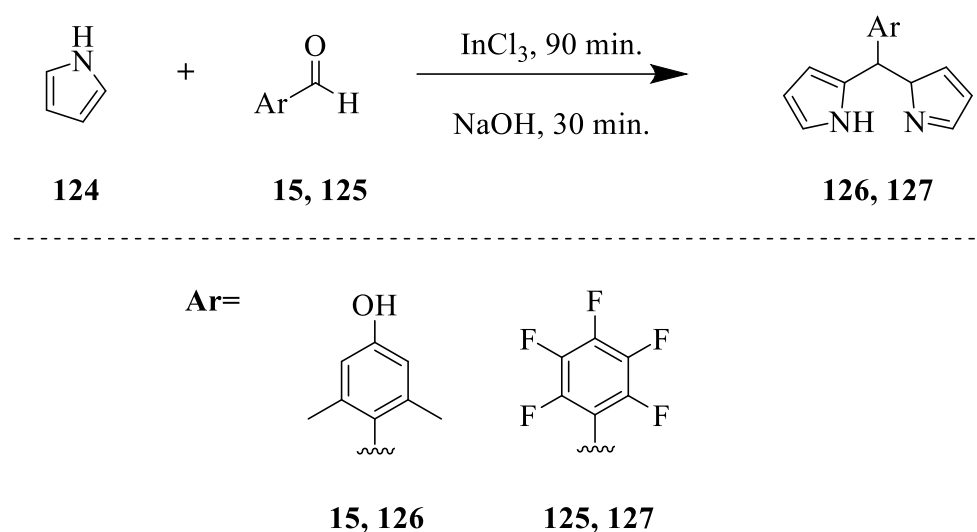
3.9 Schiff-base dipyrin macrocycles

In this paragraph are outlined the results obtained during a visiting period at the EastChem School of Chemistry of Edinburgh, in the group of Prof. J. B. Love within the context of a collaboration between our group and the University of Edinburgh.

The scientific goal mainly aimed to the synthesis of dipyrin-based macrocycles, which have emerged as versatile molecular platform suitable for a broad range of fields.^[309–311] Due to their unique properties they have demonstrated promise in sensing, detection, supramolecular chemistry and photocatalysis, particularly in multi-electron redox processes involving small molecules.^[309,311,312]

Our attention was focused on Schiff base cavities composing of a dipyrromethene unit and two imine components condensed in a cyclic manner.

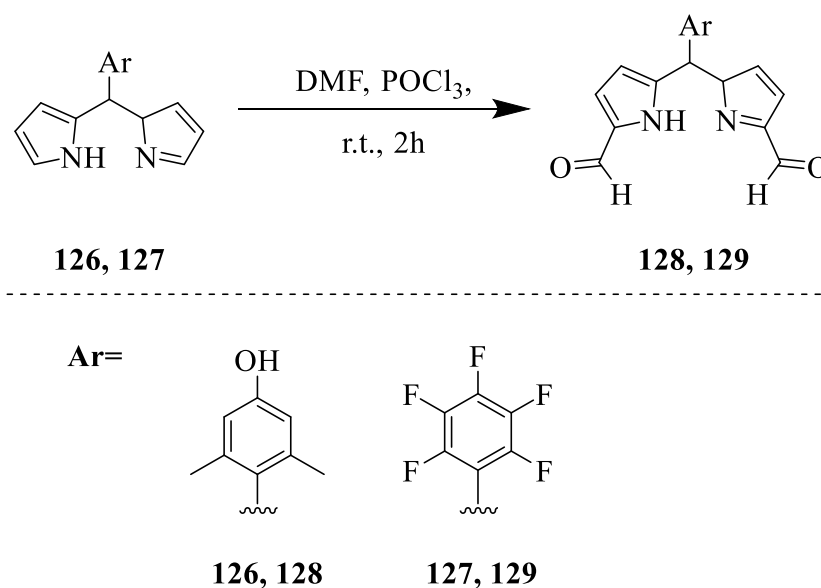
The synthesis of the macrocycles requires the use of dipyrromethanes, as they are reactive to cyclization in comparison to their dipyrin counterparts.^[313] Nevertheless, as described in §3.1.1, the condensation that leads to the formation of the dipyrromethane itself compete with the formation of oligomers and porphyrins. As depicted in **Scheme 44**, the synthesis involved the condensation between pyrrole **124** and the aromatic aldehydes **15** and **125**, in the presence of indium trichloride (InCl_3).



Scheme 44: InCl_3 catalyzed condensation between pyrrole **124** and 4-hydroxy-2,6-dimethyl benzaldehyde **15** or 2,3,4,5,6-pentafluorobenzaldehyde **125** to obtain plain dipyrromethanes **126** and **127**.

The reaction was conducted with a large excess of pyrrole **124** (100 equivalents) which served as both a reactant and a solvent in the reaction.^[195,247] InCl₃ was chosen as the catalyst due to its good catalytic activity as Lewis acid.^[200,314] The reaction between pyrrole **124** and the 2,3,4,5,6-pentafluorobenzaldehyde **125** was solvent-free and straightforward. After ninety minutes of reaction at room temperature, NaOH was added to neutralize the reaction mixture for additional thirty minutes. The simple pyrrole was then recovered by distillation using a rotary evaporator and the dipyrromethane **127** was purified through crystallization in a (1:1) mixture of ethanol/water and obtained as a crystalline grey powder with a yield of 78 %. The condensation between pyrrole **124** and 4-hydroxy-2,6-dimethylbenzaldehyde **15** required the addition of small amounts of methanol to dissolve the aromatic aldehyde **15**, insoluble in pyrrole **124**. Differently from compound **127**, the crystallization process did not yield to the pure product. Thus, the crude residue was purified with column chromatography, packed with alumina gel. The dipyrromethane **126** was isolated with a yield of 20 %. The relative low yield can be due to the formation of different byproducts.

The introduction of formyl groups in α positions of the dipyrromethane core was achieved through Vilsmeier-Haack reaction. The synthesis was carried out using the same conditions for both compounds **126** and **127**. To a solution of dipyrromethane (either **126** or **127**) in DMF at 0°C, two and a half equivalents of phosphorous oxychloride were dropwise added (**Scheme 45**).



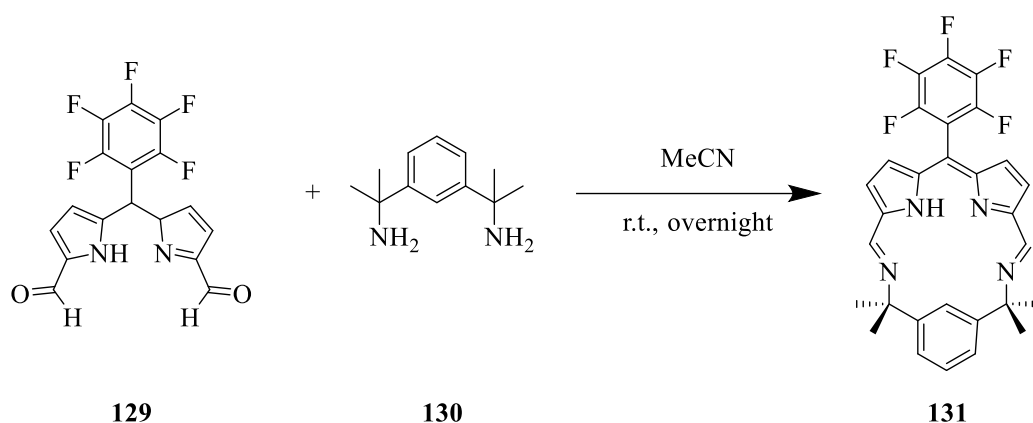
Scheme 45: Vilsmeier-Haack formylation of the dipyrromethanes **126**, **127** to obtain the 2,9-bisformylated dipyrromethenes **128**, **129**.

In both cases the reaction mixture turned immediately violet. After few minutes, the reaction was allowed to stir at room temperature for two hours. The reaction was then stopped and carefully quenched with a saturated solution of sodium acetate (NaOAc). Subsequently, the 2,9-bisformylated dipyrromethane **129** was purified through crystallization in a (1:1) mixture of ethanol/water. The resulting crystals were then collected, washed several times with hexane and then dried overnight under vacuum to obtain compound **129** as black crystals, with a yield of 50 %.

On the other hand, the crystallization of compound **128** did not lead to a pure product. The crude residue was then processed *via* column chromatography using alumina gel as stationary phase. The desired 2,9-bis-formylated dipyrromethane **128** was obtained as a black powder with a yield of 35 %.

The formation of the macrocycle **131** was then carried out. According to a literature procedure,^[315] the synthesis (**Scheme 46**) involved an imine-Schiff condensation between the 2,9-bisformylated dipyrromethane **129** and the 2,2'-(1,3-phenylene) bis (propan-2-amine) **130**, previously synthesized,^[316] in acetonitrile at room temperature, overnight. The macrocyclic product **131** precipitated spontaneously from the reaction mixture. Thus, after filtration and washing the desired product **131** was isolated as a reddish powder with a yield of 60%.

The disappearance of the *meso* proton signal (at 5.82 ppm) in the ¹H-NMR of compound **131** indicates the spontaneous dehydrogenation of the dipyrromethane to yield the corresponding dipyrin.

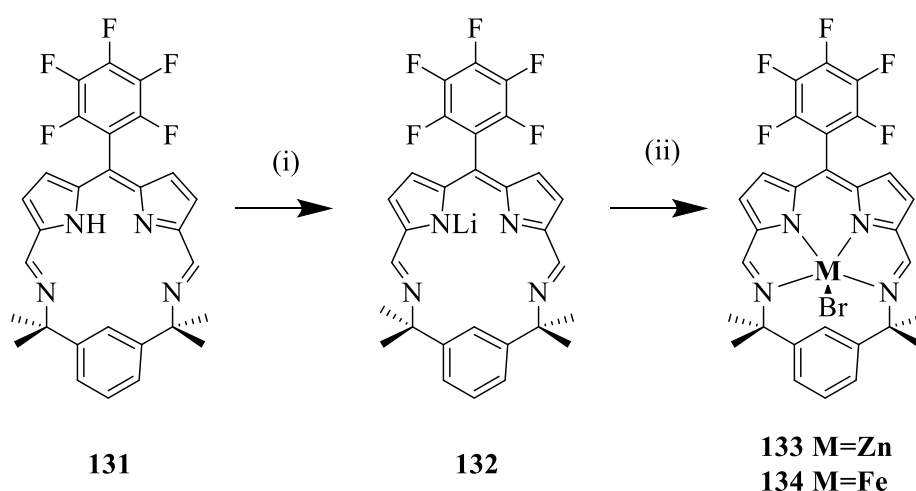


Scheme 46: Imine Schiff condensation between the 2,9-bisformylated dipyrromethane **129** and the amine derivative **130** to obtain the macrocyclic [1+1] cavity **131**.

The constrained cavity [1+1] Schiff-base dipyrin macrocycle **131** comprised a N₄ donor pocket which can accommodate several metal ions.

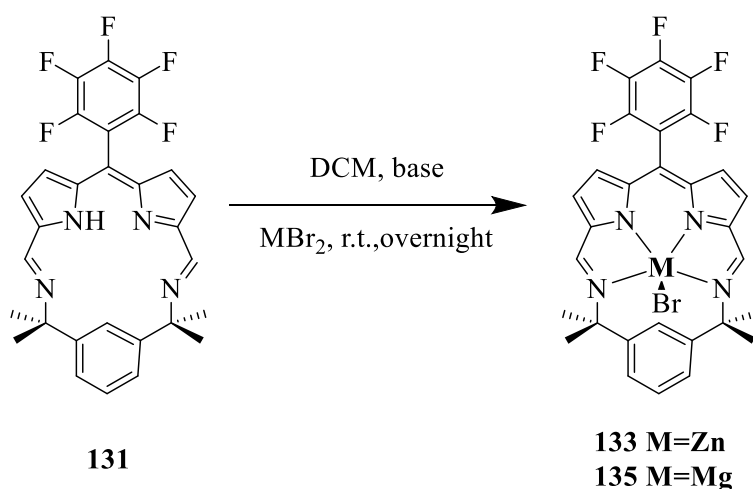
According to a procedure established in the group of Prof. Love,^[313] the introduction of metals into the cavity **131** is achieved by initially generating the lithium complex **132**, which after transmetallation with the metal salt, either ZnBr₂ or FeBr₂, generate the metal bromide complexes **133** and **134**, through salt elimination (**Scheme 47**).

Lithium bis(trimethylsilyl)amide LiN(SiMe₃)₂ is a strong non nucleophilic base, which deprotonates the nitrogen atom of the dipyrin core. It is a highly reactive compound that quickly reacts with water and atmospheric oxygen, therefore it should be handled and stored in an inert atmosphere. For this reason, the synthesis outlined in **Scheme 47** was conducted in a nitrogen-purged glovebox. The ¹H-NMR spectrum of the Li-complex **132** indicated the disappearance of the pyrrole-proton signal (at ca. 12.5 ppm for **131**) and the occurrence of a broad singlet peak at 1.47 ppm in the ⁷Li-NMR spectrum, consistent with the reported findings. Additionally, these analytics confirmed the purity of the product **132**, which did not require any purification process. Furthermore, it should be underlined that the NMR analyses were carried out using a J. Youngs NMR tube, as the compound is stable only under inert conditions. Compound **132** exhibited a remarkable red luminescence in toluene, which is significantly diminished in the analogous complexes **133** and **134**, isolated with very low yields, respectively 10 % and 5%.



Scheme 47: Synthetic pathway to obtain the metal bromide complexes **133** and **134** through the formation of the Li-complex **132** starting from the macrocyclic [1+1] cavity **131**. (i) 1equiv. of LiN(SiMe₃)₂, toluene, r.t., 16 h. (ii) ZnBr₂ or FeBr₂, toluene, r.t., 16 h. The reactions were conducted in a nitrogen-purged glovebox.

While the glove box remains a valuable tool for working with air-sensitive materials, it does have some inherent drawbacks, particularly regarding scaling up reactions. Therefore, alternative approaches for conducting the synthesis in a non-inert environment were explored. To overcome the limitations imposed by the use of $\text{LiN}(\text{SiMe}_3)_2$, the insertion of Zn^{II} into the cavity **131** involved the use of 1,4-diazabicyclo[2.2.2] octane (DABCO)^[317,318] as base (**Scheme 48**). A solution of compound **131** in dichloromethane was treated with one equivalent of DABCO and ZnBr_2 . An immediate change of the solution color from dark green to intense violet was observed. The reaction was stirred overnight at room temperature. The precipitate formed during the reaction was filtered and washed, resulting in a purple powder. Apart from the disappearance of the nitrogen proton (at ca. 12.5 ppm for **131**) no other significant shifts were observed in the ^1H .NMR spectrum of the obtained powder. However, the MALDI-TOF spectrum showed the expected molecular ion at 666.79 m/z, indicating the axially coordinated bromide ligands presents in the square pyramidal geometries showed by the Zn-complex **133**, isolated with 20 % of yield, as expected.^[315] The reaction conditions for the synthesis of the Mg-complex **135** (**Scheme 48**) were the same described above, except for the use of a different base, namely the 2,6-lutidine. This change was simply made because of a literature procedure,^[319] where they used this base to coordinate Mg^{2+} with a porphyrin, since the Mg-complex **135** has never been reported in the literature. In a similar way, compound **135** precipitated during the reaction and was isolated as an orange powder with a yield of 15 %. The MALDI-TOF spectrum showed the expected molecular ion at 624,04 m/z, confirming the ancillary bromide ligand retained also in the cavity of the Mg-complex **135**.



Scheme 48: Complexation reactions of the macrocyclic [1+1] cavity **131** with ZnBr_2 or MgBr_2 in DCM in the presence of a base to obtain the bromide complexes **133** and **135**. The reaction was conducted in a non-inert atmosphere.

The absorption spectra of compound **131** and **133** in THF are reported in the literature.^[315] To obtain a comprehensive insight to their emissive properties, the photophysical properties of compounds **131**, **133** and **135** were investigated in toluene.

The absorption profile of the free-base macrocycle **131** (orange plot, **Figure 96**) exhibits a broad band centered at 513 nm. The insertion of the Zn²⁺ into the cavity causes a noticeable increase in the band intensity (red plot, **Figure 96**) measured for the Mg complex **135**, without any further modifications in the absorption profile. On the other hand, the absorption profile of the Zn complex **133** shows the appearance of a small band, round 410 nm (blue plot, **Figure 96**). Additionally, the characteristic absorption band displays an initial bump at ca. 510 nm with a peak registered at 559 nm, a significant longer wavelength in comparison to compounds **131** and **135**.

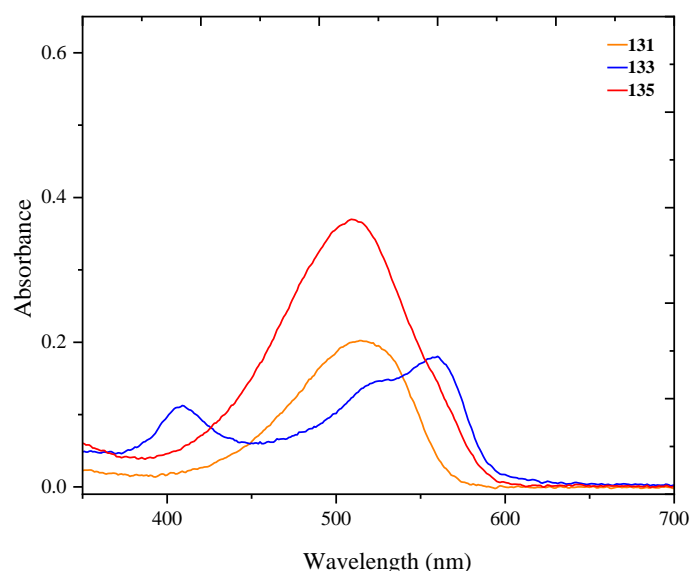


Figure 96: UV/Vis absorption spectra of the macrocyclic [1+1] cavity **131** and the corresponding bromide Zn-**133** and Mg-**135** complexes in 10⁻⁶M solutions in toluene, at 20 °C.

The emission profile of the free-base macrocycle **131** is characterized by a broad structureless band, ranging from 525 to 800 nm, with a maximum at 607 nm (orange plot, **Figure 97**). In **133**, a similar emission profile is observed in the range between 525-800 nm (blue plot, **Figure 97**). However, small shoulders are observed at 550 nm, 605nm and a more pronounced one at 660 nm. Furthermore, the emission maximum is observed at 582 nm, at lower wavelength compared to compound **131**. On the other hand, the emission profile of **135** (red plot, **Figure 97**), is shifted toward lower energies, with a peak at 624 nm and a distinct emission shoulder

at around 690 nm. It is important to underline that, in addition to the metal, either Zn²⁺ or Mg²⁺, coordinated to the four nitrogen atoms, there is also an ancillary bromide ligand within the cavity. Because of its heavy atom effect,^[320] it can be observed a tangible impact of its presence in the emission intensity, spectral shape and lifetime, as outlined in **Table 19**. One of the primary manifestations of this effect is the perturbation of the excited-state energies;^[11] thus the bromine atoms present in the complexes **133** and **135** can lead to changes in the vibrational structure of their excited state, resulting in the appearance of the humps observable in their emissive profiles (blue and red plots, **Figure 97**). Additionally, the bromine atom can induce changes in the electronic density distribution within the molecules, thereby affecting the nature and strength of intermolecular interactions.^[11]

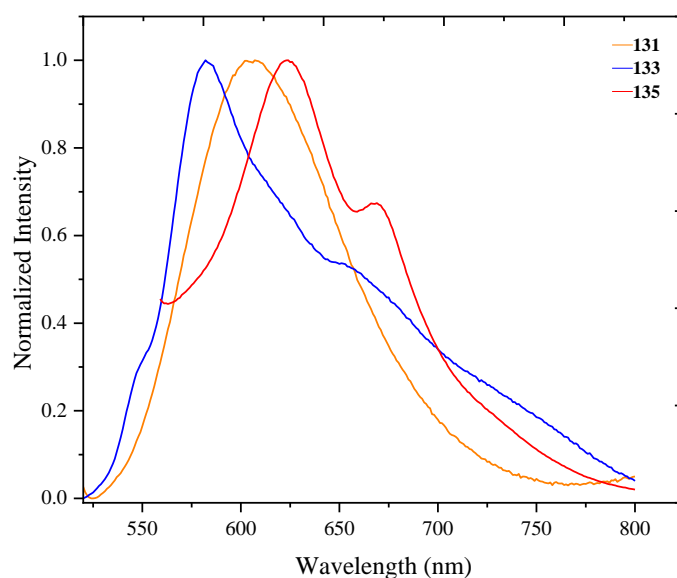


Figure 97: Emission spectra of the macrocyclic [1+1] cavity **131** and the corresponding bromide Zn-**133** and Mg-**135** complexes compounds complexes in 10⁻⁶M solutions in toluene, at 20 °C. (λ_{exc} = 500 nm for **131** and **133** and 520 nm for **135**).

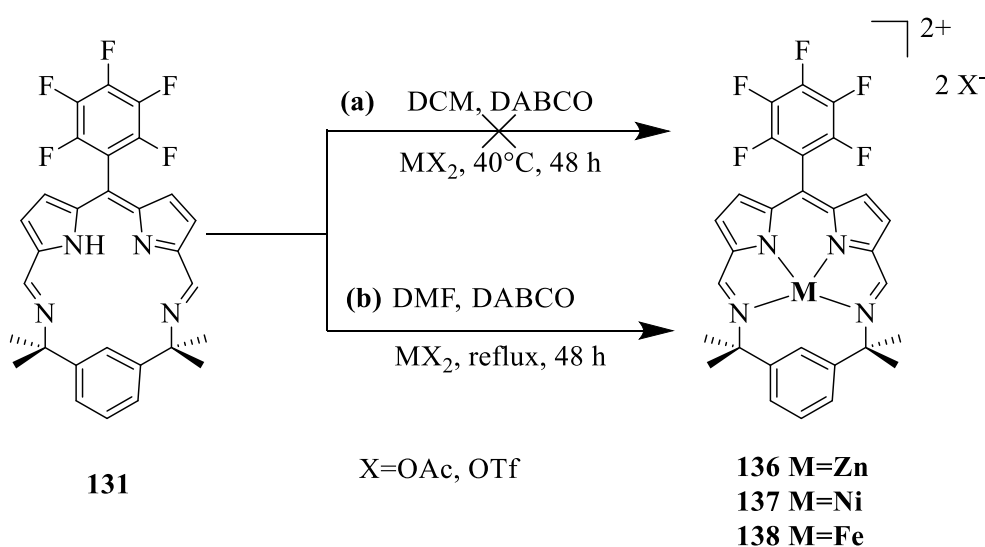
Both zinc and magnesium metals play a structural role. It is possible that the observed bands are a result of ligand-centered transitions. The interplay of electronic, spin-orbit and structural effects introduced by the heavy atom bromine is expected to be more relevant in terms of populating a triplet state, which cannot be detected under the current conditions. Further examination under an inert atmosphere and at low temperature, such as 77 K, are required.

In comparison to compound **131**, the corresponding complexes **133** and **135** show lower quantum yields, as outlined in **Table 19**.

Table 19: Photophysical properties of the macrocyclic [1+1] cavity **131** and the corresponding bromide Zn-**133** and Mg-**135** complexes compounds in toluene. ^[a] Quantum yields were determined by the relative method, using Ru(bpy)₃Cl₂ ($\Phi = 0.54$ in water, 22 °C). ^[b] Exciting with a NanoLED source at 570 nm.

Compound	λ_{abs} [nm]	λ_{em} [nm]	Φ ^[a]	τ ^[b] [ns]
131	513	607	0.32	1.2
133	559	582	0.01	1.5
135	512	624	0.10	2.2

The free-based cavity **131** showed favorable photophysical properties, such as a quantum yield of 30% circa in toluene (**Table 19**). To avoid the aforementioned photophysical issues caused by the ancillary bromide ligand, different precursors have been selected. The metallic precursors employed were acetate salt, such as Zn(OAc)₂ and Ni(OAc)₂·4H₂O or triflate salt, such as Fe(OTf)₂. As outlined in **Scheme 49a**, the first approach involved the use of dichloromethane as a solvent at 40 °C in the presence of DABCO, acting as base. Despite the reactions were carried out for 48 hours, no conversion of the starting macrocycle **131** was observed, regardless the different metal salts used. Therefore, the reactions were conducted in DMF to increase the temperature (**Scheme 49b**).



Scheme 49: Complexation reactions of the macrocyclic [1+1] cavity **131** with Zn(OAc)₂, Ni(OAc)₂·4H₂O or Fe(OTf)₂ to obtain the complexes **136**, **137** and **138**. The reactions were conducted in the presence of DABCO in (a) DCM, reflux 40 °C, 48 hours. (b) DMF, reflux 80 °C, 48 hours.

To a solution of macrocycle **131** in DMF, two equivalents of DABCO and one equivalent of Zn(OAc)_2 were added. The reaction mixture turned from dark red to purple, which was highly red emitting upon UV irradiation. The complete conversion of the starting material was confirmed after 48 hours by TLC analysis, indicating the presence of a new luminescent spot. After workup with water and removal of the dichloromethane from the extracted organic phase, the obtained purple powder was washed with hexane and dried under vacuum. The target Zn-complex **136** was obtained with a yield of 60 %. The MALDI-TOF spectrum showed the expected molecular ion at 585,18 m/z. The addition of $\text{Ni(OAc)}_2 \cdot 4\text{H}_2\text{O}$ to the orange solution of the macrocycle **131** in the presence of DABCO resulted in a color change to deep blue. The reaction took 48 hours, also in this case, and the Ni-complex **137** was isolated as a blue powder with a yield of 50 %. The MALDI-TOF spectrum showed the expected molecular ion at 579,11 m/z. The complexation with Fe^{2+} involved the use of its triflate salt instead. To a solution of the macrocycle **131** was added, along with two equivalents of DABCO. The solution turned immediately dark brown, almost black. After 48 hours, the reaction was stopped. The desired Fe-complex **138** was isolated as a black powder, with a yield of 32 %. The MALDI-TOF spectrum showed the expected molecular ion at 577,36 m/z. Photophysical and electrochemical investigations of the new compounds are currently ongoing.

4. Subproject_3DNActive

The objective of the research package being investigated in this chapter is the outcome of a collaboration that took place within the framework of the “3DNActive” program, financed by the Alexander-von-Humboldt foundation. The target of this project is to develop innovative photoresists for two-photon lithography, which could enable the selective adhesion of eukaryotic cells on three-dimensional (3D) micro-scaffolds *via* DNA hybridization.

Some of the results presented below have been published in the following scientific article: “Selective positioning of different cell types on 3D scaffold via DNA hybridization”; E. D. Lemma, R. Tabone, K. Richler, A. K. Schneider, C. Bizzarri, F. Weth, C.M. Niemeyer, M. Bastmeyer. *ACS Appl. Mater. Interfaces* 2023, 15, 11, 14048-14057.^[321]

4.1 General background

In traditional cell culture methods, cells are grown in a flat, two-dimensional (2D) surface, which does not accurately mimic the complex and dynamic three-dimensional (3D) environment of living tissue.

In contrast, 3D scaffolds provide a more realistic model of the *in-vivo* environment, allowing for better study of cell behavior, cell signaling and tissue development. Additionally, this type of framework can be designed for mimicking specific tissue structures and properties, such as mechanical stiffness and porosity, which play a crucial role in cells physiology.

Among the plethora of additive manufacturing techniques, which enable the fabrication of scaffolds with defined geometries replicating structures of typical cellular environments, 3D direct laser writing (DLW) is a peculiar, rapidly evolving tool.^[322]

DLW is a lithography technique based on multi-photon absorption, which allows polymerizing a photosensitive material in three dimensions with a resolution down to 100 nm.^[323] This technique has provided a method to create structures and scaffolds for 3D cell culture and allowed the investigation the complex interplay between cells and the surrounding microenvironment.

As an example, structures for single-cell force measurements have been developed,^[324] moreover, scaffolds surface properties can be modified to selectively induce cell adhesion.

However, control over the possibility of selectively positioning different cell types on different areas of the same structure is missing. This is mainly due to the limited specificity of the used cell-anchoring agent (e.g., an extracellular matrix protein like fibronectin).^[325]

A possible approach to address this issue includes antigen/antibody binding between cell surface antigens and the 3D structures.

Despite being a well-established technique in imaging (e.g., fluorescence microscopy and fluorescence-activated cell sorting), antibody-based functionalization remains extremely challenging for selective single-cell-type tagging. Indeed, most antibodies bind epitopes which are not specific of only one cell type, as different cell types usually express similar antigen epitopes on their membranes.

Therefore, a more selective technique, *i.e.*, DNA base pair hybridization, was identified in the “3DActive” project as a more promising way to obtain controlled 3D biological microenvironments.^[321]

In particular, the goal of the project was the development of a 3D structure obtained *via* two-photon lithography (2PL), which could be functionalized through single-stranded DNA (ssDNA), with the aim to achieve a precise spatial control of cell positioning using selective hybridization. The functionalization potential was achieved by developing a novel photoresist for 2PL, which could be decorated with ssDNA throughout a UV-induced click reaction, namely a 4+2 cycloaddition.

From a practical perspective, my contribution in this work was to synthesize the UV-reactive molecule included in the photoresist, hereafter referred as photoenol (**PE**)

Specifically, as depicted in **Figure 98**, **PE** was designed to contain two post-functionalization sites within the same molecule.

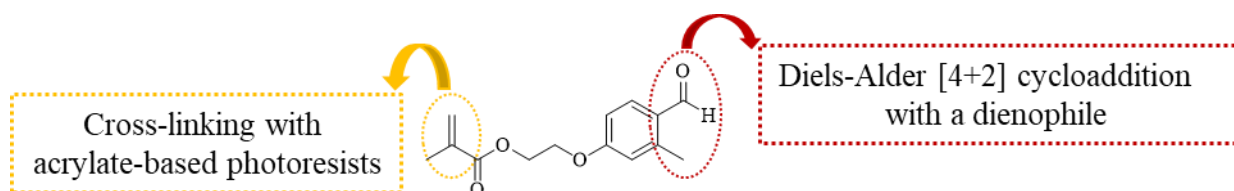


Figure 98: Schematic representation of the photoenol structure with the conjugation sites moieties used for post-functionalization. In the yellow box is highlighted the site for the cross-linking with photoresist; in the red box is underlined the site for the click cycloaddition.

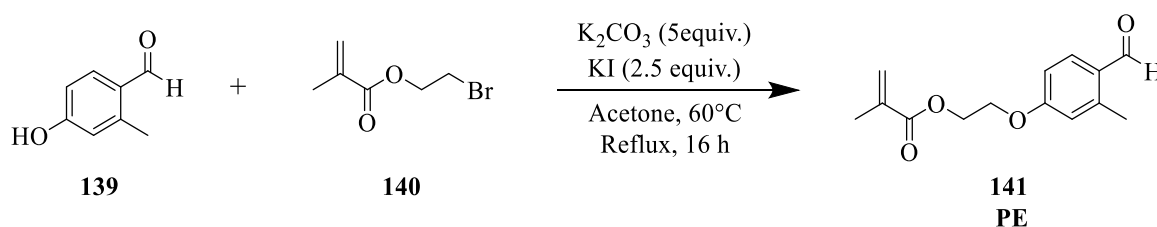
More specifically:

- A methacrylate tail (highlighted in the yellow box in **Figure 98**) which enables the crosslinking with the acrylate-based photoresists, *i.e.*, PETA and TPETA, during the 2PL polymerization process;
- An *o*-methylphenyl aldehyde, (highlighted in the red box in **Figure 98**) which, upon UV irradiation, undergoes photoisomerization, thus generating a hydroxy-*o*-quinomethanes species.^[326,327] The formed adduct can therefore face a [4+2] click conjugation, based on a Diels-Alder cycloaddition, in the presence of a dienophile, such as functionalized maleimides, by *endo* approach, involving the maximum π -orbital overlap.

4.2 Synthetic procedure

PE obtained from a Williamson ether Synthesis, as depicted in **Scheme 50**. This type of synthesis usually involves the reaction of an alkoxide ion with a primary halide *via* an S_N2 nucleophilic substitution.^[328]

In this specific case, the alkoxide ion was generated *in situ* by deprotonation of 4-hydroxy-2-methylbenzaldehyde **139** with potassium carbonate (K₂CO₃) in acetone, at 60 °C for thirty minutes. Potassium iodide (KI) was added to the reaction system because it increases the reactivity of the obtained alkoxide.



Scheme 50: Williamson ether synthesis between 4-hydroxy-2-methylbenzaldehyde **139** and 2-bromoethyl methacrylate **140** to obtain 2-(4-formyl-3-methylphenoxy) ethyl methacrylate **141**, namely photoenol (**PE**).

It was advisable to generate such ion because the conjugated base, in comparison to the corresponding phenol derivative is a better nucleophile, therefore more prone to react with the electrophilic carbon present in the halide undergoing the reaction.

Once complete deprotonation was confirmed by TLC, half equivalent of 2-bromoethyl methacrylate **140** was added dropwise to the reaction mixture, which was refluxed at 60 °C for sixteen hours, using an air-cooled condenser.

Compound **140** was deliberately used in significant defect because it was observed that, when used in equimolar ratio to compound **139**, the formation of polymeric products was favored instead of the desired product.

The crude residue was subsequently purified through flash column chromatography on silica gel, which affords the product, 2-(4-formyl-3-methylphenoxy) ethyl methacrylate) **141** with a 19% of yield. This low yield can be attributed to the non-equimolar use of reagents. The starting 4-hydroxy-2-methylbenzaldehyde **139** was recovered as the last fraction from the column.

4.3 Post-functionalization

The obtained photoenol (**PE**) was then mixed with two broadly two-photon lithography (2PL) photoresist (namely pentaerythritol triacrylate, PETA, and trimethylolpropane ethoxylate triacrylate, TPETA) in order to covalently bind maleimide-based compounds *via* a UV-induced photoenolization followed by Diels-Alder reaction.^[321]

The photoenol-mediated conjugation strategy proceeds rapidly at ambient temperature in a wide range of polar solvents and for this reason is widely applied as strategy for constructing polymeric building blocks for 3D structures.^[329]

Thus, after 2PL fabrication, the photoresist could be locally exposed to UV radiation, hence the photo-enolic moiety included in the material could react with maleimide-tagged single-strand DNA (ssDNA) under UV light, resulting in ssDNA being locally covalently bound to the 3D architectures (**Figure 99**).

To obtain a selective adhesion of cells on the 3D scaffolds, they were functionalized with the complementary ssDNA (e.g., via inclusion in the cell membranes) and seeded on the 3D structures. Hybridization between complementary ssDNA strands finally allowed for the attachment of cells on the functionalized structures.

Ongoing studies are intended to clarify whether the process can occur even in absence of the (PE), under specific conditions.

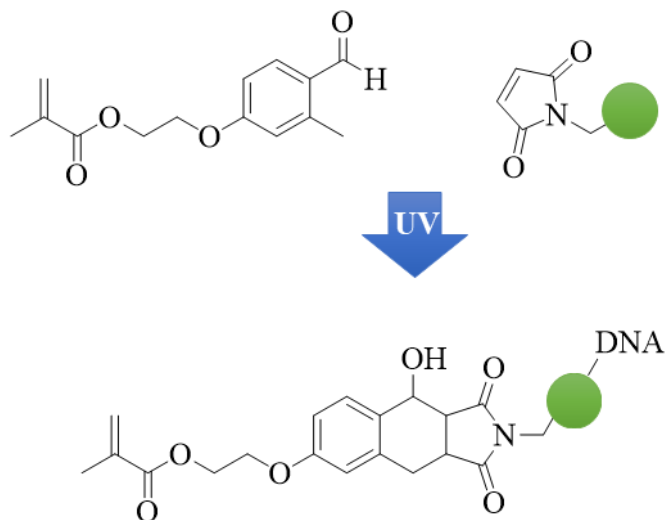


Figure 99: Workflow of the functionalization procedure. Under UV irradiation the functionalised maleimide and PE undergo a Diels-Alder cycloaddition which leads to the formation of the adduct subjected to 2PL process.

4.4 Further strategy

As previously stated, the topical reaction that enables the functionalization of the (PE) with various maleimide derivatives is the Diels-Alder, which is regarded as a useful strategy in organic and macromolecular syntheses.^[330]

To further enhance the scope of the work and observe how changes in the starting material could introduce modifications in the final 3D fabricate, it was decided to pursue a similar functionalization of anthracene. This is a well-known *across*- and *inner*-ring diene, largely employed in Diels-alder reaction forming anthracene cycloadducts. In order to be able to perform cross-linking with photoresists, the starting molecule should contain a reactive polymerizable site.

The retrosynthetic strategy led to the selection of the molecule depicted in **Figure 100**, the 2-(methacryloyloxy) ethyl-anthracene-9-carboxylate.

As sketched out for the photoenol case (**Figure 98**), also the monomer **144** contain two post-functionalization sites within the same molecule, as depicted in **Figure 100**. In addition to the

methacrylate group which participates in the formation of the relatively short sequences of chemical bonds to join the polymer chain of the photoresist, the anthracene core is known to undergo [4+2] cycloadditions with dienophiles in the central ring.

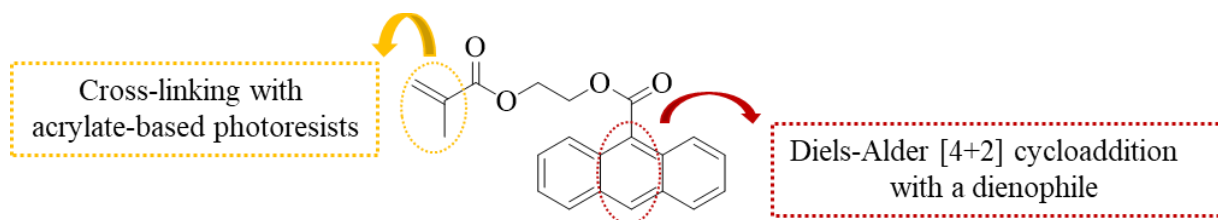
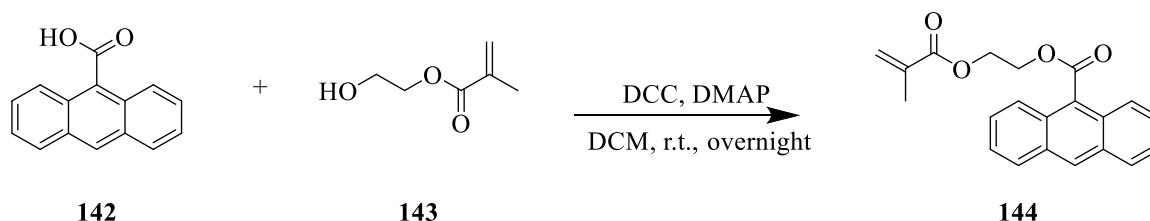


Figure 100: Schematic representation of the (**Ant-acrylate**) derivative that can be used as monomer for the fabrication of 3D structures. The conjugation sites moieties used for post-functionalization are shown in the colored box: in the yellow one is highlighted the site for the cross-linking with photoresist; in the red one is underlined the site for the click cycloaddition.

The regioselectivity of anthracenes at their 9,10-positions (central ring) over 1,4-positions (terminal rings) is guided by the relative aromatic stabilization energy of the two possible products, and also by harboring the largest orbital coefficients of the highest occupied molecular orbital (HOMO) at the 9,10-positions.^[331]

Compound **144** was obtained through a Steglich esterification (**Scheme 51**) between anthracene-9-carboxylic acid **142** and 2-hydroxymethyl methacrylate **143**. This coupling reaction, named after Wolfgang Steglich in 1978,^[332] involved the use of *N,N*-dicyclohexylcarbodiimide (DCC) as coupling reactant and 4-dimethylaminopyridine (DMAP), as a catalyst and transfer-reagent.^[333] The reaction was carried out at room temperature in dichloromethane and stirred overnight.



Scheme 51: Steglich esterification between anthracene 9-carboxylic acid **142** and 2-hydroethyl methachrylate **143** to obtain the corresponding 2(methacryloyloxy) ethyl anthracene-9-carboxylate **144**.

The crude residue was processed *via* column chromatography, packed on silica gel. The obtained product **144** was obtained as a yellow powder, highly blue luminescent, with a 17 % of yield.

Several kinetics studies on the reaction between anthracene and maleimide derivatives have been reported in literature, ^[334,335] it is therefore assumed that the novel compound highlighted in **Figure 100**, could be highly performant under our reaction conditions. Currently, studies are ongoing.

5. Conclusion

Bioimaging modalities play a pivotal role in aiding medical diagnosis, by offering valuable functional insights at the cellular level. In this regard, luminescence occurs as a fundamental phenomenon.

Among the plethora of optical-based techniques, far-red to near-infrared imaging has gained notable consideration. Within its distinctive spectral range, it presents prominent benefits, including low absorption and minimal auto-fluorescence from surrounding chromophores and tissues present in human body. These characteristics effectively reduce background interferences leading to an improvement in the tissue penetration.

Aware of the properties with which a bioimaging probe should be equipped, this thesis presents a collection of compounds that show meaningful potential in fulfilling these criteria. The strategic design involved the utilization of dipyrrens as a starting scaffold, which served as versatile platform for obtaining more sophisticated scaffolds.

5.1 *Meso* substituted plain dipyrrens

The design of the plain dipyrrens involved the incorporation of bulky aryl groups at the *meso* position to minimize the rotational motion around the bond and the integration with functional groups, such as hydroxyl and methoxyl to enhance solubility in polar solvents.

The route adopted for the synthesis of dipyrrens **11-19** relies on two essential reactions: a) condensation of 2,4-dimethyl-1*H*-pyrrole **1** and aromatic aldehydes **2-10** to afford the *meso* substituted dipyrromethane and b) one-flask transformation of the obtained dipyrromethane to the corresponding dipyrren. Several precautions were employed to increase the selectivity toward the dipyrromethane intermediate, such as diluting the reaction mixture, using an inert atmosphere, slow addition of the acid catalyst, and timely quenching of the reaction.

This refined process enabled the straightforward preparation of multigram batches of aryl *meso* substituted dipyrromethanes with a broad scope of substrates, but it requires chromatography to remove the blackish polypyrroles formed. The desired products were isolated with yields ranging from 15% to 79%.

The introduction of an alkyl chain, terminating with a sulfonate group, attached to the aromatic ring at the *meso* position of dipyrin **29**, resulted in favorable solubility in methanol but not in water. Conversely, the direct sulfonation of the dipyrin core provided water solubility of dipyrin **30**.

The photophysical investigation of the plain dipyrins **11-19** in toluene revealed intense absorptions between 448 and 483 nm, with emission centered between 500 and 554 nm, both in the visible part of the electromagnetic spectrum.

The plain dipyrin **29** showed absorptions in the same range, with an emission centered at 514 nm and a second emissive shoulder at 650 nm. The quantum yields are not particularly elevated, ranging between 2% to 16%. Moreover, the fluorescence lifetimes for the ligands **11-16** and **29** span from 1.4 to 1.8 ns. The stiffening of the core caused by introduction of highly sterically demanding groups in ligands **17-19** increases the average excited state lifetime before returning to the ground state. Fluorescence decays measured for these compounds are approximately 2 ns.

5.2 π -expanded dipyrins

To achieve a red-shifted emission, the π -conjugation of the synthesized plain dipyrromethene ligands was expanded *via* Knoevenagel condensation. Due to their strong nucleophilicity, the methyl groups in α position of the plain dipyrins were engaged in addition reactions with electron-rich aromatic aldehydes, leading to the formation of styryl groups featuring aromatic substituents.

Two different systems were employed: the classical and the microwave assisted condensations.

The first one, conducted under reflux conditions in toluene, involved the use of a Dean-Stark apparatus for the azeotropic distillation of the water formed during the reaction. Several plain dipyrins were expanded using this methodology, which required approximately twenty-four to thirty-six hours of reaction time. In each synthesis performed, the presence of both mono- and difunctionalized product was observed. The π -expanded dipyrins obtained with this method, specifically **33-39**, were isolated with yields ranging from 10% to 45%.

The second method entailed the Knoevenagel condensation upon microwave irradiation. The reaction, conducted in ethanol, was carried out for one hour in a microwave reactor. The π -

expanded dipyrrens obtained with this method were **44-48**, displaying yields ranging from 10% to 31%.

This new synthetic approach did not lead to a significant improvement in terms of yields; indeed, high power of the system has led to several side-products forming, reducing the selectivity towards the desired product. On the other hand, the reaction times have notably been reduced, *i.e.*, one hour compared to the longer reaction times required for the first method. previously needed. Nevertheless, the system is limited to a maximum volume of 5 ml, which implies the impossibility of carrying out a considerable reaction scale-up.

The heterogenization of the system can pave the way for more green and sustainable solutions. It is therefore not excluded that implementing these new techniques could also lead to an increase in efficiency and final yield in our systems. The synthetic design of this work involved obtaining symmetrical molecules. However, to take an additional step forward, it is deemed attractive to explore asymmetric functionalization with chiral compounds, which could, for instance, be derived from amino acids in their enantiomerically pure form.

The photophysical characterization of the π -expanded dipyrrens **33-39**, **44-48** in toluene provided evidence of the effective functionalization, showing absorption maxima between 511 nm to 641 nm, completed by emission profiles ranging between 600 nm up to 800nm, with peaks located around 589 nm to 665 nm. Thus, this type of modifications narrowed the $^1\pi-\pi^*$ gap of the dipyrrenato ligand considerably (**Figure 101**). The quantum yields of these ligands are ranging among 4% to 20 % with lifetimes in the order of 2.3 up to 4.2 ns.

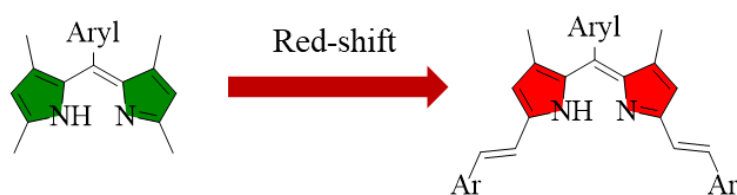


Figure 101: Effective functionalization strategy for achieving the red-shift emission from the plain dipyrrens, to obtain π -expanded systems.

5.3 Homo-and heteroleptic bis(dipyrrinato)Zn^{II} complexes

The obtained ligands were employed for the formation of both homo- and heteroleptic bis(dipyrrinato)Zn^{II} complexes.

The zinc, being a d¹⁰ metal, did not participate in any metal-centered transitions within the complexes. Nonetheless, its structural role was confirmed, displaying a tangible effect in rigidifying the system.

Specifically, similar to their precursor ligands, the homoleptic bis(dipyrrinato)Zn^{II} complexes **48-51**, formed by the simple dipyrin derivative (Homoleptic D, **Figure 102**) displayed absorption peaks in the range of 491-496 nm, with corresponding emission maxima between 508-522 nm. Notably, compared to the free-base ligands, these complexes are characterized by a significant increase in the quantum yield, showing a brighter green fluorescence with Φ ranging from 13% to 18% in toluene solution. The optical window of these systems lies below the NIR window. To address this deficiency, we shift toward the π -expanded systems.

The homoleptic bis(dipyrrinato)Zn^{II} complexes **52** and **53**, composing of the π -expanded ligands (Homoleptic D π , **Figure 102**) proved to be emissive in the far-red region, with emissions at 637 for compound **53** and 641 nm for compound **52**, because of the appended electron donating naphthalene rings and thereby the extension of conjugation. Compared to the free-base ligands they exhibit $\Phi=24\%$ in toluene, accompanied by an intense red fluorescence. However, their emission in polar solvents is limited because they suffer from symmetry breaking charge transfer processes (SBCT). Therefore, introducing dissymmetry was the strategy employed to overcome this limitation.

More precisely, the novel heteroleptic bis(dipyrrinato)Zn^{II} complexes **54-64** were designed as molecular architectures incorporating both a plain and a π -expanded dipyrin (Heteroleptic **Figure 102**), whose photophysical properties are cumulative in the absorption spectra.

The two absorption bands, corresponding to the ¹ π - π (LC) transition localized on each dipyrrinato ligand, presented very high absorption coefficient in DMSO solution (e.g., ϵ up to 9000 M⁻¹cm⁻¹ for the plain ligand and ϵ up to 38900 M⁻¹ cm⁻¹ for the π -extended ligand). Due to a rapid intraligand nonradiative transition, the emission spectra of the complexes **54-64** present a single emission profile, with maxima ranging from 635 to 644 nm accompanied by shoulders and a tail extending up to 820 nm.

The drastic difference in the electronic structures of the dipyrrens forming the heteroleptic complexes resulted in a favored emissive state, leading to extraordinary quantum yields, up to 51% in DMSO and 71% in toluene. These exceptional values make them highly attractive as far-red to near-infrared emitters

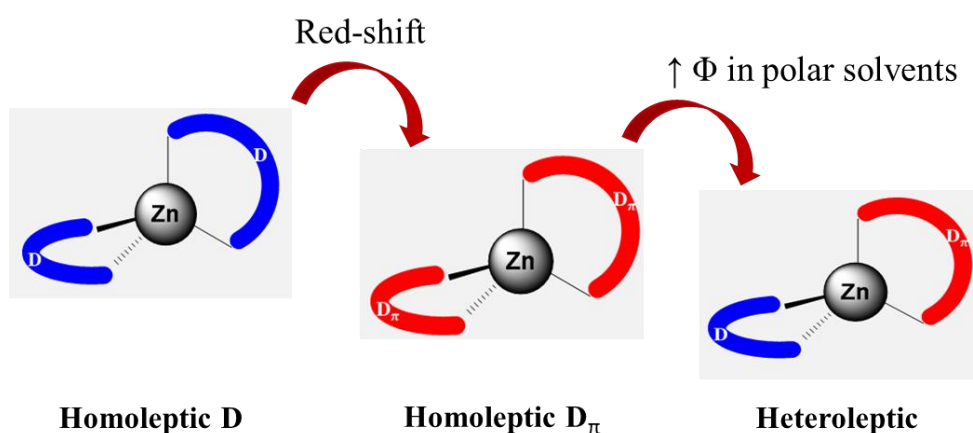


Figure 102: Schematic representation of the homoleptic and heteroleptic bis(dipyrinato) Zn^{II} complexes in this work.

The Stokes shifts of these fluorophores are relatively small (from 0.17 to 0.39·10³ cm⁻¹), as expected for fluorescent chromophores with localized excited states.

Nonetheless, it was observed that, regardless of which ¹π-π* band was photoexcited, the luminescence of all the heteroleptic complexes investigated, was exclusively emitted from the ¹π-π* state of the π-extended dipyrren. Thus, this effect prompted large *pseudo*-Stokes shifts between the absorption of the simple dipyrren and the emission of the π-expanded dipyrren, with values up to 4.6·10³ cm⁻¹.

Lowering the temperature to 77 K in the emission spectrum of the heteroleptic complex **57**, enabled the observation of the distinct electronic emission centered at 510 nm. However, this minor band, referable to the emission of the plain dipyrren composing the complex, was found to be negligible.

To delve deeper into the dynamics that occur after photoexcitation, transient absorption spectroscopy was performed. Early-time dynamics within one picosecond were observed, which can be ascribed to the formation of charge transfer states even in a nonpolar solvent, such as toluene.

Confocal laser microscopy has proven the ability of complexes **56**, **57**, **58**, **60**, **61** to cross lipophilic cell membranes of different cell lines. Counterstaining experiments evidenced the localization of complex **61** in the lysosomal compartment, with a Pearson coefficient of 0.85. This complex, which was the more promising, was further tested in fixed-cell experiments, showing its persistence within the cellular environment after cell fixation, without being degraded or released. By virtue of the large *pseudo* Stokes shift of the compound **61**, counterstaining imaging experiments on both live- and fixed cells confirmed the possibility of exciting the fluorophore at different wavelengths.

Some of the bulkier heteroleptic bis(dipyrrinato)Zn^{II} complexes synthesized are unable to penetrate the cells because of the absence of any functional groups apart from aromatic rings. To evade these intrinsic weaknesses, some complexes have been encapsulated in liposomes. Preliminary results have demonstrated that compound **60**, one of the most promising ones, once embedded within the liposome shell, is successfully taken up by cells. Current studies are ongoing to further investigate these promising results.

5.4 Expanded and azadipyrrins

The commercially available 2,4-diphenyl-1*H*-pyrrole **65** underwent a condensation reaction with benzaldehyde, to yield the 2,4,5,7,9-pentaphenyl dipyrrin **66**, which exhibited pronounced luminescence even in the solid state upon UV irradiation.

However, due to the bulky nature of the phenyl groups at the position 2 and, the formation of homoleptic bis(dipyrrinato)metal complexes by ligand **66** was not feasible. In a similar way, the attempt to form a heteroleptic complex between the π -expanded ligand **66** and the plain dipyrrin **15** did not yield successful results. In contrast, the dipyrrin **66** did successfully form a complex with boron difluoride, which allowed for the synthesis of the BODIPY derivative **69**.

As depicted in **Figure 103**, the peripheral phenyl groups attached to the core of the dipyrrin **66** resulted in a far-red emission, centered at 616 nm with a quantum yield of 17% in DMSO, demonstrating the effectiveness of this strategy to shift the emission toward the far-red alongside the rigidification of the system. Upon complexation with boron difluoride, a notable bathochromic shift occurred in both absorption and emission of the BODIPY derivative **69**, accompanied by a remarkable increase of the quantum yield, reaching values of 50% in DMSO.

Subsequently, the synthesis of the azadipyrrins **79** and **80** was successfully accomplished. Although the formation of the homoleptic bis(azadipyrrinato)Zn^{II} complex with compound **80** was not achievable, the ligand itself exhibit exceptional photophysical properties. The presence of the electronegative aza-N-atom lowered the HOMO-LUMO energy gap, thus resulting in a significant red-shift emission of the azadipyrrin **80**, centered at 642 nm (**Figure 103**). These results have thus confirmed the potential of this atom-ring modification.

Nevertheless, it should be underlined that the complexation with metals for both the expanded systems **66** and **80** was not possible because of steric reasons. Thus, with these results in hands, one strategy adopted and described in §3.6.2 was the synthesis of the azadipyrrin **82**, which replaces the four phenyl groups present in **80**, with four methyl groups that can undergo further functionalization. Further studies are ongoing.

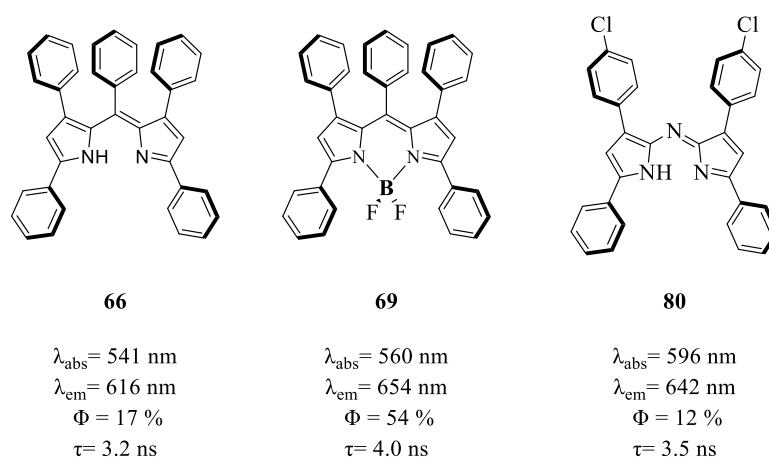


Figure 103: Chemical structures and photophysical properties of compounds **66**, **69** and **80** in DMSO.

5.5 Benzofused systems

To broaden the scope further, the exploration of new strategies for achieving molecules with narrow HOMO-LUMO gaps has led to the investigation of benzofused systems, in which annulated aromatic rings are incorporated into the pyrrole unit.

A detailed description of the methods used for obtaining these systems has been provided in §3.7 and will not be further repeated. However, among all the strategies adopted, the most effective ones have led to the formation of the benzo[*a*]fused dipyrrens **100** and **108**, reported in **Figure 104**.

Despite the purity of these compounds has not been unequivocally determined due to their changeling handling, they are believed to possess highly desirable properties.

While the use of these high bulky aromatic structures may initially raise concerns about their effectiveness within the cellular context, the introduction of sulfonate groups directly attached to the aryl rings can be a promising strategy.

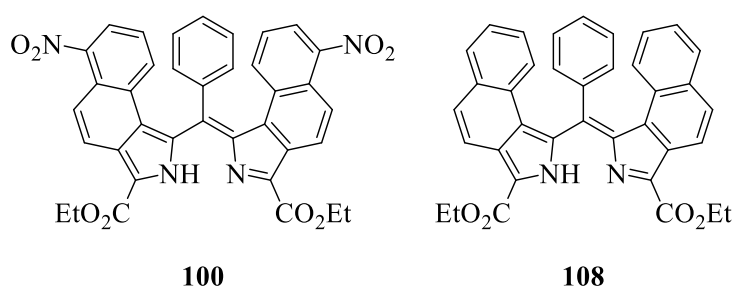


Figure 104: Benzo[*a*]fused dipyrriins obtained in this work.

5.5 Macrocycles

The visiting period at the University of Edinburgh, entailed the further exploration of functionalization pathway using dipyrriins as building block.

Specifically, the focus was on the condensation reactions with diamines, leading to the formation of the macrocyclic compound **131** (**Figure 104**). The complexation of the cavity resulted in the formation of the complexes **133,135-138**. Depending on the metal contained within the cavity, the macrocycles exhibit different colors. Compound **131** exhibited emission centered at 607 nm, extending up to 800 nm, with a quantum yield in toluene of 32%.

The use of brominated metal precursors led to the formation of the complexes **133** and **135**, both retaining an ancillary bromine atom; thus, they showed a drastic decrease of the fluorescence efficiency.

To address this issue, the metallic precursor was replaced, and analyses confirm the absence of any other atom besides the metal in complexes **135-138**, compound **135** manifested luminescent properties, such a bright luminescence, by virtue of the structural zinc atom within

the cavity. On the other hand, the compounds **137** containing Ni and **138** containing Fe, did not display properties in terms of luminescence.

Nevertheless, these Schiff-base macrocycles can be envisioned as catalysts for multi-electron donor redox reaction of small molecules. Detailed investigations are ongoing.

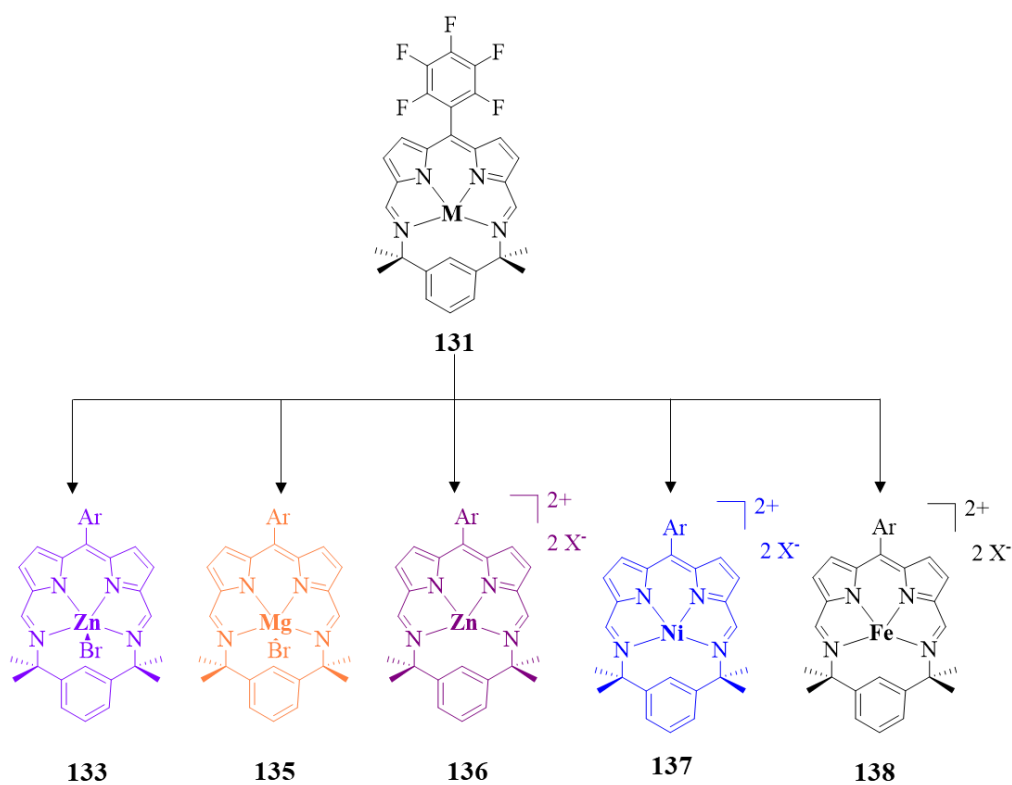


Figure 105: Schiff-base macrocycles synthesized in this thesis.

6. Experimental Section

6.1 General Remarks

6.1.1 Materials and Methods

Air- and moisture- sensitive reactions were carried out under argon atmosphere in sealable vials or flame-dried flasks using standard Schlenk technique. Liquid reagents and solvents were injected with syringes and stainless-steel cannula of different sizes, solids were transferred in a powdered shape.

For low-temperature reactions, flat Dewar flasks from Isotherm were used for cooling with the following refrigerating mixtures: -0 °C (ice/water), -78 °C (isopropanol/dry ice).

6.1.2 Solvents and chemicals

Solvents of p.a. (pro analysis) quality were commercially acquired from *Sigma Aldrich*, *Carl Roth*, *Acros Fisher Scientific* and, unless otherwise stated, used without previous purification. Absolutized solvents were either purchased from *Carl Roth*, *Acros Fisher Scientific* or *Sigma Aldrich* (<50 ppm H₂O over molecular sieves). Dry solvents were provided from an automatic solvent purification system (SPS) model 800 manuals of MRBRAUN. All reagents and chemicals were purchased from abcr, Sigma Aldrich, TCI, Chempur, Carbosynth and BDL Pharm and used without further purification.

The solvent mixtures used were volumetrically measured. Solvents were evaporated under reduce pressure at 45 °C using a rotary evaporator.

6.1.3 Reaction monitoring and product purification

Routine monitoring of reaction was performed using TLC silica gel (Supelco, 60, F₂₅₄), TLC aluminum oxide (Supelco, 60, F₂₅₄) and TLC Silica gel RP-18 (Merck, 60, F_{254s}) coated aluminum plates, analyzed under UV light at 254 nm and 365 nm. Solvent mixtures are understood as v/v. Reaction mixtures were purified by flash chromatography. For the stationary phase of the column, silica gel, produced by Merck (silica gel 60, 0.040 × 0.063 mm, 260 – 400 mesh ASTM), aluminium oxide (neutral), 50-200 µm, 60A, from Acros Organics and sea sand by Riedel de Haën (baked out and washed with hydrochloric acid) were used. Flash

chromatography was carried out either using a PureC-815 Flash device by Büchi in combination Büchi FlashPure EcoFlex columns of different sizes.

6.1.4 Devices and analytical instruments

Nuclear Magnetic Resonance Spectroscopy (NMR)

The NMR spectra were recorded on the following devices: Bruker Avance 400 NMR instrument (400 MHz for ^1H NMR and 100 MHz for ^{13}C NMR) and Bruker Avance DRX 500 NMR instrument (500 MHz for ^1H NMR and 125 MHz for ^{13}C NMR) spectrometers. The NMR spectra were recorded at room temperature in deuterated solvents commercially available. As solvents were used: acetone- d_6 (CD_3COCD_3), chloroform- d_1 (CDCl_3), deuterium oxide- d_2 (D_2O), dimethylsulfoxide- d_6 (CD_3SOCD_3), methanol- d_4 (CD_3OD), purchased at *Euristop*.

Chemical shifts are given in parts per million (δ/ppm), downfield from tetramethylsilane (TMS), and referenced to the residual solvent peaks of acetone (^1H : $\delta = 2.04$ ppm; ^{13}C : $\delta = 29.8$ ppm), chloroform- d_1 (^1H : $\delta = 7.26$ ppm; ^{13}C : $\delta = 77.16$ ppm), deuterium oxide- d_2 (^1H : $\delta = 4.65$ ppm), dimethylsulfoxide- d_6 (^1H : $\delta = 2.49$ ppm; ^{13}C : $\delta = 39.7$ ppm) and methanol- d_4 (^1H : $\delta = 3.35$ ppm, 4.78 ppm; ^{13}C : $\delta = 49.3$ ppm).^[336],2

Evaluation of the signals was done according to first order spectra. When describing couplings, the following abbreviations were used: s = singlet, d = doublet, t = triplet, m = multiplet, dd = doublet of doublet, ddd = doublet of doublet of doublet. Coupling constants “ J ” are given in Hertz [Hz] with the largest value first. Couplings are given with their respective number of bindings and binding partners, as far as they could be determined, written as index of the coupling constants.

Mass Spectrometry (MS)

Mass spectra were measured either by FAB-MS (Fast Atom Bombardment) recorded on a *Finnigan MAT 95* with *m*-nitrobenzyl alcohol (3-NBA) like matrix, by EI-MS (electron ionization) recorded on *Finnigan MAT 95*, by ESI-MS (electron spray ionization) recorded on a *Thermo Scientific Q Exactive Plus* or a *Bruker tims TOFTM* and by MALDI-ToF System recorded on a *Shimadzu Biotech Axima Confidence* (2.9.3.20110624) (80 mJ, 100 Profiles, 10 shots per profile). In the latter technique, the tuning mode was reflectron with a recentering of

600 μm of width and 600 μm of high). The matrices employed were: α -Cyano-4-hydroxycinnamic acid (αCHCA), Ferulic acid (FA) and 6-Aza-2-thiothymine (ATT).

For the interpretation of the spectra, molecular peaks $[\text{M}]^+$, peaks of protonated molecules $[\text{M}+\text{H}]^+$, and characteristic fragment peaks are indicated with their mass-to-charge ratio (m/z) and their intensity in percent, relative to the base peak (100%) is given. In the case of high-resolution measurements, the tolerated error is 0.0005 m/z .

Elemental Analysis

The elemental analysis measurements were carried out using an Elementar Vario MICRO instrument. Furthermore, the weight scale that was used was a Sartorius M2P. The calculated and found percentage by mass values for C, H, N and S are declared in fractions of 100%.

Photophysics

The absorption spectra were recorded with a *PerkinElmer Lambda 750* double-beam UV/Vis-NIR spectrometer. Correction of spectra was made automatically by the instrument with the absorption of the pure solvent (blank).

Fluorescence was measured with a Jobin-Yvon Fluoromax 4 fluorimeter with a step width of 1 nm. All measurements were performed in quartz cuvettes with septum from Hellma and, where not explicated, conducted at 20 $^{\circ}\text{C}$ through the use of an Advanced Ac200 Immersion Circulators Thermostats-Thermo Fisher Scientific. Solvents for spectroscopy were supplied by Merck (Uvasol). Photoluminescence quantum yields were determined utilizing as standard Cresyl Violet in spectroscopic methanol (Φ in MeOH, 22 $^{\circ}\text{C}$ = 0.54), $\text{Ru}(\text{bpy})_3\text{Cl}_2 \cdot 6 \text{H}_2\text{O}$ in air-equilibrated water solution (Φ in water, 22 $^{\circ}\text{C}$ = 0.028) and Zinc-Phtalocyanine in isopropanol (Φ in iPrOH, 22 $^{\circ}\text{C}$ = 0.45).^[338–340] Lifetime measurements were performed by time-correlated single-photon counting method (TCSPC) with a DeltaTime kit for DeltaDiode source on Fluoromax systems, including DeltaHuB and DeltaDiode controller. The light-sources were NanoLED sources (455nm, 570 nm and 625 nm). (Philipps 1984)

6.1.5 Cell tests

6.1.5.1 Cytotoxicity Assay

The cytotoxicity was assessed by using the CellTiter 96 Non-Radioactive Cell Proliferation Assay (Promega) according to producer's instructions. It is based on the intracellular reduction of the yellow 3-(4,5-dimethylthiazol-2-yl)-2,5-di-phenyltetrazolium bromide (MTT) to a blue formazan product. Briefly, 1×10^4 cells of respective cells type (HeLa, HepG2, NHDF, NIH3T3 and MCF7) were seeded in each well of a 96-well plate and incubated with DMEM, supplemented with 10% of FCS and 1% of Penicillin/Streptomycin (37 °C, 5% of CO₂ atmosphere) for 24 h. Then, the cell culture medium was removed and fresh DMEM containing new compounds was added to the cells which were incubated for 72 h. In order to have an accurate spectrum of the results, the colorimetric assay was performed on HeLa and HepG2 cells incubated with compounds **11-15**, **17**, **19**, **34**, **38**, **39**, **44** at different concentration (1, 2.5, 5, 7.5 μM). Viability levels of HeLa and HepG2 cells were evaluated by incubating with compounds **54-64** at different concentration (1, 2.5, 5, 7.5, 10 and 20 μM) for 72 h. Subsequently, viability levels of HeLa and NHDF cells were evaluated by incubating with complexes **56**, **57**, **58**, **60**, **61** at different concentration (1, 2.5, 5, 7.5, 10 and 20 μM) for 72 h. Considering that the concentration used for the microscopy is 20 μM and expecting a comparable trend, NIH3T3 and MCF7 were treated with compounds **56**, **57**, **58**, **60**, **61** only at 20 μM. One negative control was realized by incubating cells in DMEM + DMSO 20 μM. After adding 5 μl of Triton-X100 (20% in ultra-pure and sterile water ddH₂O) to the positive control, 15 μl of MTT-solution was added in each well and the cells were incubated for additional 3h before adding 100 μL of a stop-solution mix. The absorption was measured at 570 nm by using a Spectramax ID3 (HeLa and NHDF) or a BioTek Synergy LX (NIH3T3 and MCF7) multi-well reader after an incubation period of 24 h, to allow the solubilization of the formazan product. Each experimental well and controls were prepared in triplicates.

6.1.5.2 Confocal laser microscopy and co-staining experiments

Confocal live-cell fluorescence microscopy was performed by seeding 1.5×10^4 cells on each chamber of an μ-slide 8-well (ibidi®) (for HeLa and NHDF) and on 35mm-glass bottom dishes (ibidi®) (for NIH3T3 and MCF7) followed by an incubation period of 24 h in DMEM supplemented with 10% of FCS and 1% of Penicillin/Streptomycin (37°C, 5% of CO₂ atmosphere). Subsequently, medium was removed and fresh DMEM, containing compounds

56, 57, 58, 60, 61 (20 μ M, 0.4% v/v), was added to the cell culture which was incubated for additional 24 h. Afterwards, MitoTracker™ Green (125 nM) or LysoTracker™ Green (50 nM) was added and, after 30 min, cells were washed three times with DPBS and fresh medium with Hoechst 33342 (2 μ g/ml) was included.

Due to the possibility of exciting the fluorophores at different excitation wavelength, to prove the feasibility of different imaging conditions, BioTracker™ 405 Blue Mitochondria Dye (125 nM) and LysoTracker®Blue DND-22 (50 nM) were also employed. Co-staining experiments were performed following the same procedure as above mentioned, except for the Hoechst 33342 which, in this case, was not added. The microscopy was performed by using, for HeLa and NHDF cell type, a confocal Leica Stellaris microscope with a HC PL Apo CS2 63x oil objective (N.A.= 1.4) and, for NIH3T3 and MCF7 cell type, a confocal Zeiss LSM800 microscope with a C-Apo 40x water immersion objective (N.A.=1.2). Acquisition parameters (e.g. excitation/emission wavelengths) were adjusted according to the specific investigation as indicated in the figure captions. The Pearson correlation coefficient (PCC) was calculated by using the JACoP plugin for ImageJ program.

6.1.5.3 Cross-linking fixative procedure and fixed-cell imaging

For the fixation experiments, DMEM was removed after cell culture (containing complex **61**) and replaced with paraformaldehyde (4% in PBS) for 15min. Cells were then washed three times with PBS+ 0.1% of Triton X-100 for 5min. Subsequently, cells were incubated with a solution of phalloidin coupled to AlexaFluor488 (Invitrogen, dilution 1:200) and DAPI (4,6-diamidino-2-phenylindole) (Roth, dilution 1:1000) in PBS+ 1% of BSA for one hour, to stain the actin cytoskeleton and the nuclei, respectively. Finally, cells were washed three times with PBS, kept in buffer and imaged.

6.2 Synthetic procedures and analytical data

6.2.1 Plain dipyrrens

General procedure for HCl catalysed condensation:

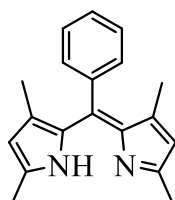
In a round bottom flask 2.5 equivalents of 2,4-dimethyl-1*H*-pyrrole were dissolved in dichloromethane and afterwards 1 equiv. of aromatic aldehyde was added to the reaction mixture. Methanol was added when required, for solubilizing the aromatic aldehyde. Thus, a diluted solution of HCl (0.2M) was added to the reaction mixture, which was allowed to react for 24 hours at room temperature. This was the time required for the complete conversion of the starting aldehyde, as confirmed by TLC monitoring, using dichloromethane as eluent. The second step involved the use of 2,3,5,6-Tetrachlorocyclohexa-2,5-diene-1,4-dione (*p*-Chloranil) to achieve the oxidation and therefore obtain the corresponding dipyririn. This stage was completed after 7 hours of reaction at room temperature. The reaction was quenched with water and then was conducted the workup with brine/dichloromethane. The product was purified with column chromatography, packed with neutral alumina, unless otherwise stated.

General procedure for TFA catalysed condensation:

In a round bottom flask 2.5 equivalents of 2,4-dimethyl-1*H*-pyrrole were dissolved in dichloromethane and afterwards 1 equiv. of aromatic aldehyde was added to the reaction mixture. Methanol was added when required, for solubilizing the aromatic aldehyde. Thus, catalytic amounts of TFA were added to the reaction mixture, which was allowed to react at room temperature. In this case the first step required different reaction times, that will be described for each procedure. The second step involved the use of 2,3,5,6-Tetrachlorocyclohexa-2,5-diene-1,4-dione (*p*-Chloranil) to achieve the oxidation and therefore obtain the corresponding dipyririn. The reaction was quenched with water and then was conducted the workup with brine/dichloromethane. The product was purified with column chromatography, packed with neutral alumina, unless otherwise stated.

1,3,7,9-tetramethyl-5- phenyl-dipyrrin (11)

In a round-bottom flask, 2,4-dimethyl-1*H*-pyrrole (1.93 g, 2.08 mL, 20 mmol, 2.50 equiv.) and benzaldehyde (1.20 g, 8.1 mmol, 1.00 equiv.) were dissolved in dichloromethane (45.0 mL), and hydrochloric acid 0,2 M (20.0 mL) was added. Thus, *p*-Chloranil was added and the reaction was left stirring for additional 7 hours. The reaction mixture was quenched with 15 mL of water and washed with 10 mL of DCM; the organic layers were then washed with brine three times. The organic phases were collected, dried over MgSO₄ anhydrous, filtered, and evaporated under vacuum. The obtained crude product was purified *via* column chromatography, packed with alumina, using a gradient eluent made of cyclohexane/dichloromethane. The target compound was isolated as a black solid in 68% yield (1.75 g, 5.5 mmol).



R_f= 0.5 (Dichloromethane).

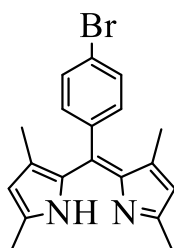
¹H-NMR (400 MHz, CDCl₃) δ/ppm: 7.34 (dd, 2H, J=8.48, 1,79), 7,23 (ddd, 2H, J=8.40, 1.75, 1.54), 7.16 (tt, 1H, J=8.47, 1.54), 5.84 (s, 2H), 2.39 (s, 6H), 1.29 (s, 6H).

¹³C-NMR (100 MHz, CDCl₃) δ/ppm: 164.65, 142.35, 135.68, 135.41, 135.10, 128.67, 127,91, 125.24, 112.94, 118.41, 19.64, 13.97, 13.54, 13.10.

HRMS (C₁₉H₂₀N₂) 276.3847 (calculated), 276.3478 (found).

5-4'-bromophenyl-1,3,7,9-tetramethyl dipyrrin (12)

In a round bottom flask, 2,4-dimethyl-1*H*-pyrrole (1.29 g, 14 mmol, 2.50 equiv.) and 4-bromobenzaldehyde (1.00 g, 5.4 mmol, 1.00 equiv.) were dissolved in dichloromethane (25.0 mL), hydrochloric acid 0,2 M (20.0 mL) was added. Thus, *p*-Chloranil (2.19 g, 8.9 mmol, 1.10 equiv.) was added and the reaction mixture was left stirring for additional 7 hours. The reaction mixture was quenched with 15 mL of water and washed with 10 mL of DCM and the organic layers were then washed with brine three times. The organic phases were collected, dried over MgSO₄ anhydrous, filtered, and evaporated under vacuum. The obtained crude product was purified *via* column chromatography, packed with alumina, using dichloromethane as eluent. The target compound was isolated as a black solid in 65% yield (1.25 g, 3.5 mmol).



R_f = 0.4 (Dichloromethane).

¹H-NMR (400 MHz, CDCl₃) δ/ppm: 7.52 (s, 2H), 7.15 (s, 2H), 5.95 (s, 2H), 2.40 (s, 6H), 1.45 (s, 6H).

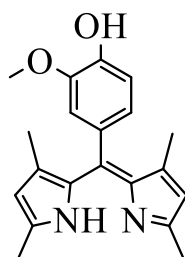
¹³C-NMR (100 MHz, CDCl₃) δ/ppm: 164.68, 141.34, 138.78, 135.63, 132.04, 131.58, 128.64, 121.14, 108.94, 19.65, 13.57.

HRMS (C₁₉H₁₉BrN₂) 354.0732 (calculated), 354.0054 (found).

1,3,7,9-tetramethyl -5-(3'-methoxy-4'-hydroxyphenyl)-dipyrrin (13)

2,4-dimethyl-1*H*-pyrrole (3.127 g, 32.86 mmol, 2.5 equiv.) and 4-hydroxy-3-methoxybenzaldehyde (2.00 g, 13.15 mmol, 1 equiv.) were solved in dichloromethane (250 ml) and methanol (10 ml); hydrochloric acid 0.2 M (60 ml) was added to the reaction mixture. Then *p*-Chloranil (2.737 g, 11.13 mmol, 1.10 equiv.) was incorporated into the system that was left stirring for 24 hours. The organic layers were then washed with saturated NaCl aqueous solution three times, collected, and dried over MgSO₄ anhydrous, filtered and evaporated under vacuum. The obtained crude product was purified *via* column chromatography, packed with alumina, using a gradient of dichloromethane/methanol as eluent.

The target compound was isolated as a black powder (1.560 g, 48.39 mmol, 37 % yield).



R_f = 0.3 (Dichloromethane).

¹H-NMR (400 MHz, CDCl₃) δ/ppm: 7.33 (m, 2 H), 7.22 (dd, J = 4.8 Hz, 1.7 Hz, 1H), 5.79 (s, 2 H), 3.5 (s, 3H), 2.24 (s, 6H), 1.20 (s, 6H).

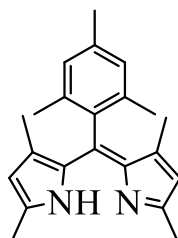
¹³C-NMR (100 MHz, CDCl₃) δ/ppm: 136.34, 134.39, 133.54, 130.06, 129.36, 129.54, 128.92, 128.42, 54.68, 26.87, 14.32.

HRMS (C₂₀H₂₂N₂O₂) 322.1681 (calculated), 321.9587 (found).

5-mesityl-1,3,7,9-tetramethyl-dipyrrin (14)

In a round bottom flask 2,4-dimethyl-1*H*-pyrrole (4.918 g, 51.69 mmol, 2.5 equiv.) and 2,4,6-trimethylbenzaldehyde (3.064 g, 20.67 mmol, 1 equiv.) were dissolved in dichloromethane (250 ml); then hydrochloric acid 0.2 M (60 ml) was added. Subsequently, *p*-Chloranil (5.592 g, 22.74 mmol, 1.10 equiv.) was added and the reaction mixture was left stirring at room temperature for 7 hours. The organic layers were then washed with saturated NaCl aqueous solution three times, collected, and dried over MgSO₄ anhydrous, filtered and evaporated under vacuum. The obtained crude product was purified *via* column chromatography, packed with alumina, using dichloromethane as eluent.

The target compound was isolated as a dark-orange powder (5.200 g, 16.33 mmol, 79 % yield).



R_f = 0.6 (Dichloromethane).

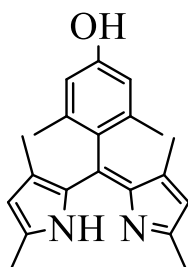
¹H-NMR (400 MHz, CDCl₃) δ/ppm: 6.91 (s, 2H), 5.86 (s, 2 H), 2.35 (s, 6H), 2.33 (s, 3H), 2.11 (s, 6H), 1.31 (s, 6H).

¹³C-NMR (100 MHz, CDCl₃) δ/ppm: 151.23, 139.77, 137.81, 137.65, 135.81, 135.60, 134.10, 128.68, 128.36, 119.11, 21.31, 19.69, 16.21, 13.72.

HRMS (C₁₉H₁₉BrN₂) 318.2096 (calculated), 318.3244 (found).

1,3,7,9-tetramethyl -5-(2',6'-dimethyl-4'-hydroxy)-phenyl-dipyrrin (15)

The reaction of 2,4-dimethyl-1*H*-pyrrole (2.376 g, 24.97 mmol, 2.5 equiv.) with 4-hydroxy-2,6-dimethylbenzaldehyde (1.500 g, 9.988 mmol, 1 equiv.) was performed in a mixture of dichloromethane (150 ml)/methanol (50 ml) and hydrochloric acid 0.2 M (30 ml). Thus, *p*-Chloranil (2.947 g, 11.99 mmol, 1.10 equiv.). The organic layers were then washed with saturated NaCl aqueous solution three times, collected, and dried over MgSO₄ anhydrous, filtered, and evaporated under vacuum. The obtained crude product was purified *via* column chromatography, packed with alumina, using dichloromethane as eluent. The target compound was isolated as a dark-green powder (2.000 g, 6.242 mmol, 62% yield).



R_f = 0.4 (Dichloromethane).

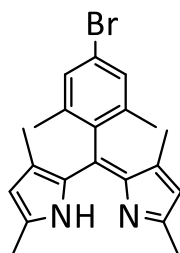
¹H-NMR (400 MHz, CDCl₃) δ/ppm: 6.57 (s, 2H), 5.86 (s, 2 H), 5.30 (s, 1H), 2.34 (s, 6H), 2.07 (s, 6H), 1.34 (s, 6H).

¹³C-NMR (100 MHz, CDCl₃) δ/ppm: 155.30, 151.37, 139.76, 137.69, 137.25, 135.75, 129.56, 119.11, 114.64, 53.45, 19.74, 16.06, 13.71.

HRMS (C₂₁H₂₄N₂O) 320.1889 (calculated), 321.4145 (found).

1,3,7,9-tetramethyl-5-(2',6'-dimethyl-4'-bromo-phenyl)-dipyrrin (16)

In a round bottom flask, 4-bromo-2,6-dimethylbenzaldehyde (2.00 g, 9.39 mmol, 1.0 equiv.) and 2,4-dimethyl-1*H*-pyrrole (2.23 g, 23.5 mmol, 2.5 equiv.) were dissolved in dichloromethane (30 ml). Subsequently, 5 ml of trifluoroacetic acid (TFA) were added to the reaction mixture, which was left stirring at room temperature for 5 hours. Thus, *p*-Chloranil (2.77 g, 11.3 mmol, 1.20 equiv.) was added and the reaction mixture was left stirring for additional 3 hours. The reaction mixture was quenched with 45 mL of water and washed with 10 mL of DCM and the organic layers were then washed with brine three times. The organic phases were collected, dried over MgSO₄ anhydrous, filtered, and evaporated under vacuum. The obtained crude product was purified *via* column chromatography, packed with alumina, using dichloromethane as eluent. The target compound was isolated as a black solid in 42 % yield (1.5 g, 3.9 mmol).



R_f = 0.3 (Dichloromethane).

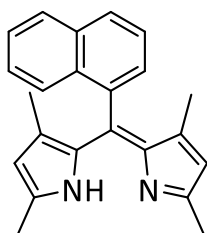
¹H-NMR (400 MHz, CDCl₃) δ/ppm: 13.25 (s, 1H), 7.27 (s, 2H), 5.86 (s, 2H), 2.33 (s, 6H), 2.12 (s, 6H), 1.30 (s, 2H).

¹³C-NMR (100 MHz, CDCl₃) δ/ppm: 151.67, 139.28, 138.54, 136.10, 135.73, 134.93, 130.63, 121.77, 119.41, 43.44, 19.49, 16.11, 13.81.

HRMS (C₂₁H₂₃BrN₂) 382.1045 (calculated), 382.2451 (found).

1,3,7,9-tetramethyl -5-naphthyl-dipyrrin (17)

In a round bottom flask, 2,4-dimethyl-1*H*-pyrrole (2.41 g, 25.5 mmol, 2.5 equiv.) and 1-naphthaldehyde (2.87 g, 21.4 mmol, 1 equiv.) were dissolved in dichloromethane (30 ml). Subsequently, 7 ml of trifluoroacetic acid (TFA) were added to the reaction mixture, which was left stirring at room temperature for 5 hours; *p*-Chloranil (2.41 g, 10.4 mmol, 1.20 equiv.) was added and the reaction mixture was left stirring for additional 3 hours. The reaction mixture was quenched with 45 mL of water and washed with 10 mL of DCM and the organic layers were then washed with brine three times. The organic phases were collected, dried over MgSO₄ anhydrous, filtered, and evaporated under vacuum. The obtained crude product was purified *via* column chromatography, packed with alumina, using dichloromethane as eluent. The target compound was isolated as a black solid in 23 % yield (1.1 g, 3.5 mmol).



R_f = 0.2 (Dichloromethane).

¹H-NMR (400 MHz, CDCl₃) δ/ppm: 7.91 (d, 1 H, J = 8.23), 7.87 (dd, 2H, J = 8.01, 1.52), 7.53 (dd, 1H, J = 8.23, 6.97), 7.47 (ddd, 1 H, J = 8.25, 6.78, 1.27), 7.44-7.35 (m, 2H), 5.83 (s, 2H), 2.39 (s, 6H), 0.95 (s, 6H).

¹³C-NMR (100 MHz, CDCl₃) δ/ppm: 151.61, 140.23, 136.91, 136.70, 135.57, 133.49, 132.86, 128.42, 127.94, 126.93, 126.67, 126.10, 125.96, 125.70, 125.52, 119.45, 26.94, 16.11, 14.05.

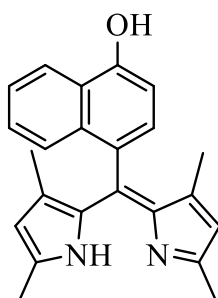
HRMS (C₂₃H₂₂N₂) 326.1783 (calculated), 326.0547 (found).

1,3,7,9-tetramethyl -5-(4'-hydroxynaphthyl)-dipyrrin (18)

In a round bottom flask, 2,4-dimethyl-1*H*-pyrrole (1.02 g, 12.7 mmol, 2.5 equiv.) and 4-hydroxy-1-naphthaldehyde (1.4 g, 10.4 mmol, 1 equiv.) were dissolved in dichloromethane (30 ml) and methanol (15 ml). Subsequently, 10 ml of trifluoroacetic acid (TFA) were added to the reaction mixture, which was left stirring at room temperature for 7 hours; *p*-Chloranil (1.4 g, 5.4 mmol, 1.20 equiv.) was added and the reaction mixture was left stirring for additional 3 hours.

The reaction mixture was quenched with 45 mL of water and washed with 10 mL of DCM and the organic layers were then washed with brine three times. The organic phases were collected, dried over MgSO₄ anhydrous, filtered, and evaporated under vacuum. The obtained crude product was purified *via* column chromatography, packed with alumina, using dichloromethane and methanol (up to 10 %) as eluent mixture.

The target compound was isolated as a red solid in 15 % yield (500 mg, 1.5 mmol).



R_f = 0.1 (Dichloromethane: Methanol 80:20).

¹H-NMR (400 MHz, CDCl₃) δ/ppm: 8.7 (s, 1H), 7.91 (d, 1 H, J= 7.5), 7.87 (d, 1H, J= 8.4), 7.68 (dd, 1H, J= 8.23, 6.97), 7.51 (ddd, 1 H, J= 8.25, 6.78, 1.27), 7.48-7.44 (m, 2H), 5.41 (s, 2H), 2.64 (s, 6H), 1.95 (s, 6H).

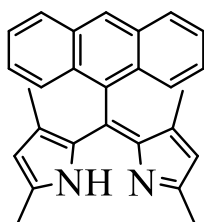
¹³C-NMR (100 MHz, CDCl₃) δ/ppm: 169.41, 150.41, 148.74, 139.12, 135.57, 133.49, 132.86, 128.42, 127.94, 126.93, 126.67, 126.10, 125.96, 125.70, 125.52, 119.45, 26.94, 16.11, 14.05.

HRMS (C₂₃H₂₂N₂O) 342.1732 (calculated), 342.7456 (found).

1,3,7,9-tetramethyl -5-anthracenyl-dipyrrin (19)

The reaction of 2,4-dimethyl-1*H*-pyrrole (3.460 g, 36.37 mmol, 2.5 equiv.) with 9-anthracenecarboxaldehyde (3.00 g, 14.55 mmol, 1 equiv.) was performed in dichloromethane (250 ml). Subsequently, 10 ml of trifluoroacetic acid (TFA) were incorporated to the system. The reaction was carried out at room temperature for 16 hours. Subsequently, *p*-Chloranil (3.934 g, 16.00 mmol, 1.10 equiv.) was added and the reaction mixture was left stirring for 3 hours. The organic layers were then washed with saturated NaCl aqueous solution three times, collected, and dried over MgSO₄ anhydrous, filtered and evaporated under vacuum.

The obtained crude product was purified *via* column chromatography, packed with alumina, using dichloromethane as eluent. The target compound was isolated as a black powder (4.286 g, 11.38 mmol, 78 % yield).



R_f = 0.5 (Dichloromethane).

¹H-NMR (400 MHz, CDCl₃) δ/ppm: 8.54 (s, 1H), 8.00 (m, 4H), 7.45 (t, J=8.3 Hz, 2H), 7.37 (t, J= 8.1 Hz, 2H), 5.78 (s, 2 H), 2.42 (s, 6H), 0.51 (s, 6H).

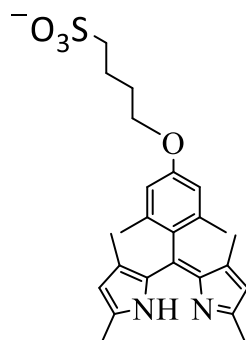
¹³C-NMR (100 MHz, CDCl₃) δ/ppm: 151.73, 140.10, 137.37, 131.78, 130.59, 130.35, 128.17, 127.35, 126.92, 125.83., 125.65, 125.44, 119.48, 108.18, 16.15, 13.60.

HRMS (C₂₇H₂₄N₂) 376.1939 (calculated), 376.1457 (found).

1,3,7,9-tetramethyl -5-(2', 6-dimethyl-4'-(butoxy)-phenyl)-dipyrrin 4'' sulfonate (29)

In a round bottom flask, 1,3,7,9-tetramethyl -5-(2',6'-dimethyl-4'-hydroxy)-phenyl-dipyrrin **15** (500.02 mg, 1.56 mmol, 1 equiv.) was dissolved in tetrahydrofuran (THF) 150 ml. Subsequently, K₂CO₃ (1.27 g, 3.90 mmol, 2.5 equiv.) was added to the reaction mixture and after few minutes 1,4 butanesultone (531.04 mg, 3.90 mmol, 2.5 equiv.) was incorporated into the system that was refluxed for 24 hours at 80 °C.

Once cooled down to room temperature, cold ethyl acetate was added to the reaction mixture to favor the precipitation of the target compound, which was isolated as a yellow powder (250.04 mg, 0.547 mmol, 35% yield).



R_f = 0.3 (Dichloromethane: Methanol 70:30).

¹H-NMR (400 MHz, D₂O) δ/ppm: 7.14 (s, 2H), 6.52 (s, 2H), 4.58 (m, 4 H), 4.10 (m, 2 H), 3.40 (m, 2 H), 2.32 (s, 6H), 1.91 (s, 6H), 0.51 (s, 6H).

¹³C-NMR (100 MHz, D₂O) δ/ppm: 161.43, 120.50, 134.47, 133.48, 132.54, 129.41, 127.47, 126.45, 126.02, 124.43., 123.65, 112.38, 100.18, 60.42, 44.54, 16.25, 12.60.

HRMS (C₂₃H₃₁N₂ O₄S) 455.5994 (calculated), 455.0741 (found).

6.2.2 π -expanded dipyrrens

General procedure for the classic Knoevenagel condensation:

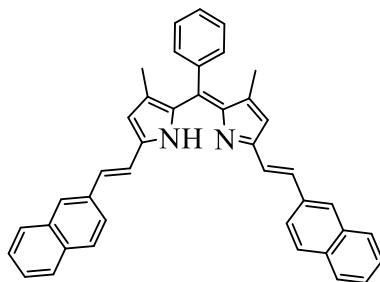
in a dried three-neck flask, under an argon atmosphere, 1 equiv. of the plain dipyrin and 6 equiv. of the aromatic aldehyde were dissolved in toluene. Subsequently, catalytic amounts of piperidine and glacial acetic acid were added to the reaction mixture. The system was equipped with a Dean-Stark apparatus, attached to the air condenser and the flask. The water distilled through the neck of the apparatus was removed once the reaction was completed. The workup involved the usual washing with brine and extraction with dichloromethane. The crude residue was purified with column chromatography, using neutral alumina gel, unless otherwise stated.

General procedure for the microwave assisted Knoevenagel condensation:

in a round bottom microwave glass vial (16mm OD X 83 mm Long) 1 equiv. of the plain dipyrin and 6 equiv. of the aromatic aldehyde were dissolved in 4 ml of ethanol and then 1 ml of piperidine and 1 ml of glacial acetic acid were added dropwise. Catalytic amount of $\text{Mg}(\text{ClO}_4)_2$ were added. The reaction was carried out for 1 hours at 110°C in a microwave reaction. After cooling down to room temperature the system, the organic layer was washed with saturated NaCl aqueous solution, and the aqueous layers were recombined and extracted with dichloromethane. The organic phases were collected and dried over MgSO_4 . The mixture was filtered, and the solvent was evaporated under reduced pressure. The crude residue was purified *via* flash automatic column chromatography on silica gel.

3,7-dimethyl-1,9-bis(2'-naphthyl-2'-yl-vinyl)-5-(phenyl)-dipyrrin (33)

In a dried three-neck flask, under an argon atmosphere and constant stirring, 5-phenyl-dipyrrin **11** (2.10 g, 9.10 mmol, 1equiv.) and naphthalene-2-carbaldehyde (9.210 g, 58.97 mmol, 6 equiv.) were dissolved in 200 ml of dry toluene. Subsequently 5 ml of piperidine and 5 ml of glacial acetic acid were added dropwise to the reaction mixture, refluxed for 24 hours, using an air-cooled condenser under argon atmosphere. After this time, the organic layer was washed with saturated NaCl aqueous solution, the aqueous layers were recombined and extracted with CH₂Cl₂. The organic phases were collected and dried over MgSO₄. The mixture was filtered, and the solvent was evaporated under reduced pressure. The crude residue was purified *via* flash column chromatography on alumina gel (gradient of cyclohexane/dichloromethane), giving the product as a purple solid (1.9g, 2.689 mmol, 36% yield).



R_f=0.3 (Dichloromethane).

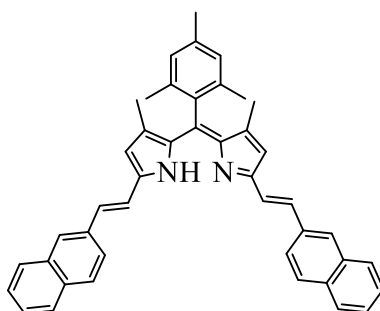
¹H-NMR (400 MHz, CDCl₃) δ/ppm: 8.17 (s, 2 H), 7.89 (s, 4 H), 7.96-7.91 (d, J= 1.5 Hz, 6 H), 7.88-7.83 (dt, J=7.7 Hz, 4 H), 7.47 (s, 2H), 7.33-7.20 (h, J=3.7 Hz, 3 H), 7.18 (s, 2 H), 7.04 (s, 2 H), 6.63 (s, 2H), 2.01 (s, 6H).

¹³C-NMR (100 MHz, CDCl₃) δ/ppm: 152.10, 140.89, 139.22, 137.14, 137.00, 136.21, 135.26, 134.66, 133.76, 128.76, 128.56, 128.09, 127.75, 127.67, 127.16, 126.68, 126.52, 123.48, 121.26, 119.48, 55.31, 24.52, 14.33.

HRMS (C₄₁H₃₃N₂) 552.2565 (calculated), 551.4835 (found).

3,7-dimethyl-1,9-bis(2'-naphthyl-2-yl-vinyl)-5-(2''', 4'', 6'''-trimethylphenyl)-dipyrrin (34)

In a dried three-neck flask, under an argon atmosphere and constant stirring, 5-mesityl-1,3,7,9-tetramethyl-dipyrrin **14** (3.130 g, 9.829 mmol, 1equiv.) and naphthalene-2-carbaldehyde (9.210 g, 58.97 mmol, 6 equiv.) were dissolved in 200 ml of dry toluene. After that, 5 ml of piperidine and 5 ml of glacial acetic acid were added dropwise to the reaction mixture, refluxed for 24 hours, using an air-cooled condenser under argon atmosphere. After this time, the organic layer was washed with saturated NaCl aqueous solution, the aqueous layers were recombined and extracted with CH₂Cl₂. The organic phases were collected and dried over MgSO₄. The mixture was filtered, and the solvent was evaporated under reduced pressure. The crude residue was purified *via* flash column chromatography on alumina gel (gradient of cyclohexane/dichloromethane), giving the product as a purple solid (1.7g, 2.539 mmol, 27% yield).



R_f=0.8 (Dichloromethane).

¹H-NMR (400 MHz, CDCl₃) δ/ppm: 7.86-7.75 (m, 8 H), 7.65 (dd, J= 7.9, 1.6 Hz, 2H), 7.45-7.36 (m, 6H), 7.22 (d, J= 2.0 Hz, 2H), 6.91 (s, 2H) 6.37 (s, 2H), 2.31 (s, 3H), 2.12 (s, 6 H), 1.37 (s, 6H).

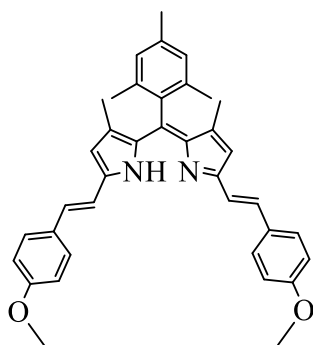
¹³C-NMR (100 MHz, CDCl₃) δ/ppm: 150.71, 140.46, 138.88, 135.89, 134.74, 133.73, 133.28, 131.82, 128.71, 128.52, 128.24, 127.73, 127.44, 126.45, 126.17, 123.47, 121.31, 119.12, 26.94, 21.26, 19.79, 13.87.

HRMS (C₄₄H₃₈N₂) 594.3035 (calculated), 594.1297 (found).

3,7-dimethyl-1,9-bis(4'-methoxyphenyl-2''-yl-vinyl)-5-(2''', 4'', 6'''-trimethylphenly)-dipyrrin (35)

In a dried three-neck flask, under an argon atmosphere and constant stirring, 5-mesityl-1,3,7,9-tetramethyl-dipyrrin **14** (300 mg, 942 μmol , 1.00 equiv.) and (939 mg, 5.7 mmol, 6.00 equiv.) of 4-methoxybenzaldehyde, were solved in 10 mL of toluene. Then, 500 μL of piperidine and 500 μL of glacial acetic acid were added dropwise. The reaction was refluxed for 24 hours using an air-cooled condenser under argon atmosphere. The reaction mixture was poured into a separation funnel and the organic layer was washed successively with 10 mL of H_2O , 30 ml of DCM and brine. The organic phases were collected and were dried over of MgSO_4 . The mixture was filtered, and the solvent was evaporated under reduced pressure. The crude residue was purified *via* column chromatography, packed with alumina, using dichloromethane and 2% of methanol as eluent.

The target compound was isolated as a violet powder, with 30 % of yield.



$R_f=0.5$ (Cyclohexane: Dichloromethane = 7:2).

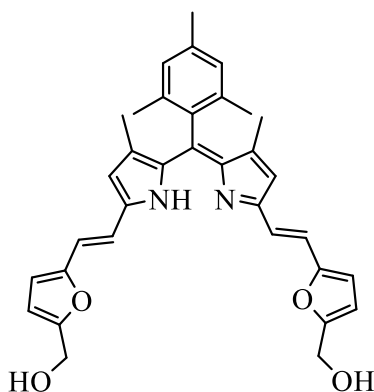
$^1\text{H-NMR}$ (400 MHz, CDCl_3) δ/ppm : 7.54 (m, 4 H), 7.02 (s, 2H), 6.95 (m, 2 H), 6.78 (m, 2H), 6.55 (m, 4 H), 6.00 (s, 2 H), 3.85 (s, 3H), 3.81 (s, 3H), 2.41 (s, 6H), 2.35 (s, 3H), 1.45 (s, 6H).

$^{13}\text{C-NMR}$ (100 MHz, CDCl_3) δ/ppm : 151.10, 140.99, 140.22, 137.34, 137.04, 136.21, 135.26, 134.66, 133.76, 128.76, 128.56, 128.09, 127.75, 127.67, 127.16, 126.68, 126.52, 123.48, 121.26, 119.48, 55.31, 24.52, 14.33.

HRMS ($\text{C}_{38}\text{H}_{38}\text{N}_2\text{O}_2$) 554.7340 (calculated), 554. 7451 (found).

3,7-dimethyl-1,9-bis(2'-hydromethylfuran-5''-yl-vinyl)-5-(2''',6'''-dimethyl-4'''-hydroxyphenly)-dipyrrin (36)

Under an argon atmosphere, in a three-neck round bottom flask, 5-mesityl-1,3,7,9-tetramethyl-dipyrrin **14** (1.30 mg, 4.08 mmol, 1.00 equiv.) and 5-(hydroxymethyl) furan-2-carbaldehyde (3.09 g, 24.5 mmol, 6.00 equiv.) were dissolved in 250 ml of dry toluene. The reaction mixture was heated up to 125 °C under reflux and piperidine (10 ml, 0.3 equiv.) and acetic acid (10 ml, 0.04 equiv.) were added to the reaction mixture which was left stirred for 48 hours at 125 °C. After cooling the system, the organic layer was washed with saturated NaCl aqueous solution, and the aqueous layers were recombined and extracted with CH₂Cl₂. The organic phases were collected and dried over MgSO₄. The mixture was filtered, and the solvent was evaporated under reduced pressure. The crude residue was purified *via* flash automatic column chromatography on silica gel (gradient of dichloromethane/methanol) giving the product as a dark red solid (20 mg, 0.124 mmol, 26% yield).



R_f=0.5 (Dichloromethane: Methanol 70:30).

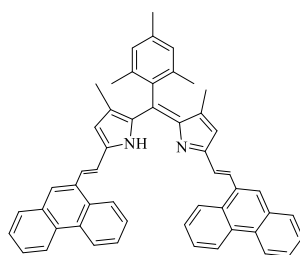
¹H-NMR (400 MHz, CDCl₃) δ/ppm: 8.36 (s, 1H), 6.97 (s, 1H), 6.90 (s, 2H), 6.36 (s, 1H), 6.25 (s, 1H), 5.87 (s, 2H), 3.92 (s, 4H), 2.32 (s, 6H), 2.25 (s, 6H), 1.35 (s, 6H).

¹³C-NMR (100 MHz, CDCl₃) δ/ppm: 158.2, 154.0, 152.8, 151.3, 139.91, 139.41, 138.8, 135.64, 132.0, 130.87, 127.84, 125.78, 122.6, 121.21, 120.76, 116.85, 115.42, 111.17, 57.46, 21.98, 20.46, 13.84.

HRMS (C₃₄H₃₄N₂O₄) 534.2519 (calculated), 535.7489 (found).

13,7-dimethyl-1,9-bis(2'-phenanthr-2''-yl-vinyl)-5-(2''',6'''-dimethyl-4'''-hydroxyphenyl)-dipyrrin (37)

Under an argon atmosphere, in a two-neck round bottom flask, 5-mesityl-1,3,7,9-tetramethyl-dipyrrin **14** (800 mg, 2.51 mmol, 1.00 equiv.) and phenanthrene-9-carbaldehyde (2.30 g, 11.2 mmol, 4.44 equiv.) were dissolved in 200 ml of dry toluene. Subsequently, piperidine (10 ml, 0.01 equiv.) and glacial acetic acid (10 ml, 0.02 equiv.) were added to the reaction mixture which was refluxed at 120 °C, through the use of an air condenser and stirred for 24 hours. After cooling the system, the organic layer was washed with saturated NaCl aqueous solution, and the aqueous layers were recombined and extracted with dichloromethane. The organic phases were collected and dried over MgSO₄. The mixture was filtered, and the solvent was evaporated under reduced pressure. The crude residue was purified *via* flash automatic column chromatography on silica gel (gradient of cyclohexane to dichloromethane) giving the product as a violet solid (500 mg, 0.7279 mmol, 26% yield).



R_f=0.54 (Cyclohexane: Dichloromethane 50:50).

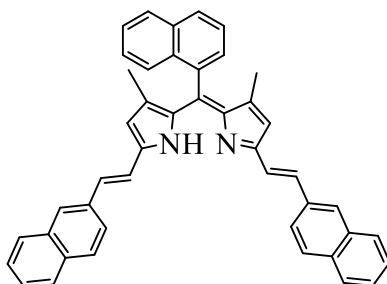
¹H-NMR (400 MHz, CDCl₃) δ/ppm: 9.00- 7.90 (m, 18H), 7.98 (s, 1H), 6.92 (s, 1H), 5.87 (s, 2H), 2.32 (s, 6H), 2.25 (s, 3H), 1.35 (s, 6H).

¹³C-NMR (100 MHz, CDCl₃) δ/ppm: 164.41, 161.41, 159.48, 158.74, 158.15, 156.32, 155.14, 154.36, 154.12, 153.21, 152.55, 152.14, 151.140, 150.65, 150.21, 149.84, 149.57, 139.14, 139.02, 138.41, 136.54, 135.20, 134.84, 133.51, 124.10, 125.10, 121.50, 120.64, 119.65, 118.70, 102.54, 98.54, 64.58, 62.47, 22.14, 20.19, 15.41.

HRMS (C₅₂H₄₂N₂) 694.3348 (calculated), 694.4132 (found).

3,7-dimethyl-1,9-bis(2'-naphth-2''-yl-vinyl)-5-(naphthyl)-dipyrrin (38)

Under an argon atmosphere, in a two-neck round bottom flask, 1,3,7,9-tetramethyl-5-naphthyl-dipyrrin **17** (900 mg, 2.51 mmol, 1.00 equiv.) and naphthalene-2-carbaldehyde (3.30 g, 15.06 mmol, 6.00 equiv.) were solved in 200 ml of dry toluene. Subsequently, piperidine (10 ml, 0.01 equiv.) and glacial acetic acid (10 ml, 0.02 equiv.) were added to the reaction mixture which was refluxed at 120 °C, through the use of an air condenser and stirred for 24 hours. After cooling the system, the organic layer was washed with saturated NaCl aqueous solution, and the aqueous layers were recombined and extracted with CH₂Cl₂. The organic phases were collected and dried over MgSO₄. The mixture was filtered, and the solvent was evaporated under reduced pressure. The crude residue was purified *via* flash automatic column chromatography on silica gel (gradient of cyclohexane to dichloromethane/dichloromethane and methanol 80:20) giving the product as a violet solid (500 mg, 0.7279 mmol, 26% yield).



R_f=0.4 (Cyclohexane: Dichloromethane = 50:50).

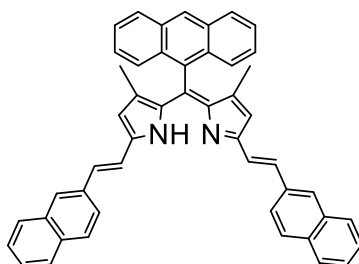
¹H-NMR (400 MHz, CDCl₃) δ/ppm: 8.42 (d, J= 2.12, 1H), 7.99-7.90 (m, 5H), 7.79-7.66 (m, 5H), 7.62-7.55 (m, 2H), 7.51-7.46 (m, 2H), 7.45-7.42 (m, 2H), 7.35 (d, J=5.29 Hz, 2H), 6.41 (s, 2H), 2.08 (s, 6H).

¹³C-NMR (100 MHz, CDCl₃) δ/ppm: 151.10, 148.17, 141.04, 140.07, 137.30, 137.14, 136.22, 135.24, 134.63, 133.71, 133.55, 132.25, 132.18, 128.79, 128.55, 128.38, 128.26, 128.08, 127.74, 127.66, 127.60, 127.57, 126.89, 126.48, 125.74, 125.63, 125.49, 123.48, 121.19, 119.40, 47.47, 42.51, 39.09, 26.45, 21.51, 14.33.

HRMS (C₄₅H₃₄N₂) 602.2722 (calculated), 602.1078 (found).

1,9-vinyl-2''-naphthalene-3,7-dimethyl -5-(anthracenyl)-dipyrrin (**39**)

Under an argon atmosphere, in a two-neck round bottom flask, 1,3,7,9-tetramethyl -5-anthracenyl-dipyrrin **19** (1.00 g, 3.51 mmol, 1.00 equiv.) and naphthalene-2-carbaldehyde (4.10 g, 21.06 mmol, 6.00 equiv.) were solved in 200 ml of dry toluene. Subsequently, piperidine (10 ml, 0.01 equiv.) and glacial acetic acid (10 ml, 0.02 equiv.) were added to the reaction mixture which was refluxed at 120 °C, through the use of an air condenser and stirred for 24 hours. After cooling the system, the organic layer was washed with saturated NaCl aqueous solution, and the aqueous layers were recombined and extracted with CH₂Cl₂. The organic phases were collected and dried over MgSO₄. The mixture was filtered, and the solvent was evaporated under reduced pressure. The crude residue was purified *via* flash automatic column chromatography on silica gel (gradient of cyclohexane to dichloromethane/dichloromethane and methanol 80:20) giving the product as a violet solid (500 mg, 0.7279 mmol, 26% yield).



R_f=0.4 (Cyclohexane: Dichloromethane 5:5).

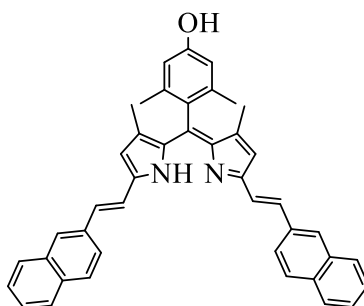
¹H-NMR (400 MHz, CDCl₃) δ/ppm: 8.33 (s, 4 H), 8.09 (s, 2H) 7.90 (m, 3 H), 7.87-7.84 (d, J=1.6 Hz, 4 H), 7.78-7.63 (dt, J=7.4 Hz, 4 H), 7.47 (s, 2H), 7.45-7.40 (m, 2 H), 7.35 (m, 2 H), 7.21 (s, 2 H), 6.63 (s, 2H), 5.75 (s, 1H), 2.01 (s, 6H).

¹³C-NMR (100 MHz, CDCl₃) δ/ppm: 164.43, 163.20, 161.18, 160.85, 160.45, 160.23, 154.12, 150.26, 148.14, 147.95, 146.65, 145.55, 143.21, 142.11, 138.29, 137.56, 136.51, 135.24, 134.14, 132.10, 131.10, 129.54, 126.41, 125.51, 124.65, 123.57, 123.10, 119.54, 118.98, 115.45, 114.54, 110.25, 55.65, 48.74, 24.54, 21.10

HRMS (C₄₉H₃₆N₂) 652.2878 (calculated), 651.1478 (found).

1,9-vinyl-2''-naphthalene-3,7-dimethyl -2',6'-dimethyl-4'-hydroxy-phenly-dipyrrin (44)

In a microwave glass vial 1,3,7,9-tetramethyl -5-(2',6'-dimethyl-4'-hydroxy)-phenyl-dipyrrin **15** (1.00 g, 3.121 mmol, 1equiv.) and naphthalene-2-carbaldehyde (2.924 g, 18.72 mmol, 6 equiv.) were dissolved in 4 ml of ethanol and then 1 ml of piperidine and 1 ml of glacial acetic acid were added dropwise. Catalytic amounts of $Mg(ClO_4)_2$ were incorporated into the system. Once the reaction was completed, the organic layer was washed with saturated NaCl aqueous solution and the aqueous layers were recombined and extracted with CH_2Cl_2 . The organic phases were collected and dried over $MgSO_4$. The mixture was filtered, and the solvent was evaporated under reduced pressure. The crude residue was purified *via* flash automatic column chromatography on silica gel (gradient of dichloromethane/methanol) giving the product as a purple solid (500 mg, 0.8379 mmol, 27% yield).



R_f=0.4 (Dichloromethane).

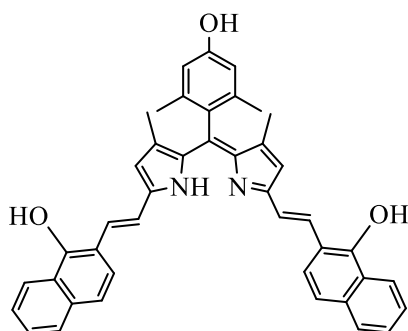
¹H-NMR (400 MHz, $CDCl_3$) δ /ppm: 8.07 (s, 2 H), 7.99 (s, 2 H), 7.96-7.91 (d, $J=1.2$ Hz, 4 H), 7.88-7.83 (dt, $J=7.1$ Hz, 4 H), 7.57 (s, 2H), 7.53-7.50 (h, $J=3.7$ Hz, 2 H), 7.48 (s, 2 H), 7.44 (s, 2 H), 6.63 (s, 2H), 5.75 (s, 1H), 2.01 (s, 6H), 1.41 (s, 6H).

¹³C-NMR (100 MHz, $CDCl_3$) δ /ppm: 151.10, 140.99, 140.22, 137.34, 137.04, 136.21, 135.26, 134.66, 133.76, 128.76, 128.56, 128.09, 127.75, 127.67, 127.16, 126.68, 126.52, 123.48, 121.26, 119.48, 55.31, 24.52, 14.33.

HRMS ($C_{44}H_{38}N_2$) 596.2828 (calculated), 596. 1432 (found).

3,7-dimethyl-1,9-bis(2'-naphthyl-1-hydroxy-vinyl)-5-(2'',6''-dimethyl-4''-hydroxyphenyl)-dipyrrin (45)

In a microwave glass vial 1,3,7,9-tetramethyl-5-(2',6'-dimethyl-4'-hydroxy)-phenyl-dipyrrin **15** (500.04 mg, 1.21 mmol, 1equiv.) and 1-hydroxy-naphthalene-2-carbaldehyde (1.424 g, 5.26 mmol, 6 equiv.) were dissolved in 4 ml of ethanol and then 1 ml of piperidine and 1 ml of glacial acetic acid were added dropwise. Catalytic amounts of $\text{Mg}(\text{ClO}_4)_2$ were incorporated into the system. Once the reaction was completed, the organic layer was washed with saturated NaCl aqueous solution, and the aqueous layers were recombined and extracted with CH_2Cl_2 . The organic phases were collected and dried over MgSO_4 . The mixture was filtered, and the solvent was evaporated under reduced pressure. The crude residue was purified *via* flash automatic column chromatography on silica gel (gradient of dichloromethane/methanol) giving the product as a purple solid (100 mg, 0.5419 mmol, 12% yield).



$R_f=0.4$ (Dichloromethane: Methanol 70:30).

$^1\text{H-NMR}$ (400 MHz, CDCl_3) δ /ppm: 8.47 (s, 3 H), 7.84 (m, 6 H), 7.76-7.51 (m, 4 H), 7.46 (s, 2H), 7.43-7.40 (m, 2 H), 7.24 (s, 2 H), 6.53 (s, 2H), 5.55 (s, 2H), 2.11 (s, 6H), 1.51 (s, 6H).

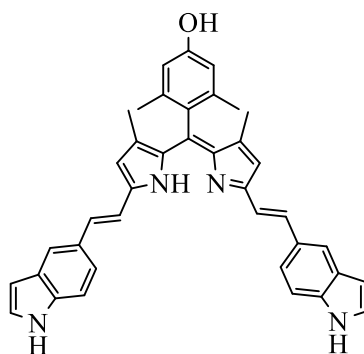
$^{13}\text{C-NMR}$ (100 MHz, CDCl_3) δ /ppm: 164.21, 160.52, 154.12, 148.41, 147.54, 146.51, 138.65, 138.10, 137.56, 137.41, 136.31, 135.41, 134.54, 133.62, 133.21, 131.14, 131.51, 130.24, 128.41, 119.81, 117.54, 115.41, 44.41, 36.51, 25.71, 12.51.

151.10, 140.99, 140.22, 137.34, 137.04, 136.21, 135.26, 134.66, 133.76, 128.76, 128.56, 128.09, 127.75, 127.67, 127.16, 126.68, 126.52, 123.48, 121.26, 119.48, 55.31, 24.52, 14.33.

HRMS ($\text{C}_{43}\text{H}_{36}\text{N}_2\text{O}_3$) 628.7720 (calculated), 628.1478 (found).

3,7-dimethyl-1,9-bis(2'-indol-5''-yl-vinyl)-5-(2''',6'''-dimethyl-4'''-hydroxyphenyl)-dipyrrin (46)

In a microwave glass vial compound 1,3,7,9-tetramethyl -5-(2',6'-dimethyl-4'-hydroxy)-phenyl-dipyrrin **15** (150 mg, 0.47 mmol, 1equiv.) and 1H-indole-5-carboxaldehyde (407.7 mg, 2.809 mmol, 6 equiv.) were dissolved in 4 ml of ethanol and then 2 ml of piperidine and 2 ml of glacial acetic acid were added dropwise. Catalytic amounts of $Mg(ClO_4)_2$ were incorporated into the system. Once the reaction was completed, the organic layer was washed with saturated NaCl aqueous solution, and the aqueous layers were recombined and extracted with CH_2Cl_2 . The organic phases were collected and dried over $MgSO_4$. The mixture was filtered, and the solvent was evaporated under reduced pressure. The crude residue was purified *via* flash automatic column chromatography on silica gel (gradient of dichloromethane/methanol) giving the product as a blue solid (70 mg, 0.1214 mmol, 31% yield).



R_f=0.2 (Dichloromethane: Methanol 70:30).

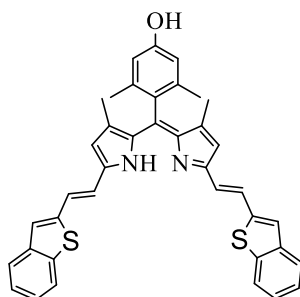
¹H-NMR (400 MHz, DMSO- d_6) δ /ppm: 9.78 (s, 2H), 8.00 (s, 2H), 7.64 (s, 1H), 7.58-7.53 (m, 1H), 7.58 (d, J= 8.3 Hz, 2H), 7.38(s, 1H), 7.30 (d, J= 3.7 Hz, 2H), 7.29-7.25 (m, 2H), 7.24 (s, 1H), 7.15 (s, 1H), 7.11 (s, 1H) 6.40 (s, 1H) 6.33 (s, 1H), 1.79 (s, 6H), 1.73 (s, 6H)

¹³C-NMR (100 MHz, DMSO- d_6) δ /ppm: 164.10, 158.41, 145.20, 140.87, 139.54, 136.70, 135.98, 132.14, 131.59, 128.47, 128.31, 128.96, 127.98, 126.54, 125.25, 124.74, 123.65, 121.87, 118.78, 117.64, 115.98, 50.41, 29.78, 14.71.

HRMS ($C_{39}H_{34}N_4O$) 574.2733 (calculated), 573.4198 (found).

3,7-dimethyl-1,9-bis(2'-benzo[b]thiophenyl-5''-yl-vinyl)-5-(2''',6'''-dimethyl-4'''-hydroxyphenyl)-dipyrrin (47)

In a microwave glass vial 1,3,7,9-tetramethyl-5-(2',6'-dimethyl-4'-hydroxy)-phenyl-dipyrrin **15** (200 mg, 0.624 mmol, 1equiv.) and 1-benzo[b]thiophene-2-carboxaldehyde (607.5 mg, 3.745 mmol, 6 equiv.) were dissolved in 4 ml of ethanol and then 2 ml of piperidine and 2 ml of glacial acetic acid were added dropwise. Catalytic amounts of $\text{Mg}(\text{ClO}_4)_2$ were incorporated into the system. Once the reaction was completed, the organic layer was washed with saturated NaCl aqueous solution, and the aqueous layers were recombined and extracted with CH_2Cl_2 . The organic phases were collected and dried over MgSO_4 . The mixture was filtered, and the solvent was evaporated under reduced pressure. The crude residue was purified *via* flash automatic column chromatography on silica gel (gradient of dichloromethane/methanol) giving the product as a violet solid (50 mg, 0.082 mmol, 13% yield).



$R_f=0.3$ (Dichloromethane: Methanol 70:30).

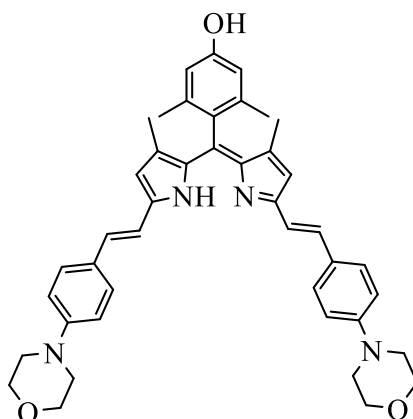
$^1\text{H-NMR}$ (400 MHz, DMSO-d_6) δ /ppm: 11.19 (s, 2H), 9.6 (s, 2H), 7.78 (s, 1H), 7.69-7.63 (m, 1H), 7.46 (d, $J=8.3$ Hz, 2H), 7.42 (s, 1H), 7.39 (d, $J=3.7$ Hz, 2H), 7.38-7.34 (m, 2H), 7.26 (s, 1H), 7.15 (s, 1H), 7.11 (s, 1H), 6.57 (s, 1H), 6.49 (s, 1H), 1.96 (s, 6H), 1.23 (s, 6H).

$^{13}\text{C-NMR}$ (100 MHz, DMSO-d_6) δ /ppm: 155.5, 152.8, 143.3, 140.6, 138.6, 137.4, 136.4, 135.5, 132.0, 131.9, 130.8, 129.5, 125.7, 124.3, 123.2, 122.6, 116.8, 121.2, 116.7, 110.4, 20.1, 13.8.

HRMS ($\text{C}_{39}\text{H}_{34}\text{N}_4\text{O}$) 608.1956 (calculated), 608.4785 (found).

3,7-dimethyl-1,9-bis(2'-morpholinylphenyl -5''-yl-vinyl)-5-(2''',6'''-dimethyl-4'''-hydroxyphenyl)-dipyrrin (48)

In a microwave glass vial 1,3,7,9-tetramethyl -5-(2',6'-dimethyl-4'-hydroxy)-phenyl-dipyrrin **15** (250 mg, 0.744 mmol, 1equiv.) and morpholino benzaldehyde (89.5 mg, 4.534 mmol, 6 equiv.) were dissolved in 4 ml of ethanol and then 2 ml of piperidine and 2 ml of glacial acetic acid were added dropwise. Catalytic amounts of $Mg(ClO_4)_2$ were incorporated into the system. Once the reaction was completed, the organic layer was washed with saturated NaCl aqueous solution, and the aqueous layers were recombined and extracted with CH_2Cl_2 . The organic phases were collected and dried over $MgSO_4$. The mixture was filtered, and the solvent was evaporated under reduced pressure. The crude residue was purified *via* flash automatic column chromatography on silica gel (gradient of dichloromethane/methanol) giving the product as a violet solid (10 mg, 0.042 mmol, 10% yield).



1H -NMR (400 MHz, $CDCl_3$) δ /ppm: 8.14 (s, 2H), 7.95 (s, 2H), 7.85-7.78 (m, 4H), 7.70-7.65 (m, 4H), 7.54 (m, 2H), 6.74 (s, 2H), 5.87 (s, 2H), 3.73 (m, 8H), 3.15 (m, 8H), 2.14 (s, 6H), 1.9 (s, 6H).

^{13}C -NMR (100 MHz, $CDCl_3$) δ /ppm: 164.14, 162.10, 162.05, 154.41, 140.87, 139.58, 138.41, 137.54, 136.51, 135.20, 135.02, 134.65, 133.25, 132.14, 130.25, 129.87, 128.78, 127.84, 126.58, 125.54, 124.74, 123.69, 122.48, 121.10, 118.74, 115.41, 58.41, 57.69, 55.87, 55.10, 25.54, 12.36.

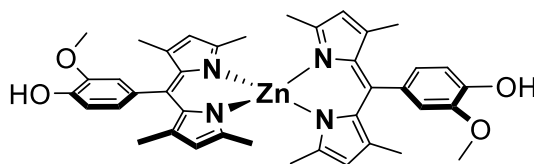
HRMS ($C_{43}H_{46}N_4O_3$) 666.8660 (calculated), 665.8746 (found).

6.2.3 Homoleptic bis (dipyrinato)Zn^{II} complexes

General procedure: to a solution of functionalized dipyrromethene (2 equiv.) in dichloromethane: methanol (2:1), anhydrous zinc acetate (1 equiv.) was added. The reaction mixture is stirred overnight and afterwards the solvent was reduced by a rotary evaporator. The colorful solid was filtered and rinsed with cold methanol.

Bis (1,3,7,9-tetramethyl -5-(3'-methoxy-4'-hydroxyphenyl)-dipyrinato) zinc (II) (**48**)

To a solution of 1,3,7,9-tetramethyl -5-(3'-methoxy-4'-hydroxyphenyl)-dipyrin **13** (61.56 mg, 0.1635 mmol, 2equiv.) in dichloromethane (10 mL), zinc acetate (15.0 mg, 0.082 mmol, 1 equiv.) pre-solved in methanol (5ml) was added and stirring overnight to give **48** as a dark-green powder (40 mg, 0.048 mmol, 60 % yield).



¹H-NMR (400 MHz, CDCl₃) δ/ppm: 7.45 (m, 2 H), 7.35 (m, 4 H), 5.79 (s, 4 H), 3.51 (s, 3H), 3.32 (s, 3H), 2.12 (s, 12 H), 1.18 (s, 12H)

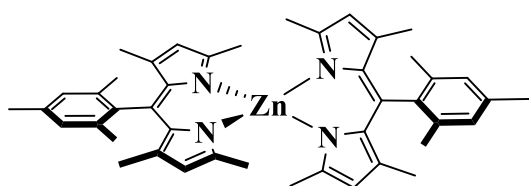
¹³C-NMR (100 MHz, CDCl₃) δ/ppm: 155.76, 143.09, 143.01, 137.20, 136.08, 135.42, 134.39, 128.59, 119.41, 21.06, 19.10, 15.96, 14.67.

HRMS (MALDI) m/z calcd for C₄₀H₄₂N₄O₄Zn⁺: 706.24975 found: 705.94350.

Elemental Analysis for C₄₀H₄₄N₄O₅Zn • 2 H₂O: C 64.56, H 6.23, N 7.53; found: C 64.80, H 6.41, N 7.64

Bis (1,3,7,9-tetramethyl-5-mesityldipyrrinato) zinc (II) (49)

5-mesityl-1,3,7,9-tetramethyl-dipyrrin **14** (500 mg, 1.975 mmol, 2equiv.) was dissolved in 25 ml of dichloromethane. A solution of anhydrous zinc acetate (0.890 g, 1.75 mmol, 1equiv.) in 10 ml of methanol was added, and the reaction mixture was stirred overnight. A dark green precipitate was collected by vacuum filtration and rinsed with methanol. The solid was recrystallized from dichloromethane/methanol, yielding dark green microcrystals **49** (241 mg, 0.987 mmol, 50 %).



R_f=0.3 (Dichloromethane).

¹H-NMR (400 MHz, CDCl₃) δ/ppm: 6.92 (s, 4H), 5.90 (s, 4H), 2.34 (s, 6H), 2.11 (s, 12 H), 2.03 (s, 12H), 1.29 (s, 12H).

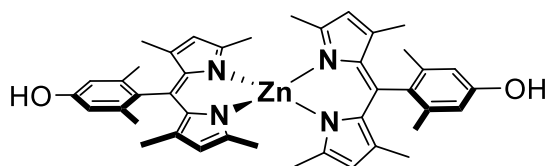
¹³C-NMR (100 MHz, CDCl₃) δ/ppm: 156.00, 143.73, 143.24, 137.44, 136.29, 135.64, 134.61, 128.83, 119.63, 21.30, 19.34, 16.20, 14.92.

HRMS (C₄₄H₅₀N₄Zn) 698.3327 (calculated), 699.3398 (found).

Elemental Analysis for C₄₄H₅₀N₄Zn : C 75.47, H 7.20, N 8.00; found: C 74.80, H 7.11, N 7.64.

Bis (1,3,7,9-tetramethyl -5-(2',6'-dimethyl-4'-hydroxy)-phenyl-dipyrrinato) zinc (II) (50)

To a solution of 1,3,7,9-tetramethyl -5-(2',6'-dimethyl-4'-hydroxy)-phenyl-dipyrrin **15** (34.93 mg, 0.1090 mmol, 2 equiv.) in dichloromethane (10 mL), zinc acetate (10.0 mg, 0.054 mmol, 1 equiv.) pre-solved in methanol (5ml) was added and stirring overnight to give **50** as a dark-green powder (25.4 mg, 0.036 mmol, 66% yield).



¹H-NMR (400 MHz, CDCl₃) δ/ppm: 6.53 (s, 4H), 5.86 (s, 4H), 5.27 (s, 1H) 2.40 (s, 12H), 2.07 (s, 12H), 1.34 (s, 12H).

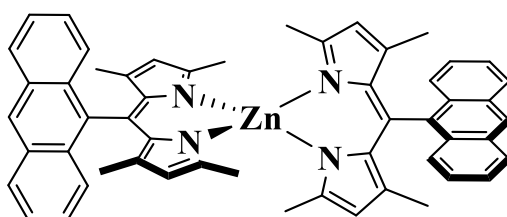
¹³C-NMR (100 MHz): 155.28, 151.34, 139.73, 137.71, 135.75, 119.10, 114.60, 19.74, 16.06, 13.72.

HRMS (MALDI) m/z calcd for C₄₂H₄₆N₄O₂Zn⁺: 702.29122; found: 702.69228.

Elemental analysis for C₄₂H₄₆N₄O₂Zn • 2H₂O calcd: C 68.15, H 6.81, N 7.57; found: C 68.74, H 6.75, N 7.41.

Bis (1,3,7,9-tetramethyl -5-anthracenyl-dipyrrinato) zinc (II) (51)

1,3,7,9-tetramethyl -5-anthracenyl-dipyrrin **19** (100 mg, 0.478 mmol, 2 equiv.) was dissolved in 25 ml of dichloromethane. A solution of anhydrous zinc acetate (0.475 mg, 0.0247 mmol, 1 equiv.) in 10 ml of methanol was added, and the reaction mixture was stirred overnight. A dark green precipitate was collected by vacuum filtration and rinsed with methanol. The solid was recrystallized from dichloromethane/methanol, yielding dark black microcrystals (70 mg, 0.475 mmol, 40 %).



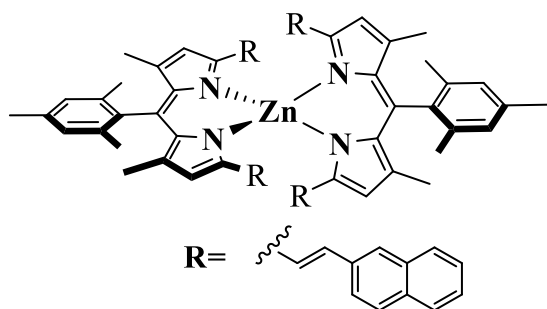
¹H-NMR (400 MHz, CDCl₃) δ/ppm: 8.57 (s, 2H), 8.00 (m, 8H), 7.45 (t, J=7.3 Hz, 4H), 7.37 (t, J= 7.9 Hz, 4H), 5.78 (s, 4 H), 2.42 (s, 12H), 0.51 (s, 12H).

¹³C-NMR (100 MHz, CDCl₃) δ/ppm: 151.73, 140.10, 137.37, 131.78, 130.59, 130.35, 128.17, 127.35, 126.92, 125.83., 125.65, 125.44, 119.48, 108.18, 16.15, 13.60.

HRMS (C₅₄H₄₆N₄Zn) 814.3014 (calculated), 814.2174 (found).

Bis (3,7-dimethyl-1,9-bis(2'-naphth-2''-yl-vinyl)-5-(2''', 4'', 6'''-trimethylphenyl)-dipyrrinato) zinc(II) (52)

3,7-dimethyl-1,9-bis(2'-naphth-2''-yl-vinyl)-5-(2''', 4'', 6'''-trimethylphenyl)-dipyrrin **34** (650 mg, 0.10 mmol, 2 equiv.) was dissolved in 15 ml of dichloromethane. A solution of anhydrous zinc acetate (9 mg, 0.05 mmol, 1 equiv.) in 5 ml of methanol was added, and the reaction mixture was stirred overnight. A dark blue precipitate was collected by vacuum filtration and rinsed with methanol. The solid was recrystallized from dichloromethane/methanol, yielding a dark blue powder (51 mg, 0.123 mmol, 75 %).



¹H-NMR (400 MHz, CDCl₃) δ/ppm: 7.74 (dd, J= 25.6, 5.9 Hz, 4H), 7.64-7.58 (m, 2H), 7.48-7.37 (m, 4H), 7.97-7.30 (m, 2H), 7.21 (dd, J=16.1, 2.6 Hz, 2H), 7.08 (dd, J=16.1, 4.8 Hz, 2H), 6.88-6.72 (m, 3H), 2.33 (s, 3H), 1.92 (d, J= 4.5 Hz, 6H), 1.51 (d, J=4.1 Hz, 6H).

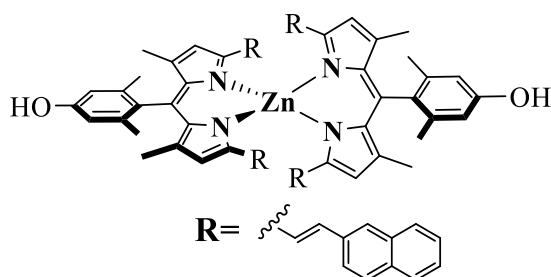
¹³C-NMR (100 MHz): 156.5, 144.0, 143.1, 138.5, 137.9, 163.3, 135.8, 135.1, 133.7, 133.1, 133.0, 128.9, 128.2, 128.1, 127.8, 127.6, 126.3, 126.0, 123.9, 122.7, 118.6, 21.4, 19.8, 15.6,

HRMS (MALDI) m/z calcd for C₈₈H₇₄N₄Zn⁺: 1252.9680; found: 125.1520.

Elemental analysis for C₈₈H₇₄N₄Zn •CH₂Cl₂ calcd: C 78.84, H 5.80, N 4.13; found: C 78.83, H 5.54, N 4.10.

Bis(1,9-vinyl-2''-naphthalene-3,7-dimethyl-2',6'-dimethyl-4'-hydroxy-phenly-dipyrinato)zinc(II) (53)

To a solution of 1,9-vinyl-2''-naphthalene-3,7-dimethyl -2',6'-dimethyl-4'-hydroxy-phenly-dipyrin **44** (65.05 mg, 0.1090 mmol, 2 equiv.) in dichloromethane (10 mL), zinc acetate (10.0 mg, 0.054 mmol, 1 equiv.) pre-solved in methanol (5ml) was added and stirring overnight to give a dark-blue powder (50 mg, 0.039 mmol, 73% yield).



¹H-NMR (400 MHz, CDCl₃) δ/ppm: 7.77-7.68 (dd, J= 1.09, 9H), 7.59 (d, J= 8.55, 4H), 7.54 (s, 4H), 7.44-7.39 (m, 8H), 7.32 (dd, J= 1.70, 8.65, 4H), 7.21(s, 2H), 7.17 (s, 2H), 7.09 (s, 2H), 7.05 (s, 1H), 6.82 (s, 4H), 6.76 (s, 4H), 1.89 (12 H), 1.52 (d, 12H).

¹³C-NMR (100 MHz, CDCl₃) δ/ppm: 156.38, 144.39, 143.41, 138.69, 138.24, 136.68, 136.18, 135.48, 134.04, 133.49, 133.35, 129.24, 128.53, 128.41, 128.08, 127.92, 126.58, 126.29, 124.29, 123.07, 118.90, 21.70, 20.12, 15.91.

HRMS (MALDI) m/z calcd for C₈₈H₇₀N₄O₂Zn⁺: 1254.47902 found: 1254.0528.

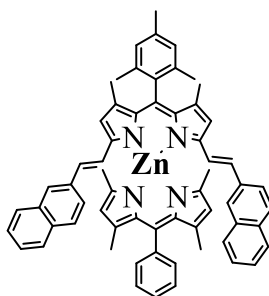
Elemental Analysis for C₈₈H₇₀N₄O₂•2 H₂O calcd: C 79.89, H 5.77, N 4.33; found: C 79.98, H 5.81, N 4.62.

6.2.4 Heteroleptic bis (dipyrinato) Zn^{II} complexes

General procedure: two different kinds of functionalized dipyrin (1 equiv. each) were dissolved in 50 ml of dichloromethane and 25 ml of methanol. Then, zinc diacetate (1.5 equiv.) was added, and the reaction was left stirring overnight at room temperature. The solvent was removed under reduced pressure and the crude residue was purified by flash chromatography.

[5-mesityl-3,7-dimethyl-1,9-bis(2'-naphth-2''-yl-vinyl)-dipyrinato] [1,3,7,9-tetramethyl-5-phenyl-dipyrinato] zinc(II) (**54**)

The reaction of **11** (300.0 mg, 0.936 mmol, 1 equiv.) and **34** (516.5 mg, 0.868 mmol, 1 equiv.) with zinc diacetate (298.7 mg, 1.628 mmol, 1.5 equiv.) was performed in a 2:1 mixture of CH₂Cl₂/MeOH. Automatic column chromatography packed with silica was used for purification (gradient of cyclohexane/dichloromethane) and gave **54** as a blue-violet powder (220.0 mg, 0.235 mmol, 22% of yield).



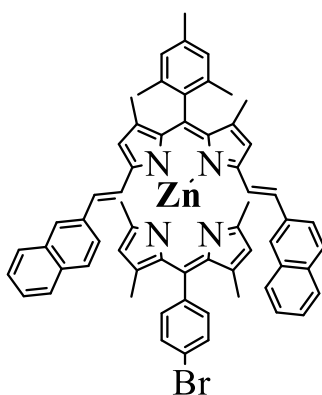
¹H NMR (500 MHz, CDCl₃) δ/ppm: 7.85 (p, *J* = 8.5 Hz, 1H), 7.78 – 7.73 (m, 1H), 7.73 – 7.69 (m, 1H), 7.60 (d, *J* = 8.6 Hz, 1H), 7.55 (s, 1H), 7.43 – 7.40 (m, 2H), 7.34 – 7.30 (m, 1H), 7.21 (s, 0H), 7.18 (s, 1H), 7.09 (s, 2H), 7.05 (d, *J* = 3.2 Hz, 2H), 6.82 (s, 2H), 6.76 (s, 2H), 2.74 (s, 3H), 2.68 (s, 6H), 2.14 (s, 6H), 1.9 (s, 6H), 0.8 (s, 6H).

¹³C NMR (126 MHz, CDCl₃) δ 156.37, 143.93, 142.95, 138.42, 137.78, 136.21, 135.02, 133.58, 133.03, 132.89, 128.79, 128.24, 128.08, 127.96, 127.63, 127.48, 126.13, 125.84, 123.82, 122.61, 118.44, 77.28, 77.03, 76.77, 21.26, 19.79, 19.67, 15.47.

HRMS (MALDI) *m/z* calcd for C₆₃H₅₆N₄Zn⁺: 932.3796; found: 932.4789.

[5-mesityl-3,7-dimethyl-1,9-bis(2'-naphth-2'-yl-vinyl)-dipyrrinato] [5-4'-bromophenyl- -dipyrrinato] zinc(II) (55**)**

The reaction of **12** (500.0 mg, 0.8406 mmol, 1 equiv.) and **34** (298.7 mg, 0.8406 mmol, 1 equiv.) with zinc diacetate (169.7 mg, 0.9247 mmol, 1.1 equiv.) was performed in a 2:1 mixture of CH₂Cl₂/MeOH. The crude residue was purified *via* column chromatography packed with alumina (gradient of cyclohexane/dichloromethane) and gave the compound **55** as a blue-violet powder (254.0 mg, 0.2501 mmol, 30 % yield).



¹H-NMR (400 MHz, CDCl₃) δ/ppm: 7.78-7.74 (m, 2H), 7.73-7.67 (m, 2H), 7.60 (d, J= 8.6 Hz, 2H), 7.55 (d, J=1.7 Hz, 4H), 7.45-7.39 (m, 5H), 7.33 (dd, J= 8.6, 1.7 Hz, 3H), 7.22 (s, 1H), 7.18 (s, 2H) 7.10 (s, 1H), 7.06 (s, 2H), 6.82 (s, 2H), 6.76 (s, 2H), 2.33 (s, 3H), 1.91 (s, 6H), 1.50 (s, 6H), 1.43 (s, 12H).

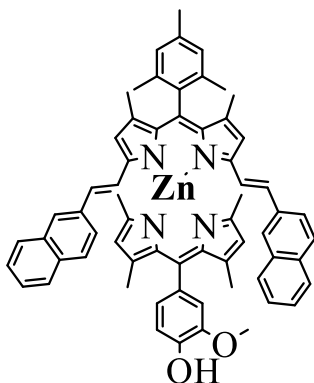
¹³C NMR (101 MHz, CDCl₃) δ/ppm: 156.38, 143.93, 142.96, 138.43, 137.79, 136.22, 135.73, 135.03, 133.59, 133.04, 132.90, 128.79, 128.08, 127.96, 127.63, 127.47, 126.13, 125.83, 123.84, 122.62, 118.45, 77.34, 77.02, 76.71, 29.72, 26.93, 21.25, 19.67, 15.46.

HRMS (MALDI) m/z calcd for C₆₃H₅₅N₄BrZn⁺: 1013.4450; found: 1013.1489.

Elemental Analysis for C₆₃H₅₅N₄BrZn•CH₂Cl₂: C 74.67, H 5.47, N 5.53; found: C 75.01, H 5.20, N 5.70.

[5-mesityl-3,7-dimethyl-1,9-bis(2'-naphth-2'-yl-vinyl)-dipyrrinato] [1,3,7,9-tetramethyl - 5-(3'-methoxy-4'-hydroxyphenyl)-dipyrrinato] zinc(II) (56)

The reaction of **13** (135.5 mg, 0.420 mmol, 1 equiv.) and **34** (250 mg, 0.420 mmol, 1 equiv.) with zinc diacetate (154.2 mg, 0.841 mmol, 1.5 equiv.) was performed in a 2:1 mixture of CH₂Cl₂/MeOH. Column chromatography packed with alumina was used for purification (gradient of dichloromethane/methanol as eluent mixture) and gave **56** as a blue-violet powder (150 mg, 0.153 mmol, 36 % yield).



¹H-NMR (400 MHz, CDCl₃) δ/ppm: 7.72-7.61 (m, 5H), 7.52 (d, J=8.6 Hz, 3 H), 7.50-7.43 (m, 2H), 7.39-7.31 (m, 5H), 7.25 (dd, J=8.6, 1.7 Hz, 3H), 7.15 (s, 1H), 7.11 (s, 2H), 7.02 (s, 2H), 6.97 (s, 1H), 6.75 (s, 2H), 6.69 (s, 2H), 2.25 (s, 3H), 1.83 (s, 6H), 1.47 (s, 3H), 1.43 (s, 6H), 1.35 (s, 9H).

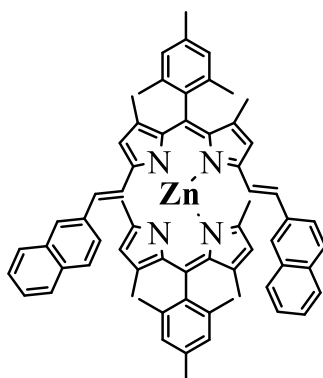
¹³C-NMR (100 MHz, CDCl₃) δ/ppm: 156.52, 144.07, 138.57, 137.92, 136.36, 135.17, 133.72, 133.18, 133.03, 128.92, 128.21, 128.09, 127.77, 127.61, 126.61, 126.26, 125.97, 123.98, 122.75, 118.59, 27.07, 21.39, 19.81, 15.60.

HRMS (MALDI) m/z calcd for C₆₄H₅₈N₄O₂Zn⁺:978.38512; found:978.3020.

Elemental Analysis for C₆₄H₅₈N₄O₂Zn • 2 H₂O: C 75.61, H 6.15, N 5.51 found: C 75.12, H 6.10, N 5.49.

[5-mesityl-3,7-dimethyl-1,9-bis(2'-napht-2''-yl-vinyl)-dipyrrinato] [5-mesityl-1,3,7,9-tetramethyl-dipyrrinato] zinc(II) (57**)**

The reaction of **14** (369.0 mg, 1.738 mmol, 1equiv.) and **34** (551.4 mg, 0.9270 mmol, 1 equiv.) with zinc diacetate (318.9 mg, 1.783 mmol, 1.5 equiv.) was performed in a 2:1 mixture of CH₂Cl₂/MeOH. Column chromatography packed with alumina neutral was used for purification (gradient of cyclohexane/dichloromethane as eluent mixture) and gave **57** as a blue powder (200 mg, 0.204 mmol, 18 % yield).



¹H-NMR (400 MHz, CDCl₃) δ/ppm: 7.80-7.72 (m, 6H), 7.63 (s, 1H), 7.61 (s, 1H), 7.58 (s, 2H), 7.44 (ddd, J=7.0, 2.6, 1.5 Hz, 6H), 7.30 (dd, J=8.6, 8.1 Hz, 2H), 7.18 (s, 1H), 7.13 (s, 1H), 7.00 (s, 2H), 6.82 (s, 2H), 6.67 (s, 2H), 2.40 (s, 3H), 2.31 (s, 3H), 2.19 (s, 12H), 1.91 (s, 6H), 1.44 (s, 12H).

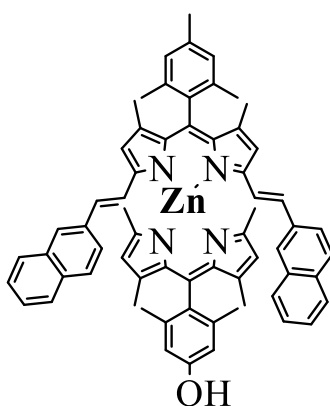
¹³C-NMR (100 MHz, CDCl₃) δ/ppm: 150.85, 140.59, 139.02, 138.07, 137.61, 136.02, 134.87, 133.86, 133.41, 131.96, 128.85, 128.65, 128.37, 127.86, 127.57, 126.58, 126.31, 123.60, 121.45, 119.26, 27.07, 21.39, 19.92, 14.00.

HRMS (MALDI) m/z calcd for C₆₆H₆₂N₄Zn⁺: 974.42659; found: 974.4455.

Elemental analysis for C₆₆H₆₂N₄Zn: C 81.17, H 6.40, N 5.74; found C 81.77, H 6.50, N 5.90

[5-mesityl-3,7-dimethyl-1,9-bis(2'-naphth-2''-yl-vinyl)-dipyrrinato] [1,3,7,9-tetramethyl-5-(2',6'-dimethyl-4'-hydroxy)-phenyl- dipyrrinato] zinc(II) (58)

The reaction of **15** (150.0 mg, 0.4681 mmol, 1 equiv.) and **34** (167.1 mg, 0.281 mmol, 1 equiv.) with zinc diacetate (103.1 mg, 0.562 mmol, 1.5 equiv.) was performed in a 2:1 mixture of CH₂Cl₂/MeOH. Automatic column chromatography packed with silica gel was used for purification (gradient of dichloromethane/methanol as eluent mixture) and gave **58** as a blue-violet powder (180.0 mg, 0.1836 mmol, 39 % yield).



¹H-NMR (400 MHz, CDCl₃) δ/ppm: 7.77-7.69 (m, 4 H), 7.59 (d, J=8.6 Hz, 2H), 7.55 (s, 2H), 7.44-7.38 (m, 4H), 7.24 (d, J= 1.9 Hz, 2 H), 7.19 (s, 1H), 7.15 (s, 1H), 7.07 (s, 1H), 7.03 (s, 1H), 6.98 (s, 2H), 6.65 (s, 2H), 6.48 (s, 2H), 6.04 (s, 2H), 2.38 (s, 3H), 2.16 (s, 12 H), 1.84 (s, 6H), 1.46 (s, 6H), 1.40 (s, 6H).

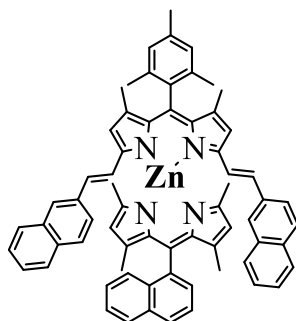
¹³C-NMR (100 MHz): 151.17, 140.91, 139.33, 138.39, 137.94, 136.34, 135.19, 134.18, 133.73, 132.28, 129.17, 128.98, 128.69, 126.90, 126.63, 123.92, 121.77, 119.57, 53.88, 27.39, 21.71, 20.24, 14.32.

HRMS (MALDI) m/z calcd for C₆₅H₆₀N₄OZn⁺: 974.2659; found: 974.4455.

Elemental Analysis for C₆₅H₆₀N₄OZn • CH₂Cl₂: C 74.54, H 5.88, N 5.27; found: C 74.69, H 5.90, N 5.42.

[5-mesityl-3,7-dimethyl-1,9-bis(2'-naphth-2''-yl-vinyl)-dipyrrinato] [1,3,7,9-tetramethyl-5-naphthyl- dipyrinato] zinc(II) (59)

The reaction of **17** (369.0 mg, 1.159 mmol, 1equiv.) and **34** (551.4 mg, 0.927 mmol, 0.8 equiv.) with zinc diacetate (318.9 mg, 1.738 mmol, 1.5 equiv.) was performed in a 2:1 mixture of CH₂Cl₂/MeOH. The crude residue was purified *via* column chromatography packed with alumina (gradient of cyclohexane/dichloromethane) and gave the compound **59** as a blue-violet powder (170.0 mg, 0.204 mmol, 18% of yield).



¹H NMR (500 MHz, CDCl₃) δ/ppm: 7.71 – 7.66 (m, 4H), 7.65 – 7.61 (m, 3H), 7.53 (d, *J* = 8.5 Hz, 2H), 7.48 (d, *J* = 1.7 Hz, 4H), 7.37 – 7.31 (m, 4H), 7.25 (dd, *J* = 8.6, 1.7 Hz, 4H), 7.11 (s, 2H), 7.02 (s, H), 6.75 (s, 2H), 6.69 (s, 2H), 2.26 (s, 3H), 1.84 (s, 6H), 1.45 (s, 6H), 1.36 (s, 6H).

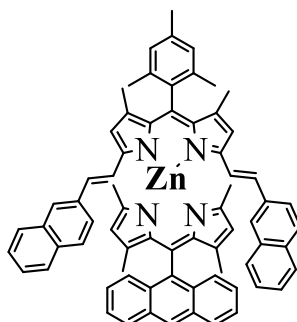
¹³C NMR (126 MHz, CDCl₃) δ/ppm: 156.37, 143.93, 142.95, 138.42, 137.78, 136.21, 135.72, 135.02, 133.58, 133.03, 132.90, 128.79, 128.08, 127.96, 127.63, 127.48, 126.13, 126.02, 125.84, 123.82, 123.00, 122.61, 118.44, 117.36, 77.28, 77.03, 76.77, 53.44, 29.72, 26.93, 25.51, 21.26, 19.68, 15.47, 15.20.

HRMS (MALDI) *m/z* calcd for C₆₇H₅₈N₄Zn⁺: 982.353; found: 982.458.

Elemental Analysis for C₆₇H₅₈N₄Zn•CH₂Cl₂: C 81.73, H 5.94, N 5.69; found: C 81.01, H 5.20, N 5.70.

[5-mesityl-3,7-dimethyl-1,9-bis(2'-napht-2''-yl-vinyl)-dipyrrinato] [1,3,7,9-tetramethyl - 5-anthracenyl- dipyrrinato] zinc(II) (60)

The reaction of **19** (500.0 mg, 1.382 mmol, 1equiv.) and **34** (656.9 mg, 1.382 mmol, 1 equiv.) with zinc diacetate (365.5 mg, 1.992 mmol, 1.5 equiv.) was performed in a 2:1 mixture of CH₂Cl₂/MeOH. Column chromatography packed with neutral alumina was used for purification (gradient of cyclohexane/dichloromethane as eluent mixture) and gave **60** as a blue-violet powder (315 mg, 0.304 mmol, 23 % yield).



¹H-NMR (400 MHz, CDCl₃) δ/ppm: 8.50 (s, 1H), 7.88 (t, J= 8.2 Hz, 4 H), 7.67-7.63 (m, 4 H), 7.62-7.58 (m, 2H), 7.43-7.30 (m, 13 H), 7.05-6.98 (m, 4 H), 6.75 (s, 2H) 6.26 (ddd, J= 7.9, 6.5, 1.3 Hz, 2 H), 5.97 (s, 2H) 2.42 (s, 3H), 2.26 (d, J=9.7, 2H), 1.49 (s, 6H), 0.64 (s, 6H).

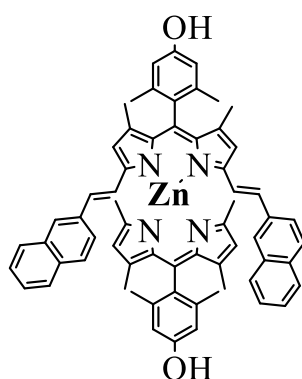
¹³C-NMR (100 MHz, CDCl₃) δ/ppm: 157.72, 156.32, 144.66, 144.17, 142.97, 141.86, 138.74, 136.44, 135.50, 134.14, 133.51, 132.90, 131.78, 131.17, 129.39, 128.95, 128.55, 127.92, 127.37, 126.78, 126.41, 126.30, 126.19, 125.48, 124.55, 123.33, 121.28, 117.95, 27.37, 21.73, 20.12, 17.09, 15.71, 15.51.

HRMS (MALDI) m/z calcd for C₇₁H₆₀N₄Zn⁺: 1032.41094; found: 11032.9434.

Elemental analysis for C₇₁H₆₀N₄Zn•H₂O: C 81.01, H 5.94, N 5.32; found: C 81.17, H 5.03, N 5.44.

[1,9-vinyl-2''-naphthalene-3,7-dimethyl -2',6'-dimethyl-4'-hydroxy-dipyrrinato] [1,3,7,9-tetramethyl -5-(2',6'-dimethyl-4'-hydroxy)-phenyl- dipyrrinato] zinc(II) (61)

The reaction of **15** (300.0 mg, 0.936 mmol, 1 equiv.) and **44** (391.1 mg, 0.655 mmol, 1 equiv.) with zinc diacetate (257.7 mg, 1.404 mmol, 1.5 equiv.) was performed in a 2:1 mixture of CH₂Cl₂/MeOH. Automatic column chromatography packed with silica was used for purification (gradient of cyclohexane/dichloromethane) and gave **61** as a blue-violet powder (98.60 mg, 0.099 mmol, 40 % yield).



¹H-NMR (400 MHz, CDCl₃) δ/ppm: 7.83-7.72 (m, 12H), 7.62 (dd, J= 8.0, 1.6 Hz), 7.44-7.31 (m, 7H), 7.23 (s, 2H), 6.89 (s, 2H), 6.34 (s, 2H), 2.29 (s, 6H), 2.09 (s, 9 H), 1.35 (s, 12H), 1.18 (s, 3 H).

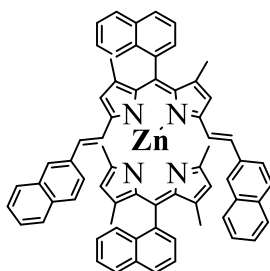
¹³C-NMR (101 MHz): 151.17, 140.91, 139.34, 138.39, 137.94, 136.34, 135.49, 135.19, 134.18, 133.73, 129.17, 128.97, 126.69, 128.18, 127.89, 126.90, 126.93, 123.92, 121.77, 119.57, 30.17, 21.71, 20.23, 15.91, 14.32.

HRMS (MALDI) m/z calcd for C₆₄H₅₈N₄O₂Zn⁺: 978.3851; found: 978.5610.

Elemental Analysis for C₆₄H₅₈N₄O₂Zn•2H₂O: C 75.61, H 6.15, N 5.51; found: C 76.02, H 6.20, N 5.70.

[3,7-dimethyl-1,9-bis(2'-naphthyl-2''-yl-vinyl)-5-(naphthyl)-dipyrrinato] [1,3,7,9-tetramethyl-5-naphthyl dipyrrinato] zinc(II) (62)

The reaction of **14** (270.8 mg, 0.829 mmol, 1equiv.) and **38** (500.0 mg, 0.829 mmol, 1 equiv.) with zinc diacetate (228.3 mg, 1.244 mmol, 1.5 equiv.) was performed in a 2:1 mixture of CH₂Cl₂/MeOH. Automatic column chromatography packed with silica was used for purification (gradient of cyclohexane/dichloromethane) and gave **62** as a violet powder (238.0 mg, 0.239 mmol, 29 % yield).



¹H NMR (500 MHz, CDCl₃) δ/ppm: 8.01 – 7.95 (m, 3H), 7.90 (dd, *J* = 8.4, 4.4 Hz, 4H), 7.86 – 7.79 (m, 2H), 7.76 – 7.70 (m, 3H), 7.67 – 7.60 (m, 3H), 7.60 – 7.54 (m, 2H), 7.52 (dd, *J* = 8.8, 1.7 Hz, 3H), 7.46 (ddd, *J* = 6.7, 4.2, 1.6 Hz, 2H), 7.41 – 7.37 (m, 3H), 7.32 (ddd, *J* = 12.4, 5.6, 3.1 Hz, 3H), 7.23 (s, 2H), 7.16 (d, *J* = 7.1 Hz, 2H), 6.71 (s, 2H), 6.58 (s, 2H), 1.54 (s, 6H), 1.23 (s, 6H), 0.98 (s, 6H).

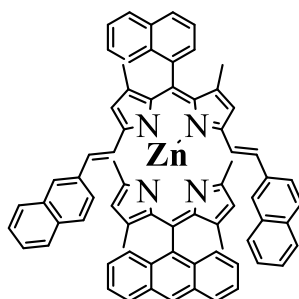
¹³C NMR (126 MHz, CDCl₃) δ 156.66, 156.24, 144.37, 144.30, 141.54, 139.70, 139.31, 137.48, 137.39, 135.20, 135.07, 133.68, 133.63, 133.51, 133.46, 133.17, 133.04, 133.03, 132.78, 132.41, 128.81, 128.63, 128.40, 128.36, 128.28, 128.25, 128.23, 128.01, 127.85, 127.70, 127.55, 127.51, 127.46, 127.32, 126.32, 126.28, 126.08, 126.05, 126.02, 125.86, 125.74, 125.66, 123.73, 123.38, 122.92, 122.83, 120.97, 118.79, 118.70, 117.86, 77.29, 77.03, 76.78, 16.68, 16.49, 15.77, 15.72, 15.68, 15.63, 15.43, 15.40.

HRMS (MALDI) *m/z* calcd for C₆₈H₅₄N₄Zn⁺: 990.3640; found: 990.3658.

Elemental Analysis for C₆₈H₅₄N₄Zn•CH₂Cl₂: C 82.28, H 5.48, N 5.64; found: C 82.01, H 5.30, N 5.14.

[3,7-dimethyl-1,9-bis(2'-naphthyl-2'-yl-vinyl)-5-(naphthyl)-dipyrrinato] [1,3,7,9-tetramethyl-5-anthracenyl-dipyrrinato] zinc(II) (63**)**

The reaction of **19** (270.8 mg, 0.829 mmol, 1 equiv.) and **38** (500.1 mg, 0.829 mmol, 1 equiv.) with zinc diacetate (228.3 mg, 1.244 mmol, 1.5 equiv.) was performed in a 2:1 mixture of CH₂Cl₂/MeOH. Automatic column chromatography packed with silica was used for purification (gradient of cyclohexane/dichloromethane) and gave **63** as a blue-violet powder (238.0 mg, 0.293 mmol, 29 % yield).



¹H NMR (500 MHz, CDCl₃) δ/ppm: 8.49 (s, 2H), 8.01 – 7.89 (m, 5H), 7.86 – 7.70 (m, 3H), 7.68 – 7.59 (m, 4H), 7.58 – 7.48 (m, 4H), 7.47 – 7.33 (m, 5H), 7.27 – 7.24 (m, 3H), 7.13 – 7.07 (m, 4H), 6.69 (s, 2H), 6.64 (s, 2H), 6.52 (s, 2H), 5.82 (d, *J* = 1.0 Hz, 2H), 5.23 (s, 1H), 2.26 (s, 3H), 2.01 (s, 3H), 1.14 (s, 6H), 0.96 (s, 6H).

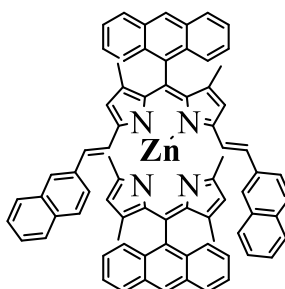
¹³C NMR (126 MHz, CDCl₃) δ 156.82, 143.91, 140.81, 136.53, 134.06, 131.63, 130.90, 128.16, 127.69, 127.32, 127.24, 126.33, 126.07, 125.85, 125.65, 125.41, 120.34, 77.28, 77.03, 76.77, 47.47, 42.50, 26.45, 25.51, 24.52, 21.52, 16.61, 15.76, 15.62, 14.96.

HRMS (MALDI) *m/z* calcd for C₇₂H₅₆N₄Zn⁺: 1042.6480; found: 1042.4789.

Elemental Analysis for C₇₂H₅₆N₄Zn•CH₂Cl₂: C 82.94, H 5.41, N 5.37; found: C 82.41, H 5.40, N 5.30.

[1,9-vinyl-2''-naphthalene-3,7-dimethyl -5-(anthracenyl)-dipyrinato] [1,3,7,9-tetramethyl -5-anthracenyl- dipyrinato] zinc(II) (64)

The reaction of **19** (300.0 mg, 0.459 mmol, 1equiv.) and **39** (173.0 mg, 0.459 mmol, 1 equiv.) with zinc diacetate (126.5 mg, 0.689 mmol, 1.5 equiv.) was performed in a 2:1 mixture of CH₂Cl₂/MeOH. Automatic column chromatography packed with silica was used for purification (gradient of cyclohexane/dichloromethane) and gave the compound **64** as a blue-violet powder (164.0 mg, 0.149 mmol, 33 % yield).



¹H NMR (500 MHz, CDCl₃) δ/ppm: 8.57 (d, *J* = 8.5 Hz, 1H), 8.11 – 7.99 (m, 1H), 7.98 – 7.92 (m, 2H), 7.88 (ddd, *J* = 10.4, 7.4, 5.9 Hz, 4H), 7.71 (d, *J* = 7.9 Hz, 2H), 7.64 – 7.55 (m, 2H), 7.52 – 7.42 (m, 5H), 7.38 – 7.28 (m, 3H), 7.07 – 7.00 (m, 2H), 6.69 (s, 2H), 6.33 (d, *J* = 1.2 Hz, 2H), 5.89 (s, 4H), 2.34 (s, 6H), 1.43 (s, 6H), 0.63 (s, 6H).

¹³C NMR (126 MHz, CDCl₃) δ/ppm: 156.88, 156.82, 151.17, 143.91, 140.86, 140.71, 140.31, 136.53, 134.67, 133.73, 133.34, 132.29, 131.63, 131.43, 130.90, 130.77, 128.57, 128.29, 128.16, 127.76, 127.61, 127.53, 126.50, 126.33, 126.27, 125.82, 125.65, 125.56, 125.41, 123.48, 121.25, 120.33, 119.45, 77.28, 77.03, 76.77, 26.93, 16.61, 15.47, 14.96, 13.82.

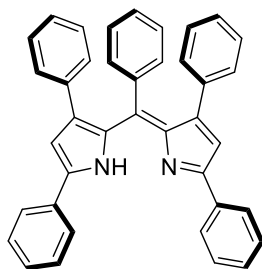
HRMS (MALDI) *m/z* calcd for C₇₆H₅₈N₄Zn⁺: 1090.3953; found: 1090.4895.

Elemental Analysis for C₇₆H₅₈N₄Zn•CH₂Cl₂: C 83.54, H 5.35, N 5.13; found: C 83.41, H 5.30, N 5.20.

6.2.5 π -extended systems

2,4,5,7,9-pentaphenyl-dipyrrin (**66**)

In a round bottom flask, 2,4-diphenyl-1H-pyrrole (501 mg, 2.29 mmol, 2.50 equiv.) and benzaldehyde (97.0 mg, 0.914 mmol, 1.00 equiv.) were dissolved in dichloromethane (50 ml). Subsequently, few drops of trifluoroacetic acid (TFA) were added to the reaction mixture which was stirred at room temperature for 16 hours. During this time the reaction mixture changed color from light blue to intense turquoise. After TLC confirming the complete conversion of the starting benzaldehyde, *p*-Chloranil (270 mg, 1.10 mmol, 1.20 equiv.) was incorporated into the system which turned instantly dark green. The reaction was carried out at room temperature for additional 3 hours. After this time, water was added to the reaction mixture. Thus, the aqueous layers were extracted with dichloromethane, while the organic layers were collected and dried by the addition of MgSO₄. After filtration, the solvent was evaporated under reduce pressure. The crude residue was processed with column chromatography packed with alumina gel using as eluent mixture a gradient of cyclohexane/dichloromethane. The target compound **66** was isolated as a pink solid (214 mg, 1.21 mmol, 54% yield).



R_f=0.6 (Cyclohexane: Dichloromethane 50:50).

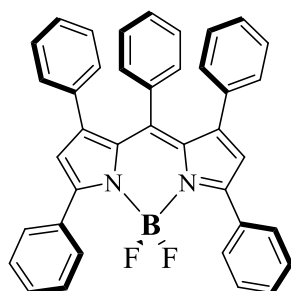
¹H NMR (400 MHz, CDCl₃) δ /ppm: 14.50 (s, 1H), 7.94-7.86 (m, 2H), 7.44 (dd, *J*=8.4, 6.8 Hz, 2H) 7.39 – 7.30 (m, 1H), 6.89 – 6.83 (m, 1H), 6.83 – 6.72 (m, 4H), 6.76 – 6.69 (m, 2H), 6.54 (t, *J* = 7.5 Hz, 1H), 6.37 (t, *J* = 7.6 Hz, 1H).

¹³C NMR (100 MHz, CDCl₃) δ /ppm: 124.9, 125.4, 125.6, 126.0, 126.4, 126.4, 127.8, 127.9, 129.2, 129.6, 129.7, 129.8, 130.8, 131.1, 131.2, 132.2, 133.5, 133.9, 143.6, 147.0, 154.9.

HRMS (C₃₉H₂₈N₂) 524.6670 calculated), 524.4140 (found).

1,3,5,7,8-pentaphenyl BODIPY (69)

Under an argon atmosphere 2,4,5,7,9-pentaphenyl-dipyrrin **66** (30.0 mg, 0.574 mmol, 1.00 equiv.) was dissolved in dry dichloromethane (40 ml). To this solution 2 ml of DIPEA were added. The reaction mixture was stirred at room temperature for 20 minutes. Subsequently, $\text{BF}_3 \cdot \text{OEt}_2$ (0.35 mL, 40.6 mg, 0.286 mmol, 5 equiv.) was incorporated into the system which was stirred for additional 40 minutes. After addition of a 1 M aqueous solution of NaHCO_3 , the aqueous layer was extracted with 20 mL of dichloromethane three times. The combined organic layer was dried over MgSO_4 , filtered, and concentrated under reduced pressure. The resulting mixture was purified by an alumina gel column chromatography, to afford the target compound **69** as a dark red solid powder (26.6 mg, 0.046 mmol, 81 % yield).



$R_f=0.6$ (Dichloromethane 50:50).

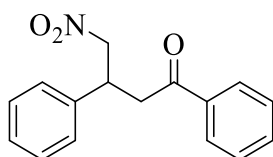
$^1\text{H NMR}$ (400 MHz, CDCl_3) δ /ppm: 6.48 (d, $J = 7.8$ Hz, 2H), 6.52 (s, 2H), 6.66 (d, $J = 7.4$ Hz, 1H), 6.74 (d, $J = 7.0$ Hz, 4H), 6.83–6.92 (m, 8H), 7.39–7.46 (m, 6H), 7.87 (d, $J = 7.8$ Hz, 2H), 7.89 (d, $J = 7.8$ Hz, 2H).

$^{13}\text{C NMR}$ (100 MHz, CDCl_3) δ /ppm: 123.5, 126.2, 126.5, 127.2, 128.1, 128.6, 128.9, 129.45, 129.48, 131.1, 131.8, 132.5, 132.6, 146.4, 148.0, 156.9

HRMS ($\text{C}_{39}\text{H}_{27}\text{BF}_2\text{N}_2$) 572.2235 calculated), 572.2140 (found).

4-nitro-1,3-diphenylbutan-1-one (77)

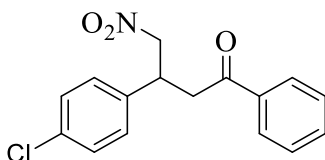
In a round bottom flask, chalcone **75** (7.06 g, 33.9 mmol, 1.00 equiv.) was dissolved in methanol (300 ml). Diethyl amine (DEA) (5.37 g, 73.4 mmol, 6.00 equiv.) and nitromethane (10.4 g, 169 mmol, 5.00 equiv.) were added to the reaction which was then heated under reflux for 24 hours. The solvent was removed under reduced pressure to yield compound **77** as a brown oil, which was used in the next step without further purification.



¹H NMR (400 MHz, CDCl₃): δ /ppm = 7.94-7.89 (m, 2H), 7.61-7.55 (m, 1H), 7.49-7.43 (m, 2H), 7.38-7.26 (m, 5H), 4.84 (dd, J = 12.4, 6.7 Hz, 1H), 4.70 (dd, J = 12.5, 7.9 Hz, 1H), 4.23 (p, J = 7.1 Hz, 1H), 3.53-3.38 (m, 2H).

3-(4-chlorophenyl)-4-nitro-1-phenylbutan-1-one (78)

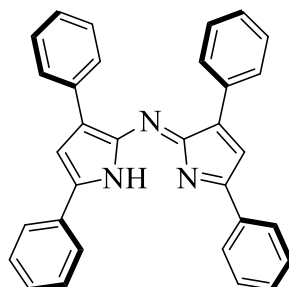
In a round bottom flask, 4-chlorocalcone **76** (2.97 g, 12.2 mmol, 1 equiv.) was dissolved in methanol (50 ml). Subsequently, DEA (5.37 g, 73.4 mmol, 6.00 equiv.) and nitromethane (3.74 g, 61.2 mmol, 5.00 equiv.) were added to the reaction mixture which was refluxed for 24 hours. The solvent was removed under reduced pressure to give compound **78** as a brownish oil, which was used in the next step without purification.



¹H NMR (400 MHz, CDCl₃): δ /ppm = 7.94-7.87 (m, 2H), 7.61-7.55 (m, 1H), 7.49-7.43 (m, 2H), 7.33-7.28 (m, 2H), 7.25-7.20 (m, 2H), 4.82 (dd, J = 12.6, 6.5 Hz, 1H), 4.66 (dd, J = 12.5, 8.1 Hz, 1H), 4.22 (p, 1H), 3.51-3.37 (m, 2H).

2,4,8,10 pentaphenyl-azadipyrin or (Z)-N-(3,5-diphenyl-1H-pyrrol-2-yl)-3,5-diphenyl-2H-pyrrol-2-imine (79)

In a round bottom flask, 4-nitro-1,3-diphenylbutan-1-one **77** was dissolved in *n*-butanol (50 ml). Then, ammonium acetate NH₄OAc (50.47 g, 0.654 mmol, 20.0 equiv.) was added to the reaction mixture which was stirred under reflux conditions for 24 hours. After this time, the system was allowed to reach room temperature and then concentrated to 10 ml. The precipitate was filtered and washed with ethanol (3x10 ml). The product was obtained as a black solid (142 mg, 1.245 mmol, 18% yield).



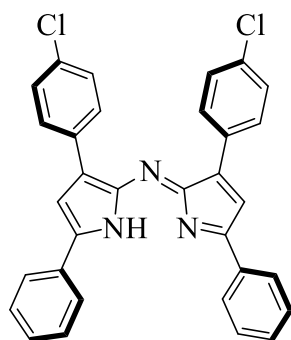
¹H NMR (400 MHz, CDCl₃): δ/ppm = 8.09-8.04 (m, 4H), 7.98-7.94 (m, 4H), 7.57-7.33 (m, 12H), 7.21 (s, 2H) (NH not observed).

¹³C NMR (100 MHz, CDCl₃) δ/ppm: 154.10, 149.5, 143.51, 134.57, 132.10, 130.54, 129.64, 129.41, 128.79, 126.54, 114.87.

HRMS (C₃₂H₂₃N₃) 449.1970 calculated), 449.2147 (found).

(Z)-3-(4-chlorophenyl)-N-(3-(4-chlorophenyl)-5-phenyl-1H-pyrrol-2-yl)-5-phenyl-2H-pyrrol-2-imine (80)

In a round bottom flask, 3-(4-chlorophenyl)-4-nitro-1-phenylbutan-1-one **78** (3.99 g, 13.1 mmol, 1.0 equiv.) was dissolved in *n*-butanol (50 ml). Then, ammonium acetate NH₄OAc (20.30 g, mmol, 0.262 mmol, 20.0 equiv.) was added to the reaction mixture which was stirred under reflux conditions for 24 hours. After this time, the system was allowed to reach room temperature and then concentrated to 10 ml. The precipitate was filtered and washed with ethanol (3x10 ml). The crude residue was purified with column chromatography packed with silica gel, using as eluent mixture dichloromethane/methanol. The product was obtained as a violet powder (1.22 g, 2.34 mmol, 20 % yield).



¹H NMR (400 MHz, CDCl₃): δ/ppm = 8.00-7.91(m, 8H), 7.59-7.37 (m, 10H), 7.19 (s, 2H) (NH not observed).

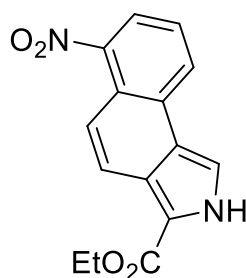
¹³C NMR (100 MHz, CDCl₃) δ/ppm: 159.71, 155.01, 149.54, 142.35, 132.47, 130.24, 129.94, 129.10, 126.74, 126.41, 113.87, 55.41.

HRMS (C₃₂H₂₁N₃Cl₂) 517.1147 calculated), 517.4789 (found).

6.2.3 Benzofused systems

(8'-nitro-naphtho[3',4'-b]-fused) isoindole 1- (ethyl ester carboxylic acid)

In a round bottom flask, (2-ethoxyethyl)-methylidynetanium (ethyl isocyanoacetate) (6.22 g, 55.50 mmol, 2 equiv.) and 1,5-dinitronaphthalene (6.00 g, 27.50 mmol, 1 equiv.) were dissolved in 200 ml of tetrahydrofuran. The reaction mixture was vigorously stirred for 30 minutes at room temperature and subsequently cooled down at 0°C in order to add dropwise 1,8-Diazabicyclo [5.4.0] undec-7-ene (DBU) (5.00 g, 34.38 mmol, 1.5 equiv.). The reaction mixture is slowly allowed to stir at room temperature for 24 hours. Subsequently, the solvent was removed under reduce pressure and the resultant oil is dissolved in 200 ml of dichloromethane. The reaction mixture is poured into a separation funnel and the organic layer is washed successively with 200 ml of brine and then 200 ml of water. The aqueous layers were recombined and reextracted with dichloromethane. The organic layers were collected and were dried by the addition of MgSO₄. The mixture was filtered through a glass funnel and the solvent was evaporated under reduce pressure. The crude residue was adsorbed on a small amount of silica gel and was purified *via* column chromatography (cyclohexane: ethyl acetate; 80:20 →ethyl acetate). The target compound was isolated as a bright yellow powder (3.00 g, 10.55 mmol, 38% yield).



R_f=0.4 (Cyclohexane: Ethyl acetate, 50:50)

¹H-NMR (400 MHz, DMSO-d₆) δ/ppm: 13.38 (s, 1H), 8.76 (d, J= 8.0 Hz, 1H), 8.21 (d, J= 9.5 Hz, 1H), 8.08 (dd, J= 7.8, 1.2 Hz), 7.87 (d, J= 9.5 Hz, 1H), 7.74 (t, J= 7.9 Hz, 1H), 4.40 (q, J= 7.1 Hz, 2H), 1.41 (t, J= 7.1 Hz, 3H).

¹³C NMR (101 MHz, DMSO-d₆) δ/ppm: 161.08, 147.99, 130.03, 129.07, 126.61, 124.30, 121.70, 121.57, 120.93, 119.20, 118.64, 113.94, 60.33, 40.68, 40.63, 40.47, 40.42, 40.26, 40.21, 40.00, 39.79, 39.59, 39.38, 14.97.

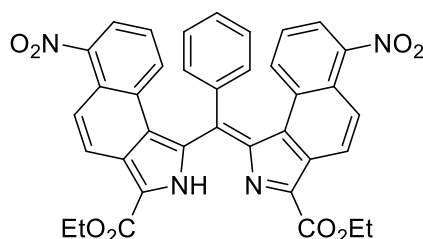
HRMS C₁₅H₁₂N₂O₄: 284.2710 (calculated), 284.4789 (found).

(8'-nitro-naphtho[3',4'-b]-fused)-5-phenyl-dipyrromethen-1,9-bis(ethyl ester carboxylic acid) 100

Under an argon atmosphere, compound **99** (335 mg, 1.18 mmol, 2.50 equiv.) and benzaldehyde (50.0 mg, 471 μ mol, 1.00 equiv.) were dissolved in dry THF in the presence of catalytic amount of TFA (2 ml). Subsequently, *p*-toluenesulfonic acid (*p*TsOH) (50.0 mg, 471 μ mol, 1.00 equiv.) and tetrabutylammonium chloride (*n*Bu₄NCl) (45.8 mg, 165 μ mol, 0.350 equiv.) were added to the reaction mixture, which was left stirring at room temperature for 72 hours.

The starting material **99** was still present in the TLC control; regardless *p*-chloranil (139 mg, 565 μ mol, 1.20 equiv.) was added to the reaction mixture, which was stirred at room temperature for additional 4 hours.

The reaction mixture was poured into a separation funnel and the organic layer was washed with of brine and water. The aqueous layers were recombined and reextracted with dichloromethane. The organic layers were collected and were dried by the addition of MgSO₄. The mixture was filtered through a glass funnel and the solvent was evaporated under reduced pressure. The crude residue was adsorbed on a small amount of silica and was purified *via* column chromatography. The target compound **100** was eluted as first from the column chromatography as a green powder (50.04 mg, 0.0763 mmol, 12% yield). It should be underlined that from the mass spectrum can be stated the purity of the compound, however in the NMR is present one additional proton.



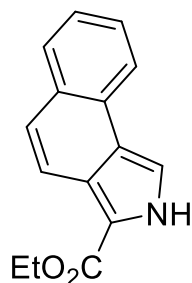
¹H NMR (400 MHz, CDCl₃) δ /ppm: 9.39 (s, 2H), 8.21 (d, *J* = 9.6 Hz, 2H), 7.98 (dd, *J* = 15.6, 9.0 Hz, 4H), 7.83 (d, *J* = 7.8 Hz, 2H), 7.39 (dd, *J* = 5.2, 1.8 Hz, 3H), 7.23 – 7.17 (m, 3H), 6.99 (s, 1H), 4.33 (q, *J* = 7.1 Hz, 4H), 1.36 (t, *J* = 7.1 Hz, 6H).

¹³C NMR (100 MHz, CDCl₃) δ /ppm: 161.03, 148.62, 136.22, 130.31, 129.43, 129.38, 127.60, 126.03, 125.62, 124.01, 123.62, 121.26, 120.74, 117.54, 113.89, 61.02, 46.11, 14.50.

HRMS C₃₇H₂₆N₄O₄: 654.1751 (calculated), 654.6243 (found).

(naphtho[3',4'-b]-fused) isoindole 1- (ethyl ester carboxylic acid) 107

In a round bottom flask, (2-ethoxyethyl)-methyldiyneazanium (ethyl isocyanoacetate) (7.838 g, 69.30 mmol, 2 equiv.) and 1-nitronaphthalene (6.00 g, 34.5 mmol, 1equiv.) were dissolved in 200 ml of tetrahydrofuran. The reaction mixture was vigorously stirred for 30 minutes at room temperature and subsequently cooled down at 0°C in order to add dropwise tert-butylimino-tri(pyrrolidino) phosphorane (BTPP) (12.99g, 41.58 mmol, 1.2 equiv.) The reaction mixture is slowly allowed to reach room temperature and then heated up to 70 °C for 48 hours. Subsequently, the solvent was removed under reduce pressure and the resultant oil is dissolved in 200 ml of dichloromethane. The reaction mixture is poured into a separation funnel and the organic layer is washed successively with 200 ml of brine and then 200 ml of water. The aqueous layers were recombined and reextracted with dichloromethane. The organic layers were collected and were dried by the addition of MgSO₄. The mixture was filtered through a glass funnel and the solvent was evaporated under reduce pressure. The crude residue was adsorbed on a small amount of silica gel and was purified *via* column chromatography (cyclohexane: ethyl acetate; 80:20 →ethyl acetate). The target compound was isolated as an off- white solid (2.00 g, 8.359 mmol, 24% yield).



R_f=0.6 (Cyclohexane: Ethyl acetate, 50:50).

¹H-NMR (400 MHz, DMSO-d₆) δ/ppm: 9.95 (s, 1H), 8.14 (d, *J* = 7.9 Hz, 1H), 8.02 (d, *J* = 9.1 Hz, 1H), 7.86 (d, *J* = 3.3 Hz, 1H), 7.83 – 7.79 (m, 1H), 7.56 – 7.50 (m, 2H), 7.46 (td, *J* = 7.5, 7.1, 1.3 Hz, 1H), 4.47 (q, *J* = 7.2 Hz, 2H), 1.48 (t, *J* = 7.1 Hz, 3H).

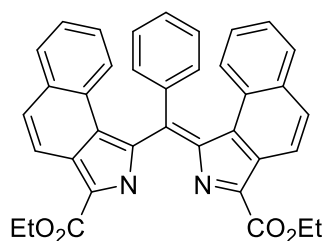
¹³C-NMR (101 MHz, DMSO-d₆) δ/ppm: 161.08, 147.99, 130.03, 129.06, 126.60, 124.29, 121.70, 121.57, 120.93, 119.20, 118.64, 113.94, 60.33, 40.68, 40.63, 40.47, 40.42, 40.26, 40.21, 40.00, 39.79, 39.59, 39.38, 14.97.

HRMS C₁₅H₁₃NO₂: 239.2946 (calculated), 239.2478 (found).

**(naphtho[3',4'-b]-fused)-5-phenyl-dipyrromethen-1,9-bis(ethyl ester carboxylic acid)
108**

Under an argon atmosphere, compound **107** (450.9 mg, 1.18 mmol, 2.00 equiv.) and benzaldehyde (10.0 mg, 0.942 mmol, 1.00 equiv.) were dissolved in dry THF in the presence of catalytic amount of TFA (2 ml). Subsequently, *p*-toluenesulfonic acid (*p*TsOH) (70.0 mg, 0.120 mmol, 1.00 equiv.) and tetrabutylammonium chloride (*n*Bu₄NCl) (74.42 mg, 0.02 mmol, 0.350 equiv.) were added to the reaction mixture, which was left stirring at room temperature for 72 hours. TLC analysis confirmed the complete conversion of the starting material **107**, thus *p*-chloranil (278mg, 1.31 mmol, 1.20 equiv.) was added to the reaction mixture, which was stirred at room temperature for additional 4 hours.

The reaction mixture was poured into a separation funnel and the organic layer was washed with of brine and water. The aqueous layers were recombined and reextracted with dichloromethane. The organic layers were collected and were dried by the addition of MgSO₄. The mixture was filtered through a glass funnel and the solvent was evaporated under reduced pressure. The crude residue was adsorbed on a small amount of silica and was purified *via* column chromatography. The target compound **108** was eluted as a violet powder (32.04 mg, 0.0563 mmol, 6% yield). It should be underlined that from the mass spectrum can be stated the purity of the compound, however in the ¹HNMR and ¹³C-NMR are not clear, thereby are not reported.



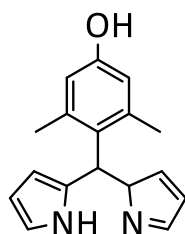
R_f=0.6 (Cyclohexane: Ethyl acetate, 50:50).

HRMS C₃₇H₂₇N₂O₄: 563.1917 (calculated), 565.1614 (found).

6.2.4 Schiff-base dipyrin macrocycles

5-(2',6'-dimethyl-4'-hydroxy)-phenyl-dipyrromethane **126**

Before starting the reaction, the pyrrole was distilled through the use of a rotary evaporator, (70 °C, 70 mbar) which will yield the pyrrole as a colourless viscous liquid. In a round bottom flask, approximately 250 ml of pyrrole were reacted with 4-hydroxy-2,6-dimethylbenzaldehyde (5.00 g, 33.3 mmol, 1 equiv.). Since the starting aldehyde was not completely soluble in the reaction mixture, 25 ml of methanol were added. Then, InCl₃ (1.41 g, 0.0063 mmol, 0.2 equiv.) was incorporated into the reaction mixture which was stirred at room temperature for 90 minutes. Subsequently, NaOH (660 mg, 16.65 mmol, 0.5 equiv.) was added and left stirring for additional 30 minutes. Subsequently, the residual precipitate was filtered, and the pyrrole recovered by distilling it at reduce pressure. The crude residue oil was then subjected to column chromatography packed with alumina, using dichloromethane/methanol as eluent mixture. The product **126** was a black powder (1 g, 3.76 mmol, 20% yield).



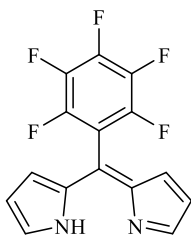
R_f = 0.2 (Dichloromethane).

¹H-NMR (400 MHz, CDCl₃) δ/ppm: 12.31 (s, 1H), 6.91 (s, 2H), 6.24 (s, 2H), 6.15 (s, 2H), 6.02 (s, 1H), 2.11 (s, 6H).

5-(2', 3', 4', 5', 6', pentafluoroyl)-phenyl-dipyrromethane **127**

Before starting the reaction, the pyrrole was distilled through the use of a rotary evaporator, (70 °C, 70 mbar) which will yield the pyrrole as a colorless viscous liquid. In a round bottom flask, approximately 350 ml of pyrrole were reacted with 2,3,4,5,6-pentafluorobenzaldehyde (10.00 g, 51.0 mmol, 1 equiv.). Then, InCl₃ (2.26 g, 10.2 mmol, 0.2 equiv.) was incorporated into the reaction mixture which was stirred at room temperature for 90 minutes. Subsequently, NaOH (408 mg, 10.2 mmol, 0.2 equiv.) was added and left stirring for additional 30 minutes. Subsequently, the residual precipitate was filtered, and the pyrrole recovered by distilling it at reduce pressure.

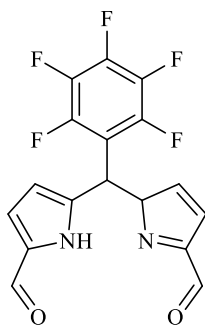
The obtained viscous oil was then crystallized with hot ethanol /water (1:1). The formed crystals were washed several times with hexane and dried under vacuum, to yield the product **127** as grey crystals (6.7 g, 21.6 mmol, 78% yield).



¹H-NMR (400 MHz, CDCl₃) δ/ppm: 12.24 (s, 1H), 8.09 (s, 2H), 6.72 (m, 2H), 6.17 (m, 2H), 6.03 (s, 2H), 5.89 (s, 1H).

1,9-diformyl-5-(2', 3', 4', 5', 6', pentafluorophenyl)-phenyl-dipyrromethane (**129**)

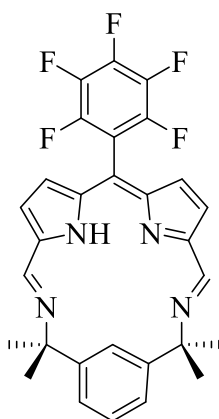
Under an argon atmosphere, compound **127** (2.50 g, 8.01 mmol, 1.00 equiv.) was dissolved in DMF. Once the system was cooled down to 0°C, Phosphorous oxychloride (POCl₃) (4.911 g, 5.985 ml, 32.03 mmol, 4 equiv.) was added dropwise. The reaction mixture changed immediately color from grey to intense violet. After few minutes, the reaction was allowed to stir at room temperature for 2 hours. Subsequently, a saturated solution of NaOAc was added to the reaction mixture which was left stirring for additional 30 minutes at room temperature. The reaction mixture was poured into a separation funnel and the organic layer was washed successively with water several times. The aqueous layers were recombined and reextracted with dichloromethane. The organic layers were collected and were dried by the addition of MgSO₄. The mixture was filtered through a glass funnel and the solvent was evaporated under reduced pressure. The crude compound was recrystallized from a mixture of hot ethanol/ water (1:1). The resulting crystals were washed several times with hexane and dried under vacuum. The desired product **129** was obtained as black crystals (1.02 g, 2.715 mmol, 35% yield).



¹H-NMR (400 MHz, DMSO-d₆) δ/ppm: 12.24 (s, 1H), 9.42 (s, 2H), 6.95 (s, 2H), 5.99-5.91 (m, 3H).

1,9-methanimino-(1', 3'-bis(dimethyl)benzene)-5-(2', 3', 4', 5', 6', pentafluorophenyl)-phenyl-dipyrrin (131)

In a round bottom flask, compound **129** and 2,2'-(1,3-phenylene) bis (propan-2-amine) **130** were dissolved in acetonitrile. The reaction was stirred at room temperature overnight. The precipitate observed was filtered under vacuum and washed several times with hexane; thus, dried under vacuum overnight. The target product **131** was isolated as a reddish powder (3.04 g, 5.741 mmol, 60% yield).



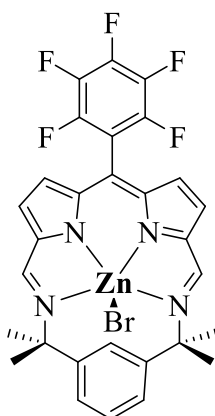
¹H NMR (400 MHz, DMSO) δ /ppm 12.50 (s, 1H), 9.27 (s, 1H), 8.60 (s, 2H), 7.34 (d, $J = 1.5$ Hz, 2H), 6.91 (d, $J = 4.2$ Hz, 2H), 6.83 (dd, $J = 4.2, 1.1$ Hz, 2H), 1.53 (s, 12H).

¹³C-NMR (101 MHz, DMSO- d_6) δ /ppm: 154.30, 149.24, 147.87, 144.74, 142.65, 141.70, 137.54, 138.94, 128.71, 125.41, 125.10, 122.21, 119.87, 64.41, 23.96

HRMS $C_{29}H_{23}F_5N_4$: 522.1843 (calculated), 522.1478 (found).

1,9-methanimino-(1', 3'-bis(dimethyl)benzene)-5-(2', 3', 4', 5', 6', pentafluorophenyl)-phenyl-dipyrin-ZnBr (133)

In a round bottom flask, compound **133** (30 mg, 0.057 mmol, 1 equiv.) was dissolved in dichloromethane (25 ml). Subsequently, DABCO (6.44 mg, 0.057 mmol, 1 equiv.) and ZnBr₂ (7.26 mg, 0.057 mmol, 1 equiv.) were added to the reaction mixture, which was stirred at room temperature overnight. The resultant precipitate was filtered and washed with hexane, to afford the title compound **133** as a violet powder (10.04 mg, 0.03 mmol, 20 % yield).



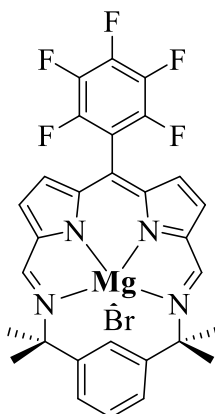
¹H NMR (400 MHz, DMSO) δ/ppm: 9.67 (s, 1H), 7.87 (s, 2H), 7.24 (m, 2H), 7.15 (dd, J= 7.2, 1.8 Hz, 2H), 6.48 (s, 2H), 6.26 (s, 2H), 1.80 (s, 6H), 1.34 (s, 6H).

¹³C-NMR (101 MHz, DMSO-d₆) δ/ppm: 154.14, 149.84, 144.54, 140.21, 138.97, 132.54, 131.54, 129.87, 127.84, 124.84, 118.74, 64.54, 31.28, 26.57.

HRMS C₂₉H₂₂Br₂F₅N₄Zn: 666.7790 (calculated), 666.6487 (found).

1,9-methanimino-(1', 3'-bis(dimethyl)benzene)-5-(2', 3', 4', 5', 6', pentafluorophenyl)-phenyl-dipyrin-MgBr (135)

In a round bottom flask, compound **133** (30 mg, 0.057 mmol, 1 equiv.) was dissolved in dichloromethane (25 ml). Subsequently, 5 ml of 2,6-lutidine and MgBr₂ (10.10 mg, 0.0507 mmol, 1 equiv.) were added to the reaction mixture, which was stirred at room temperature overnight. The resultant precipitate was filtered and washed with hexane, to afford the title compound **135** as an orange powder (7.04 mg, 0.04 mmol, 15 % yield).



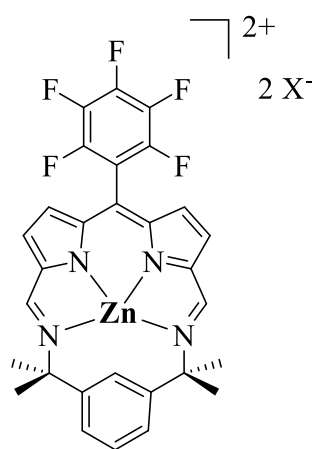
¹H NMR (400 MHz, DMSO) δ /ppm: 9.17 (s, 1H), 7.87 (s, 2H), 7.41 (m, 2H), 7.35 (dd, J = 8.2, 1.85Hz, 2H), 6.87 (s, 2H), 6.46 (s, 2H), 1.70 (s, 6H), 1.20 (s, 6H).

¹³C-NMR (101 MHz, DMSO- d_6) δ /ppm: 157.44, 150.74, 146.84, 141.81, 139.45, 133.41, 131.54, 127.87, 124.74, 122.14, 116.44, 65.34, 34.18, 25.87.

HRMS C₂₉H₂₂Br₂F₅N₄Mg: 625.7240 (calculated), 625.4789 (found).

1,9-methanimino-(1', 3'-bis(dimethyl)benzene)-5-(2', 3', 4', 5', 6', pentafluorophenyl)-phenyl-dipyrrin-Zn (136)

In a round bottom flask, compound **133** (30 mg, 0.057 mmol, 1 equiv.) was dissolved in DMF. Then, DABCO (12.88 mg, 0.114 mmol, 2 equiv.) Zn(OAc)₂ (20.02 mg, 0.057 mmol, 1 equiv.) and was incorporated into the reaction mixture, which was refluxed at 80 °C for 48 hours, through the use of an air condenser. Once confirmed the conversion of the starting material, the reaction was allowed to reach the room temperature. The reaction mixture was poured into a separation funnel and the organic layer was washed successively with water several times. The aqueous layers were recombined and reextracted with dichloromethane. The organic layers were collected and were dried by the addition of MgSO₄. The mixture was filtered through a glass funnel and the solvent was evaporated under reduced pressure. The target compound was isolated as a violet powder (15 mg, 0.024 mmol, 60 % yield).

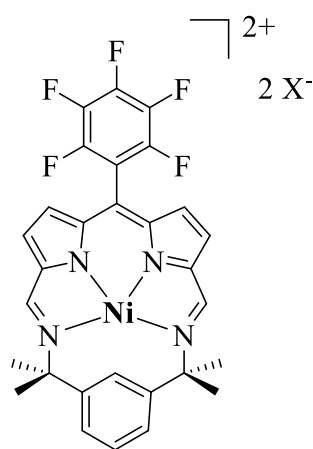


Despite zinc atom being diamagnetic, it was not possible to obtain defined NMR spectra, and therefore they are not reported. However, MALDI-TOF analysis revealed the presence of the expected fragmentation peak.

HRMS C₂₉H₂₂F₅N₄Zn: 585.1056 (calculated), 585.1824 (found).

1,9-methanimino-(1', 3'-bis(dimethyl)benzene)-5-(2', 3', 4', 5', 6', pentafluorophenyl)-phenyl-dipyrrin-Ni (137)

In a round bottom flask, compound **133** (30 mg, 0.057 mmol, 1 equiv.) was dissolved in DMF. Then, DABCO (12.88 mg, 0.114 mmol, 2 equiv.) Ni(OAc)₂·H₂O (22.02 mg, 0.57 mmol, 1 equiv.) and was incorporated into the reaction mixture, which was refluxed at 80 °C for 48 hours, through the use of an air condenser. Once confirmed the conversion of the starting material, the reaction was allowed to reach the room temperature. The reaction mixture was poured into a separation funnel and the organic layer was washed successively with water several times. The aqueous layers were recombined and reextracted with dichloromethane. The organic layers were collected and were dried by the addition of MgSO₄. The mixture was filtered through a glass funnel and the solvent was evaporated under reduced pressure. The target compound was isolated as a blue powder (10 mg, 0.017 mmol, 50 % yield).

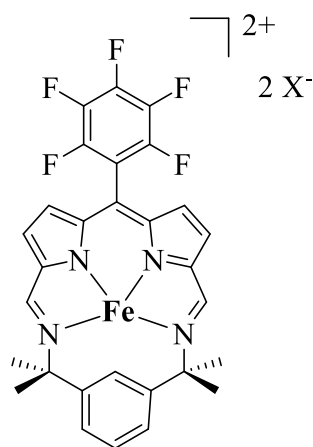


The presence of the paramagnetic Ni atom leads to short relaxation times; therefore, it was not possible to obtain defined NMR spectra. However, MALDI-TOF analysis revealed the presence of the expected fragmentation peak.

HRMS C₂₉H₂₂F₅N₄Ni: 579.1118 (calculated), 579.1125 (found).

1,9-methanimino-(1', 3'-bis(dimethyl)benzene)-5-(2', 3', 4', 5', 6', pentafluorophenyl)-phenyl-dipyrrin-Fe (138)

In a round bottom flask, compound **133** (30 mg, 0.057 mmol, 1 equiv.) was dissolved in DMF. Then, DABCO (12.88 mg, 0.114 mmol, 2 equiv.) Fe(OTf)₂ (24.02 mg, 0.57 mmol, 1 equiv.) and was incorporated into the reaction mixture, which was refluxed at 80 °C for 48 hours, through the use of an air condenser. Once confirmed the conversion of the starting material, the reaction was allowed to reach the room temperature. The reaction mixture was poured into a separation funnel and the organic layer was washed successively with water several times. The aqueous layers were recombined and reextracted with dichloromethane. The organic layers were collected and were dried by the addition of MgSO₄. The mixture was filtered through a glass funnel and the solvent was evaporated under reduced pressure. The target compound was isolated as a black powder (7 mg, 0.012 mmol, 32 % yield).



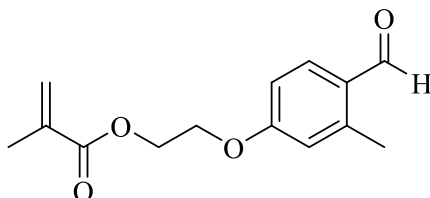
The presence of the paramagnetic Fe atom leads to short relaxation times; therefore, it was not possible to obtain defined NMR spectra. However, MALDI-TOF analysis revealed the presence of the expected fragmentation peak.

HRMS C₂₉H₂₂F₅N₄Fe: 577.1114 (calculated), 577.1119 (found).

6.2.5 Subproject

2-(4-formyl-3-methylphenoxy) ethyl methacrylate (141)

In a round-bottom flask, 4-hydroxy-2-methylbenzaldehyde (2.8 g, 20.57 mmol, 1 equiv.) was dissolved in 100 ml of acetone. Subsequently potassium carbonate K_2CO_3 (14.21 g, 102.8 mmol, 5equiv.) and potassium iodide KI (8,535 g, 51.41 mmol, 2,5 equiv.) were added and the reaction mixture was refluxed at 60 °C for 30 minutes. After this time, 2-bromoethyl methacrylate (2.382 g, 12.34 mmol, 0.6 equiv.) was added dropwise to the reaction mixture which was refluxed at 60 °C for 16 hours, using an air-cooled condenser. The formed precipitated was then filtered off and the solvent was removed under reduced pressure. The resulting oil was washed with saturated NaCl aqueous solution, and the organic layers were recombined, extracted with CH_2Cl_2 and dried over anhydrous $MgSO_4$. The mixture was filtered, and the solvent was evaporated under reduced pressure. The crude residue was purified *via* flash column chromatography on silica gel (gradient of cyclohexane/dichloromethane), giving the product as a light-yellow oil (0.9753 g, 3.928 mmol, 19% yield).



R_f = 0.66 (dichloromethane).

1H -NMR (400 MHz, acetone- d_6) δ /ppm: 9.62 (s, 1H), 7.32 (d, J = 8.6 Hz, 1 H), 6.54 (dd, J = 8.5, 2.6 Hz, 1 H), 6.48 (d, J = 2.6 Hz, 1 H), 5.58 (dt, J = 2.0, 1.0, 1 H), 5.24 (p, J = 1.6 Hz, 1 H), 4.02-3.97 (m, 2 H), 3.93-3.88 (m, 2 H), 2.13 (s, 3H), 1.42 (t, J = 1.3 Hz, 3H).

^{13}C -NMR (101 MHz, acetone d_6) δ /ppm: 205.53, 191.09, 169.98, 163.14, 143.66, 136.74, 134.61, 128.84, 125.28, 118.20, 112.60, 66.68, 63.04, 19.35, 17.73.

7. List of abbreviations

Ar	Argon
°C	Grad <i>Celsius</i>
calc.	Calculated
BODIPY	4-difluoro-4-borata-3a-azonia-4a-aza-s-indacene
CDCl ₃	Chloroform-d ₁
CHX	Cyclohexane
CS	Charge-separated
DABCO	1,4-diazabicyclo[2.2.2] octane
DBU	1,8-diazabicyclo-[5.4.0]-undec-7-ene
DCM	Dichloromethane
DLW	Direct Laser Writing
DIPA	Diisopropylamine
DMAP	4-dimethylaminopyridine
DFT	Density Functional Theory
DMF	Dimethylformamide
DMSO	Dimethylsulfoxide
equiv.	Equivalents
EtOH	Ethanol
ESA	Excited state absorption
g	gramm
GSB	Ground State Bleach
h	hour(s)
HCl	Hydrochloric acid
HRMS	High-Resolution Mass Spectrometry (MS)
HOMO	Highest Occupied Molecular Orbital
Hz	Hertz
<i>i.e.</i>	lat. <i>id est</i>
IC	Internal Conversion
ISC	Intersystem Crossing
IUPAC	International Union of Pure and Applied Chemistry
IVR	Intramolecular vibrational redistribution
K	Kelvin
LCL	Ligand-centered
LLCT	Ligand-to-ligand charge transfer
LUMO	Lowest Unoccupied Molecular Orbital
M	Molar
m/z	mass/charge-ratio
MeOH	Methanol
MW	MicroWave
Min	minute
ml:	milliliter
mmol:	millimole

M:	Metal
MO	Molecular Orbital
MeOH:	Methanol
MTT:	(3-(4,5-dimethylthiazol-2-yl)-2'-5'-diphenyltetrazolium bromide
NIR:	Near-Infrared
nm:	nanometer
NMR:	Nuclear Magnetic Resonance
OAc:	acetate
<i>p</i> -chloranil:	tetrachloro-1,4-benzoquinone
ppm:	parts per million
q:	quartet (NMR)
r.t.	room temperature
R_f	Retardation factor
s:	singlet (NMR), strong (IR)
SE:	Stimulated emission
SBCT:	Symmetry-breaking charge transfer
T:	Temperature
t:	triplet (NMR), tertiary
TA	Transient absorption
TFA:	Trifluoro Acetic acid
THF:	Tetrahydrofuran
TLC:	Thin Layer Chromatography
Vis:	visible
<i>via</i>	through
VR:	Vibronic relaxation
UV:	Ultraviolet
δ	chemical shift
ϵ	extinction coefficient
λ	wavelength
$h\nu$	light
Φ	quantum yield
$\tilde{\nu}$	wavenumber

8. Bibliography

- [1] J. R. Lakowicz, *Principles of Fluorescence Spectroscopy Third Edition*.
- [2] S. E. Braslavsky, *Pure and Applied Chemistry* **2007**, *79*, 293–465.
- [3] M. A. Omary, H. H. Patterson, in *Encyclopedia of Spectroscopy and Spectrometry*, Elsevier, **2016**, pp. 636–653.
- [4] E. N. Harvey, *The American Philosophical Society*, **1957**.
- [5] G. G. Stokes, *Philosophical Transactions*, **1852**, *142*.
- [6] F. Perrin, *Ann. Phys.*, **1929**, *12*, 169–275.
- [7] A. Jablonski, *Nature*, **1993**.
- [8] J. R. Albani, *Principles and Applications of Fluorescence Spectroscopy*, **2014**.
- [9] M. Kasha, *Disc. Faraday Soc.* **1950**, *9*, 14–19.
- [10] A. Jablonski, *Zeitschrift für Physik*, **1935**, *94*, 38–64.
- [11] B. Valeur, *Molecular Fluorescence*, Wiley-VCH, **2012**.
- [12] H. T. Feng, J. Zeng, P. A. Yin, X. D. Wang, Q. Peng, Z. Zhao, J. W. Y. Lam, B. Z. Tang, *Nat. Commun.*, **2020**, *11*, 754–758.
- [13] G. A. Reynolds, K. H. Drexhage, *Optics communications* **1975**, *13*.
- [14] J. Han, A. Engler, J. Qi, C. H. Tung, *Tetrahedron Lett.* **2013**, *54*, 502–505.
- [15] R. Guliyev, A. Coskun, E. U. Akkaya, *J. Am. Chem. Soc.*, **2009**, *131*, 9007–9013.
- [16] J. Yang, A. Dass, A. M. Rawashdeh, C. Sotiriou-Leventis, M. J. Panzner, D. S. Tyson, J. D. Kinder, N. Leventis, *Chem. Mater.* **2004**, *16*, 3457–3468.
- [17] T. B. Ren, W. Xu, W. Zhang, X. X. Zhang, Z. Y. Wang, Z. Xiang, L. Yuan, X. B. Zhang, *J. Am. Chem. Soc.* **2018**, *140*, 7716–7722.
- [18] M. Jiang, X. Gu, J. W. Y. Lam, Y. Zhang, R. T. K. Kwok, K. S. Wong, B. Z. Tang, *Chem. Sci.* **2017**, *8*, 5440–5446.
- [19] W. Lin, L. Yuan, Z. Cao, Y. Feng, J. Song, *Angew. Chem. Int. Ed.*, **2010**, *49*, 375–379.
- [20] Y. Wu, Y. Chen, G. Gou, W. Mu, F. Fu, *Org. Lett.*, **2012**, *14*, 5226–5229.
- [21] C. Wang, X. Zhang, W. Hu, *Chem. Soc. Rev.*, **2020**, *49*, 653–670.

- [22] Y. Huang, E. L. Hsiang, M. Y. Deng, S. T. Wu, *Light Sci Appl.*, **2020**, *9*, 415-547.
- [23] A. Barbier, E. Bandini, F. Monti, V. K. Praveen, N. Armaroli, *Top. Curr. Chem. Z* **2016**, *347*.
- [24] A. Zampetti, A. Minotto, F. Cacialli, *Adv. Funct. Mater.*, **2019**, *29*, 484-598.
- [25] F. C. Spano, C. Silva, *Ann. Rev. Phys. Chem.*, **2014**, *65*, 477–500.
- [26] R. Englman, J. Jortner, *J. Lumin.*, **1970**, 134–142.
- [27] G. Qian, Z. Y. Wang, *Chem. Asia. J.*, **2010**, *5*, 1006–1029.
- [28] J. Lee, H. Cha, H. Yao, J. Hou, Y. H. Suh, S. Jeong, K. Lee, J. R. Durrant, *ACS Appl. Mater. Interfaces*, **2020**, *12*, 32764–32770.
- [29] M. Kono, H. Ueki, S.-I. Umemura, *Near-Infrared Finger Vein Patterns for Personal Identification*, **2002**.
- [30] E. C. Lee, H. Jung, D. Kim, *Sensors* **2011**, *11*, 2319–2333.
- [31] S. T. Le, T. Kanesan, F. Bausi, P. A. Haigh, S. Rajbhandari, Z. Ghassemlooy, I. Papakonstantinou, W. O. Popoola, A. Burton, H. Le Minh, F. Cacialli, A. D. Ellis, *Opt. Lett.*, **2014**, *39*, 3876.
- [32] K. Kawabata, M. Saito, I. Osaka, K. Takimiya, *J. Am. Chem. Soc.*, **2016**, *138*, 7725–7732.
- [33] J. Zaumseil, H. Sirringhaus, *Chem. Rev.*, **2007**, *107*, 1296–1323.
- [34] A. Graf, M. Held, Y. Zakharko, L. Tropic, M. C. Gather, J. Zaumseil, *Nat. Mater.*, **2017**, *16*, 911–917.
- [35] R. Krämer, C. Krämer, Wiley-VCH, *Fluorescent Molecular Labels and Probes*, **2017**.
- [36] J. V. Jun, D. M. Chenoweth, E. J. Petersson, *Org. Biomol. Chem.*, **2020**, *18*, 5747–5763.
- [37] S. A. Hilderbrand, R. Weissleder, *Curr. Opin. Chem. Biol.*, **2010**, *14*, 71–79.
- [38] “Globacan,” Web site.
- [39] A. Gerd Rosenbusch, *The Birth of Radiology*, **2019**.
- [40] W.C. Röntgen, *Science*, **1896**, *3*, 227–231.
- [41] L. Fass, *Mol. Oncol.*, **2008**, *2*, 115–152.
- [42] *A Definition of Molecular Imaging*, Website.
- [43] P. Suetens, *Fundamentals of Medical Imaging, Second Edition*, **2018**.

- [44] M. A. Pysz, S. S. Gambhir, J. K. Willmann, *Clin. Radiol.*, **2010**, *65*, 500–516.
- [45] R. Bonmati, *Contrast Media Mol. Imaging*, **2015**, *5*, 180–189.
- [46] I. Wacker, W. Spomer, A. Hofmann, M. Thaler, S. Hillmer, U. Gengenbach, R. R. Schröder, *BMC Cell. Biol.*, **2016**, *17*, 741–785.
- [47] Y. Garini, I. T. Young, G. McNamara, *Cytometry Part A*, **2006**, *69*, 735–747.
- [48] G. Luker, *J. Nucl. Med.*, **2008**, *49*, 514–518.
- [49] A. Gibson, J. Hebden, S. Arridge, *Phys. Med. Biol.*, **2005**, *50*, 1–43.
- [50] A. Grinvald, R. Frostig, E. Lieke, R. Hildesheim, *Physiol. Rev.*, **1988**, *68*.
- [51] M. Fox, *Optical Properties of Solids*, Oxford University Press, **2001**.
- [52] E. Hemmer, A. Benayas, F. Légaré, F. Vetrone, *Nanoscale Horiz.*, **2016**, *1*, 168–184.
- [53] R. Anderson, J. Parrish, *J. Investigat. Derm.*, **1981**, *77*, 13–19.
- [54] S. A. Hilderbrand, R. Weissleder, *Curr. Opin. Chem. Biol.*, **2010**, *14*, 71–79.
- [55] S. Diao, J. L. Blackburn, G. Hong, A. L. Antaris, J. Chang, J. Z. Wu, B. Zhang, K. Cheng, C. J. Kuo, H. Dai, *Angew. Chem.* **2015**, *127*, 14971–14975.
- [56] M. Sameiro, T. Gonçalves, *Chem. Rev.* **2009**, *109*, 190–212.
- [57] F. Yang, Q. Zhang, S. Huang, D. Ma, *J. Mater. Chem. B*, **2020**, *8*, 7856–7879.
- [58] K. Welsher, S. Sherlock, H. Dai, *Applied Physical Sciences*, **2011**, *108*.
- [59] C. Li, G. Shi, *J. Photochem. and Photobiology C*, **2014**, *19*, 20–34.
- [60] P. Reineck, B. C. Gibson, *Adv. Opt. Mater.*, **2017**, *5*, 123–129.
- [61] B. L. Neumeier, M. Khorenko, F. Alves, O. Goldmann, J. Napp, U. Schepers, H. M. Reichardt, C. Feldmann, *ChemNanoMat* **2019**, *5*, 24–45.
- [62] S. Luo, E. Zhang, Y. Su, T. Cheng, C. Shi, *Biomaterials* **2011**, *32*, 7127–7138.
- [63] M. B. Reinhart, C. R. Huntington, L. J. Blair, B. T. Heniford, V. A. Augenstein, *Surg Innov* **2016**, *23*, 166–175.
- [64] G. Hong, A. L. Antaris, H. Dai, *Nat Biomed Eng* **2017**.
- [65] B. Dá. X. F. Atam Dhawan, *Reviews in Biomedical Engineering* **2010**, *3*.
- [66] J. Bin Li, H. W. Liu, T. Fu, R. Wang, X. B. Zhang, W. Tan, *Trends Chem.* **2019**, *1*, 224–234.

- [67] W. E. Meador, S. A. Autry, R. N. Bessetti, J. N. Gayton, A. S. Flynt, N. I. Hammer, J. H. Delcamp, *J. Org. Chem.* **2020**, DOI 10.1021/acs.joc.9b03108.
- [68] S. Sreejith, P. Carol, P. Chithra, A. Ajayaghosh, *J. Mater. Chem.* **2008**, *18*, 264–274.
- [69] G. Ulrich, R. Ziessel, A. Harriman, *Angew. Chem. – Int. Ed.* **2008**, *47*, 1184–1201.
- [70] A. Loudet, K. Burgess, *Chem. Rev.* **2007**, *107*, 4891–4932.
- [71] R. G. Clarke, M. J. Hall, in *Adv. Heterocycl. Chem.*, Academic Press Inc., **2019**, pp. 181–261.
- [72] T. A. Wood T. E., *Chem. Rev. 2007* **2006**, *107*, 1831–1861.
- [73] O. H. Fischer H., *Leipzig* **1937**.
- [74] S. J. , D. E. Piloty O., *Eur. J. Inorg. Chem.* **1914**.
- [75] H. P. , Fischer V. H., *Annalen Der Chemie* **1927**, 183.
- [76] G. A. , V. E. , K. K. , S. R. , G. Sessler J., *J. Porphyr. Phthalocyanines* **2000**, *4*, 331–336.
- [77] C.-B. a. , L. C. , L. K. L. , M. G. P. , R. J. , V. S. F. , V. P. , V. J. F. G. Dixon H. B. F., *Pure Appl. Chem.* **1987**, *59*, 779–832.
- [78] L. J. Van Knoevering J. A., *Recl. Trav. Chim. Pays- Bas* **1977**, 96.
- [79] R. E. V. , D. N. A. , M. Yu. , S. A. L. L. Antina E.V., *Russ. J. Gen. Chem.* **2016**, *86*, 2209–2225.
- [80] Dolhaine H., *Comput. Chem.* **1980**, *5*, 41–48.
- [81] L. D. A. Datta S., *Monatsh. Chem.* **2008**, *139*, 1113–1117.
- [82] B. A. Sheldrick W. S., *Acta Cryst.* **1978**, *34*, 329–332.
- [83] Nishinaga T., *Organic Redox Properties: Synthesis, Properties and Applications*, **2015**.
- [84] Falk H., *The Chemistry of Linear Oligopyrroles and Bile Pigments*, Springer , **1989**.
- [85] N. Barata Joana, *Chem. Rev.* **2017**, *117*, 3192–3253.
- [86] S. Sene Mathias, *Chem. Soc. Rev.* **2021**, *40*, 4730–4789.
- [87] G. Tardieux, *J. Heterocycl. Chem.* **1998**, 35.
- [88] B. Thompson , *J. Porphyr. Phthalocyanines* **2008**, *12*, 918–931.
- [89] S. A. Baudron, *Dalton Trans.* **2020**, *49*, 6161–6175.
- [90] D. J. Sessler, *Acc. Chem. Res.* **2001**, *34*, 989–997.

- [91] N. Rockwell, C. Lagarias, *ChemPhysChem* **2010**, *11*, 1172–1180.
- [92] O. D. Vitek Libor, *Curr. Pharm. Des.* **2009**, *15*, 2869–2883.
- [93] B. R. Bennet, *Adv. Appl. Microbiol.* **2000**, *47*, 1–32.
- [94] T. Perez Vinas, *Curr. Med. Chem.* **2010**, *17*, 2222–2231.
- [95] B. C. Bröring, *Chem. Comm.* **2001**, 499500.
- [96] G. Martin, *J. Porphyr. Phthalocyanines* **2008**, *12*.
- [97] R. Sharma, Rao M. Rajeswara, R. Mangalampalli, *Coord. Chem. Rev.* **2017**, *348*, 92–120.
- [98] Y. Chengee Li, *Chem. Sci.* **2020**, *11*, 2790–2795.
- [99] C. Bruckner, V. Karunaratne, S. J. Rettig, D. Dolphin, *Synthesis of Mesophenyl-4,6-Dipyrrins, I Preparation of Their Cu(Ll), Ni(Ll), and Zn(Ll) Chelates, and Structural Characterization of Bis[Meso-Phenyl=4,6=dipyrinato]Ni(Ll)*, **1992**.
- [100] C. Bruckner, Y. Zhang, S. J. Rettig, D. Dolphin, *Synthesis, Derivatization and Structural Characterization of Octahedral Tris(5-Phenyl-4,6-Dipyrinato) Complexes of Cobalt(III) and Iron(m)*, **1997**.
- [101] M. Yamamura, M. Albrecht, M. Albrecht, Y. Nishimura, T. Arai, T. Nabeshima, *Inorg. Chem.* **2014**, *53*, 1355–1360.
- [102] A. Sumiyoshi, Y. Chiba, R. Matsuoka, T. Noda, T. Nabeshima, *Dalton Transactions* **2019**, *48*, 13169–13175.
- [103] C. Ikeda, S. Ueda, T. Nabeshima, *Chem. Comm.* **2009**, 2544–2546.
- [104] M. Yamamura, H. Takizawa, Y. Gobo, T. Nabeshima, *Dalton Trans.* **2016**, *45*, 6834–6838.
- [105] M. Yamamura, H. Takizawa, Y. Gobo, T. Nabeshima, *Dalton Trans.* **2017**, *44*, 5678–5768.
- [106] N. Sakamoto, C. Ikeda, M. Yamamura, T. Nabeshima, *J. Am. Chem. Soc.* **2011**, *133*, 4726–4729.
- [107] M. Yamamura, H. Takizawa, N. Sakamoto, T. Nabeshima, *Tetrahedron Lett.* **2013**, *54*, 7049–7052.
- [108] L. Lystrom, M. Shukla, W. Sun, S. Kilina, *J. Phys. Chem. Lett.* **2021**, *12*, 8009–8015.
- [109] M. Yamamura, H. Takizawa, T. Nabeshima, *Org. Lett.* **2015**, *17*, 3114–3117.
- [110] J. Lindsey, I. Schreiman, H. Hsu, P. Kearney, A. Marguerattaz, *J. Org. Chem.* **1987**, *52*, 827–836.

- [111] N. Falk, *Monatsh. Chem.* **1981**, *112*, 391–403.
- [112] N. Falk, F. Neufingerl, *Beitrige Zur Chemie Der Pyrrolpigmente, 26. Mitt. 1: Zur Anaeroben Photochemie Von Gallenpigmenten: Die Lumineszenz Von Gallenpigment-Partia]Struktursyste-Men Und Integralen Farbstoffen*, **1979**.
- [113] L. Yu, K. Muthukumaran, I. V. Sazanovich, C. Kirmaier, E. Hindin, J. R. Diers, P. D. Boyle, D. F. Bocian, D. Holten, J. S. Lindsey, *Inorg. Chem.* **2003**, *42*, 6629–6647.
- [114] F. Li, S. I. Yang, Y. Ciringh, J. Seth, C. H. Martin, D. L. Singh, D. Kim, R. R. Birge, David, F. Bocian, D. Holten, J. S. Lindsey, *Design, Synthesis, and Photodynamics of Light-Harvesting Arrays Comprised of a Porphyrin and One, Two, or Eight Boron-Dipyrrin Accessory Pigments*, **1998**.
- [115] I. Sazanovich, C. Kirmaier, H. Eve, Y. Lianhe, D. Bocian, J. S. Lindsey, D. Holten, *J. Am. Chem. Soc.* **2004**, *426*, 2664–2665.
- [116] I. V. Sazanovich, J. S. Lindsey, D. Holten, *Chem. Comm.* **2006**, *12*, 278–281.
- [117] S. Kusaka, R. Sakamoto, Y. Kitagawa, M. Okumura, H. Nishihara, *Chem. Asian J.* **2012**, *7*, 907–910.
- [118] R. Sakamoto, T. Iwashima, J. Kögel, S. Kusaka, M. Tsuchiya, Y. Kitagawa, H. Nishihara, *J. Am. Chem. Soc.* **2016**, *138*, 5666–5677.
- [119] M. Tsuchiya, R. Sakamoto, S. Kusaka, Y. Kitagawa, M. Okumura, H. Nishihara, *Chem. Comm.* **2014**, *50*, 5881–5883.
- [120] M. A. Filatov, A. Y. Lebedev, S. N. Mukhin, S. A. Vinogradov, A. V. Cheprakov, *J. Am. Chem. Soc.* **2010**, *132*, 9552–9554.
- [121] M. Kasha, *Radiat. Res.* **1963**, *20*, 55–70.
- [122] C. Trinh, K. Kirlikovali, S. Das, M. E. Ener, H. B. Gray, P. Djurovich, S. E. Bradforth, M. E. Thompson, *J. Phys. Chem. C* **2014**, *118*, 21834–21845.
- [123] M. Cacioppo, T. Scharl, L. Đorđević, A. Cadranel, F. Arcudi, D. M. Guldi, M. Prato, *Angew. Chem. – Int. Ed.* **2020**, *59*, 12779–12784.
- [124] L. Estergreen, A. Mencke, D. Cotton, N. Korovina, J. Michl, S. Roberts, M. Thompson, S. Bradforth, *Acc. Chem. Res.* **2022**, *55*, 1561–1572.
- [125] D. Tungulin, J. Leier, A. B. Carter, A. K. Powell, R. Q. Albuquerque, A. N. Unterreiner, C. Bizzarri, *Chem. Eur. J.* **2019**, *25*, 3816–3827.

- [126] F. Hoeben, P. Jonkheijm, E. Meijer, A. Schenning, *Chem. Rev.* **2005**, *105*, 1491–1546.
- [127] S. A. Baudron, H. Ruffin, M. W. Hosseini, *Chem. Comm.* **2015**, *51*, 5906–5909.
- [128] F. Zhang, S. A. Baudron, M. W. Hosseini, *New J. Chem.* **2018**, *42*, 6997–7004.
- [129] V. S. Thoi, J. R. Stork, D. Magde, S. M. Cohen, *Inorg. Chem.* **2006**, *45*, 10688–10697.
- [130] R. Sakamoto, T. Iwashima, M. Tsuchiya, R. Toyoda, R. Matsuoka, J. F. Kögel, S. Kusaka, K. Hoshiko, T. Yagi, T. Nagayama, H. Nishihara, *J. Mater. Chem. A* **2015**, *3*, 15357–15371.
- [131] S. A. Baudron, *Dalton Trans.* **2020**, *49*, 6161–6175.
- [132] S. A. Baudron, *CrystEngComm* **2016**, *18*, 4671–4680.
- [133] S. A. Baudron, *CrystEngComm* **2010**, *12*, 2288–2295.
- [134] A. Béziau, S. A. Baudron, M. W. Hosseini, *Dalton Trans.* **2012**, *41*, 7227–7234.
- [135] D. Pogozhev, S. A. Baudron, M. W. Hosseini, *Inorg. Chem.* **2010**, *49*, 331–338.
- [136] S. A. Baudron, *CrystEngComm* **2013**, *11*, 458–510.
- [137] D. Salazar-Mendoza, S. A. Baudron, M. W. Hosseini, *Chem. Comm.* **2007**, 2252–2254.
- [138] B. Kilduff, D. Pogozhev, S. A. Baudron, M. W. Hosseini, *Inorg. Chem.* **2011**, *19*, 11231–11239.
- [139] C. Bronner, S. A. Baudron, M. W. Hosseini, C. A. Strassert, A. Guenet, L. De Cola, *Dalton Trans.* **2010**, *39*, 180–184.
- [140] A. Béziau, S. A. Baudron, A. Guenet, M. W. Hosseini, *Chem. Eur. J.* **2013**, *19*, 3215–3223.
- [141] D. L. Murphy, M. R. Malachowski, C. F. Campana, S. M. Cohen, *Chem. Comm.* **2005**, 5506–5508.
- [142] S. R. Halper, L. Do, J. R. Stork, S. M. Cohen, *J. Am. Chem. Soc.* **2006**, *128*, 15255–15268.
- [143] R. Sakamoto, T. Yagi, H. Nishihara, *J. Mater. Chem. B* **2016**, *4*, 678–689.
- [144] R. Matsuoka, T. Nabeshima, *Front. Chem.* **2018**, *6*.
- [145] S. A. Baudron, *Dalton Trans.* **2013**, *42*, 7498–7509.
- [146] D. Salazar-Mendoza, S. A. Baudron, M. W. Hosseini, *Inorg Chem* **2008**, *47*, 766–768.
- [147] R. Sakamoto, K. Hoshiko, Q. Liu, T. Yagi, T. Nagayama, S. Kusaka, M. Tsuchiya, Y. Kitagawa, W. Y. Wong, H. Nishihara, *Nat. Commun.* **2015**, *6*.

- [148] R. Aoki, R. Toyoda, J. F. Kögel, R. Sakamoto, J. Kumar, Y. Kitagawa, K. Harano, T. Kawai, H. Nishihara, *J. Am. Chem. Soc.* **2017**, *139*, 16024–16027.
- [149] U. Sani, D. Tungulin, C. Bizzarri, F. Cucinotta, *RSC Adv.* **2020**, *10*, 2841–2845.
- [150] M. Tsuchiya, R. Sakamoto, M. Shimada, Y. Yamanoi, Y. Hattori, K. Sugimoto, E. Nishibori, H. Nishihara, *Inorg. Chem.* **2016**, *55*, 5732–5734.
- [151] J. Karges, O. Blacque, H. Chao, G. Gasser, *Inorg. Chem.* **2019**, *58*, 12422–12432.
- [152] J. Karges, U. Basu, O. Blacque, H. Chao, G. Gasser, *Angew. Chem.* **2019**, *131*, 14472–14478.
- [153] J. Karges, O. Blacque, G. Gasser, *Inorg. Chim Acta* **2020**, *505*.
- [154] B. F. Hohlfield, B. Gitter, C. J. Kingsbury, K. J. Flanagan, D. Steen, G. D. Wieland, N. Kulak, M. O. Senge, A. Wiehe, *Chem. Eur. J.* **2021**, *27*, 6440–6459.
- [155] A. Treibs, F.-H. Kreuzer, *Justus Liebigs Ann. Chem.* **1968**, *718*, 208–223.
- [156] N. Boens, B. Verbelen, M. J. Ortiz, L. Jiao, W. Dehaen, *Coord. Chem. Rev.* **2019**, *399*.
- [157] G. Ulrich, R. Ziessel, A. Harriman, *Angew. Chem. Int.* **2008**, *47*, 1184–1201.
- [158] H. Wang, W. Zhao, X. Liu, S. Wang, Y. Wang, *ACS Appl. Bio. Mater.* **2020**, *3*, 593–601.
- [159] T. Kowada, H. Maeda, K. Kikuchi, *Chem. Soc. Rev.* **2015**, *44*, 4953–4972.
- [160] S. Auferie, *CrystEngComm* **2019**, *1*, 471–480.
- [161] H. Lu, J. MacK, Y. Yang, Z. Shen, *Chem. Soc. Rev.* **2014**, *43*, 4778–4823.
- [162] N. Boens, V. Leen, W. Dehaen, *Chem. Soc. Rev.* **2012**, *41*, 1130–1172.
- [163] H. Watanabe, M. Ono, K. Matsumura, M. Yoshimura, H. Kimura, H. Saji, *Mol. Imaging* **2013**, *12*, 338–347.
- [164] L. Quan, S. Liu, T. Sun, X. Guan, W. Lin, Z. Xie, Y. Huang, Y. Wang, X. Jing, *ACS Appl. Mater. Interfaces* **2014**, *6*, 16166–16173.
- [165] E. Bassan, A. Gualandi, P. G. Cozzi, P. Ceroni, *Chem. Sci.* **2021**, *12*, 6607–6628.
- [166] A. Kamkaew, S. H. Lim, H. B. Lee, L. V. Kiew, L. Y. Chung, K. Burgess, *Chem. Soc. Rev.* **2013**, *42*, 77–88.
- [167] A. Turksoy, D. Yildiz, E. Akkaya, *Coord. Chem. Rev.* **2017**, *379*, 47–64.
- [168] D. Wang, X. Wang, S. Zhou, P. Gu, X. Zhu, C. Wang, Q. Zhang, *Coord. Chem. Rev.* **2023**, *482*.

- [169] *Fluorescent Materials for Cell Imaging*, Springer Singapore, **2020**.
- [170] S. H. Chan, K. H. Leung, H. Z. He, C. H. Leung, *Coord. Chem. Rev.* **2011**, *26*, 387–313.
- [171] C. Lee, K. W. Lo, *J. Am. Chem. Soc.* **2022**, *144*, 14420–14440.
- [172] J. A. Drewry, P. T. Gunning, *Coord. Chem. Rev.* **2011**, *255*, 459–472.
- [173] P. W. Ayers, in *Faraday Discuss.*, **2007**, pp. 161–190.
- [174] A. B. P. Lever, *Comprehensive Coordination Chemistry II: From Biology to Nanotechnology*, Elsevier, **2005**.
- [175] J. Tang, H. Y. Yin, J. L. Zhang, *Inorganic and Organometallic Transition Metal Complexes with Biological Molecules and Living Cells*, Elsevier Inc., **2017**, pp. 1–53.
- [176] A. Vogler, H. Kunkely, *Chem. Comm.* **2001**, *213*, 143–182.
- [177] F. Chen, M. F. Wu, G. N. Liu, M. S. Wang, F. K. Zheng, C. Yang, Z. N. Xu, Z. F. Liu, G. C. Guo, J. S. Huang, *Eur. J. Inorg. Chem.* **2000**, 482–491.
- [178] G. A. Lawrance, *Introduction to Coordination Chemistry*, **2009**.
- [179] W. Maret, *J. Inorg. Biochem.* **2012**, *111*, 110–116.
- [180] N. Roohani, R. Hurrell, R. Kelishadi, R. Schulin, *Zinc and Its Importance for Human Health: An Integrative Review*, **2013**.
- [181] B. L. Vallee, D. S. Auld, *Zinc: Biological Functions and Coordination Motifs*, **1993**.
- [182] A. S. Prasad, *Adv. Nutr.* **2013**, *4*, 176–190.
- [183] W. Maret, *BioMetals*, **2009**, pp. 149–157.
- [184] E. Kimura, S. Aoki, E. Kikuta, T. Koike, *A Macrocyclic Zinc(II) Fluorophore as a Detector of Apoptosis*, **n.d.**
- [185] H. Wang, Z. Wu, S. Li, K. Hu, G. Tang, *Apoptosis* **2017**, *22*, 585–595.
- [186] D. Oltmanns, S. Zitzmann-Kolbe, A. Mueller, U. Bauder-Wuest, M. Schaefer, M. Eder, U. Haberkorn, M. Eisenhut, *Bioconjug. Chem.* **2011**, *22*, 2611–2624.
- [187] C. Kowol, R. Trondl, V. Arion, A. Jakupec, I. Lichtscheidl, K. Keppler, *Dalton Trans.* **2010**, *39*, 704–706.
- [188] P. G. Cozzi, *Chem. Soc. Rev.* **2004**, *33*, 410–421.

- [189] K. Splan, M. Massari, A. Morris, E. Reina, T. Nguyen, J. Hupp, *Eur. J. Inorg. Chem.*, **2003**, 2348–2351.
- [190] S. Singh, *Coord. Chem. Rev.* **2020**, *414*, 768–980.
- [191] G. P. Arsenault, E. Bullock, S. F. MacDonald, *J. Am. Chem. Soc.* **1960**, *82*, 4384–4389.
- [192] D. M. Wallace, S. H. Leung, M. O. Senge, K. M. Smith, *Rational Tetraarylporphyrin Syntheses: Tetraarylporphyrins from the MacDonald Route*, Elsevier, **1993**.
- [193] C.-H. Lee', J. S. Lindsey, *One-Flask Synthesis of Meso-Substituted Dipyrromethanes and Their Application in the Synthesis of Trans-Substituted Porphyrin Building Blocks*, Part a, **1994**.
- [194] D. Nascimento, *Molecules* **2019**, *24*.
- [195] C.-H. Lee', J. S. Lindsey, *One-Flask Synthesis of Meso-Substituted Dipyrromethanes and Their Application in the Synthesis of Trans-Substituted Porphyrin Building Blocks*, Part b, **1994**.
- [196] N. M. Pereira, D. Pinho E Melo, *Org. Prep. Proced. Int.* **2014**, *46*, 183–213.
- [197] D. M. Wallace, S. H. Leung, M. O. Senge, K. M. Smith, *Rational Tetraarylporphyrin Syntheses: Tetraarylporphyrins from the MacDonald Route*, Elsevier, **1993**.
- [198] Y. Chiba, T. Nakamura, R. Matsuoka, T. Nabeshima, *Synlett.* **2020**, *31*, 1663–1681.
- [199] J. S. Lindsey, *Acc. Chem. Res.* **2010**, *43*, 300–311.
- [200] J. Littler, A. Miller, H. Hung, W. Wagner, D. O'Shea, D. Boyle, J. Lindsey, **1999**.
- [201] D. Brückner, *Can. J. Chem.*, **1996**, *74*.
- [202] P. Rao, S. Dhanalekshmi, B. Littler, J. Lindsey, *J. Org. Chem.* **2001**, *5*, 323–344.
- [203] S. Hawkins, M. Ratcliffe, *J. Mater. Chem.*, **2000**, *10*, 2057–2062.
- [204] L. Zoli, P. G. Cozzi, *ChemSusChem* **2009**, *2*, 218–220.
- [205] S. Alsharif, *RSC Adv.*, **2021**, *11*, 98–102.
- [206] A. Wendlandt, S. Stahl, *Angew. Chem. Int. Engl.* **2015**, *54*, 879–890.
- [207] M. Alsharif, A. Raja, A. Ahmed, *RSC Adv.* **2021**, *11*, 29826–29858.
- [208] B. Coulson, *Phys. Rev.* **2023**, *75*, 134–243.
- [209] S. Hawkins, M. Ratcliffe, *J. Mater. Chem. C*, **2000**, *10*, 2057–2062.

- [210] J. Littler, Y. Ciringh, J. Lindsey, *J. Org. Chem.*, **1999**, *64*, 2864–2872.
- [211] J. Lindsey, *J. Org. Chem.* **1998**, *4*, 64–72.
- [212] N. Boens, B. Verbelen, W. Dehaen, *Eur. J. Org. Chem.*, **2015**, *2015*, 6577–6595.
- [213] S. Riese, M. Holzapfel, A. Schmiedel, I. Gert, D. Schmidt, F. Würthner, C. Lambert, *Inorg. Chem.*, **2018**, *57*, 12480–12488.
- [214] S. Faramawy, A. Naggar, A. M. El-Fadly, S. M. El-Sabagh, A. Ibrahim, *Arab. J. Chem.*, **2016**, *9*, S765–S775.
- [215] A. Boto, D. Hernández, R. Hernández, E. Suárez, *J. Org. Chem.* **2006**, *71*, 1938–1948.
- [216] A. Loudet, K. Burgess, *Chem. Rev.* **2007**, *107*, 4891–4932.
- [217] J. Kim, Y. Kim, *Analyst* **2014**, *139*, 2986–2989.
- [218] Y. Kim, *An. Chem.*, **2015**, *8*, 90–98.
- [219] A. Loudet, K. Burgess, *Chem Comm.* **2009**, *7*, 321–325.
- [220] R. Khare, J. Pandey, S. Smriti, R. Ruchi, *Orient. J. Chem.*, **2019**, *35*, 423–429.
- [221] H. Collin, L. Guimarães, M. Valle, J. Pliego, *J. Phys. Chem. B* **2017**, *121*, 5300–5307.
- [222] G. Koumba, P. Constant, F. Belval, H. Duran, N. Saffon, M. Daffé, M. Baltas, *J. Med. Chem.* **2011**, *54*, 1449–1461.
- [223] X. Ding, G. Li, P. Zhang, C. Xiao, *ACS Macro Lett.* **2020**, *9*, 830–835.
- [224] J. S. Yadav, B. V. Subba Reddy, A. K. Basak, B. Visali, A. V. Narsaiah, K. Nagaiah, *Eur. J. Org. Chem.* **2004**, 546–551.
- [225] R. Khare, R. Ruchi, *J. Org. Chem.*, **2018**, *5*, 672–679.
- [226] J. McNulty, J. A. Steere, S. Wolf, *J. Mater. Chem. C*, **1998**, *67*, 9876–9934.
- [227] K. Mouterde, F. Allais, *Front. Chem.* **2018**, *6*, DOI 10.3389/fchem.2018.00426.
- [228] S. Chehab, A. Souizi, *Mediterr. J. Chem.* **2018**, *7*, 39–55.
- [229] S. Chehab, Y. Merroun, T. Ghailane, N. Habbadi, S. Boukhris, A. Hassikou, M. Akhazzane, A. Kerbal, R. Ghailane, A. Daich, A. Souizi, *angew. Chem.*, **2020**, *8*, 99–105.
- [230] J. R. Pliego, *J. Org. Chem.*, **2018**, *21*, 300–307.
- [231] A. Taher, B. J. Lumbiny, *Org. Chem.*, **2010**, *8*, 960–978.

- [232] M. Venkatanarayana, P. Kumar Dubey, *Heteroat. Chem.*, **2012**, *23*, 41–48.
- [233] R. Gresser, H. Hartmann, M. Wrackmeyer, K. Leo, M. Riede, *Tetrahedron* **2011**, *67*, 7148–7155.
- [234] H. Jaffé, *A REEXAMINATION OF THE HAMMETT EQUATION*, **1953**.
- [235] I. V. Sazanovich, J. Lindsey, D. Holten, *J. Mater. Chem. C*, **2006**, *19*, 264–265.
- [236] R. Tabone, D. Feser, E. D. Lemma, U. Schepers, C. Bizzarri, *Front. Chem.*, **2021**, *9*, DOI 10.3389/fchem.2021.754420.
- [237] P. Djurovich, S. E. Bradforth, E. Thompson, *J. Phys. Chem. C*, **2017**, *11*, 834–845.
- [238] M. Kellogg, A. Akil, D. S. Muthiah Ravinson, L. Estergreen, S. Bradforth, E. Thompson, *Faraday Discuss.*, **2019**, *216*, 379–394.
- [239] R. Sakamoto, T. Iwashima, H. Nishihara, *J. Org. Chem.*, **2013**, *38*, 566–587.
- [240] R. Sakamoto, T. Iwashima, J. F. Kögel, H. Nishihara, *Inorg. Chem.*, **2017**, *6*, 86–97.
- [241] R. Sakamoto, H. Nishihara, *RSC Adv.*, **2016**, *6*, 234–238.
- [242] R. Sakamoto, T. Iwashima, J. F. Kögel, S. Kusaka, M. Tsuchiya, Y. Kitagawa, H. Nishihara, *Angew. Chem.*, **2018**, *5*, 769–777.
- [243] D. Jameson, *Introduction to Fluorescence*, CRC press, **2018**.
- [244] P. Djurovich, E. Thompson, *J. Org. Chem.*, **2013**, *18*, 834–845.
- [245] D. Kim, J. Yoo, W. Jang, J. Kim, *J. Phys. Chem. Lett.*, **2016**, 3127–3134.
- [246] J. Leier, *Transiente Untersuchungen Zu Ladungstransferprozessen Photoangeregter Moleküle in Lösung Im Uv-Vis-NIR-Bereich*, Dissertation, Karlsruher Insitutes für Technologie (KIT), **2021**.
- [247] L. Lee Chang, *Tetrahedron* **1994**, *50*, 11427–11440.
- [248] Y. Ni, J. Wu, *Org. Biomol. Chem.* **2014**, *12*, 3774–3791.
- [249] J. B. Mann, *Atomic Structure Calculations. Hartree-Fock Wavefunctions and Radial Expectation Values: Hydrogen to Lawrencium.*, United States, **1968**.
- [250] A. Wakamiya, N. Sugita, S. Yamaguchi, *Chem. Lett.*, **2008**, *37*, 1094–1095.
- [251] D. Wu, D. Giles, *Adv. Func. Mater.*, **2020**, *14*, 97–104.

- [252] E. Y. Zhou, H. J. Knox, C. Liu, W. Zhao, J. Chan, *J. Am. Chem. Soc.*, **2019**, *141*, 17601–17609.
- [253] P. Shrestha, K. C. Dissanayake, E. J. Gehrman, C. S. Wijesooriya, A. Mukhopadhyay, E. A. Smith, A. H. Winter, *J. Am. Chem. Soc.*, **2020**, *142*, 15505–15512.
- [254] A. F. Khlebnikov, M. S. Novikov, *Tetrahedron* **2013**, *69*, 3363–3401.
- [255] E. M. Campi, G. D. Fallon, W. R. Jacksona, *J. Chem. Soc.*, **1992**, 1434–1436.
- [256] S. Rajasekar, P. Anbarasan, *J. Org. Chem.*, **2014**, *79*, 8428–8434.
- [257] M. Kucukdisli, D. Ferenc, M. Heinz, C. Wiebe, T. Opatz, *Beilstein J. Org. Chem.* **2014**, *10*, 466–470.
- [258] M. Jones, D. O’Shea, *Chem. Rev.*, **2020**, *120*, 12345–12367.
- [259] C. Schäfer, J. Mony, T. Olsson, K. Börjesson, *J. Org. Chem.*, **2022**, *87*, 2569–2579.
- [260] T. Olsson, C. Schäfer, K. Börjesson, *RSC Adv.*, **2023**, *19*, 765–789.
- [261] C. Staudinger, J. Breininger, I. Klimant, S. M. Borisov, *Analyst* **2019**, *144*, 2393–2402.
- [262] W. Zhao, E. M. Carreira, *Angew. Chem.* **2005**, *117*, 1705–1707.
- [263] M. Rogers, *J. Chem. Soc.* **1943**, 590–596.
- [264] A. Palma, J. F. Gallagher, H. Müller-Bunz, J. Wolowska, E. J. L. McInnes, D. F. O’Shea, *Dalton Trans.* **2009**, 273–279.
- [265] H. Ş. Çınar, Ş. Özçelik, K. Kaya, Ö. D. Kutlu, A. Erdoğan, A. Gül, *J. Mol. Struct.* **2020**, *1200*, 567–587.
- [266] O. Buyukcakilir, A. Bozdemir, S. Kolemen, S. Erbas, E. Akkaya, *Org. Lett.* **2009**, *11*, 4644–4647.
- [267] L. Jean-Gérard, W. Vasseur, F. Scherninski, B. Andrioletti, *Chem. Comm.*, **2018**, *54*, 12914–12929.
- [268] A. Bessette, T. Auvray, D. Désilets, G. S. Hanan, *Dalton Trans.* **2016**, *45*, 7589–7604.
- [269] A. Wakamiya, T. Murakami, S. Yamaguchi, *Chem. Sci.*, **2013**, *4*, 1002–1007.
- [270] B. H. Novak, T. D. Lash, *J. Org. Chem.*, **1998**, *63*, 1265–1276.
- [271] M. A. Filatov, A. V. Cheprakov, I. P. Beletskaya, *Eur. J. Org. Chem.*, **2007**, 3468–3475.

- [272] Y. Hayashi, N. Obata, M. Tamaru, S. Yamaguchi, Y. Matsuo, A. Saeki, S. Seki, Y. Kureishi, S. Saito, S. Yamaguchi, H. Shinokubo, *Org. Lett.*, **2012**, *14*, 866–869.
- [273] H. Zhu, B. Oswald, H. Fan, W. Roesky, Q. Ma, Z. Yang, H. G. Schmidt, M. Noltemeyer, K. Starke, N. S. Hosmane, *J. Am. Chem. Soc.*, **2006**, *128*, 5100–5108.
- [274] T. Back, *Tetrahedron*, **2001**, 5263–5301.
- [275] Y. Abel, E. Haake, G. Haake, W. Schmidt, D. Struve, A. Walter, F. P. Montforts, *Helv. Chim. Acta*, **1998**, *81*, 1978–1996.
- [276] D. Barton, J. Kervagoret, S. Zard, *Tetrahedron*, **1987**, 567–577.
- [277] D. Barton, S. Zard, *J. Chem. Soc. Chem. Commun.* **1985**, 1098–1100.
- [278] D. Barton, J. Kervagoret, S. Zard, *Tetrahedron* **1990**, *46*, 7587–7589.
- [279] N. Ono, H. Hironaga, K. Ono, S. Kaneko, T. Marashima, T. Ueda, C. Tsukamura, T. Ogawa, *J. Chem. Soc. Perkin Trans. 1* **1996**, 471–423.
- [280] S. Swavey, J. Quinn, M. Coladipietro, K. G. Cox, M. K. Brennaman, *RSC Adv.* **2017**, *7*, 173–179.
- [281] P. Kancharla, J. X. Kelly, K. A. Reynolds, *J. Med. Chem.*, **2015**, *58*, 7286–7309.
- [282] T. D. Lash, M. L. Thompson, T. M. Werner, J. D. Spence, *Tetrahedron Lett.*, **1994**, *35*, 2493–2494.
- [283] J. M. Manley, T. J. Roper, T. D. Lash, *J. Org. Chem.*, **2005**, *70*, 874–891.
- [284] S. Rao Allu, L. Ravotto, T. Troxler, S. A. Vinogradov, *J. Phys. Chem. A.*, **2021**, *15*, 2977–2988.
- [285] N. Bag, S.-S. Chern, S.-M. Peng, C. K. Chang, *Tetrahedron Lett.*, **1995**, *36*, 6409–6412.
- [286] Y. Kawamata, S. Ito, M. Furuya, K. Takahashi, K. Namai, S. Hashimoto, M. Roppongi, T. Oba, *Tetrahedron Lett.*, **2019**, *60*, 707–712.
- [287] M. A. Filatov, A. Y. Lebedev, S. N. Mukhin, S. A. Vinogradov, A. V. Cheprakov, *J. Am. Chem. Soc.*, **2010**, *132*, 9552–9554.
- [288] V. F. Donyagina, S. Shimizu, N. Kobayashi, E. A. Lukyanets, *Tetrahedron Lett.* **2008**, *49*, 6152–6154.

- [289] H. W. Heine, W. H. Graham, H. Berneth, S. Hünig, R. A. Moss, J. Wlostowska, W. Guo, M. Fedorynski, J. P. Springer, J. M. Hirshfield, K. Krogh-Jespersen, K. Krogh-Hespersen, C. M. Young, M. Wlostowski, *J. Am. Chem. Soc.*, **1985**, *107*, 1346-1358.
- [290] T. Roe, R. T. Oakley, R. W. Reed, *Tetrahedron Lett.*, **1987**, *28*, 1903-1906.
- [291] V. K. Aggarwal, T. Wirth., *J. Org. Chem.* , **2003**, *67*, 879-895.
- [292] M. Hellal, G. D. Cuny, *Tetrahedron Lett.* **2011**, *52*, 5508–5511.
- [293] O. Wallach, *Ber. Dtsch. Chem. Ges.*, **1981**, *24*, 2253–4270.
- [294] L. Yang, H. Luo, Y. Sun, Z. Shi, K. Ni, F. Li, D. Chen, *Synthesis*, **2017**, *49*, 2535.
- [295] C. J. Kirkpatrick, F. Bittinger, M. Wagner, H. Kohler, T. G. Van Kooten, C. L. Klein, M. Otto, *Proc. Inst. Mech. Eng. H* **1998**, *212*, 75–84.
- [296] D. F. Williams, *Biomaterials* **2008**, *29*, 2941–2953.
- [297] Dorland, *Dorland's Illustrated Medical Dictionary* , Elsevier, **2019**.
- [298] A. V. B. Pintor, L. D. Queiroz, R. Barcelos, L. S. G. Primo, L. C. Maia, G. G. Alves, *Int. Endod. J.* **2020**, *53*, 1348–1373.
- [299] H. J. Johnson, S. J. Northup, P. A. Seagraves, M. Atallah, P. J. Garvin, L. Lin, T. D. Darby, *J. Biomed. Mater. Res.* **1985**, *19*, 489–508.
- [300] Tim Mossmann, *J. Immunol. Methods* **1983**, *65*, 55–63.
- [301] H. R. Thom S., *J. Appl. Bacteriol.*, **1993**.
- [302] E. V. Garn H., *J. Immunol. Methods*, **1994**.
- [303] A. M. Brouwer, *Pure Appl. Chem.*, **2011**, *83*, 2213–2228.
- [304] N. Holmgaard List, J. Knoops, J. Rubio-Magnieto, J. Idé, D. Beljonne, P. Norman, M. Surin, M. Linares, *J. Am. Chem. Soc.* **2017**, *139*, 14947–14953.
- [305] K. W. Dunn, M. M. Kamocka, J. H. McDonald, *Am. J. Physiol. Cell. Physiol.* **2011**, *300*.
- [306] D. C. Barral, L. Staiano, C. Guimas Almeida, D. F. Cutler, E. R. Eden, C. E. Futter, A. Galione, A. R. A. Marques, D. L. Medina, G. Napolitano, C. Settembre, O. V. Vieira, J. M. F. G. Aerts, P. Atakpa-Adaji, G. Bruno, A. Capuozzo, E. De Leonibus, C. Di Malta, C. Escrevente, A. Esposito, P. Grumati, M. J. Hall, R. O. Teodoro, S. S. Lopes, J. P. Luzio, J. Monfregola, S. Montefusco, F. M. Platt, R. Polishchuck, M. De Risi, I. Sambri, C. Soldati, M. C. Seabra, *Traffic* **2022**, *23*, 238–269.

- [307] I. Canton, G. Battaglia, *Chem. Soc. Rev.* **2012**, *41*, 2718–2739.
- [308] D. Zhu, Z. Wang, S. Zong, Y. Zhang, C. Chen, R. Zhang, B. Yun, Y. Cui, *Theranostics* **2018**, *8*, 941–954.
- [309] J. B. Love, P. A. Salyer, A. S. Bailey, C. Wilson, A. J. Blake, E. S. Davies, D. J. Evans, *Chem. Comm.* **2003**, *3*, 1390–1391.
- [310] K. A. Ames, S. R. Collinson, A. J. Blake, C. Wilson, J. B. Love, D. W. Bruce, B. Donnio, D. Guillon, M. Schröder, *Chem. Eur. J. In. Chem.* **2008**, 5056–5066.
- [311] G. Givaja, M. Volpe, M. A. Edwards, A. J. Blake, C. Wilson, M. Schröder, J. B. Love, *Angew. Chem. Int. Ed.*, **2007**, *46*, 584–586.
- [312] J. B. Love, *Chem. Comm.*, **2009**, 3154–3165.
- [313] K. van Rees, J. B. Love, *Dalton Trans.* **2021**, *50*, 1610–1613.
- [314] N. A. M. Pereira, T. M. V. D. Pinho E Melo, *Org. Prep. Proced. Int.* **2014**, *46*, 183–213.
- [315] K. van Rees, J. B. Love, *Inorg. Chem.* **2022**, *61*, 3249–3255.
- [316] J. R. Pankhurst, T. Cadenbach, D. Betz, C. Finn, J. B. Love, *Dalton Trans.* **2015**, *44*, 2066–2070.
- [317] D. K. Jangid, *Curr. Green Chem.* **2019**, *7*, 146–162.
- [318] M. Baidya, S. Kobayashi, F. Brotzel, U. Schmidhammer, E. Riedle, H. Mayr, *Angew. Chem. Int. Ed.* **2007**, *46*, 6176–6179.
- [319] P. Wang, K. Chau Nguyen, J. S. Lindsey, *J. Org. Chem.* **2019**, *84*, 11286–11293.
- [320] J. R. Brown, A. B. Brown, *Modern Fluorescence Spectroscopy*, Springer US, **1976**.
- [321] E. D. Lemma, R. Tabone, K. Richler, A. K. Schneider, C. Bizzarri, F. Weth, C. M. Niemeyer, M. Bastmeyer, *ACS Appl. Mater. Interfaces* **2023**, *15*, 11, 14048–14057.
- [322] M. Hippler, E. D. Lemma, S. Bertels, E. Blasco, C. Barner-Kowollik, M. Wegener, M. Bastmeyer, *Adv. Mater.* **2019**, *31*, 26.
- [323] C. Barner-Kowollik, M. Bastmeyer, E. Blasco, G. Delaittre, P. Müller, B. Richter, M. Wegener, *Angew. Chem. Int. Ed.* **2017**, *56*, 15828–15845.
- [324] K. Dayanand, E. Atherton, *Physiol. Behav.*, **2018**, *176*, 139–148.
- [325] T. K. Claus, B. Richter, V. Hahn, A. Welle, S. Kayser, M. Wegener, M. Bastmeyer, G. Delaittre, C. Barner-Kowollik, *Angew. Chem. Int. Ed.*, **2016**, *55*, 3817–3822.

- [326] A. Vigovskaya, D. Abt, I. Ahmed, C. M. Niemeyer, C. Barner-Kowollik, L. Fruk, *J. Mater. Chem. B* **2016**, *4*, 442–449.
- [327] J. L. Charlton, M. M. Alauddin, *Tetrahedron* **1987**, *43*, 2873–2889.
- [328] S. Mandal, S. K. Ghosh, P. Sar, B. Saha, *RSC Adv* **2016**, *6*, 69605–69614.
- [329] T. Pauloehrl, G. Delaittre, V. Winkler, A. Welle, M. Bruns, H. G. Börner, A. M. Greiner, M. Bastmeyer, C. Barner-Kowollik, *Angew. Chem. Int. Ed.* **2012**, *51*, 1071–1074.
- [330] B. Briou, B. Améduri, B. Boutevin, *Chem. Soc. Rev.* **2021**, *50*, 11055–11097.
- [331] C. Baumann, N. Willis-Fox, D. Campagna, E. Rognin, P. Marten, R. Daly, R. Göstl, *J. Polym. Sci.* **2022**, *60*, 3128–3133.
- [332] B. Neises, W. Steglich, *Angew. Chem. Int. Ed. Engl.* **1978**, *17*.
- [333] A. Sakakura, K. Kawajiri, T. Ohkubo, Y. Kosugi, K. Ishihara, *J. Am. Chem. Soc.* **2007**, *129*, 14775–14779.
- [334] B. Gacal, H. Durmaz, M. A. Tasdelen, G. Hizal, U. Tunca, Y. Yagci, A. L. Demirel, *Macromolecules* **2006**, *39*, 5330–5336.
- [335] N. Alkayal, N. Hadjichristidis, *Polym. Chem.* **2015**, *6*, 4921–4926.
- [336] H. E. Gottlieb, V. Kotlyar, A. Nudelman, *J. Org. Chem.*, **1997**, *62*, 7512–7515.
- [337] G. R. Fulmer, A. J. M. Miller, N. H. Sherden, H. E. Gottlieb, A. Nudelman, B. M. Stoltz, J. E. Bercaw, K. I. Goldberg, *Organometallics* **2010**, *29*, 2176–2179.
- [338] J. N. Demas, G. A. Crosby, *J. Phys. Chem.* **1971**, *75*, 991–1025.
- [339] K. Lawson-Wood, S. Upstone, K. Evans, *J. Phys. Chem.*, **2018**, *76*.
- [340] J. C. Scaiano, *Handbook of Organic Photochemistry*, CRC Press, **1989**.

9. Appendix

9.1 Curriculum Vitae

EDUCATIONAL BACKGROUND

15/ 01/2020 – 07/2023	PhD student in Chemistry, Karlsruhe Institute of Technology. Funding project: GRK 2039, A4. Topic: “ <i>Far-red to near-infrared emitters for cell imaging</i> ”.
05/2022 - 08/2022	Visiting research period at the University of Edinburgh.
10/2017 - 10/2017	Master Degree in Industrial Chemistry, Alma Mater Studiorum, University of Bologna, Department “Toso Montanari”, Final grade: 110/110.
11/2013 - 03/2017	Bachelor Degree in Industrial Chemistry, University of Bologna, Department “Toso Montanary”, Final grade: 101/110
09/2007 - 07/2013	Liceo Classico V. Linares, Grade 97/100

EXPERIENCE

09/2021 – Today	Online Tutor. Teaching activities on scientific subjects
01/2017-01/2018	Laboratory technical assistant, University of Bologna, Department of Industrial Chemistry “Toso Montanari”
05/2017-10/2017	Research intern, Quality Control Team, Chemical Center

FELLOWSHIPS

05/2022 - 08/2023	<i>EaSI</i> CAT, East of Scotland Industrial Catalysis Scholarship, European Research Program
05/2022 - 08/2023	Research travel grant KHYS, Karlsruhe House of Young Scientists

LANGUAGES

Italian: mother language.

English: fluently spoken and written, C1 level.

German: A2.2 level.

9.2 Publications and conference contribution

Peer reviewed publications:

- **R. Tabone**, D. Feser, E. D. Lemma, U. Schepers, C. Bizzarri, *Front Chem* **2021**, *9*, DOI 10.3389/fchem.2021.754420.
- E. D. Lemma, **R. Tabone**, K. Richler, A. K. Schneider, C. Bizzarri, F. Weth, C. M. Niemeyer, M. Bastmeyer, *ACS Appl Mater Interfaces* **2023**, DOI 10.1021/acsami.2c23202.

Poster contributions:

- “*Far-red emitters for cell imaging*” - International School of Chemistry “Chemistry for Everyday Life”, (2020, online).

Oral contributions:

- “*Novel heteroleptic bis(dipyrrinato)Zn^{II} complexes as far-red emitters for live cell imaging*” International conference on photochemistry (ICP 2021, online).
- “*Interesting homo-and heteroleptic bis(dipyrrinato) Zn^{II} complexes for cell imaging*” Supramolecular Chemistry days for Young Researchers (2021, online).
- “*Far-red to near-infrared bis(dipyrrinato)Zn^{II} complexes for live-and fixed-cell imaging*” EuChemS Chemistry Congress (Lisbon 2022, in presence).

9.3 Acknowledgments

I do not believe that there is a standard formula for demonstrating appreciation and I hope that with these words I can effectively convey the range of emotions and feelings that have been with me throughout these three and a half years.

Firstly, I would like to cordially thank my doctoral supervisor, Dr. Claudia Bizzarri, to whom I express my deepest gratitude for her supervision during these years and for deeply correcting this thesis. I sincerely hope that her vision of chemistry and the academic world can come to fruition, and she can achieve the position she desires so dearly. I would also like to extend my appreciation to Prof. Stefan Bräse, who hosted me into his laboratory. I am truly thankful for his kindness and courtesy, accompanied by his witty remarks in Italian.

In addition to providing financial support, the GRK 2039 has also given me the opportunity to meet many new people and access to a wide range of courses, for which I am extremely grateful. In this regard, I would like to express my thanks to Prof. Wagenknecht and to Dr. Franziska Röncke for always being available and supportive.

I would like to thank Prof. Unterreiner for accepting to be co-supervisor of this thesis and for his utmost kindness and encouragement. Despite the demanding period, thanks to the help of Pascal, you both managed to make me feel supported, providing me with valuable insights that have been precious in shaping this thesis.

On that note, I am sincerely grateful to Dr. Afonin for his collaboration and invaluable support in proofreading and adding important comments in a portion of this thesis.

The period in Edinburgh has been one of the most beautiful and joyful windows of my doctoral journey. I am profoundly grateful to Prof. Love for being available from the very beginning in starting our collaboration and warmly welcoming into his group. I experienced a different academic world where students were prioritized over results. The view beyond the horizon of different types of chemistry shaped my chemical education extensively. Many thanks also to Susanne, Andrew, Joey and especially Tom for making your experience to carry out air-sensitive experiments without reclaiming something back; you have always supported me with great calm, making me feel very comfortable and at ease.

Christiane, Christin and Janine, thank you for always being so cheerful and sweet. You have helped me over the years with courtesy, even managing to overcome language barriers. I will always remember you with affection.

When I think back to the early stages of my PhD, I remember the moments with Jasmine Busch, her help characterized by her remarkable calmness and courtesy, with Stefan Marschner with whom I shared the laboratory and funny moments and with Susanne. My dear “zuccherina” you are the person who made me feel the most welcome when I arrived here. Thank you for making me feel included and for encouraging others to speak in English to include me. I admire you for your incredible strength and sensitivity. I am pleased for our friendship.

Over the years I have met many people. Philipp, Cecilia and Julia, during the last period I was thinking back to our lunches together, our laughter and our friendship. Julia, with your almost supernatural cheerfulness, you always involved me, bringing a smile to my face and making me feel lighter.

Cecilia, how many hours we spent together, experiencing all the different facets of emotions, through both the ups and downs. We have changed and grown significantly over the years, and despite everything, I will remember you with great fondness. I hope you can find yourself, aware that you still have a world to discover.

Philipp, I cannot even count the moments we have shared together. From the most fun to the saddest, you have been a wonderful lab mate and friend. With you, I have gone from tears to laughter in two seconds. Thank you for always being there to help me with anything, for your kindness and sweetness. Sometimes I even forgot you are the younger one. You will always hold a special place in my hearth and I hope you find your path in life. You are a wonderful person and worth more than you realize.

On one hand, I think it is right to bring this journey to the end, as is the nature of all things in life. On the other hands, I am saddened to leave the group of people I have found, especially Jasmine S., Janine, Yuting and Mike. Thank you for being there for me with kindness, especially during the latest difficult moments and being such valuable friend. Dear Jasmine, even though you may sometimes appear strict, I know that deep down you have a sensitive side and I am glad that you have shared this with me. Janine, your sweetness has amazed me day after day, always being understanding during moments when I felt misunderstood by everyone else. Yuting and Mike, I love when you speak in Chinese and have lively discussions. Yuting, in addition to being my fashion guru, I adore your sincerity and straightforwardness,

accompanied by incredible kindness. Mike, I appreciate your peculiar way of showing affection and your tenacity.

Valentina, I cannot explain how much I regret that you arrived only recently. In this final period, you have helped me tremendously and I will be forever grateful to you. I am confident that you will go far in life.

Aleo, I have known you for a short time, but we share an incredible sensitivity. Thank you for being so friendly and helpful with me.

Dear Roman, you are exactly the person that comes to mind whenever a chemical problem arises. I always think “Roman surely knows this”. Thank you for all the assistance, our brainstorming sessions on challenging syntheses and the conversations we have had in our labs or in the IOC corridor.

I have had many students over the course of my PhD, through thesis supervision and practical works. The ones I will always carry with me are Cedric, my first student, who has always been marked by extreme kindness; Verena, who never gave up despite the challenging project and showed great determination; and Rabia, who was helping me during these months of thesis writing with her reserved and sensitive nature, becoming very independent and precious.

Mom, you are my anchor, and Angelo you are my giant, always by my side.

And then there is my Italian gang, composed of Enrico, Gian, Federico, Celeste, Michela, Noelia, Luisa and Gabriella, those who have always been my side, for whom I have so much more in store.